CHANGING THE PERSPECTIVES OF NOBLE GAS REACTIVITY

EDITED BY: Sudip Pan, Pratim Kumar Chattaraj and Gabriel Merino
PUBLISHED IN: Frontiers in Chemistry and Frontiers in Physics

frontiers Research Topics

ISSN 1664-8714
ISBN 978-2-88966-817-5
DOI 10.3389/978-2-88966-817-5

About Frontiers

Frontiers is more than just an open-access publisher of scholarly articles: it is a pioneering approach to the world of academia, radically improving the way scholarly research is managed. The grand vision of Frontiers is a world where all people have an equal opportunity to seek, share and generate knowledge. Frontiers provides immediate and permanent online open access to all its publications, but this alone is not enough to realize our grand goals.

Frontiers Journal Series

The Frontiers Journal Series is a multi-tier and interdisciplinary set of open-access, online journals, promising a paradigm shift from the current review, selection and dissemination processes in academic publishing. All Frontiers journals are driven by researchers for researchers; therefore, they constitute a service to the scholarly community. At the same time, the Frontiers Journal Series operates on a revolutionary invention, the tiered publishing system, initially addressing specific communities of scholars, and gradually climbing up to broader public understanding, thus serving the interests of the lay society, too.

Dedication to Quality

Each Frontiers article is a landmark of the highest quality, thanks to genuinely collaborative interactions between authors and review editors, who include some of the world's best academicians. Research must be certified by peers before entering a stream of knowledge that may eventually reach the public - and shape society; therefore, Frontiers only applies the most rigorous and unbiased reviews.
Frontiers revolutionizes research publishing by freely delivering the most outstanding research, evaluated with no bias from both the academic and social point of view. By applying the most advanced information technologies, Frontiers is catapulting scholarly publishing into a new generation.

What are Frontiers Research Topics?

Frontiers Research Topics are very popular trademarks of the Frontiers Journals Series: they are collections of at least ten articles, all centered on a particular subject. With their unique mix of varied contributions from Original Research to Review Articles, Frontiers Research Topics unify the most influential researchers, the latest key findings and historical advances in a hot research area! Find out more on how to host your own Frontiers Research Topic or contribute to one as an author by contacting the Frontiers Editorial Office: frontiersin.org/about/contact

CHANGING THE PERSPECTIVES OF NOBLE GAS REACTIVITY

Topic Editors:
Sudip Pan, University of Marburg, Germany
Pratim Kumar Chattaraj, Indian Institute of Technology Kharagpur, India
Gabriel Merino, Center for Research and Advanced Studies - Mérida Unit, Mexico

Citation: Pan, S., Chattaraj, P. K., Merino, G., eds. (2021). Changing the Perspectives of Noble Gas Reactivity. Lausanne: Frontiers Media SA.
doi: 10.3389/978-2-88966-817-5

Table of Contents

frontiers in Chemistry

EDITORIAL
published: 26 March 2021
doi: 10.3389/fchem.2021.658318

Editorial: "Changing the Perspective of the Noble Gas Reactivity"

Sudip Pan[1,2]*, *Gabriel Merino*[3]* and *Pratim K. Chattaraj*[4,5]*

[1]Institute of Advanced Synthesis, School of Chemistry and Molecular Engineering, Jiangsu National Synergetic Innovation Center for Advanced Materials, Nanjing Tech University, Nanjing, China, [2]Fachbereich Chemie, Philipps-Universitt Marburg, Hans-Meerwein-Straße, Marburg, Germany, [3]Departamento de Física Aplicada, Centro de Investigación y de Estudios Avanzados, Unidad Mérida, Mérida, Mexico, [4]Department of Chemistry, Indian Institute of Technology Kharagpur, Kharagpur, India, [5]Department of Chemistry, Indian Institute of Technology Bombay, Mumbai, India

Keywords: Reactivity, Noble gas, Fullerene (C_{60}), Bonding, Structure

Editorial on the Research Topic

Changing the Perspective of the Noble Gas Reactivity

Noble gas (Ng) is undoubtedly a lazy element in the periodic table to show any kind of chemical reactivity toward other chemical entities because of its completely filled valence electronic shell, and large ionic potential and low electron affinity. Thanks to the recent advancements both in the experimental and theoretical domains, it is now known that one can force them to work with the proper chemical environment, and so a noble gas is no longer very "noble" (Grochala, 2007; Khriachtchev et al., 2009; Brock and Schrobilgen, 2013; Pan et al., 2014; Pan et al., 2019; Saha et al., 2019; Jalife et al., 2020). Since with an increase in the size of Ng atoms, the outer electronic shell is more loosely bound by nucleus, and therefore the heavier Ng atoms have better aptitude to take part in bonding with other elements. The compounds of Kr, Xe, and Rn are well-known, albeit to a smaller number for the latter case because of the associated radioactivity. The first Ar compound, HArF was only isolated in 2000 in a low-temperature Ar matrix (Khriachtchev et al., 2000). Ne was reported to form very weak complexes with highly electrophilic centers as in NeAuF, NeBeS, $NeBeCO_3$, $NeBeSO_2$, $(Ne)_2Be_2O_2$, $(NeAr)Be_2O_2$, and $(NeKr)Be_2O_2$ (Zhang et al., 2014; Yu et al., 2016; Zhang et al., 2017). In a remarkable study, recently Dong et al. synthesized solid compound of helium and sodium Na_2He at a high pressure (Dong et al., 2017). Therefore, presently all the members of Ng group are known to form chemical bonds. The aim of the present research topic is to highlight the present status of the noble gas chemistry to the readers as well as to report new molecules of Ng and the study of bonding therein. This collection includes nine articles involving 48 authors, among them three are minireviews and six are original articles.

The minireview by Grandinetti summarizes the contributions made in the cationic noble gas hydrides, which are relevant in outer space (Grandinetti, 2020). The author beautifully shows the structure, stability and mode of formation of different such species that range from simple NgH^+ diatomic molecule to $(H_3^+)(Ng)_n$. In a comprehensive review, Sanloup elaborates how high temperature and high pressure in planetary interiors induce interesting reactivity in Ng atoms (Sanloup, 2020). This review shows different kind of cage compounds, stoichiometric oxides and metals, and non-stoichiometric compounds having Ng atoms (mostly Xe and in some cases He) which are formed in planetary interiors. Xe was found to take part in a different kind of bonding, however, helium does not take part in bonding. Another review by Miao plays the same tone that Ng can display a nice variety of chemistry under pressure (Miao, 2020). He highlights the types of chemical roles and interactions that Ng exhibits under high pressure, including their oxidizing and reducing properties, Ng-Ng bond formation, aerogen bonding, and reliever of repulsive electrostatic interactions. In an elegant perspective article, Warneke and co-workers elaborated their

OPEN ACCESS

Edited and reviewed by:
Michal Fárník,
J. Heyrovsky Institute of Physical Chemistry (ASCR), Czechia

Correspondence:
Sudip Pan
pans@chemie.uni-marburg.de
Gabriel Merino
gmerino@cinvestav.mx
Pratim K. Chattaraj
pkc@chem.iitkgp.ac.in

Specialty section:
This article was submitted to Physical Chemistry and Chemical Physics, a section of the journal Frontiers in Chemistry

Received: *25 January 2021*
Accepted: *01 February 2021*
Published: *26 March 2021*

Citation:
Pan S, Merino G and Chattaraj PK (2021) Editorial: "Changing the Perspective of the Noble Gas Reactivity". Front. Chem. 9:658318. doi: 10.3389/fchem.2021.658318

contributions where anionic systems act as superb electrophiles to bind Ng atoms (Rohdenburg et al., 2020).

Zhang et al. in their study on the bonding in HXeY (Y = Cl, Br, I) and HXeY HX (X = OH, Cl, Br, I, CN, CCH) introduced another view on the H-Xe bond (Zhang et al., 2020). They argued that the H-Xe bond in HXeY is not a classical covalent bond rather a charge-shift bond. In their contribution, Gomila and Frontera showed the systems having "noble gas bond" where an Ng center acts as a Lewis acid (Gomila and Frontera, 2020). On the other hand, Ghara and Chattaraj theoretically proposed viable Ng-Au complexes where frustrated Lewis pair is also involved (Ghara and Chattaraj, 2020). Special emphasis is made on the related bonding situation. In a couple of contributions, Liu and co-workers (Li et al., 2020), and Sarkar and co-workers (Paul et al., 2020) studied confinement effects on the bonding and reactivity of Ng_2 inside fullerenes.

As guest editors, we would like to thank all the contributing authors, particularly for their work in this pandemic time. We hope that this collection of noble gas chemistry will provide an excellent account of the present state-of-the-art in this field.

AUTHOR CONTRIBUTIONS

All authors listed have made a substantial, direct, and intellectual contribution to the work and approved it for publication.

REFERENCES

Brock, D. S., and Schrobilgen, G. J. (2013). "Noble-gas chemistry," in *Comprehensive inorganic chemistry II. Chapter 1.25*. Editors J. Reedijk and K. Poepplemeier (Oxford, United Kingdom: Elsevier), 1, 755–822.

Dong, X., Oganov, A. R., Goncharov, A. F., Stavrou, E., Lobanov, S., Saleh, G., et al. (2017). A stable compound of helium and sodium at high pressure. *Nat. Chem* 9, 440–445. doi:10.1038/nchem.2716

Grochala, W. (2007). Atypical compounds of gases, which have been called "noble". *Chem. Soc. Rev.* 36, 1632. doi:10.1039/b702109g

Jalife, S., Arcudia, J., Pan, S., and Merino, G. (2020). Noble gas endohedral fullerenes. *Chem. Sci.* 11, 6642–6652. doi:10.1039/d0sc02507k

Khriachtchev, L., Pettersson, M., Runeberg, N., Lundell, J., and Räsänen, M. (2000). A stable argon compound. *Nature* 406, 874. doi:10.1038/35022551

Khriachtchev, L., Räsänen, M., and Benny, R. B. (2009). Noble-gas hydrides: new chemistry at low temperatures. *Acc. Chem. Res.* 42, 183–191. doi:10.1021/ar800110q

Pan, S., Jana, G., Merino, G., and Chattaraj, P. K. (2019). Noble-noble strong union: gold at its best to make a bond with a noble gas atom. *ChemistryOpen* 8, 173–187. doi:10.1002/open.201800257

Pan, S., Moreno, D., Merino, G., and Chattaraj, P. K. (2014). Stability of the noble gas bound SiH_3^+ clusters. *ChemPhysChem.* 15, 3554–3564. doi:10.1002/cphc.201402370

Saha, R., Jana, G., Pan, S., Merino, G., and Chattaraj, P. K. (2019). How far can one push the noble gases towards bonding? a personal account. *Molecules* 24, 2933. doi:10.3390/molecules24162933

Sanloup, C. (2020). Noble gas reactivity in planetary interiors. *Front. Phys.* 8, 157. doi:10.3389/fphy.2020.00157

Yu, W., Liu, X., Xu, B., Xing, X., and Wang, X. (2016). Infrared spectra of novel $NgBeSO_2$ complexes (Ng = Ne, Ar, Kr, Xe) in low temperature matrixes. *J. Phys. Chem. A.* 120, 8590–8598. doi:10.1021/acs.jpca.6b08799

Zhang, Q., Chen, M., Zhou, M., Andrada, D. M., and Frenking, G. (2014). Experimental and theoretical studies of the infrared spectra and bonding properties of $NgBeCO_3$ and a comparison with NgBeO (Ng = He, Ne, Ar, Kr, Xe). *J. Phys. Chem. A.* 119, 2543–2552. doi:10.1021/jp509006u

Zhang, Q., Li, W.-L., Zhao, L., Chen, M., Zhou, M., Li, J., et al. (2017). A very short Be-Be distance but No bond: synthesis and bonding analysis of Ng-Be_2 O_2 -Ng′ (Ng, Ng′=Ne, Ar, Kr, Xe). *Chem. Eur. J.* 23, 2035–2039. doi:10.1002/chem.201605994

Conflict of Interest: The authors declare that the research was conducted in the absence of any commercial or financial relationships that could be construed as a potential conflict of interest.

frontiers in Chemistry

ORIGINAL RESEARCH
published: 23 April 2020
doi: 10.3389/fchem.2020.00277

Charge-Shift Bonding in Xenon Hydrides: An NBO/NRT Investigation on HXeY···HX (Y = Cl, Br, I; X = OH, Cl, Br, I, CCH, CN) via H-Xe Blue-Shift Phenomena

Guiqiu Zhang, Yue Su, Xiaoran Zou, Lei Fu, Junjie Song, Dezhan Chen and Chuanzhi Sun**

Key Laboratory of Molecular and Nano Probes, College of Chemistry, Chemical Engineering and Materials Science, Collaborative Innovation Center of Functionalized Probes for Chemical Imaging, Ministry of Education, Shandong Normal University, Jinan, China

OPEN ACCESS

Edited by:
Sudip Pan,
University of Marburg, Germany

Reviewed by:
Felice Grandinetti,
University of Tuscia, Italy
Gabriel Merino,
Centro de Investigacion y de Estudios Avanzados–Unidad Mérida, Mexico
Lili Zhao,
Nanjing Tech University, China

***Correspondence:**
Guiqiu Zhang
gqzhang@sdnu.edu.cn
Chuanzhi Sun
suncz@sdnu.edu.cn

Specialty section:
This article was submitted to Physical Chemistry and Chemical Physics, a section of the journal Frontiers in Chemistry

Received: *04 February 2020*
Accepted: *23 March 2020*
Published: *23 April 2020*

Citation:
Zhang G, Su Y, Zou X, Fu L, Song J, Chen D and Sun C (2020) Charge-Shift Bonding in Xenon Hydrides: An NBO/NRT Investigation on HXeY···HX (Y = Cl, Br, I; X = OH, Cl, Br, I, CCH, CN) via H-Xe Blue-Shift Phenomena. Front. Chem. 8:277. doi: 10.3389/fchem.2020.00277

Noble-gas bonding represents curiosity. Some xenon hydrides, such as HXeY (Y = Cl, Br, I) and their hydrogen-bonded complexes HXeY···HX (Y = Cl, Br, I; X = OH, Cl, Br, I, CN, CCH), have been identified in matrixes by observing H-Xe frequencies or its monomer-to-complex blue shifts. However, the H-Xe bonding in HXeY is not yet completely understood. Previous theoretical studies provide two answers. The first one holds that it is a classical covalent bond, based on a single ionic structure $H\text{-}Xe^{+}\ Y^{-}$. The second one holds that it is resonance bonding between $H\text{-}Xe^{+}\ Y^{-}$ and $H^{-}\ Xe^{+}\text{-}Y$. This study investigates the H-Xe bonding, via unusual blue-shifted phenomena, combined with some NBO/NRT calculations for chosen hydrogen-bonded complexes HXeY···HX (Y = Cl, Br, I; X = OH, Cl, Br, I, CN, CCH). This study provides new insights into the H-Xe bonding in HXeY. The H-Xe bond in HXeY is not a classical covalent bond. It is a charge-shift (CS) bond, a new class of electron-pair bonds, which is proposed by Shaik and Hiberty et al. The unusual blue shift in studied hydrogen-bonded complexes is its H-Xe CS bonding character in IR spectroscopy. It is expected that these studies on the H-Xe bonding and its IR spectroscopic property might assist the chemical community in accepting this new-class electron-pair bond concept.

Keywords: chemical bonding, charge-shift bonds, electron-pair bonds, resonance bonding, noble-gas hydride, hypervalent molecule, blue shifts, NBO/NRT methods

INTRODUCTION

The chemical bond is the most central concept in chemistry. The model of chemical bonding can help chemists to understand and design matter. Despite the apparent utility of the model of chemical bonding, it is incomplete. Developing bonding models is undoubtedly important to our understanding of novel molecules, such as the molecules of noble gas chemistry (Grandinetti, 2018).

The challenge to noble-gas bonding comes mainly from the inertness of noble-gas atoms. However, significant progress has been made in noble-gas chemistry during the past 20 years. Besides noble-gas hydrides (Khriachtchev et al., 2009), noble gas–noble metal complexes have been studied for their thermodynamic and kinetic stabilities in theory (Jana et al., 2017, 2018a,b; Pan et al., 2019; Saha et al., 2019). Experimentally, about 30 noble-gas hydrides had been identified by

the beginning of 1995 (Pettersson et al., 1995; Räsänen et al., 2000; Lundell et al., 2002; Feldman et al., 2003; Khriachtchev et al., 2003, 2009; Duarte and Khriachtchev, 2017). About 10 hydrogen-bonded complexes between HNgY (Ng = Xe, Kr) and H_2O/HCl/HBr/HI/HCCH have been well-characterized via infrared (IR) spectroscopy. Interestingly, these complexes show unusual shifts of the H-Xe stretching vibration. For example, the H-Xe stretching mode of the complex HXeI···HCCH exhibits a blue shift of 49 cm^{-1}, in comparison with the monomer HXeI (Zhu et al., 2015). Some other complexes such as HXeBr···H_2O and HXeI···H_2O are characterized by much larger experimental blue shifts of the H-Xe stretching frequency (>100 cm^{-1}) (Tsuge et al., 2014). The largest blue shift (300 cm^{-1}) has been reported for the H-Kr stretching mode of the complex HKrCl···HCl (Corani et al., 2009). These experimental findings provide theoretical chemistry researchers with excellent opportunities to develop a bonding model for noble-gas hydrides.

In pioneering theoretical work, Last and George put forward one simple ionic structure model H-Ng^+Y^- (Last and George, 1988), where H-Ng^+ belongs to a classical covalent bond, to be exact, an electron-sharing bond, while the interaction between H-Ng^+ and Y^- comes from electrostatic attraction. Energy decomposition analyses (EDAs) carried out by Frenking for HArF provided a consistent bonding picture (Lein et al., 2004). Besides this ionic structure model, empirical resonance bonding models were proposed by Räsänen's group (Pettersson et al., 1999) and Alabugin's group (Alabugin et al., 2004). Recently, our group has carried out the resonance bonding analyses for noble-gas hydrides (Zhang et al., 2016) by using Natural Bond Orbital (NBO) and Natural Resonance Theory (NRT) methods (Glendening and Weinhold, 1998a,b; Glendening et al., 1998, 2001, 2013a,b; Weinhold and Klein, 2014; Weinhold et al., 2016). We found that each molecule HNgY could be best described as three structures, H-Xe^+Y^-, H^-Xe^+-Y, and H^Y, where the first two resonance structures mix to form hyperbonding of H-Xe^+Y^- ↔ H-Xe^+-Y, as proposed by Weinhold and Landis (2005b). Such bonding provides a picture of resonance covalency for noble-gas hydrides (Weinhold and Klein, 2012, 2014; Landis and Weinhold, 2013; Zhang et al., 2015, 2017a; Jiao and Weinhold, 2019).

It is important to note that they are two variants of covalent bonding, which are related to two kinds of electron-pair bonds. They are our familiar electron-sharing bonds and dative bonds. The difference between these two types of bonds is due to the origin of the bonding electrons. In electron-sharing bonds, each fragment provides one electron. In dative bonds, both electrons come from one fragment, which donates two electrons to the vacant orbital of the other. Also note that besides our familiar electron-sharing bonds and dative bonds there is one new kind of electron-pair bonds, charge-shift (CS) bonds. The concept of charge-shift bonds was first proposed by Shaik and Hiberty et al. in 1992, to describe a new-class electron-pair bonds, such as F_2 (Shaik et al., 1992). Ten years later, they further presented experimental manifestations of CS bonding (Shaik et al., 2005, 2009). They have applied the concept of CS bonds to the understanding of bonding and stabilities of several hypervalent molecules (Braïda and Hiberty, 2013; Braïda et al., 2014), such as XeF_2. In 2018, Grandinetti pointed out that a stabilization like HNgY is, generally, known as CS bonding (Grandinetti, 2018). Indeed, the decades following their original work saw more CS bonding molecules. Very recently, they published their latest review on CS bonds (Shaik et al., 2020).

Given that XeF_2 and HXeY are similar in geometrical and electronic structures, two obvious questions arise: (1) Is the H-Xe bond in HXeY a charge-shift bond? (2) What is the H-Xe CS bonding character in IR spectroscopy? This study explores these two questions through blue-shifted phenomena, with the help of NBO/NRT analyses. We choose HXeY···HX (Y = Cl, Br, I; X = OH, Cl, Br, I, CN, CCH) as study systems. Some of them are identified in the matrix experiment. We analyze the relationship between the H-Xe bonding and H-Xe blue shifts. We aim to understand the H-Xe bonding in HXeY and to extend CS bonding concepts to noble-gas hydrides.

This paper will be organized as follows. Firstly, we summarize the computational details and discuss the geometrical structural details and H-Xe IR spectroscopic properties for our studied monomers and complexes. Secondly, we analyze the resonance bonding of HXeY, especially for the bonding between H and Xe. Thirdly, we analyze the H-Xe bond order. And we determine that the H-Xe bond order must include the contributions of two resonance structures. Fourthly, we confirm that the H-Xe in HXeY is a charge-shift bond, and further analyze its CS bonding character. Finally, we present the concluding summary, with emphasis on the H-Xe CS bonding and its bonding character.

COMPUTATIONAL DETAILS

The geometry optimization and vibrational frequency calculations were carried out with the Gaussian 09 program at the level of the second order MØller-Plesset perturbation theory (MP2) (Head-Gordon et al., 1988; Frisch et al., 2009). The def2-TZVPPD basis set was used. This basis set, taken from the EMSL basis set library (Feller, 1996; Schuchardt et al., 2007), is the triple-zeta-valence basis set augmented with two sets of polarization and diffuse basis functions. No imaginary frequencies were found in any case, which confirms that our obtained structures are true local minima on the potential energy surface. The NBO and NRT were employed to analyze the bonding of our studied systems with the NBOPro 6.0 program (Glendening and Weinhold, 1998a,b; Weinhold, 2012, 2013). Directed NBO analyses could provide the second order perturbation energy of a donor-acceptor interaction in the best Lewis structure. For any other resonance structure, we use $CHOOSE keylist to calculate the second order perturbation energy of a donor-acceptor interaction. It is important to attach the $NRTSTR keylist in NRT analyses, for it insures a consistent set of reference structures for NRT comparisons of studied complexes. The NBO-based natural resonance theory complements and extends NBO analyses to other resonance structures. By using $NRTSTR keylist to specify key structures as reference structures, we can obtain accurate weightings (ω_I, ω_{II}, ω_{III}...) of resonance structures, and NRT bond orders (b_{AB}) that express the strength of resonance-weighted chemical bonds

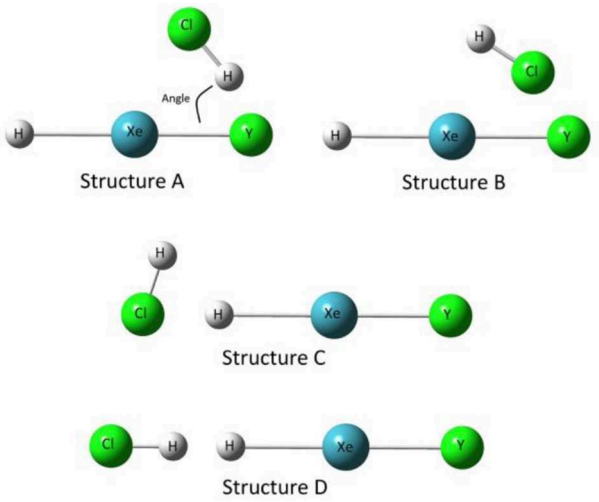

FIGURE 1 | Four structures of complexes HXeY···HCl (Y = Cl, Br, I).

between any atom pair. More importantly, the NBO/NRT-based models provide a framework for analyzing chemical bonding in terms of familiar concepts, such as Lewis structures, resonance, and donor-acceptor interactions. Herein, we use NBO/NRT methods to analyze H-Xe bonding. Besides, the NBOview 2.0 module was acquired to obtain the orbital overlap graphics.

RESULTS AND DISCUSSIONS

Geometry and Blue Shifts

In general, four structures need to be considered for each of the complexes HXeY···HX (Y = Cl, Br, I; X = OH, Cl, Br, I, CN, CCH). Take HXeY···HCl, as shown in **Figure 1**, as one representative example. In the first two structures (A and B), the HCl moiety is closed to the halogen atom of the monomer HXeY to form a bent structure. Structure A is stabilized with the Cl-H•••Y hydrogen bond, whereas Structure B is dependent on the Xe-Y•••Cl halogen bond. Structure C, whose halogen atom in the moiety is collinear with the monomer HXeY, is formed by the Cl atom interacting with the H atom. Structure D is stabilized with the dihydrogen Cl-H•••H-Xe bond with all atoms in line. Experimentally, it has been observed that several infrared absorption bands originate from the H-Xe stretching mode for our chosen complexes. With the aid of quantum chemical calculations, they are assigned to Structure A (Lignell et al., 2008; Tsuge et al., 2013, 2014; Zhu et al., 2015). Therefore, the following analyses are restricted to Structure A.

As shown in Structure A in **Figure 1**, HXeY maintains its original linear structure for all the HXeY···HX (Y = Cl, Br, I; X = OH, Cl, Br, I, CN, CCH) optimized geometry. At the MP2/def2-TZVPPD level, the calculated H-Xe and Xe-Y bond lengths (R_{H-Xe}, R_{Xe-Y}) and vibrational frequency shifts of H-Xe stretching mode in complexes HXeY···HX (Y = Cl, Br, I; X = OH, Cl, Br, I, CN, CCH) as well as in monomers HXeY are collected in **Table S1** and compared with the available experimental data. Note that Räsänen's group has computed R_{H-Xe} and R_{Xe-Y} as well as a variety of H-Xe frequency blue shifts for some of the complexes HXeY···HX (Y = Cl, Br, I; X = OH, Cl, Br, I, CN, CCH) at the CCSD(T) level. The difference in calculated H-Xe bond lengths at both MP2 and CCSD(T) levels is <0.060 Å, whereas for Xe-Y bond lengths the largest difference is 0.048 Å in the monomer HXeI. These comparisons show that the MP2/def2-TZVPPD is an appropriate model chemistry for this study. Thus, the following discussion will be based on the calculated data at the MP2/def2-TZVPPD level.

Data in **Table S1** show that the complexation has non-negligible influences on monomers HXeY. On the one hand, the bond lengths of H-Xe in complexes become shorter as compared with the value in the corresponding HXeY monomer. Taking HXeCl species as one example, H-Xe bond lengths R_{H-Xe} in complexes are 1.646, 1.645, 1.644, 1.646, 1.648, and 1.655 Å for HX = H_2O/HCl/HBr/HI/HCN/HCCH, respectively, while the H-Xe bond length of the monomer HXeCl is 1.666 Å. This indicates that the interaction between H and Xe atoms in monomers HXeY is weaker than that in corresponding complexes HXeY···HX (Y = Cl, Br, I; X = OH, Cl, Br, I, CN, CCH). On the contrary, the bond lengths of Xe-Y within complexes are slightly larger than that in the corresponding monomer HXeY, which means that the interaction between Xe and Y atoms is stronger in monomers than in corresponding complexes. It is worthwhile noting that the calculated R_{H-Xe} ranges from 1.644 to 1.708 Å, slightly larger than the covalent limits $R_{cov}[r_{cov}(H)+r_{cov}(Xe)]$ for 1.63 Å and significantly shorter than VdW limits $R_{vdw}[r_{vdw}(H)+r_{vdw}(Xe)]$ for 3.86 Å (Pyykkö, 2015; Rahm et al., 2016). This indicates strong covalency of the H-Xe bond.

On the other hand, the complexation leads to experimentally observable blue shifts of the H-Xe stretching frequency, which seems to be normal phenomena according to Khriachtchev's group studies. The calculated and experimental vibrational frequency shifts of the H-Xe stretching mode are also collected in **Table S1**. Taking hydrogen-bonded complexes HXeCl···H_2O, HXeBr···H_2O and HXeI···H_2O as one example group, calculations at the MP2 level predict blue shifts of 101, 116, and 139 cm^{-1}, respectively. The experimental data are 82, 101, and 138 cm^{-1}, respectively. Obviously, the calculated complexation-induced spectroscopic shift of the H-Xe stretching mode at the MP2 level is in qualitative agreement with the experimental values. These preliminary structural and blue-shifted analyses provide the backdrop for the following exploration of H-Xe bonding for Xe hydrides.

H-Xe Resonance Bonding in HXeY

Earlier studies have found that the NBO/NRT method is a helpful tool to explore the resonance bonding because NBO analyses can provide the best Natural Lewis Structure (NLS), identify donor-acceptor orbital interactions, and estimate the second-order perturbation energy [$E^{(2)}$] of each donor-acceptor orbital interaction (Glendening et al., 2013a,b; Weinhold, 2013; Weinhold et al., 2016).

Our studies begin with NBO/NRT analyses for HXeY species. The results show that each of the studied HXeY could be better described as a hybrid of the three structures (I,II,and III) as

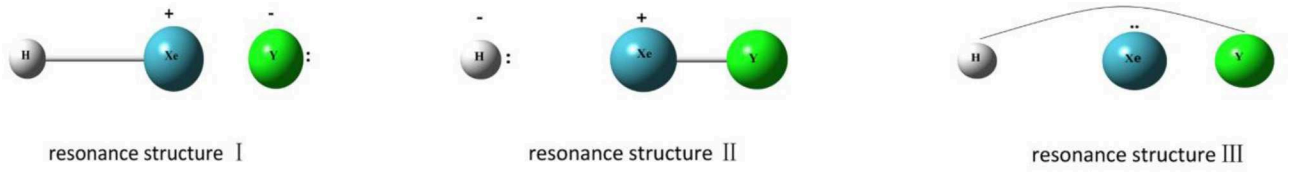

FIGURE 2 | Three resonance structures for HXeY. A pair of dots represents a lone pair.

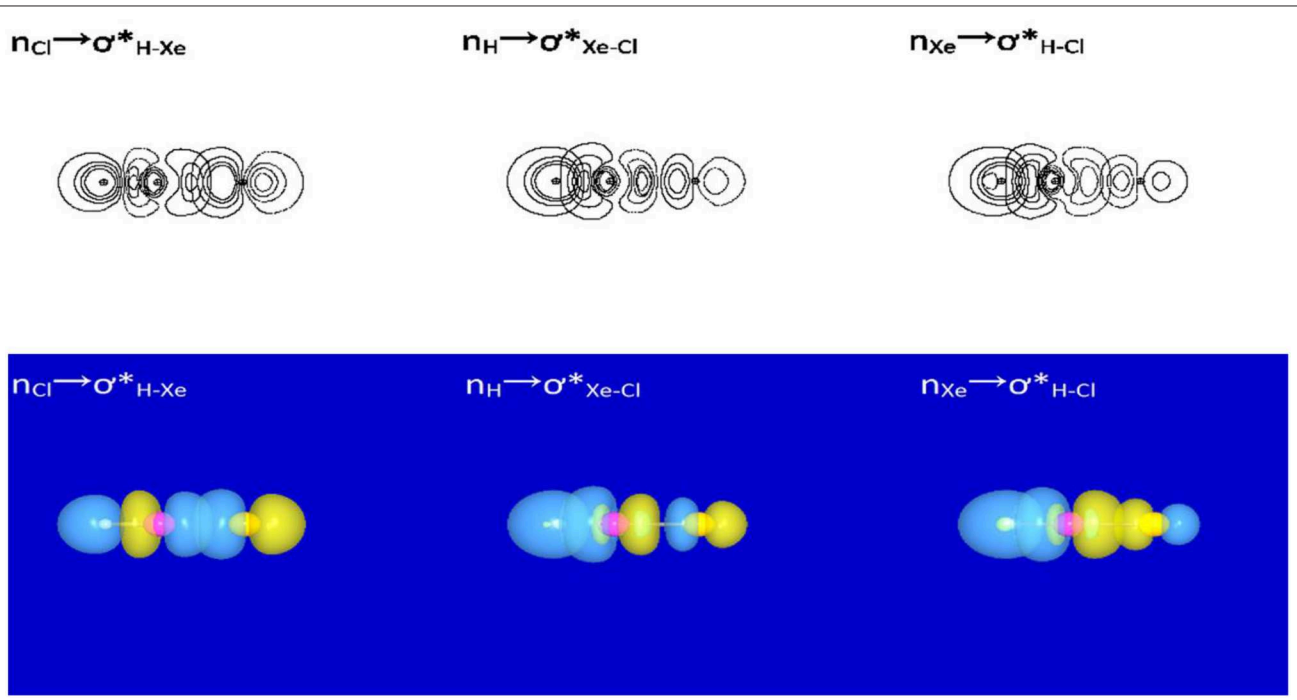

FIGURE 3 | NBO orbital contour diagrams and 3-D surface views of donor-acceptor interactions for HXeCl.

shown in **Figure 2**, where the H-Xe^+:Y^- (I) is the best NLS. **Table S2** lists three types of donor-acceptor interactions and the value of the second-order perturbation energies [$E^{(2)}$] of the studied HXeY. For the best NLS H-Xe^+:Y^- (I), the donor-acceptor interaction ($n_Y \rightarrow \sigma^*_{H-Xe}$) takes place between the lone pair orbital of Y (n_Y) and the antibonding orbital of H-Xe moiety (σ^*_{H-Xe}). Pay particular attention to such a delocalization interaction. It represents resonance mixing between H-Xe^+:Y^- (I) and H:$^-$ Xe^+-Y (II), where the latter corresponds to the lone pair of H atom (n_H) delocalizing to the antibonding orbital of Xe-Y moiety (σ^*_{Xe-Y}). As proposed by Weinhold et al., these two structures make up resonance bonding. Additionally, there is a non-negligible long-bonding structure H^Y (III), shown in the final entry in **Figure 2**. It arises from the delocalization of Xe atom lone pair (n_{Xe}) to the antibonding orbital of H-Y moiety (σ^*_{H-Y}). Special attention is paid to the unusual values of $E^{(2)}$ for $n_{Xe} \rightarrow \sigma^*_{H-Y}$ and $n_H \rightarrow \sigma^*_{Xe-Y}$ interactions. Such results show that they are no longer suitable for the description of low-order perturbative NLS limit. Even in the unavailable value of some second-order perturbation energies, the importance of these three donor-acceptor interactions can be exhibited by the orbital overlap contour diagrams or 3-D surface views. **Figure 3** presents one illustrative example. These results are consistent with our previous studies for HXeY noble-gas hydrides (Y = Cl, Br, I) at the B3LYP level of theory (Zhang et al., 2016).

Once again, the importance of resonance bonding H-Xe^+ Y^- ↔ H^- Xe^+-Y is emphasized. On the one hand, resonance bonding is an essential feature of H-Xe bonding in HXeY. On the other hand, we note that earlier studies on the bonding of noble-gas hydrides have already analyzed the leading resonance structure H-Xe^+ Y^- (Pérez-Peralta et al., 2009; Juarez et al., 2011). In the next section, we will carry out detailed analyses on H^- Xe^+-Y, as well as H-Xe^+ Y^-.

H-Xe Bond in HXeY Is Not a Classical Covalent Bond

HXeY is a particularly simple and interesting molecule. Its H-Xe stretching modes provide experimental probes to learn more about the bonding of noble-gas hydrides. It was reported that the H-Xe stretching vibration frequencies of HXeY species are blue shifts upon complexation. In this section, we will explore the H-Xe bonding via this complexation

effect, combining with quantitative NRT analyses on chosen hydrogen-bonded complexes. **Table 1** displays the weighting of three resonance structures upon complexation for Xe cases. Obviously, the moiety H_2O/HCl/HBr/HI/HCN/HCCH complexing with HXeY has a significant influence on the weighting of three resonance structures for HXeY. To be specific, for the long-bonding structure (Weinhold et al., 2016; Zhang et al., 2017b, 2018), its weighting always decreases upon complexation. This indicates that the complexation of the moiety H_2O/HCl/HBr/HI/HCN/HCCH studied here is not beneficial to the stability of long-bonding in HXeY. For two other resonance structures, the ω_I decreases while ω_{II} increases relative to the corresponding monomer in studied hydrogen-bonded complexes except for the complex HXeCl···HCCH. For example, the weightings of H-Xe^+:I^- and H:$^-$ Xe^+-I in the hydrogen-bonded complex HXeI···HI are 62.8 and 19.2%, compared with 66.4 and 9.5% in the monomer HXeI. In contrast, the complex HXeCl···HCCH shows a different trend. As it is easily seen, the weightings of H-Xe^+:Cl^- and H:$^-$ Xe^+-Cl structures in the monomer HXeCl are 74.3 and 10.9% respectively; in the complex HXeCl···HCCH they are 76.1 and 9.7%, respectively. In short, for all of our studied complexes, the HXeY complexation with small molecules always leads to a decrease of the weighting about the long-bonding structure. For weightings of these two other resonance structures, one structure always shows a decreasing trend while the other exhibits an increasing trend for all of the studied complexes. In most of the Xe cases studied here, the complexation results in an increasing weighting of the resonance structure H-Xe^+:Cl^-, with a decreasing weighting of the resonance structure H:$^-$ Xe^+-Cl. In HXeCl···HCCH the situation is different. An opposite trend is seen for the complex HXeCl···HCCH. From preliminary NBO analyses on our studied complexes, peculiarities in HCCH complexes shown here, in **Tables 1**–**3**, and **Figure 4**, may be due to $n_{Xe(d)} \rightarrow \pi^*_{C-C}$ donor-acceptor interaction.

Table 2 lists natural bond orders of the H-Xe and H^-Y bonds in the monomer HXeY and its complex. It is worthwhile noting that the weighting and the corresponding bond order are equivalent for our studied cases in NBO/NRT framework if the former is expressed as a fraction rather than a percentage. For instance, the weightings of the H-Xe^+:Cl^- in the monomer HXeCl and in the complex HXeCl···HCl are 74.3% and 71.8%, with corresponding bond order b_{H-Xe} 0.743 and 0.718, respectively. Generally, the larger the bond order is, the stronger the bond is. The data obtained from current NBO programs show the decrease of H-Xe bond orders, reflecting the weakening H-Xe bonds upon complexation. Obviously, these calculated results do not reflect the experimental fact: the strengthened H-Xe bond. This disagreement confirms that the H-Xe bond in HXeY is not a classical covalent bond.

This conclusion deserves some illustration. According to the natural bond orders' definition (Weinhold and Landis, 2005a), the H-Xe bond in HXeY is regarded as a classical covalent bond. The resonance structure H:$^-$ Xe^+-Y does not contribute to the H-Xe bond order at all. The H-Xe bond order is only contributed to by the resonance structure H-Xe^+:Y^-. Thus, the H-Xe bond order in **Table 2** reflects merely the electron-sharing contribution in the H-Xe bond. It is insufficient to reflect the real strength between H and Xe in HXeY.

TABLE 1 | The weighting and its change of three resonance structures (H-Xe^+:Y^-, H:$^-$ Xe^+-Y, H^Y) upon HXeY complexation with H_2O/HCl/HBr/HI/HCN/HCCH, compared with the monomer HXeY.

Monomers/complexes	ω_I	ω_{II}	ω_{III}	Sum
HXeCl	74.3%	10.9%	14.9%	100.1%
HXeCl···H_2O	70.3% (−4.0%)	16.4% (+5.5%)	12.7% (−2.2%)	99.4%
HXeCl···HCl	71.8% (−2.5%)	15.6% (+4.7%)	12.2% (−2.7%)	99.6%
HXeCl···HBr	72.3% (−2.0%)	15.3% (+4.4%)	12.0% (−2.9%)	99.6%
HXeCl···HI	72.0% (−2.3%)	15.4% (+4.5%)	12.1% (−2.8%)	99.5%
HXeCl···HCN	69.9% (−4.4%)	16.9% (+6.0%)	13.1% (−1.8%)	99.8%
HXeCl···HCCH	76.1% (+1.8%)	9.7% (−1.2%)	13.8% (−1.1%)	99.6%
HXeBr	71.3%	11.6%	17.1%	100.0%
HXeBr···H_2O	67.0% (−4.3%)	17.8% (+6.2%)	14.6% (−2.5%)	99.4%
HXeBr···HCl	68.2% (−3.1%)	17.2% (+5.6%)	14.3% (−2.8%)	99.7%
HXeBr···HBr	68.7% (−2.6%)	16.8% (+5.2%)	13.9% (−3.2%)	99.4%
HXeBr···HI	68.4% (−2.9%)	17.0% (+5.4%)	14.1% (−3.0%)	99.5%
HXeBr···HCN	66.4% (−4.9%)	18.2% (+6.6%)	15.0% (−2.1%)	99.6%
HXeBr···HCCH	64.3% (−7.0%)	19.4% (+7.8%)	16.0% (−1.1%)	99.7%
HXeI	66.4%	9.5%	24.1%	100.0%
HXeI···H_2O	61.6% (−4.8%)	20.3% (+10.8%)	18.1% (−6.0%)	100.0%
HXeI···HCl	62.5% (−3.9%)	17.1% (+7.6%)	20.0% (−4.1%)	99.6%
HXeI···HBr	63.1% (−3.3%)	19.2% (+9.7%)	17.2% (−6.9%)	99.5%
HXeI···HI	62.8% (−3.6%)	19.2% (+9.7%)	17.3% (−6.8%)	99.3%
HXeI···HCN	61.4% (−5.0%)	20.3% (+10.8%)	18.1% (−6.0%)	99.8%
HXeI···HCCH	59.0% (−7.4%)	21.6% (+12.1%)	19.3% (−4.8%)	99.9%

Note that the ω_I in this table represents the sum of the weightings for the structures closely related with the best NLS H-Xe^+ :Y^-. Taking HXeCl···HI complex as one example, resonance structures H-Xe^+ :Cl^-···HI, H-Xe^+ Cl-H :I,$^-$ and H-Xe^+ Cl^I were considered. Also note that the sum in this table is a maximum of 100%. The error in 100.1% is due to the weightings 74.3, 10.9, 14.9% of the resonance structures (H-Xe^+ :Cl^-, H:$^-$ Xe^+-Cl, H^Cl) in HXeCl, where they are from 74.28, 10.85, 14.87%.

H-Xe Bond in HXeY Is a CS Bond

The above studies on the H-Xe bond in HXeY confirm that it is not a classical covalent bond. Then, is it a CS bond? To address this question, we first need to solve the problem of the H-Xe bond order. Let us return to the original NBO/NRT theory. In the framework of NRT theory (Weinhold and Landis, 2005a), the

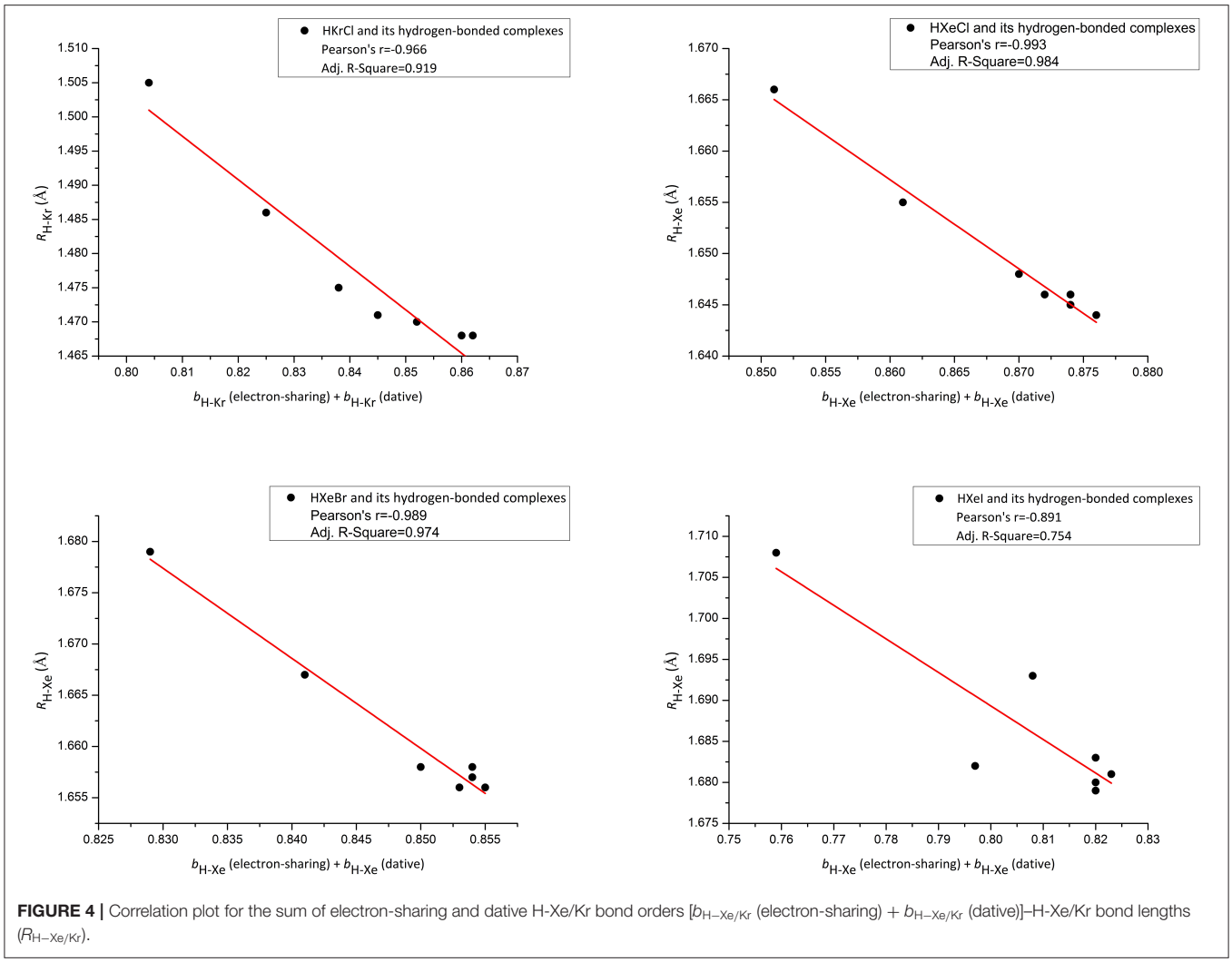

FIGURE 4 | Correlation plot for the sum of electron-sharing and dative H-Xe/Kr bond orders [$b_{H-Xe/Kr}$ (electron-sharing) + $b_{H-Xe/Kr}$ (dative)]–H-Xe/Kr bond lengths ($R_{H-Xe/Kr}$).

H-Xe total bond strength in HXeY could be written in resonance-averaged form D(H-Xe) = ω_Ix D_I + ω_{II}x D_{II}, where "ω_I" and "ω_{II}" respectively correspond to the weighting of H-Xe^+ Y^- and H:$^-$ Xe^+-Y; "D_I" and "D_{II}" represent the H-Xe bond strength in H-Xe^+ Y^- and in H:$^-$ Xe^+-Y respectively. As we know, a bond order is roughly proportional to the bond strength or the bond length. If introducing two arbitrary constants is presumed to be expressed in terms of the same factor k, D_I, and D_{II} can be written in the form, D_I = k x b_I and D_{II} = k x b_{II}. Importantly, we obtain that b(H-Xe) = ω_Ix b_I + ω_{II}x b_{II}, where b_I represents the H-Xe bond order in resonance structure I, as we know, b_I = 1; b_{II} refers to the H-Xe bond order in resonance structure II. Therefore, a calculation that includes two resonance structures is needed to deal with the H-Xe bond order. Note that the procedure employed to calculate the H-Xe CS bond order can be found in **Supplementary Material** "Explanation of the Procedure Employed to Calculate the BO of the H-Xe Bond."

To obtain b_{II}, we have to carry out some analyses on H:$^-$ Xe^+-Y. For this structure, where does the H-Xe bonding originate from? Here we emphasize that the H:$^-$ Xe^+-Y structure is a natural Lewis structure, in the NBO/NRT language. Consideration of the antibond of the Xe^+-Y could lead to extension of the elementary Lewis structure concept to include hyperconjugative delocalization corrections in simple NBO perturbative estimates (Weinhold, 2012). Such hyperconjugative delocalization forms one starting point for our understanding of bonding about the H:$^-$ Xe^+-Y structure. As shown in **Figure 3**, one donor-acceptor interaction $n_H \rightarrow \sigma^*_{Xe-Y}$ exists in the H:$^-$ Xe^+-Y structure. On the basis of this result, we propose that the H-Xe bonding about the structure H:$^-$ Xe^+-Y is attributed to this donor-acceptor interaction. In our familiar language, it is dative bonding due to hyperconjunctive interaction.

However, the question was still left open: How do we estimate the degree of this H-Xe dative covalency? For this question, our research ideas are from the natural bond orders' definition proposed by Weinhold and Landis (2005b). If such a single dative bond order b_{II} is defined as 1, the NRT bond order of the dative structure is equal to the corresponding fractional weighting. Taking HXeCl as one illustrative example, the dative weightings of monomer HXeCl and hydrogen-bonded complex HXeCl···HCl are 10.9 and 14.6%, respectively. This simple

TABLE 2 | The bond orders (*b*) of H-Xe and H^Y bonds for the monomer and their hydrogen-bonded complex, with the changes shown in parentheses.

Monomers/complexes	b_{H-Xe}	b_{H-Y}
HXeCl	0.743	0.149
HXeCl···H_2O	0.705 (−0.038)	0.127 (−0.022)
HXeCl···HCl	0.718 (−0.025)	0.122 (−0.027)
HXeCl···HBr	0.723 (−0.020)	0.120 (−0.029)
HXeCl···HI	0.720 (−0.023)	0.121 (−0.028)
HXeCl···HCN	0.701 (−0.042)	0.131 (−0.018)
HXeCl···HCCH	0.764 (+0.021)	0.138 (−0.011)
HXeBr	0.713	0.171
HXeBr···H_2O	0.675 (−0.038)	0.146 (−0.025)
HXeBr···HCl	0.682 (−0.031)	0.143 (−0.028)
HXeBr···HBr	0.687 (−0.026)	0.140 (−0.031)
HXeBr···HI	0.684 (−0.029)	0.141 (−0.030)
HXeBr···HCN	0.668 (−0.045)	0.150 (−0.021)
HXeBr···HCCH	0.646 (−0.067)	0.159 (−0.012)
HXeI	0.664	0.241
HXeI···H_2O	0.616 (−0.048)	0.181 (−0.060)
HXeI···HCl	0.625 (−0.039)	0.200 (−0.041)
HXeI···HBr	0.631 (−0.033)	0.172 (−0.069)
HXeI···HI	0.628 (−0.036)	0.173 (0.068)
HXeI···HCN	0.616 (−0.048)	0.181 (−0.060)
HXeI···HCCH	0.591 (−0.073)	0.193 (−0.048)

TABLE 3 | The H-Xe bond orders: b_{H-Xe} (electron-sharing), b_{H-Xe} (dative), and the total [b_{H-Xe} (electron-sharing) + b_{H-Xe} (dative)], for the monomer and their hydrogen-bonded complex, with the changes shown in parentheses.

Monomers/complexes	b_{H-Xe} (electron-sharing)	b_{H-Xe} (dative)	b_{H-Xe} (total)
HXeCl	0.743	0.109	0.852
HXeCl···H_2O	0.705 (−0.038)	0.164 (+0.055)	0.869 (+0.017)
HXeCl···HCl	0.718 (−0.025)	0.156 (+0.047)	0.874 (+0.022)
HXeCl···HBr	0.723 (−0.020)	0.153 (+0.044)	0.876 (+0.024)
HXeCl···HI	0.720 (−0.023)	0.154 (+0.045)	0.874 (+0.022)
HXeCl···HCN	0.701 (−0.042)	0.169 (+0.060)	0.870 (+0.018)
HXeCl···HCCH	0.764 (+0.021)	0.097 (−0.012)	0.861 (+0.009)
HXeBr	0.713	0.116	0.829
HXeBr···H_2O	0.675 (−0.038)	0.178 (+0.062)	0.853 (+0.024)
HXeBr···HCl	0.682 (−0.031)	0.172 (+0.056)	0.854 (+0.025)
HXeBr···HBr	0.687 (−0.026)	0.168 (+0.052)	0.855 (+0.026)
HXeBr···HI	0.684 (−0.029)	0.170 (+0.054)	0.854 (+0.025)
HXeBr···HCN	0.668 (−0.045)	0.182 (+0.066)	0.850 (+0.021)
HXeBr···HCCH	0.646 (−0.067)	0.194 (+0.078)	0.840 (+0.011)
HXeI	0.664	0.095	0.759
HXeI···H_2O	0.616 (−0.048)	0.203 (+0.108)	0.819 (+0.060)
HXeI···HCl	0.625 (−0.039)	0.171 (+0.076)	0.796 (+0.037)
HXeI···HBr	0.631 (−0.033)	0.192 (+0.097)	0.823 (+0.064)
HXeI···HI	0.628 (−0.036)	0.192 (+0.097)	0.820 (+0.061)
HXeI···HCN	0.616 (−0.048)	0.203 (+0.108)	0.819 (+0.060)
HXeI···HCCH	0.591 (−0.073)	0.216 (+0.121)	0.807 (+0.048)

method lets us respectively estimate the dative bond orders: 0.109 and 0.146.

The above discussion is an effort to rationalize b_{II}. We now begin a discussion with a sum of ω_Ix $b_{I,}$ and ω_{II}x b_{II}. For convenience, we use b_{H-Xe} (electron-sharing) = ω_Ix $b_{I,}$, b_{H-Xe} (dative) = ω_{II}x b_{II}. As shown in NRT theory, it is a sum of b_{H-Xe} (dative) and b_{H-Xe} (electron-sharing) that can reflect the H-Xe total strength in HXeY. **Figure 4** shows correlation plots between the H-Xe bond order [b_{H-Xe} (dative) + b_{H-Xe} (electron-sharing) and the H-Xe bond length R_{H-Xe} for our studied Xe species. One additional example is also shown in **Figure 4** for Kr analogs. Good correlation shown in **Figure 4** for our studied species except Y = I, provides evidence to support our estimated method. Not enough good correlation in Y = I case may be due to a larger coupling effect between $n_Y \rightarrow o^*_{H-Xe}$ in HXeY and $n_Y \rightarrow o^*_{H-X}$ in its H-bonding complex.

On the basis of the data of the H-Xe bond order, we can analyze the H-Xe total bonding of HXeY. From preceding NRT analyses, we have shown that the electron-sharing bond orders [b_{H-Xe} (electron-sharing)] in the monomer and in the complex are 0.743 and 0.718, respectively, and 0.109 and 0.146 for the dative bond orders [b_{H-Xe} (dative)]. Thus, summing b_{H-Xe} (dative) to b_{H-Xe} (electron-sharing) yields 0.852 and 0.864 for the HXeCl monomer and the HXeCl···HCl complex, respectively. Obviously, the HXeCl complexing with the molecule HCl leads to an increase of the H-Xe bond order. The same is true for other complexes studied here. **Table 3** lists the total bond order of the H-Xe bond in HXeY and in its hydrogen-bonded complexes. Note that it includes dative contribution and electron-sharing contribution of H-Xe bonding. As shown in **Table 3**, the HXeY complexing with the small molecule leads to an increase of the H-Xe bond order. In other words, it is an enhancement of the H-Xe bond. Such a result is consistent with experimental observations about our studied cases.

It becomes clear that the bonding between H and Xe in HXeY must meet two conditions. First, the resonance bonding between H^- Xe^+-Y and H-Xe^+ Y^- is a necessary condition. Second, for the H-Xe bond order, including contribution of these two resonance structures is essential. These two conditions are, in effect, consistent with emphases in original CS bonding concept paper (Shaik et al., 1992). The mixed covalent-ionic description, such as F· ·F↔F^- F^+, is an essential feature of CS bonding, wherein most, if not the entire, bond energy is provided by the covalent-ionic resonance energy. And both the covalent and ionic

structures must be treated explicitly and on an equal footing. Thus, we conclude that the H-Xe bond in HXeY is a charge-shift bond.

It should be noted, however, that neither the H-Xe bond length nor its bond strength can be reliable probes for addressing the question on whether the bond between H and Xe in HXeY should be classified as a CS bond or a classical covalent bond.

H-Xe CS Bonding Character

Now that the H-Xe bond in HXeY is a charge-shift bond, a new and unique form bonding, one question which arises is whether the unusual H-Xe blue shift is its CS bonding character in IR spectroscopy.

Deep analyses on the data in **Table 3** show that the complexation leads to an increase of b_{H-Xe} (dative) while b_{H-Xe} (electron-sharing) decreases, for most Xe cases. The competition of these two opposite factors results in the strengthened H-Xe bonds, corresponding to the blue shifts. Here, we want to point out that unlike other Xe complexes, the HXeCl···HCCH complex shows a difference in the dominant factor. It is the electron-sharing factor that dominates the H-Xe frequent shifts. The overall effect of two opposing factors is still an enhancement of the H-Xe bond and a blue shift for the H-Xe stretching frequency. These analyses reflect that the monomer-to-complex blue shifts of H-Xe stretching modes for HXeY species should be attributed to the balance of dative and electron-sharing covalency in H-Xe bonds, corresponding to H^- Xe^+-Y and H-Xe^+ Y^- resonance structures. In brief, the H-Xe frequent shifts in HXeY···H_2O/HCl/HBr/HI/HCCH/HCN hydrogen-bonded complexes is controlled by a balance of two factors acting in opposite directions.

All in all, blue shifts of H-Xe vibrational frequencies are controlled by a balance of two opposing factors for dative and electron-sharing covalency. The blue shift in our studied complexes can be seen as a normal spectroscopic phenomenon. It is natural for us to conclude that the H-Xe blue shift is the H-Xe CS bonding character in IR spectroscopy.

SUMMARY AND CONCLUSIONS

The H-Xe bonding in HXeY has been a debated question in the chemical community. The usual answer is that it is classically covalent in character, or to be exact, it is electron-sharing. The unusual blue shifts of complexes HXeY···HX (Y = Cl, Br, I; X = OH, Cl, Br, I, CN, CCH) definitely reflect the unusual features of H-Xe bonding in noble gas hydrides. Via observed blue-shifted phenomena, we have computationally investigated the H-Xe bonding in HXeY from an NBO/NRT perspective.

We establish that the resonance bonding between H-Xe^+ Y^- and H^- Xe^+-Y is an essential feature of the H-Xe bonding, and that the H-Xe bonding in these two resonance structures must be considered explicitly. Specifically, its bonding includes the $n_H \rightarrow \sigma^*_{Xe-Y}$ donor-acceptor interaction in H^- Xe^+-Y, as well as the electron-sharing interaction in H-Xe^+ Y^-; the H-Xe bond order is contributed to by these two resonance structures. We confirm that the H-Xe bond in HXeY is not a classical covalent bond but a charge-shift bond, and that H-Xe blue shifts is a normal spectroscopic phenomenon.

Our conclusions are (1) the H-Xe bond in HXeY is a charge-shift bond. (2) The H-Xe blue shift in its hydrogen-complexes is its CS bonding character in IR spectroscopy.

The first conclusion is consistent with ab initio VB methods' insight into the F-Xe CS bonding in XeF_2 (Braïda and Hiberty, 2013). But we note a little difference in the understanding of CS bonding mechanism. We stress the point that the H-Xe CS bonding is due to the resonance between H-Xe^+:I^- and H:$^-$ Xe^+-I, based on the natural Lewis structures' concept, whereas Shaik et al. (1992) think that CS bonding is due to strong mixing between the covalent structure and the ionic structure, based on Pauling-type Lewis structures' concepts.

Finally, we want to point out that H-Xe CS bonding is significantly different from some two-structure resonance bonding, such as hydrogen-bonding, although there is a formal resemblance in their resonance description. We have noticed that the bond order of hydrogen-bonding in literature (Jiao and Weinhold, 2019) is only considered a contribution from one resonance structure; the other does not contribute to bond orders of hydrogen-bonding at all. Why is CS bonding not important in hydrogen-bonding? More studies are on the way to answer such a question and to generalize CS bonding models. We believe that more surprise will be gained via NBO/NRT methods, in particular, new-type NBO-based NRT methods on analyses for larger CS bonding species (Glendening et al., 2019).

DATA AVAILABILITY STATEMENT

The raw data supporting the conclusions of this article will be made available by the authors, without undue reservation, to any qualified researcher.

AUTHOR CONTRIBUTIONS

GZ, CS, and DC made contributions to the design of the study. YS, XZ, JS and LF performed the calculations. GZ and YS wrote the draft of the manuscript. All the authors contributed to the manuscript revision, read and approved the submitted version.

FUNDING

This work was supported by the Natural Science Foundation of Shandong Province (No. ZR2015BM025).

ACKNOWLEDGMENTS

We thank Professor Frank Weinhold of the University of Wisconsin-Madison for his continuous help. Especially his help and important suggestions during the last few months, which helped us make great improvements to our manuscript.

SUPPLEMENTARY MATERIAL

The Supplementary Material for this article can be found online at: https://www.frontiersin.org/articles/10.3389/fchem.2020.00277/full#supplementary-material

REFERENCES

Alabugin, I. V., Manoharan, M., and Weinhold, F. (2004). Blue-shifted and red-shifted hydrogen bonds in hypervalent rare-gas FRg–H···Y sandwiches. *J. Phys. Chem. A* 108, 4720–4730. doi: 10.1021/jp049723l

Braïda, B., and Hiberty, P. C. (2013). The essential role of charge-shift bonding in hypervalent prototype XeF_2. *Nat. Chem.* 5, 417–422. doi: 10.1038/nchem.1619

Braïda, B., Ribeyre, T., and Hiberty, P. C. (2014). A valence bond model for electron-rich hypervalent species: application to SF_n ($n = 1, 2, 4$), PF_5, and ClF_3. *Chem. Eur. J.* 20, 9643–9649. doi: 10.1002/chem.201402755

Corani, A., Domanskaya, A., Khriachtchev, L., Räsänen, M., and Lignell, A. (2009). Matrix-isolation and ab initio study of the HKrCl···HCl complex. *J. Phys. Chem. A* 113, 10687–10692. doi: 10.1021/jp9044622

Duarte, L., and Khriachtchev, L. (2017). An aromatic noble-gas hydride: C_6H_5CCXeH. *Sci. Rep.* 7:3130. doi: 10.1038/s41598-017-02869-9

Feldman, V. I., Sukhov, F. F., Orlov, A. Y., and Tyulpina, I. V. (2003). Experimental evidence for the formation of HXeCCH: the first hydrocarbon with an inserted rare-gas atom. *J. Am. Chem. Soc.* 125, 4698–4699. doi: 10.1021/ja034585j

Feller, D. (1996). The role of databases in support of computational chemistry calculations. *J. Comput. Chem.* 17, 1571–1586. doi: 10.1002/(SICI)1096-987X(199610)17:13<1571::AID-JCC9>3.0.CO;2-P

Frisch, M. J., Trucks, G. W., Schlegel, H. B., Scuseria, G. E., Robb, M. A., Cheeseman, J. R., et al. (2009). *Gaussian 09, Revision B.01.* Wallingford CT: Gaussian Inc.

Glendening, E. D., Badenhoop, J. K., Reed, A. E., Carpenter, J. E., Bohmann, J. A., Morales, C. M., et al. (2001). *NBO 5.0., Theoretical Chemistry Institute.* Madison: University of Wisconsin.

Glendening, E. D., Badenhoop, J. K., and Weinhold, F. (1998). Natural resonance theory: III. chemical applications. *J. Comput. Chem.* 19, 628–646. doi: 10.1002/(SICI)1096-987X(19980430)19:6<628::AID-JCC5>3.0.CO;2-T

Glendening, E. D., Landis, C. R., and Weinhold, F. (2013b). NBO 6.0: natural bond orbital analysis program. *J. Comput. Chem.* 34, 1429–1437. doi: 10.1002/jcc.23266

Glendening, E. D., Landis, C. R., and Weinhold, F. (2019). Resonance theory reboot. *J. Am. Chem. Soc. 141,* 4156–4166. doi: 10.1021/jacs.8b12336

Glendening, E. D., and Weinhold, F. (1998a). Natural resonance theory: I. general formalism. *J. Comput. Chem.* 19, 593–609. doi: 10.1002/(SICI)1096-987X(19980430)19:6<593::AID-JCC3>3.0.CO;2-M

Glendening, E. D., and Weinhold, F. (1998b). Natural resonance theory: II. natural bond order and valency. *J. Comput. Chem.* 19, 610–627. doi: 10.1002/(SICI)1096-987X(19980430)19:6<610::AID-JCC4>3.0.CO;2-U

Glendening, E. D., Badenhoop, J. K., Reed, A. E., Carpenter, J. E., Bohmann, J. A., Morales, C. M., et al. (2013a). *NBO 6.0.* Madison, WI: Theoretical Chemistry Institute, University of Wisconsin. Available online at: http://nbo6.chem.wisc.edu/ (accessed March 24, 2018).

Grandinetti, F. (2018). *Noble Gas Chemistry: Structure, Bonding, and Gas-phase Chemistry*. Weinheim: Wiley-VCH. doi: 10.1002/9783527803552

Head-Gordon, M., and Pople, J. A., Frisch., M. J. (1988). MP2 energy evaluation by direct methods. *J. Chem. Phys. Lett.* 153, 503–506. doi: 10.1016/0009-2614(88)85250-3

Jana, G., Pan, S., Merino, G., and Chattaraj, P. K. (2017). MNgCCH (M = Cu, Ag, Au; Ng = Xe, Rn): the first set of compounds with M–Ng–C bonding motif. *J. Phys. Chem. A* 121, 6491–6499. doi: 10.1021/acs.jpca.7b04993

Jana, G., Pan, S., Merino, G., and Chattaraj, P. K. (2018a). Noble gas inserted metal acetylides (metal = Cu, Ag, Au). *J. Phys. Chem. A* 122, 7391–7401. doi: 10.1021/acs.jpca.8b05404

Jana, G., Pan, S., Osorio, E., Zhao, L., Merino, G., and Chattaraj, P. K. (2018b). Cyanide–isocyanide isomerization: stability and bonding in noble gas inserted metal cyanides (metal = Cu, Ag, Au). *Phys. Chem. Chem. Phys.* 20, 18491–18502. doi: 10.1039/C8CP02837K

Jiao, Y., and Weinhold., F. (2019). What is the nature of supramolecular bonding? comprehensive NBO/NRT picture of halogen and pnicogen bonding in RPH_2···IF/FI complexes (R = CH_3, OH, CF_3, CN, NO_2). *Molecules*. 24:2090. doi: 10.3390/molecules24112090

Juarez, R., Zavala-Oseguera, C., Jimenez-Halla, J. O. C., Bickelhaupt, F. M., and Merino, G. (2011). Radon hydrides: structure and bonding. *Phys. Chem. Chem. Phys.* 13, 2222–2227. doi: 10.1039/C0CP01488E

Khriachtchev, L., Räsänen, M., and Gerber, R. B. (2009). Noble-gas hydrides: new chemistry at low temperatures. *Acc. Chem. Res.* 42, 183–191. doi: 10.1021/ar800110q

Khriachtchev, L., Tanskanen, H., Lundell, J., Pettersson, M., Kiljunen, H., and Räsänen, M. (2003). Fluorine-free organoxenon chemistry: HXeCCH, HXeCC, and HXeCCXeH. *J. Am. Chem. Soc.* 125, 4696–4697. doi: 10.1021/ja034485d

Landis, C. R., and Weinhold, F. (2013). 3c/4e σ-type long-bonding: a novel transitional motif toward the metallic delocalization limit. *Inorg. Chem.* 52, 5154–5166. doi: 10.1021/ic4000395

Last, I., and George, T. F. (1988). Electronic states of the Xe_nHCl systems in gas and condensed phases. *J. Chem. Phys.* 89, 3071–3078. doi: 10.1063/1.454963

Lein, M., Frunzke, J., and Frenking, G. (2004). Christian Klixbull Jørgensen and the nature of the chemical bond in HArF. *Struct. Bond.* 181–191. doi: 10.1007/b11312

Lignell, A., Lundell, J., Khriachtchev, L., and Räsänen, M. (2008). Experimental and computational study of HXeY···HX complexes (X, Y = Cl and Br) : an example of exceptionally large complexation effect. *J. Phys. Chem. A* 112, 5486–5494. doi: 10.1021/jp801363u

Lundell, J., Cohen, A., and Gerber, R. B. (2002). Quantum chemical calculations on novel molecules from xenon insertion into hydrocarbons. *J. Phys. Chem. A* 106, 11950–11955. doi: 10.1021/jp026777r

Pan, S., Jana, G., Merino, G., and Chattaraj, P. K. (2019). Noble-noble strong union: gold at its best to make a bond with a noble gas atom. *ChemistryOpen* 8. 173–187. doi: 10.1002/open.201800257

Pérez-Peralta, N., Juárez, R., Cerpa, E., Bickelhaupt, F. M., and Merino, G. (2009). Bonding of xenon hydrides. *J. Phys.* Chem. *A* 113, 9700–9706. doi: 10.1021/jp903266a

Pettersson, M., Lundell, J., and Räsänen, M. (1995). Neutral rare-gas containing charge-transfer molecules in solid matrices. I. HXeCl, HXeBr, HXeI, and HKrCl in Kr and Xe. *J. Chem. Phys.* 102, 6423–6431. doi: 10.1063/1.469357

Pettersson, M., Lundell, J., and Räsänen, M. (1999). New rare-gas-containing neutral molecules. *Eur. J. Inorg. Chem.* 1999, 729–737. doi: 10.1002/(SICI)1099-0682(199905)1999:5<729::AID-EJIC729>3.0.CO;2-M

Pyykkö, P. (2015). Additive covalent radii for single-, double-, and triple-bonded molecules and tetrahedrally bonded crystals: a summary. *J. Phys. Chem. A* 119, 2326–2337. doi: 10.1021/jp5065819

Rahm, M., Hoffmann, R., and Ashcroft, N. W. (2016). Atomic and ionic radii of elements 1-96. *Chem. Eur. J.* 22, 14625–14632. doi: 10.1002/chem.201602949

Räsänen, M., Khriachtchev, L., Pettersson, M., Runeberg, N., and Lundell, J. (2000). A stable argon compound. *Nature*. 406, 874–876. doi: 10.1038/35022551

Saha, R., Jana, G., Pan, S., Merino, G., and Chattaraj, P. K. (2019). How far can one push the noble gases towards bonding?: a personal account. *Molecules.* 24:2933. doi: 10.3390/molecules24162933

Schuchardt, K. L., Didier, B. T., Elsethagen, T., Sun, L., Gurumoorthi, V., Chase, J., et al. (2007). Basis set exchange: a community database for computational sciences. *J. Chem. Inf. Model.* 47, 1045–1052. doi: 10.1021/ci600510j

Shaik, S., Danovich, D., Galbraith, J. M., Braida, B., Wu, W., and Hiberty, P. C. (2020). Charge-shift bonding: a new and unique form of bonding. *Angew. Chem. Int. Ed.* 59, 984–1001. doi: 10.1002/anie.201910085

Shaik, S., Danovich, D., Silvi, B., Lauvergnat, D. L., and Hiberty, P. C. (2005). Charge-shift bonding—a class of electron-pair bonds that emerges from valence bond theory and is supported by the electron localization function approach. *Chem. Eur. J.* 11, 6358–6371. doi: 10.1002/chem.200500265

Shaik, S., Danovich, D., Wu, W., and Hiberty, P. C. (2009). Charge-shift bonding and its manifestations in chemistry. *Nat. Chem.* 1, 443–449. doi: 10.1038/nchem.327

Shaik, S., Maitre, P., Sini, G., and Hiberty, P. C. (1992). The charge-shift bonding concept. Electron-pair bonds with very large ionic-covalent resonance energies. *J. Am. Chem. Soc.* 114, 7861–7866. doi: 10.1021/ja00046a035

Tsuge, M., Berski, S., Räsänen, M., Latajka, Z., and Khriachtchev, L. (2013). Experimental and computational study of the HXeI···HY complexes (Y = Br and I). *J. Chem. Phys.* 138:104314. doi: 10.1063/1.4794309

Tsuge, M., Berski, S., Räsänen, M., Latajka, Z., and Khriachtchev, L. (2014). Matrix-isolation and computational study of the HXeY···H_2O complexes (Y = Cl, Br, and I). *J. Chem. Phys.* 140:044323. doi: 10.1063/1.4862692

Weinhold, F. (2012). Natural bond orbital analysis: a critical overview of relationships to alternative bonding perspectives. *J. Comput. Chem.* 33, 2363–2379. doi: 10.1002/jcc.23060

Weinhold, F. (2013). *NBOPro 6.0*. Madison: Theoretical Chemistry Institute, U. Wisconsin. Available online at: http://nbo6.chem.wisc.edu/~nbopro_adv.htm (accessed March 24, 2018).

Weinhold, F., and Klein, R. A. (2012). What is a hydrogen bond? mutually consistent theoretical and experimental criteria for characterizing H-bonding interactions. *Mol. Phys.* 110, 565–579. doi: 10.1080/00268976.2012.661478

Weinhold, F., and Klein, R. A. (2014). What is a hydrogen bond? resonance covalency in the supramolecular domain. *Chem. Educ. Res. Pract.* 15, 276–285. doi: 10.1039/C4RP00030G

Weinhold, F., and Landis, C. R. (2005a). "Natural resonance structures and weightings," in *Valency and Bonding: A Natural Bond Orbital Donor-acceptor Perspective*. (New York, NY: Cambridge University Press), 32–36.

Weinhold, F., and Landis, C. R. (2005b). "The NBO donor-acceptor picture of hypervalency: hyperbonds," in *Valency and Bonding: A Natural Bond Orbital Donor-acceptor Perspective*. (New York, NY: Cambridge University Press), 281–285.

Weinhold, F., Landis, C. R., and Glendening, E. D. (2016). What is NBO analysis and how is it useful? *Int. Rev. Phys. Chem.* 35, 399–440. doi: 10.1080/0144235X.2016.1192262

Zhang, G., Fu, L., Li, H., Fan, X., and Chen, D. (2017a). Insight into the bonding mechanism and the bonding covalency in noble gas-noble metal halides: an NBO/NRT investigation. *J. Phys. Chem. A* 121, 5183–5189. doi: 10.1021/acs.jpca.7b02047

Zhang, G., Li, H., Weinhold, F., and Chen, D. (2016). 3c/4e -type long-bonding competes with ω-bonding in noble-gas hydrides HNgY (Ng = He, Ne, Ar, Kr, Xe, Rn; Y = F, Cl, Br, I): a NBO/NRT perspective. *Phys. Chem. Chem. Phys.* 18, 8015–8026. doi: 10.1039/C5CP07965A

Zhang, G., Song, J., Fu, L., Tang, K., Su, Y., and Chen, D. (2018). Understanding and modulating the high-energy properties of noble-gas hydrides from their long-bonding: an NBO/NRT investigation on $HNgCO^+/CS^+/OSi^+$ and HNgCN/NC (Ng = He, Ar, Kr, Xe, Rn) molecules. *Phys. Chem. Chem. Phys.* 20, 10231–10239. doi: 10.1039/C8CP00306H

Zhang, G., Yue, H., Weinhold, F., Wang, H., Li, H., and Chen, D. (2015). Resonance character of Cu/Ag/Au bonding in small molecule···M-X (X=F, Cl, Br, CH_3, CF_3) complexes. *Chem. Phys. Chem.* 16, 2424–2431. doi: 10.1002/cphc.201500211

Zhang, G., Zhang, S., and Chen, D. (2017b). Long-bonding in HNgCN/NC (Ng = noble gas) molecules: an NBO/NRT investigation. *J. Phys. Chem. A* 121, 5524–5532. doi: 10.1021/acs.jpca.7b03177

Zhu, C., Tsuge, M., Räsänen, M., and Khriachtchev, L. (2015). Experimental and theoretical study of the HXeI···HCl and HXeI···HCCH complexes. *J. Chem. Phys.* 142:144306. doi: 10.1063/1.4917167

Conflict of Interest: The authors declare that the research was conducted in the absence of any commercial or financial relationships that could be construed as a potential conflict of interest.

frontiers in Chemistry

ORIGINAL RESEARCH
published: 06 May 2020
doi: 10.3389/fchem.2020.00395

Covalent and Non-covalent Noble Gas Bonding Interactions in XeF_n Derivatives (n = 2–6): A Combined Theoretical and ICSD Analysis

Rosa M. Gomila[1] *and Antonio Frontera*[2]*

[1] Serveis Cientificotècnics, Universitat de les Illes Balears, Palma, Spain, [2] Department of Chemistry, Universitat de les Illes Balears, Palma, Spain

A noble gas bond (also known in the literature as aerogen bond) can be defined as the attractive interaction between any element of group-18 acting as a Lewis acid and any electron rich atom of group of atoms, thus following the IUPAC recommendation available for similar π,σ-hole interactions involving elements of groups 17 (halogens) and 16 (chalcogens). A significant difference between noble gas bonding (NgB) and halogen (HaB) or chalcogen (ChB) bonding is that whilst the former is scarcely found in the literature, HaB and ChB are very common and their applications in important fields like catalysis, biochemistry or crystal engineering have exponentially grown in the last decade. This article combines theory and experiment to highlight the importance of non-covalent NgBs in the solid state of several xenon fluorides $[XeF_n]^{m+}$ were the central oxidation state of Xe varies from +2 to +6 and the number of fluorine atoms varies from n = 2 to 6. The compounds with an odd number of fluorine atoms (n = 3 and 5) are cationic (m = 1). The Inorganic Crystal Structural Database (ICSD) strongly evidences the relevance of NgBs in the solid state structures of xenon derivatives. The ability of Xe compounds to participate in π,σ-hole interactions has been studied using different types of electron donors (Lewis bases and anions) using DFT calculations (PBE1PBE-D3/def2-TZVP) and the molecular electrostatic potential (MEP) surfaces.

Keywords: σ-hole interactions, π-hole interactions, supramolecular chemistry, inorganic crystal structural database, DFT calculations

OPEN ACCESS

Edited by:
Pratim Kumar Chattaraj,
Indian Institute of Technology Kharagpur, India

Reviewed by:
Jose A. Gamez,
Covestro Deutschland AG, Germany
Peifeng Su,
Xiamen University, China

***Correspondence:**
Antonio Frontera
toni.frontera@uib.es

Specialty section:
This article was submitted to Theoretical and Computational Chemistry, a section of the journal Frontiers in Chemistry

Received: *03 March 2020*
Accepted: *15 April 2020*
Published: *06 May 2020*

Citation:
Gomila RM and Frontera A (2020) Covalent and Non-covalent Noble Gas Bonding Interactions in XeF_n Derivatives (n = 2–6): A Combined Theoretical and ICSD Analysis. Front. Chem. 8:395. doi: 10.3389/fchem.2020.00395

INTRODUCTION

The starting point of the noble gas chemistry was in 1962 with the discovery of $XePtF_6$ and XeF_2 compounds by Bartlett (1962) and Zirin groups (Chernick et al., 1962), respectively. This discovery opened a new field of research that has grown in the last two decades due to the improvements in the experimental techniques and instrumentation to carry out reactions and measurements in extreme conditions (Haner and Schrobilgen, 2015; Grandinetti, 2018). Another interesting step in this field was the synthesis in 2000 by Seidel and Seppelt of the first compound having a noble gas–noble metal bond $[AuXe_4]^{2+}$ (Seidel and Seppelt, 2000). The formation of an Au–Xe covalent bond itself is counterintuitive if gold is considered as a truly noble metal and xenon a truly noble gas. Nevertheless, after the synthesis and characterization of the XeAuF molecule by Cooke and Gerry (2004), numerous reports have been published in the literature

studying the chemistry of Au–Xe–X (X = electron withdrawing group) compounds (Grochala, 2007; Belpassi et al., 2008).

Supramolecular chemistry and molecular recognition (including self-assembly) are intimately related concepts (Busschaert et al., 2015) that rely on the understanding of non-covalent interactions. For instance, chemists working on solid state crystal engineering or solution state supramolecular chemistry aspire to control molecular recognition, designing individual molecules enable to interact with other molecules or themselves conducting the formation of assemblies spontaneously through non-covalent interactions (Schneider, 2009; Desiraju, 2013). The final aim is to control the molecular recognition process precisely to be able to build selective molecular receptors, sensors, supramolecular catalysts, polymers, etc.

A deep understanding of the physical nature of non-covalent interactions (directionality, strength, cooperativity) is essential to dictate supramolecular chemistry processes since they are usually governed by an intricate combination of forces (Schneider and Yatsimirski, 2000). Therefore, a precise description of the non-covalent interactions is essential for the incessant expansion of the supramolecular chemistry. Crystal engineering and molecular recognition commonly trust in moderately strong and directional H-bonding interactions (Desiraju and Steiner, 2001) in combination with less directional but stronger forces like ion pairing. In this sense, charge assisted H-bonds combine strength of an ion-pair and the directionality of dipole dipole interactions. Furthermore, ion–π interactions, either between cations and electron rich π-systems or between anions and acidic rings (Frontera et al., 2011), are also active players in crystal engineering or solution state supramolecular chemistry, including supramolecular catalysis (Zhao et al., 2015). The π-π stacking is another non-covalent interaction that is widely used in molecular recognition and crystal engineering, being particularly relevant in the construction of supramolecular polymers (Meyer et al., 2003).

In addition to the aforementioned conventional interactions, other types of more unconventional interactions where elements of the p-block play the role of hydrogen in H-bonds are gaining importance in supramolecular chemistry (Bauzá et al., 2015; Legon, 2017). Recent advances in host-guest chemistry, catalysis and membrane transport are good examples that illustrate how these interactions are gaining attention. This is particularly true in the fields of crystal engineering and theoretical chemistry, where tetrel (Tr) (Bauzá et al., 2019), pnictogen (Pn) (Scheiner, 2013), chalcogen (Ch) (Scilabra et al., 2019) and halogen bonding (HaB) (Cavallo et al., 2016) are largely utilized and studied. These X–D···A interactions, where X is any atom, D is the σ-hole donor atom (Lewis acid) from groups 13–17 of elements, and A is any electron rich entity (Lewis base) have several common features. The magnitude of the π,σ-hole depends on two factors: (i) the polarizability of D and (ii) the electron withdrawing ability of the X atom. The atomic polarizability increases in a given group on going from lighter to heavier elements. For noble gases (group 18) the polarizability values in atomic units are He = 1.36, Ne = 2.62, Ar = 11.10, Kr = 16.70 and Xe = 27.06 (Bauzá and Frontera, 2020); thus a more intense π,σ-hole is expected for Xe, and, consequently, it is expected to form the strongest interactions.

There are several works and reviews available in the literature where noble gas bonding or aerogen bonding interactions (NgBs) have been studied both experimental and theoretically (Haner and Schrobilgen, 2015; Grandinetti, 2018; Bauzá and Frontera, 2020), which were named as such in 2015 (Bauzá and Frontera, 2015). The purpose of this manuscript is to combine searches on the inorganic crystal structural database (ICSD) and theoretical calculations to explore the ability of XeF_n ($n = 2$–6) compounds to form non-covalent NgBs. The theoretical part includes molecular electrostatic potential (MEP) surfaces to identify the directional preference of Xe to participate in NgBs depending on the number of fluorine atoms. Moreover, a set of complexes has been calculated at the PBE1PBE-D3/def2-TZVP level of theory to investigate both the energetic and geometric features of the complexes. The survey of crystal structures retrieved from the ICSD evidences that NgBs between xenon fluorides and lone-pair-possessing atoms are very common.

THEORETICAL METHODS

The energies of all complexes included in this study were computed at the PBE1PBE-D3/def2-TZVP level of theory. The geometries have been fully optimized imposing either C_s or C_{nv} (n = 3,4) symmetry constraints (unless otherwise noted) by using the program Gaussian-16 (Frisch et al., 2016). The interaction energy (or binding energy in this work) ΔE, is defined as the energy difference between the optimized complex and the sum of the energies of the optimized monomers. For the calculations we have used the Weigend def2-TZVP (Weigend and Ahlrichs, 2005; Weigend, 2006) basis set and the PBE1PBE (Adamo and Barone, 1999) DFT functional. The MEP (Molecular Electrostatic Potential) surfaces calculations have been computed at the same level of theory and plotted using the 0.001 a.u. isosurface as the best estimate of the van der Waals surface. The QTAIM formalism has been used to analyse the topology of the electron density (Bader, 1985), using the same level of theory and optimized geometries and making use of the AIMAll program (Keith, 2013). The natural bond orbital (NBO) analysis was performed on some optimized complexes at the same level. The NBO analysis is adequate to study the role of intermolecular orbital interactions or charge transfer in the complexes (Reed et al., 1988). It takes into consideration all possible interactions between filled donor and empty acceptor NBOs and calculating their energetic stabilization by using the second-order perturbation theory. The NBO 3.1 program, as implemented in Gaussian-16 program (Frisch et al., 2016) was used for the calculations.

RESULTS AND DISCUSSION

XeF_2

X-ray Crystal Structure

The ICSD has been inspected manually to investigate the ability of xenon difluoride to participate in NgBs. The sum of van der Waal radii of Xe and F is ΣR_{vdw} = 3.63 Å and the

sum of their covalent radii is $\Sigma R_{cov} = 1.97$ Å. **Figure 1** (top) shows several assemblies retrieved from the X-ray structure of XeF_2 (Templeton et al., 1963) and three of its cocrystals, i.e., $[XeF_2]\cdot[IF_5]$ (Jones et al., 1970), $[XeF_2]\cdot[XeF_4O]$ (Hughes et al., 2011) and $[XeF_2]\cdot[XeF_4]$ (Burns et al., 1965). It can be observed that all X-ray structures present Xe···F contacts with distances that are clearly longer than ΣR_{cov} and shorter than ΣR_{vdw} thus suggesting the non-covalent nature of these NgBs. Another geometrical aspect that it is worthy to comment is that the F–Xe···F angle is smaller than 90° thus evidencing that the directionality of the NgBs interaction is not strictly perpendicular. This is likely due to the presence of three lone pairs at Xe located perpendicular to the F–Xe–F axis. In the case of $[XeF_2]\cdot[XeF_4]$, the Xe establishes four NgBs, two with the XeF_4 and two with the XeF_2 (see **Figure 1C**). The assemblies of $[XeF_2]\cdot[IF_5]$, $[XeF_2]\cdot[XeF_4O]$, are very similar and both the $[IF_5]$ and $[XeF_4O]$ moieties exhibit a square pyramid geometry with one fluorine atom pointing to the Xe (see **Figures 1A,B**). Finally, the XeF_2 crystal structure forms self-assembled supramolecular polymers where two symmetrically equivalent Xe···F contacts are established (see **Figure 1D**).

The XeF_2 molecule has been also used as a ligand for synthesizing a great variety of coordination compounds. The first compound was isolated in 1991 and it was a silver complex of formula $[Ag(XeF_2)_2](AsF_6)$ (Hagiwara et al., 1991). In the last decade, many coordination complexes have been synthesized using alkaline, alkaline-earth, divalent transition metals, trivalent lanthanides and Pb as the unique element of the p-block (Tavčar and Tramšek, 2015). Several reviews describing coordination compounds with XeF_2 as a ligand to metal cations of the type $[M(XeF_2)_n]$ are available in the literature (Tavčar et al., 2004; Tramšek and Žemva, 2006).

Figure 1 (bottom) shows two examples of XeF_2 coordination compounds where the Xe participates in NgBs. The X-ray represented in **Figure 1E** corresponds to a silver compound (Ag ions not shown for clarity) where four symmetrically equivalent Xe···F contacts are formed (Hagiwara et al., 1991). It is expected that the coordination of XeF_2 to the metal center enhances the ability of Xe to act as Lewis acid. The coordination compound with Pb(II) is shown in **Figure 1F**, where each XeF_2 molecule bridges two Pb metal centers, thus generating a 3D coordination polymer (Tramšek et al., 2002). Two Xe···F NgBs are formed

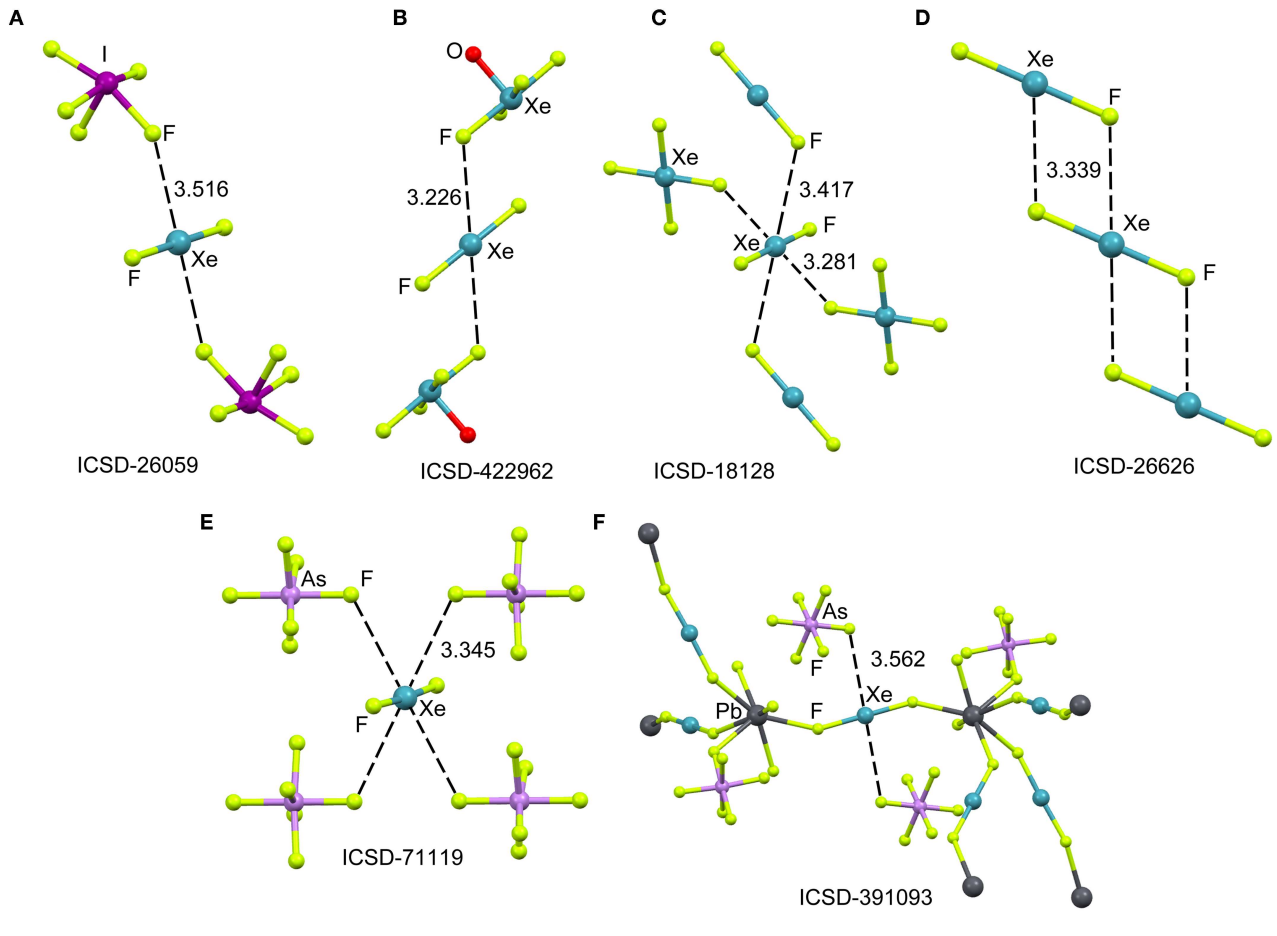

FIGURE 1 | Partial views of the X-ray structures ICSD-26059 **(A)**, ICSD-422962 **(B)**, ICSD-18128 **(C)**, ICSD-26626 **(D)**, ICSD-71119 **(E)**, and ICSD-391093 **(F)**, Distances in Å. NgBs represented as dashed lines.

with the AsF_6^- counterions with Xe···F distances that are slightly shorter than ΣR_{vdw}.

Theoretical Study

The molecular electrostatic potential (MEP) surface analysis is used herein to rationalize the ability of XeF_2 to establish NgBs, as illustrated above in **Figure 1**. The MEP plotted onto the van der Waals surface is useful to know the most electrophilic and nucleophilic parts of the molecule and to rationalize donor-acceptor non-covalent interactions. **Figure 2** shows the MEP surface of XeF_2 and it reveals the existence of a positive belt around the Xe atom and two negative regions at both ends of the molecule (F-atoms). A close examination of the positive belt indicates that the maximum value of MEP is not located strictly perpendicular to the molecular axis at the position of the Ng-atom. Instead they are located in two symmetric belts that are slightly displaced toward the F-atoms (see **Figure 2**, right). The MEP analysis suggests that Xe(II) molecules should have a strong tendency to establish Ng-bonding interactions with electron rich atoms with some deviation from the perpendicular trajectory.

Scheme 1A shows the electron donor molecules and complexes of XeF_2 that have been optimized at the PBE1PBE-D3/def2TZVP. A variety of Lewis bases and anions have been selected to analyze the influence of the basicity and neutral/anion nature of the donor on the interaction energies. We also represent the expected directionality assuming the stereo-active character of the lone pairs and their location is proposed based on the well-known valence-shell electron-pair repulsion (VSEPR) theory, that has been recently revisited (Munárriz et al., 2019).

The interaction energies and distances for complexes **1**–**6** are gathered in **Table 1**, showing that the interaction energies are favorable in all cases. The energetic results indicate that the CO complex **1** is the weakest one and the Br^- the strongest one. In fact, the equilibrium distance of the CO complex is very close to the sum of van der Waals radii whilst the R values for the rest of complexes is much shorter than ΣR_{vdw}. As expected, the interaction energies involving the anionic donors are stronger than those with neutral donors, being more favorable for bromide. The interaction energy of complex **4** is moderately strong, in agreement with the stronger basicity of NH_3 molecule. Finally, it is interesting to highlight that the Xe···F distance computed for the HF complex in in the range of experimental distances observed in the X-ray structures commented above (see **Figure 1**).

The geometries of the XeF_2 complexes are given in **Figure 3** (left panel), where it can be observed that the directionality of their NgB interaction agrees well with the expectation derived from the VSEPR theory and also the MEP surface represented in **Figure 3**. The X:···Xe–F angle varies from 60 to 75°. In the stronger anionic complexes **5** and **6**, the XeF_2 molecule bents as a consequence of the formation of strong NgBs. In complexes **2** and **3**, where an acidic proton is present in the electron donor molecule, the optimization of the complexes using C_s symmetry yields either a H-bonded complex in case of HF (see **Figure 3E**) or a combination of HB and NgB interactions in case of HCN (see **Figure 3F**). In order to estimate the energies associated to the NgBs in these complexes without the contribution of the HBs, optimizations imposing C_{2v} symmetry (**Figures 3B,C**) have been performed and only the interaction energies corresponding to the C_{2v} geometries are given in **Table 1**.

The NgB interaction in complexes **1**-**6** has been characterized using the quantum theory of "atoms-in-molecules" (QTAIM) (Bader, 1985). For all complexes the NgB is characterized by a bond critical point (CP) and bond path connecting the electron rich atom to the Xe (see **Figure 3**, right panel). The values of electron charge density ρ(r) at the bond CPs are tabulated in **Table 1**. Interestingly, the values of ρ(r) at the bond CPs that characterize the NgB correlate well with the interaction

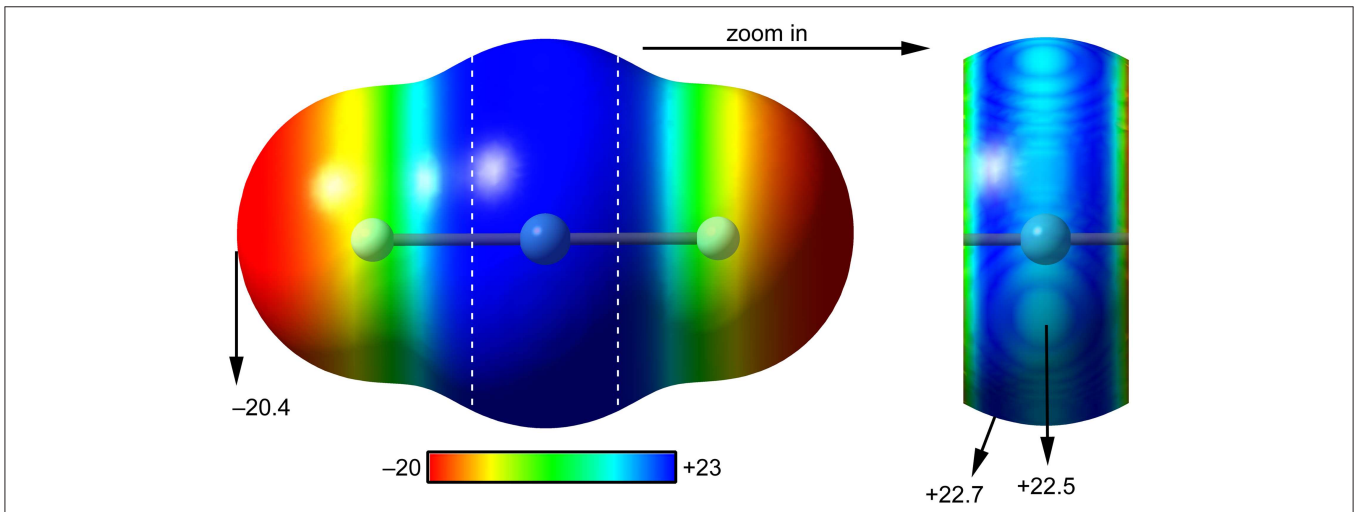

FIGURE 2 | MEP surfaces (0.001 a.u.) of XeF_2 (left) and a "zoom-in" representation at the PBE1PBE-D3/def2-TZVP level of theory. The MEP energies at selected points are indicated in kcal/mol.

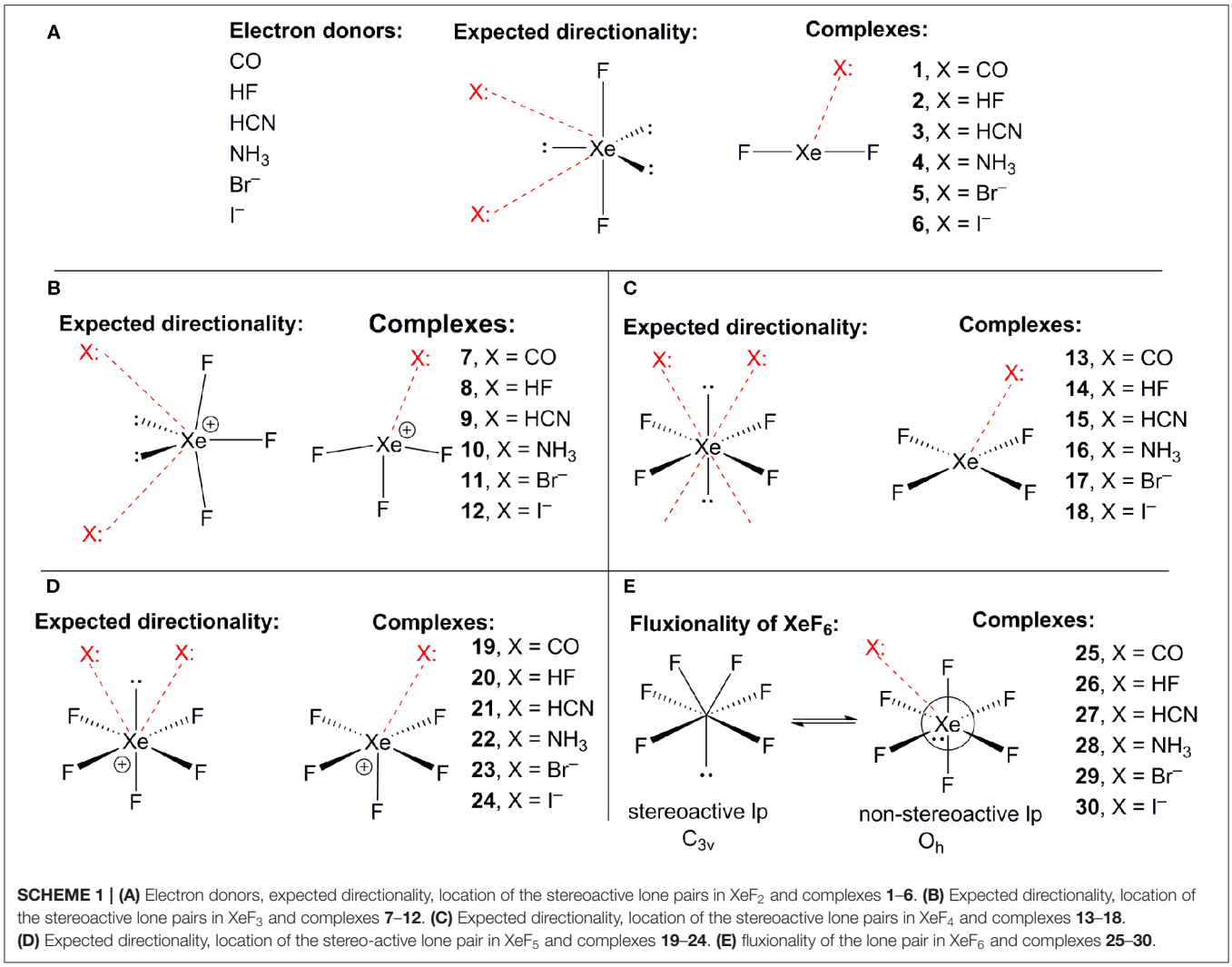

SCHEME 1 | (A) Electron donors, expected directionality, location of the stereoactive lone pairs in XeF_2 and complexes **1**–**6**. **(B)** Expected directionality, location of the stereoactive lone pairs in XeF_3 and complexes **7**–**12**. **(C)** Expected directionality, location of the stereoactive lone pairs in XeF_4 and complexes **13**–**18**. **(D)** Expected directionality, location of the stereo-active lone pair in XeF_5 and complexes **19**–**24**. **(E)** fluxionality of the lone pair in XeF_6 and complexes **25**–**30**.

energies by using a logarithmic fitting (regression coefficient, $r = 0.972$, see **Supplementary Material**) as previously described in the literature (Bader, 1990). Therefore, the value of ρ(r) at the bond CP can be used as a measure of the strength of the NgB interaction. The values of the total energy density [H(r)] at the bond CPs are also summarized in **Table 1** since they are adequate to differentiate covalent and non-covalent interactions. Positive values of H(r) indicate non-covalent bonding, negative and small values of H(r) are indicative of partial covalent character, and large and negative values of H(r) along with large values of ρ(r) designate covalent bonding (Bader et al., 1987; Bader, 1990). The examination of the values of H(r) in **Table 1** evidences the non-covalent nature of the interaction in all complexes.

As exemplifying system, we have selected the complex with NH_3 to perform the NBO analysis. This type of study is adequate to analyse the importance of orbital donor-acceptor interactions. In the $XeF_2\cdots NH_3$ system, we have found a modest donor-acceptor interaction from the lone pair orbital of N to the Xe–F antibonding orbital [LP(n)→ σ*(Xe–F)] with a concomitant stabilization energy of $E^{(2)} = 1.02$ kcal/mol. Although the orbital contribution is small, it is not negligible compared to the total interaction energy (∼25%).

XeF_3^+

X-ray Crystal Structures

At the beginning of the development of noble gas chemistry, several adducts of XeF_2 and XeF_6 with strong fluoride ion acceptor molecules were synthesized (Holloway, 1968; Sladky et al., 1969). Moreover, several works (Edwards et al., 1963; Cohen and Peacock, 1966; Bartlett and Sladky, 1968) tried to synthesize XeF_4 adducts in combination to fluoride acceptors like SbF_5, TaF_5, AsF_5 etc. without success. In fact, instead to forming the adducts, the $[XeF_3]^+$ cation is generated, for instance by simply dissolving XeF_4 or XeF_2/XeF_4 in SbF_5.

The cationic nature of xenon trifluoride, anticipates a strong binding with electron rich atoms due to the strong contribution of electrostatic forces (charge-charge or charge-dipole). In **Figure 4** (top panel), several X-ray structures are represented to illustrate the characteristics of the Xe···F bonds in $[XeF_3]^+$ salts. The X-ray structure of the $[XeF_3]^+[Sb_2F_{11}]^-$ salt (**Figure 4A**)

TABLE 1 | Interaction energies (ΔE in kcal/mol), F_nXe X equilibrium distances (R, Å), sum of van der Waals and covalent radii of interacting atoms (ΣR_{vdw} and ΣR_{cov}, Å), electron charge density and total energy density at the bond critical point [ρ(r) and H(r), respectively, in a.u.] at the PBE1PBE-D3/def2-TZVP level of theory for complexes **1** to **30**.

Complex	ΔE	R	ΣR_{vdw}	ΣR_{cov}	ρ(r)	H(r)
1 (XeF_2··CO)	−1.14	3.831	3.86	2.16	0.0044	0.0009
2 (XeF_2··FH)	−1.83	3.342	3.63	1.97	0.0064	0.0018
3 (XeF_2··NCH)	−2.36	3.547	3.71	2.11	0.0067	0.0012
4 (XeF_2··NH_3)	−4.43	3.361	3.71	2.11	0.0105	0.0009
5 (XeF_2··Br)$^-$	−11.59	3.442	4.01	2.60	0.0163	0.0004
6 (XeF_2··I)$^-$	−9.10	3.758	4.14	2.79	0.0121	0.0005
7 (XeF_3··CO)$^+$	−17.44	2.704	3.86	2.16	0.0403	−0.0033
8 (XeF_3··FH)$^+$	−18.26	2.545	3.63	1.97	0.0333	0.0018
9 (XeF_3··NCH)$^+$	−35.67	2.438	3.71	2.11	0.0586	−0.0096
10 (XeF_3··NH_3)$^+$	−54.66	2.337	3.71	2.11	0.0813	−0.0230
11 (XeF_3··Br)	−198.55	2.563	4.01	2.60	0.0831	−0.0248
12 (XeF_3··I)	−193.96	2.776	4.14	2.79	0.0682	−0.0230
13 (XeF_4··CO)	−2.50	3.539	3.86	2.16	0.0073	0.0010
14 (XeF_4··FH)	−4.18	3.159	3.63	1.97	0.0105	0.0020
15 (XeF_4··NCH)	−4.29	3.330	3.71	2.11	0.0103	0.0015
16 (XeF_4··NH_3)	−7.02	3.141	3.71	2.11	0.0168	0.0008
17 (XeF_4··Br)$^-$	−19.80	3.238	4.01	2.60	0.0240	−0.0004
18 (XeF_4··I)$^-$	−15.81	3.530	4.14	2.79	0.0183	0.0001
19 (XeF_5··CO)$^+$	−10.83	3.010	3.86	2.16	0.0228	0.0004
20 (XeF_5··FH)$^+$	−16.04	2.675	3.63	1.97	0.0257	0.0032
21 (XeF_5··NCH)$^+$	−26.73	2.685	3.71	2.11	0.0366	−0.0013
22 (XeF_5··NH_3)$^+$	−36.73	2.610	3.71	2.11	0.0508	−0.0070
23 (XeF_5··Br)	−179.14	2.585	4.01	2.60	0.0816	−0.0233
24 (XeF_5··I)	−174.20	2.798	4.14	2.79	0.0673	−0.0172
25 (XeF_6··CO)	−3.47	3.162	3.86	2.16	0.0149	0.0012
26 (XeF_6··FH)	−3.47	2.964	3.63	1.97	0.0116	0.0029
27 (XeF_6··NCH)	−6.92	2.870	3.71	2.11	0.0231	0.0012
28 (XeF_6··NH_3)	−18.36	2.586	3.71	2.11	0.0502	−0.0069
29 (XeF_6··Br)$^-$	−43.29	2.807	4.01	2.60	0.0556	−0.0098
30 (XeF_6··I)$^-$	−36.75	3.050	4.14	2.79	0.0449	−0.0066

(McKee et al., 1973) shows a short contact between one F-atom of the anion and the Xe-atom that exhibits the typical T-shaped geometry. It is worth mentioning that the F-atom of the anion that makes the short contact is in the same plane defined by the four atoms of the XeF_3 cation. Although the contact is significantly shorter than ΣR_{vdw}, (indicating some degree of covalency), the two lone pairs located at the Xe(IV) atom are not involved in the bonding since they are not located in the molecular plane. It is interesting to comment the structure ICSD-193743 that has the following formula $[H_5F_4][SbF_6]\cdot 2[XeF_3\cdot HF][Sb_2F_{11}]$, thus including HF units in the structure (Brock et al., 2013). In **Figure 4B** only the $[XeF_3\cdot HF][Sb_2F_{11}]$ fragment is represented, where the H-atom has been added in an arbitrary position. Again the interacting F-atom of the HF is located in the molecular plane and establishes a very short NgBs with the Xe-atom. It is also remarkable the solid state structure of the $[XeF_3]^+[SbF_6]^-$ salt that forms tetrameric assemblies in the solid state where two different Xe···F NgB contacts are established (Brock et al., 2013). A common feature of all X-ray structures presented in **Figures 4A–C** is that the electron rich atom is not located exactly opposite to the F–Xe bond, in fact the F_{ax}-Xe···F angle varies from 154 to 160° in these salts. Interestingly, if $[BiF_6]^-$ is used as anion instead of $[SbF_6]^-$ (see **Figure 4D**) (Gillespie et al., 1977), the Xe····F bond becomes very short (close to ΣR_{cov}) and the F–Xe···F is close to linearity, thus suggesting the formation of a partial covalent bond. The approximation of the fluoride lone-pair to the middle of the edge of the trigonal bipyramid containing the two stereo-active lone pairs, forces the geometry around the Xe to be approximately square-planar. Thus the overall stereochemistry changes from a T-shaped AX_3E_2 in the $[XeF_3]^+[BiF_6]^-$ salt to a square-planar AX_4E_2 structure in the $[XeF_3]^+[SbF_6]^-$ salt. This behavior agrees well with the low acidity of BiF_5 molecule compared to SbF_5 (Gillespie and Pez, 1969).

In 2014 the synthesis and X-ray characterization of several $[C_6F_5XeF_2]^+$ salts were published (Koppe et al., 2014). The ligand arrangement around xenon in the three salts shown in **Figure 4** (bottom panel) is T-shaped, in accordance with the expected arrangement of three bonding electron pairs and two additional electron lone pairs in the xenon valence shell. The electron lone pairs cause the F–Xe(I)–F angles to bend toward the C_6F_5 group producing nonlinear F–Xe(I)–F angles (∼170°). The distances of the NgB contacts are longer in these salts compared to the $[XeF_3]^+$ salts because the C_6F_5 group (Xe–C bond) is less electron withdrawing than fluorine atom (Xe–F bond). Again the electron donor atom is not located exactly opposite to the Xe–C bond, as further commented below (DFT study). It is interesting to highlight the QOYRIH structure (see **Figure 4F**) where two HF molecules connect the anion and cation by establishing two Xe···F NgBs with the Xe atom and two F–H···F H-bonds with the $[BF_4]^-$ anion. In the $[C_6F_5XeF_2]^+$ $[BF_4]^-$ salt (**Figure 4G**), the anion establishes two NgBs with the counter-cation. In spite the NgB contacts in $[C_6F_5XeF_2]^+$ salts are longer than those in $[XeF_3]^+$ salts, the distances are significantly shorter than ΣR_{vdw}, due to the electrostatic attraction between the counterions.

DFT Calculations

The molecular electrostatic potential (MEP) surface analysis of $[XeF_3]^+$ cation has been computed to rationalize its ability to establish charge assisted NgBs, as shown in the X-ray structures represented **Figure 4**. **Figure 5** shows the MEP surfaces of $[XeF_3]^+$ using two different orientations and it reveals the existence of a positive region at the Xe atom and opposite to the equatorial F-atom (see **Scheme 1B**). A close examination of the positive σ-hole shows that the maximum value of MEP is not located strictly along the extension of the Xe–F bond. Instead there are two symmetric σ-holes that are slightly displaced toward the axial F-atoms (see **Figure 5**, bottom-right). The MEP analysis agrees well with the directionality of the NgBs observed in the aforementioned X-ray structures.

The same electron donors used above for XeF_2 complexes (see **Scheme 1A**) have been also used for the theoretical study of the $[XeF_3]^+$ cation. The structure of $[XeF_3]^+$ is T-shaped with C_{2v}

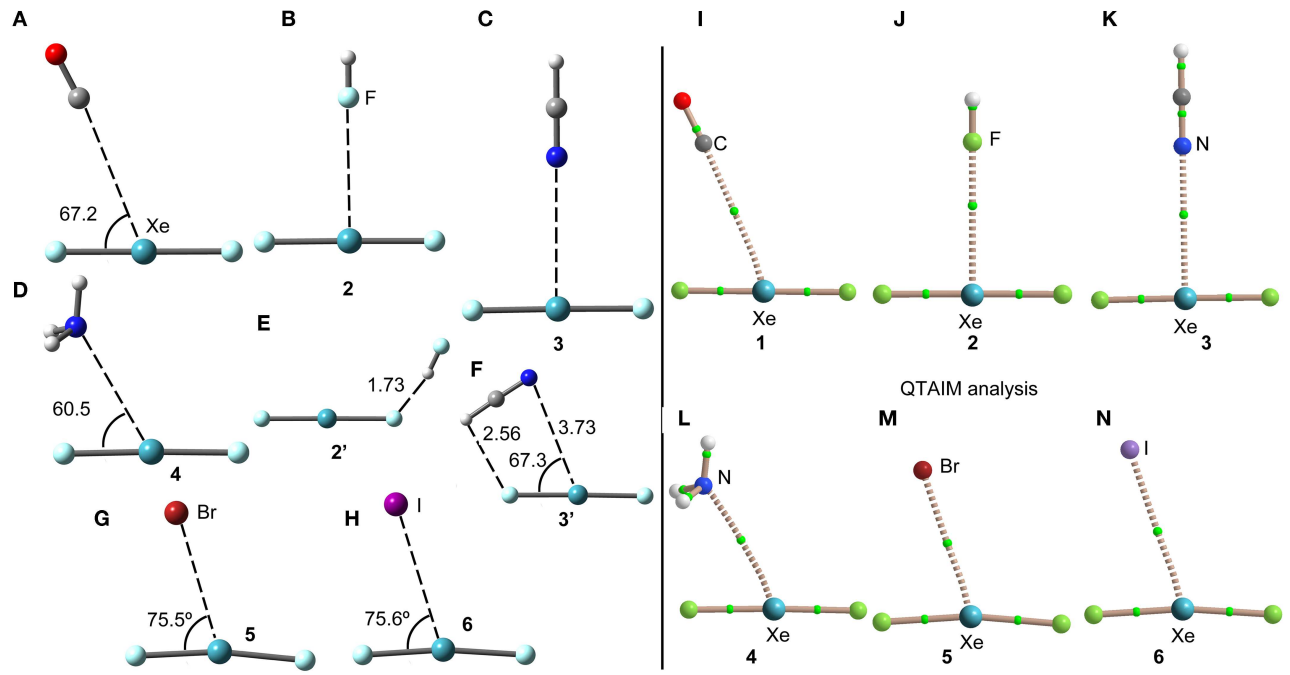

FIGURE 3 | Left panel: PBE1PBE-D3/def2-TZVP Optimized geometries of complexes **1 (A)**, **2 (B)**, **3 (C)**, **4 (D)**, **2' (E)**, **3' (F)**, **5 (G)** and **6 (H)**. Distances in Å. Right panel: QTAIM distribution of bond critical points (green spheres) and bond paths for complexes **1 (I)**, **2 (J)**, **3 (K)**, **4 (L)**, **5 (M)**, and **6 (N)** at the PBE1PBE-D3/def2-TZVP level of theory.

symmetry and it is derived from a trigonal bipyramid with two stereo-active lone pairs occupying the equatorial positions with a Xe in the +4 oxidation state (see **Scheme 1B**). Taking into consideration the location of the lone pairs the most favorable approximation of an electron rich atom should avoid the spatial region of these lone pairs. Thus, the expected directionality of the NgB interaction is indicated by the red dashed lines in **Scheme 1** and agrees well with and the position of the σ-holes revealed by the MEP surface.

The interaction energies and distances for complexes **7**–**12** are gathered in **Table 1**. It can be observed that the interaction energies are very large in all cases, as expected taking into consideration the cationic nature of the electron acceptor. Complexes **7** and **8** are the weakest ones and present equilibrium distances that are ∼0.5 Å longer than the sum of their covalent radii (also tabulated in **Table 1**). The equilibrium distances of complexes **9** and **10** are slightly longer (0.2–0.3 Å) than ΣR_{cov} thus indicative of partial covalency, especially in the NH_3 complex **10**. Finally, the equilibrium distance of anionic complexes **11** and **12** is very similar to their ΣR_{cov} thus suggesting the formation of a covalent bond. In fact, the binding energies computed for these complexes are very large (<-193 kcal/mol) due to the covalent nature of the bond.

The geometries of the $[XeF_3]^+$ complexes are given in **Figure 6** (left panel), where it can be observed that for most of the complexes the electron rich atom is located along the extension of the Xe–F bond, yielding to the typical square planar geometry of XeX_4E_2 compounds with the stereo-active lone pairs pointing to the axial positions (Haner and Schrobilgen, 2015). This fact confirms the great degree of covalency in $[XeF_3]^+$ complexes. Only the complex with HF follows the expected orientation, also in good agreement with the X-ray structures involving HF as electron donor (see **Figures 4B,F**). It is surprising the location of the CO in complex **7**, exactly opposite to the Xe–F_{eq} bond, due to the apparent non-covalent nature of the NgB interaction in this complex.

The NgB covalent/non-covalent nature of the interaction in complexes **7**-**12** has been unveiled by using the quantum theory of "atoms-in-molecules" (QTAIM) (Bader, 1985). Similarly to XeF_2 complexes, the NgB in $[XeF_3]^+$ complexes are characterized by a bond critical point (CP) and bond path interconnecting the electron rich and Xe atoms (see **Figure 6**, right panel). The values of electron charge density ρ(r) at the bond CPs are listed in **Table 1**. They are significantly larger than those observed in complexes **1**–**6**, in line with the stronger interaction. For this set of complexes, the logarithmic fitting [ρ(r) vs ΔE] shows a modest relationship with a regression coefficient of $r = 0.818$, see **Supplementary Material**. The values of the total energy density [H(r)] at the bond CPs summarized in **Table 1** are indicative of partial covalent character in all complexes apart from complex **8**, in good agreement with the geometric features of the complexes. Surprisingly, the CO complex also exhibits a covalent character [$H(r) = -0.0033$ a.u.], which is probably due to the fact that the equilibrium distance (2.704 Å) is more than 1 Å shorted than ΣR_{vdw} (3.86 Å).

The covalent character of these complexes is also confirmed by the NBO analysis. Again, using the $(XeF_3 \cdot\cdot NH_3)^+$ as model

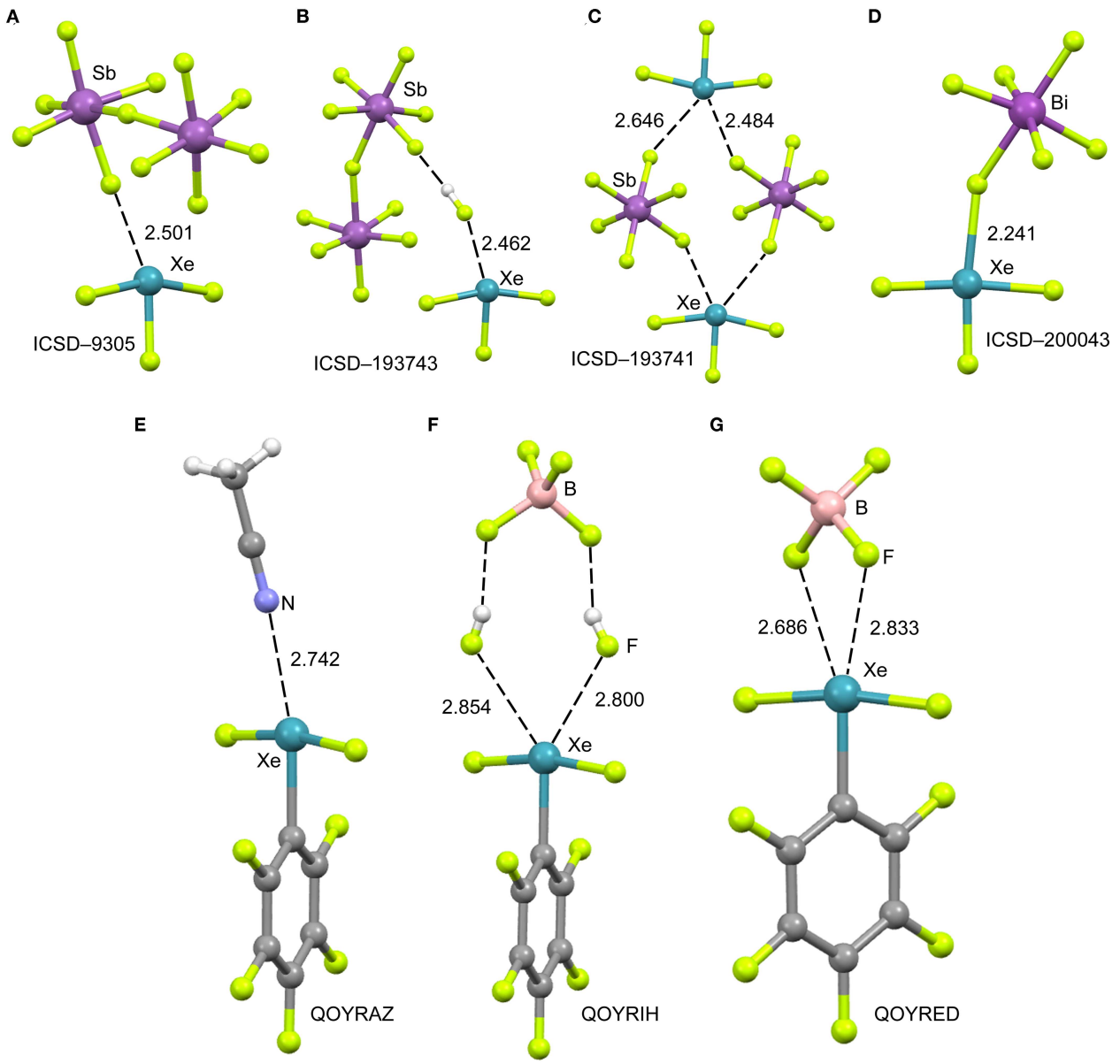

FIGURE 4 | Top panel: Partial views of the X-ray structures ICSD-9305 **(A)**, ICSD-193743 **(B)**, ICSD-193741 **(C)** and ICSD-200043 **(D)**. Distances in Å. NgBs represented as dashed lines. Bottom panel: Partial views of the X-ray structures with Cambridge Structural Database reference codes QOYRAZ **(E)**, QOYRIH **(F)** and QOYRED **(G)**. Distances in Å. NgBs represented as dashed lines.

complex, the NBO treats the N–Xe bond as covalent since the energetic contribution of the orbital [LP(n)→ σ*(Xe–F)] donor-acceptor interaction is −73.14 kcal/mol, significantly stronger that the interaction energy (see **Table 1**).

XeF_4

X-ray Crystal Structures

In spite of XeF_4 was the first fluoride of xenon to be discovered, it is the most difficult to synthesize among the series of binary xenon fluorides (XeF_2, XeF_4, and XeF_6). There is a few number of X-ray structures including the XeF_4 moiety and they are represented in **Figure 7**. One of them is the XeF_2·XeF_4 adduct (Burns et al., 1965) already described above from the perspective of XeF_2 as NgB donor. In this section, the X-ray structure is analyzed from the opposite point of view, that is considering XeF_4 as electron acceptor and XeF_2 as electron donor. The XeF_4 participates in two short Xe···F contacts with the adjacent XeF_2 molecules, establishing two symmetrically equivalent NgBs (see **Figure 7A**). A similar arrangement is observed in the X-ray structure of XeF_4 (Ibers and Hamilton,

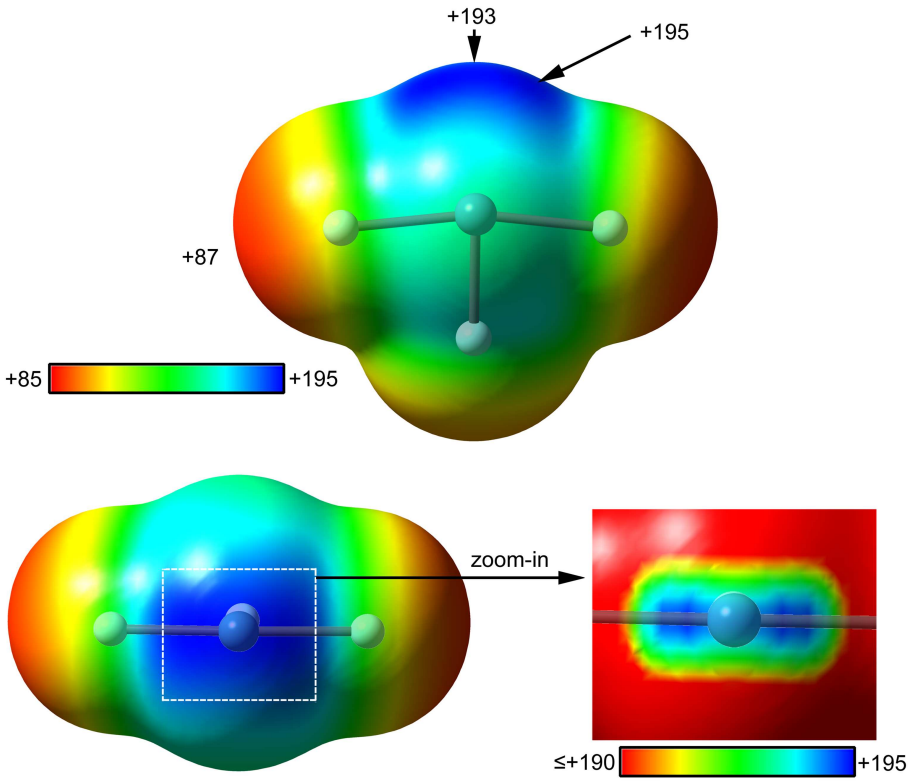

FIGURE 5 | MEP surfaces (0.001 a.u.) of XeF_3^+ (top and bottom-left) and a "zoom-in" representation at the PBE1PBE-D3/def2-TZVP level of theory. The MEP energies at selected points are indicated in kcal/mol.

1963), where the central Xe atom participates in two NgBs above and below the molecular plane (see **Figure 7B**). In contrast to the behavior of XeF_2, coordination compounds involving XeF_4 acts ligand are scarce in the literature due to lower fluorobasicity of XeF_4. One example is given in **Figure 7C** (Tavčar and Žemva, 2009), where it is coordinated to Mg(II) and, simultaneously, establishes a NgB interaction with the adjacent (also coordinated) AsF_6^- anion. A partial view of the X-ray structure $([XeF_5][CrF_5])_4{\cdot}XeF_4$ adduct is shown in **Figure 7D** (Lutar et al., 1992), where the XeF_5 units have been omitted for clarity. The distorted CrF_6-octahedra are connected to each other via Xe···F bridging NgBs. The stereo-active electron lone pairs lie above and below the XeF_4-plane, preventing the approximation of the electron rich atom along the C_4 axis. Therefore, in all X-ray structures gathered in **Figure 7**, the approach occurs between the lone pairs and the molecular plane to minimize the repulsions between the lone pairs of Xe and the electron rich atom.

DFT Calculations

The molecular electrostatic potential (MEP) surface of $[XeF_4]$ is represented in **Figure 8**. The minimum MEP is located at the F-atoms and, remarkably, the value (−10 kcal/mol) is half the one of XeF_2, confirming the less fluorobasicity of this molecule and explaining the weak ability of this molecule as coordination ligand. The MEP surface plot also shows a large π-hole located at the Xe-atom above and below the molecular plane. A close examination of the positive region reveals the existence of four symmetric π-holes that are displaced toward the bisectrix of the F–Xe–F angle (see **Figure 8**, right). The MEP analysis strongly agrees with the directionality of the NgBs observed in the X-ray structures represented in **Figure 5**. The MEP maximum in XeF_4 is significantly larger than that in XeF_2, thus stronger NgB interactions are expected.

Using the same set of electron donors the energetic and geometric features of XeF_4 complexes have been studied, as indicated in **Scheme 1C**. The structure of XeF_4 is square planar with D_{4h} symmetry and it is derived from an octahedral geometry with two stereo-active lone pairs occupying the axial positions with a Xe in the +4 oxidation state (see **Scheme 1C**). Taking into consideration the location of the lone pairs the most favorable approximation of an electron rich atom should avoid the spatial region of these lone pairs, as aforementioned. Thus, the expected directionality of the NgB interaction is indicated by the red dashed lines in **Scheme 1C** and agrees well with and the position of the four π-holes revealed by the MEP surface.

The interaction energies and equilibrium distances of NgB complexes **13**–**18** are summarized in **Table 1**. It can be observed that the NgB interaction energies are stronger in XeF_4 complexes than those in XeF_2 complexes, as predicted by the MEP analysis. Similarly, to the behavior of XeF_2, complexes **13** (X = CO), **14** (X = HF) and **15** (X = HCN) are the weakest ones. All

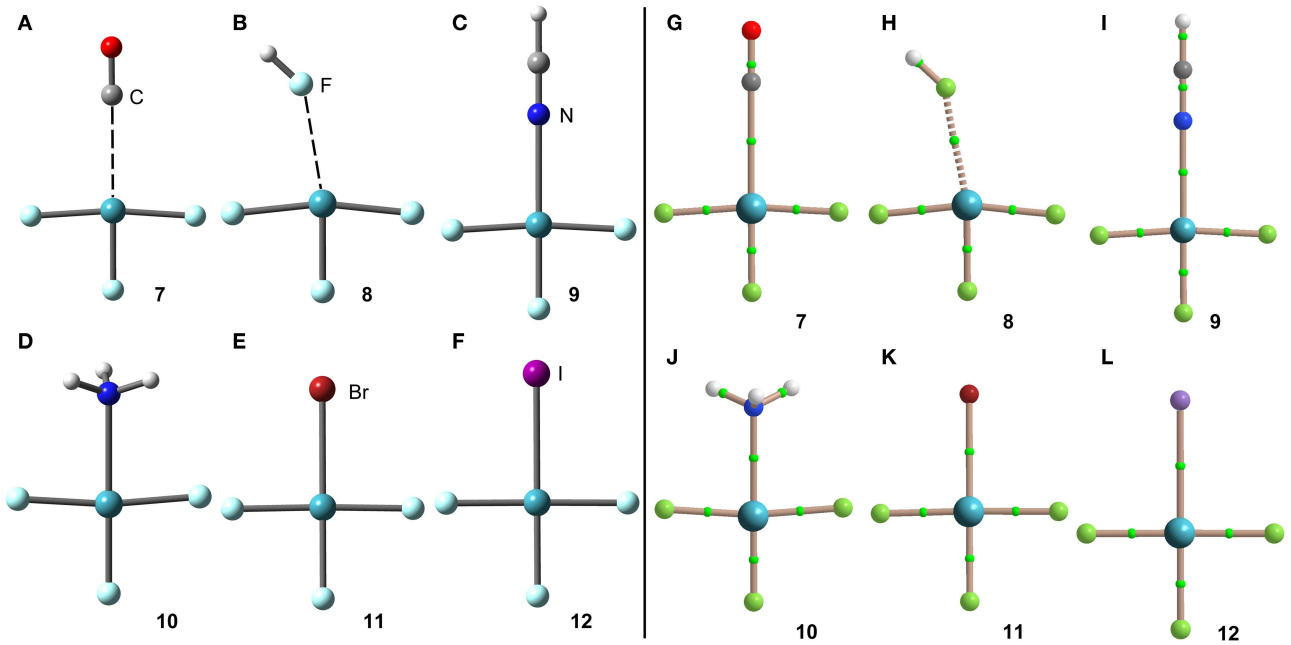

FIGURE 6 | Left panel: PBE1PBE-D3/def2-TZVP Optimized geometries of complexes **7 (A)**, **8 (B)**, **9 (C)**, **10 (D)**, **11 (E)** and **12 (F)**. Distances in **Table 1**. Right panel: QTAIM distribution of bond critical points (green spheres) and bond paths for complexes **7 (G)**, **8 (H)**, **9 (I)**, **10 (J)**, **11 (K)**, and **12 (L)** at the PBE1PBE-D3/def2-TZVP level of theory.

complexes exhibit equilibrium distances that are shorter than ΣR_{vdw} and significantly longer than ΣR_{cov} thus suggesting the non-covalent nature of the interaction. As expected, the most favorable neutral complex corresponds to the ammonia (**16**) and the anionic complexes **17** and **18** present the stronger interactions of this series.

The optimized geometries of the XeF_4 complexes are given in **Figure 9**, left panel, where it can be observed that the electron rich atom in complexes **13**–**16** is located over the bisector of the F–Xe–F bond at distances that range from 3.1 to 3.6 Å (see **Table 1**), in good agreement with the X-ray structures and MEP surface. It should be mentioned that the optimization of anionic complexes has been performed imposing C_s symmetry and locating the anion over one Xe–F bond. In case it is located over the bisector, the optimization yields to the nucleophilic attack of the anion to the Xe-atom, yielding a planar and pentacoordinated $[XeF_4X]^-$ anion (X = Br, I). This result agrees well with the X-ray structure of the $[XeF_5]^-$ anion that is planar ($\sim D_{5h}$-geometry) (Christe et al., 1991).

The NgB interaction in complexes **13**–**18** has been further characterized using the QTAIM analysis. In agreement with previous observations, the NgB is characterized by a bond critical point (CP) and bond path that connects the electron rich atom to the Xe (see **Figure 9**, right panel). The values of electron charge density ρ(r) at the bond CPs are tabulated in **Table 1** and analogously to XeF_2 complexes the values of ρ(r) at the bond CPs that characterize the NgB correlate remarkably well with the interaction energies by using a logarithmic fitting (regression coefficient, $r = 0.965$, see **Supplementary Material**), thus confirming that the value of ρ(r) at the bond CP can be used as a measure of the strength of the NgB interaction. The values of the total energy density [H(r)] at the bond CPs are also summarized in **Table 1**, which corroborate the non-covalent nature of the interaction in all complexes. Only the Br^- complex exhibit some covalent character as deduced by its negative and small H(r) value and strong binding energy.

The NBO analysis has been carried out for the $XeF_4\cdots NH_3$ complex and the orbital interaction is similar to the $XeF_2\cdots NH_3$ complex with a LP(N)→ σ*(Xe–F) interaction of $E^{(2)} = 1.12$ kcal/mol, however it is smaller compared to the total interaction energy (∼14%). Therefore the interaction is clearly dominated by electrostatic effects.

XeF_5^+

X-ray Crystal Structures

The mixture of XeF_6 and RuF_5 yields the $[XeF_5]^+[RuF_6]^-$ salt, as represented in **Figure 10A** (Christe et al., 1991). The structural analysis shows that each xenon atom is bonded to five fluorine atoms in an approximately square-pyramidal arrangement. Each ruthenium atom is surrounded by six fluorine atoms in an octahedral coordination mode. The xenon atom in $[XeF_5]^+$ cation retains an stereo-active lone pair, therefore it can be assumed that it is pseudooctahedrally coordinated with five F atoms and the sterically active valence-electron pair that is located along the fourfold axis. Therefore, the approximation of any electron rich atom is expected to be below the basal plane of the $[XeF_5]^+$ cation and off axis, as observed in the crystal structures represented in **Figure 10**. In the particular case of

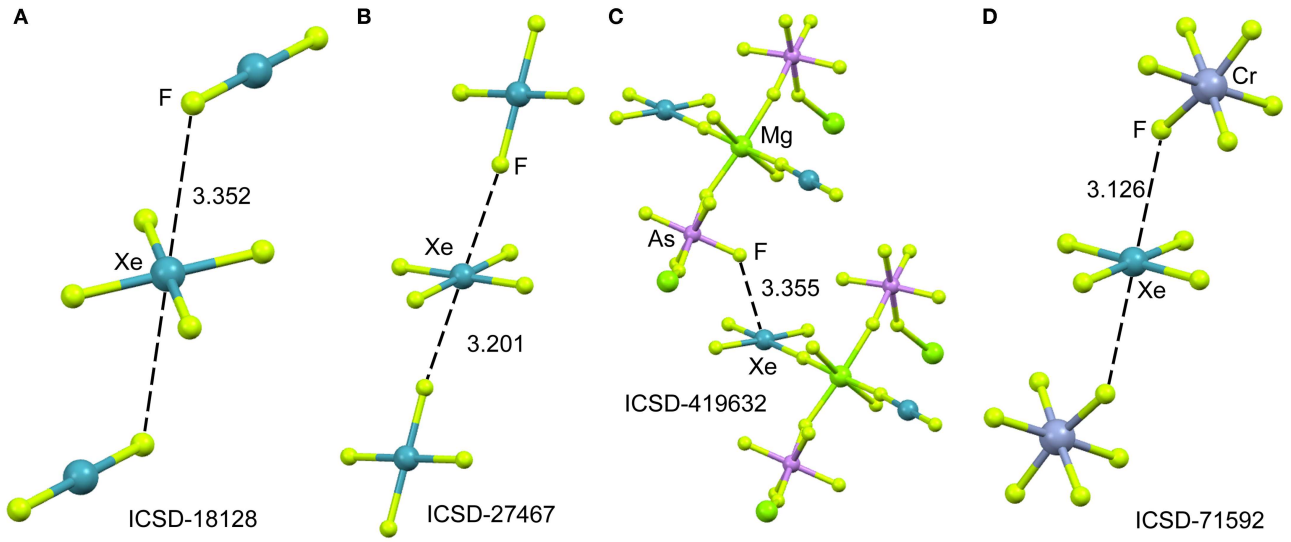

FIGURE 7 | Partial views of the X-ray structures ICSD-18128 **(A)**, ICSD-27467 **(B)**, ICSD-419632 **(C)** and ICSD-71592 **(D)**. Distances in Å. NgBs represented as dashed lines.

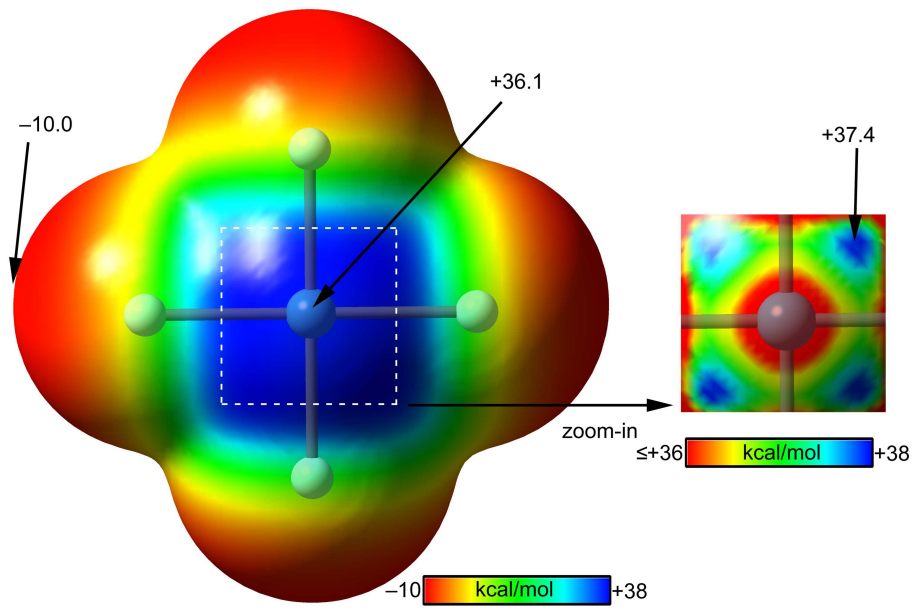

FIGURE 8 | MEP surfaces (0.001 a.u.) of XeF_4 (left) and a "zoom-in" representation at the PBE1PBE-D3/def2-TZVP level of theory. The MEP energies at selected points are indicated in kcal/mol.

$[XeF_5]^+[RuF_6]^-$ salt, the Xe atom establishes two NgB contacts with two F-atoms of the counterions that are located below the F–Xe–F bisector.

When XeF_6 is crystallized from anhydrous HF, an interesting compound is obtained that corresponds to the formulae $([XeF_5]^+)_2\cdot([HF_2]^-)_2\cdot HF$ (Hoyer et al., 2006). The most interesting feature observed in the solid state of this structure is the existence of dimeric units of $[XeF_5]^+[F]^-$ (see **Figure 10B**) that are stabilized by the formation of four Xe···F contacts. The $[XeF_5]^+[F]^-$ dimer also interacts with two HF molecules by H-bonding interactions. The same type of dimers has been also obtained without the co-crystalized solvent molecules upon recrystallization using CF_2Cl_2. It is also interesting to highlight the product (see **Figure 10C**) that is obtained by recrystallization from inert solvents at low temperature. It is a regular tetrameric unit $([XeF_5]^+\cdot F^-)_4$ formed by four square pyramidal $[XeF_5]^+\cdot$ that are connected by four Xe···F···Xe bridges with similar distances and angles (118–121°). **Figure 10D** shows a partial view

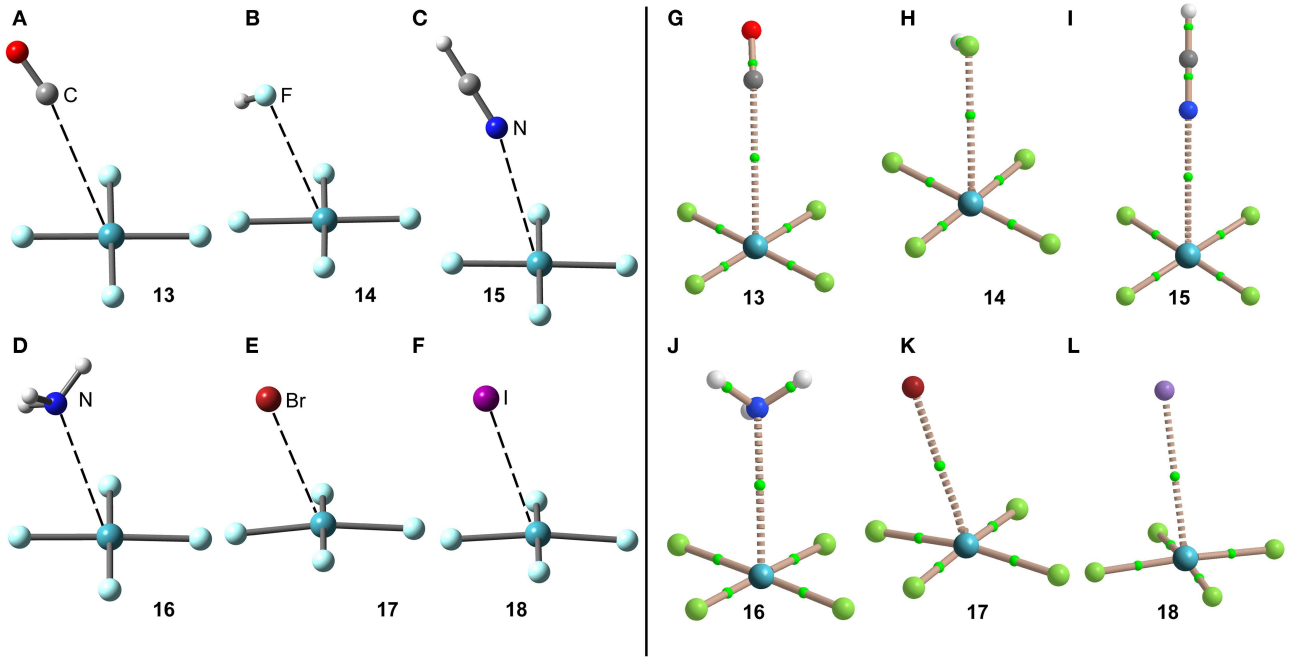

FIGURE 9 | Left panel: PBE1PBE-D3/def2-TZVP Optimized geometries of complexes **13 (A)**, **14 (B)**, **15 (C)**, **16 (D)**, **17 (E)** and **18 (F)**. Distances in Å. Right panel: QTAIM distribution of bond critical points (green spheres) and bond paths for complexes **13 (G)**, **14 (H)**, **15 (I)**, **16 (J)**, **17 (K)**, and **18 (L)** at the PBE1PBE-D3/def2-TZVP level of theory.

of the X-ray structure of $[XeF_5]_2^+ \cdot [PdF_6]^{2-}$ salt (Lutar et al., 1998). It can be observed that each $[XeF_5]^+$·cation establishes three charge assisted NgBs with the surrounding $[PdF_6]^{2-}$ units. In general the Xe···F distances in the four X-ray structures shown in **Figure 10** are shorter than those preciously described for the $[XeF_3]^+$ cation, thus suggesting stronger binding and higher covalency.

DFT Calculations

The molecular electrostatic potential (MEP) surface analysis of $[XeF_5]^+$ cation has been computed to rationalize its ability to establish charge assisted NgBs. **Figure 11** shows the MEP surfaces of $[XeF_5]^+$ using two different orientations and it reveals the existence of a large and positive region at the Xe atom and opposite to the axial F-atom. A close examination of the positive σ-hole shows that the maximum value of MEP is not located strictly along the extension of the Xe–F bond. Instead there are four symmetric σ-holes that are slightly displaced toward the bisectors of the F–Xe–F (F atoms in *cis*, see **Figure 11**, bottom-right), similarly to the behavior described above for the neutral XeF_4. The MEP analysis strongly agrees with directionality of the NgBs observed in the X-ray structures shown in **Figure 10**.

The computed $[XeF_5]^+$ complexes are shown in **Scheme 1D** where the geometry of $[XeF_5]^+$ is square-pyramidal with C_{4v} symmetry that derives from a pseudooctahedral with the stereoactive lone pair occupying the remaining axial position with a Xe in the +6 oxidation state (see **Scheme 1D**). Taking into consideration the location of this lone pair the most favorable approximation of an electron rich atom should avoid the spatial region occupied by this lone pair, as depicted using red dashed lines.

The interaction energies and distances for complexes **19**–**24** are gathered in **Table 1**. It can be observed that the interaction energies are larger than those of XeF_4 in all cases, as expected taking into consideration the cationic nature of the electron acceptor. Complexes **19** and **20** are the weakest ones and present equilibrium distances that are longer than the sum of their covalent radii (also tabulated in **Table 1**). Complexes **21** and **22** exhibit moderately strong binding energies and equilibrium distances that are 0.5 Å longer than ΣR_{cov}. Taken together, these results suggest a partial covalency of the NgB in these complexes. Interestingly, **Figure 12** (left panel) shows that in all complexes with neutral electron donors the electron rich atom points to one of the four σ-holes described in **Figure 11**. This behavior is opposite to the previously described for the $[XeF_3]^+$ complexes, where all electron rich atoms were located opposite to the Xe–F_{eq} bond apart from the HF complex. Finally, the equilibrium distance of anionic complexes **23** and **24** is very similar to their ΣR_{cov} thus suggesting the formation of a pure covalent bond. In fact, the interaction energies for these complexes are very large and the geometry around the Xe atom is octahedral.

The NgB covalent/ non-covalent nature of the interaction in complexes **19**–**24** has been analyzed by using the quantum theory of "atoms-in-molecules" (QTAIM). Similarly to the rest of NgB complexes of XeF_2, $[XeF_3]^+$ and XeF_4, the NgB in $[XeF_5]^+$ complexes is characterized by a bond critical point (CP) and bond path interconnecting the electron rich and Xe atoms (see

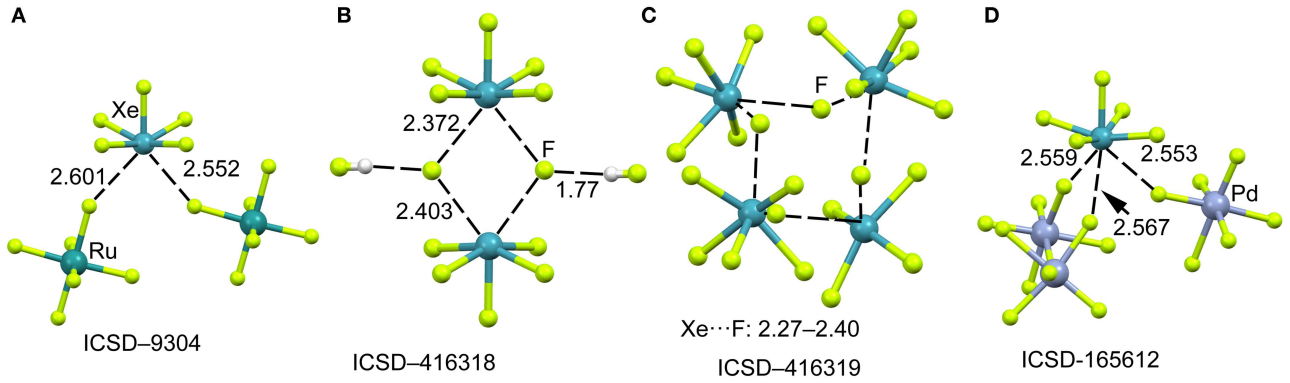

FIGURE 10 | Partial views of the X-ray structures ICSD-9304 **(A)**, ICSD-416318 **(B)**, ICSD-416319 **(C)** and ICSD-165612 **(D)**. Distances in Å. NgBs represented as dashed lines.

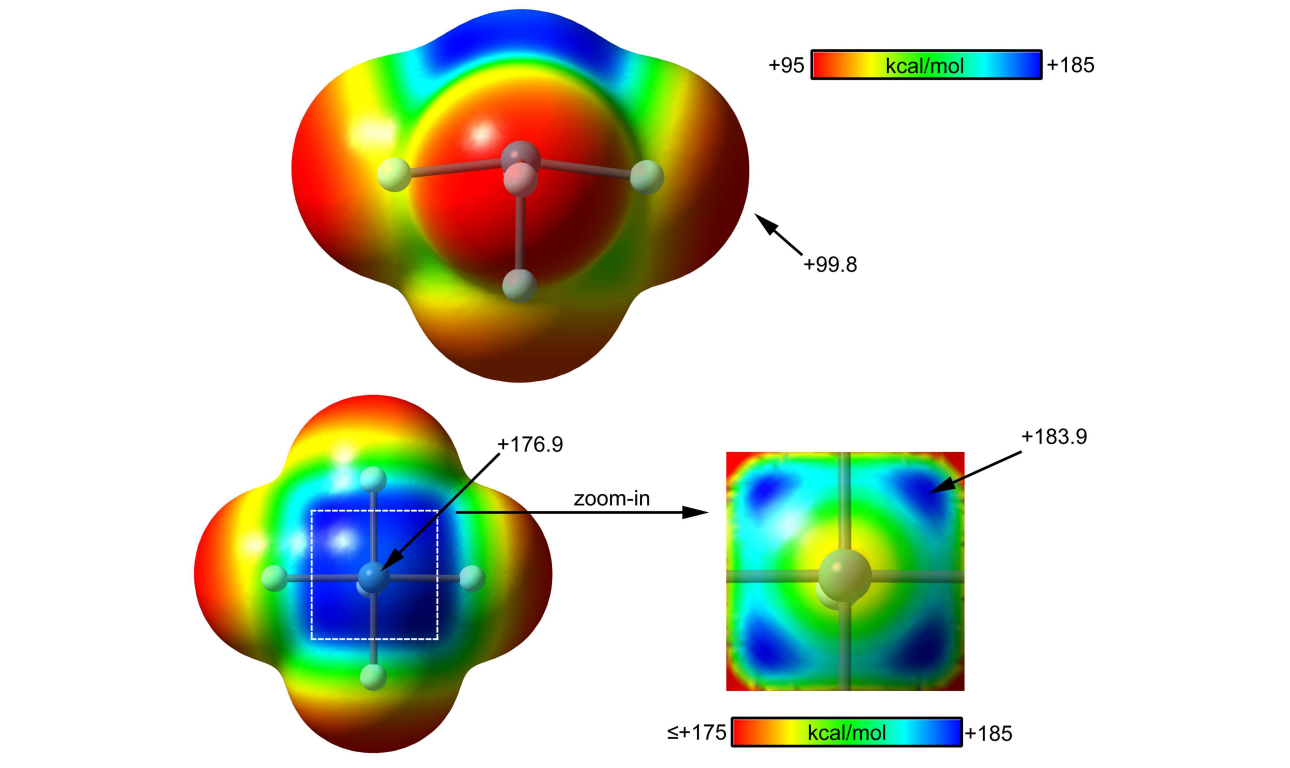

FIGURE 11 | MEP surfaces (0.001 a.u.) of XeF_5^+ (top and bottom-left) and a "zoom-in" representation at the PBE1PBE-D3/def2-TZVP level of theory. The MEP energies at selected points are indicated in kcal/mol.

Figure 12, right panel). The values of electron charge density ρ(r) at the bond CPs are listed in **Table 1** and they are significantly larger than those observed in complexes **13**–**18**, and similar to those of complexes **7**–**12**. For this set of complexes, the value of ρ(r) at the bond CP also correlates well with the interaction energy, since the logarithmic fitting gives a regression coefficient of $r = 0.973$, see **Supplementary Material**. The values of the total energy density [H(r)] at the bond CPs summarized in **Table 1** are indicative of partial covalent character in complexes **21** and **22**, in good agreement with the energetic features of these complexes. The H(r) values also confirm the covalent nature of the NgBs in complexes **23** and **24**, in line with the covalent distances and strong binding energies.

The NBO analysis of complex **22** (X = NH_3) shows a moderately strong orbital donor acceptor interaction [LP(N)–σ*(Xe–F)] with an associated stabilization energy of $E^{(2)} = -11.5$ kcal/mol. This result agrees well with the QTAIM analysis that anticipated partial covalent character [small and negative H(r)]. In fact, the orbital contribution accounts for the 31% of the total interaction energy.

XeF_6

X-ray Crystal Structures

It has been recently reported (Matsumoto et al., 2015) the syntheses and X-ray characterization of two adducts of XeF_6 with acetonitrile of composition $F_6Xe(NCCH_3)$ and $F_6Xe(NCCH_3)_2{\cdot}CH_3CN$. They are good examples of σ-hole NgB interactions and are the first X-ray structures where the electron donor is a nitrogen atom. In the $F_6Xe(NCCH_3)$, the XeF_6 unit

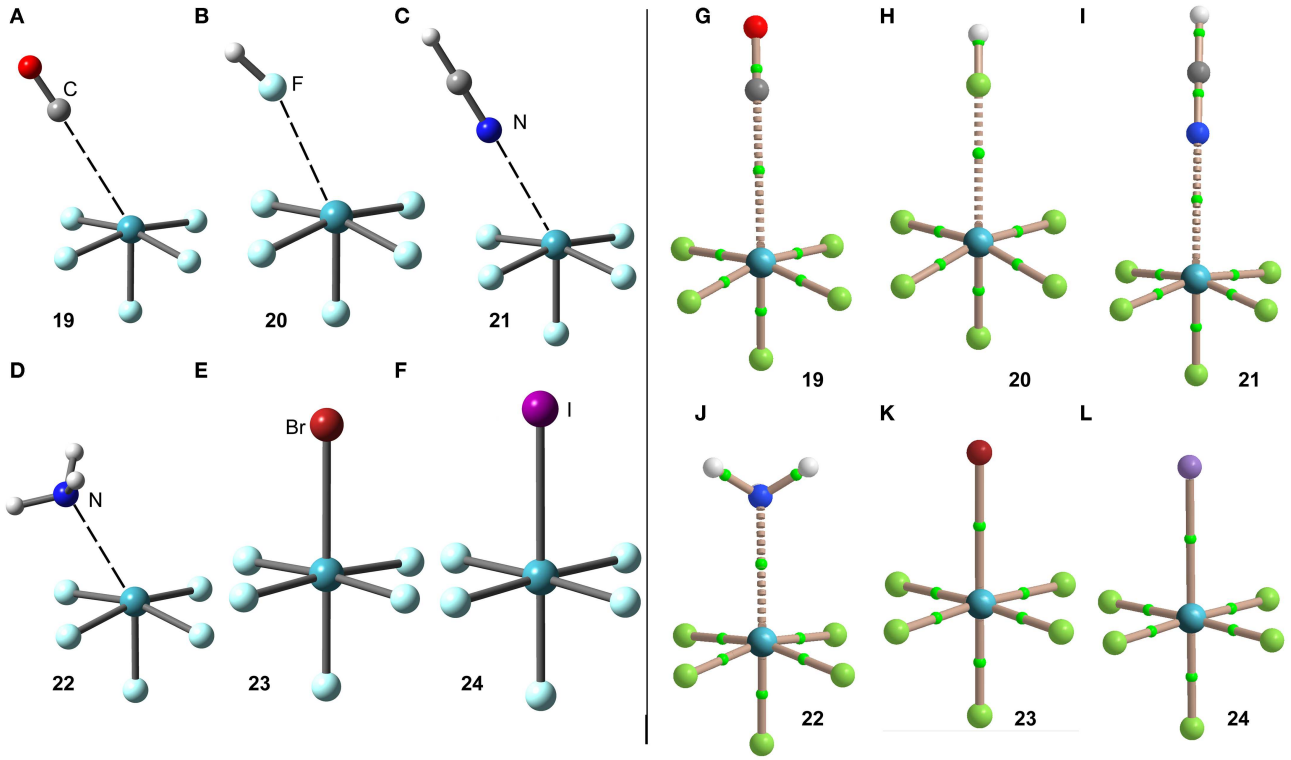

FIGURE 12 | Left panel: PBE1PBE-D3/def2-TZVP Optimized geometries of complexes **19 (A)**, **20 (B)**, **21 (C)**, **22 (D)**, **23 (E)** and **24 (F)**. See **Table 1** for distances. Right panel: QTAIM distribution of bond critical points (green spheres) and bond paths for complexes **19 (G)**, **20 (H)**, **21 (I)**, **22 (J)**, **23 (K)**, and **24 (L)** at the PBE1PBE-D3/def2-TZVP level of theory.

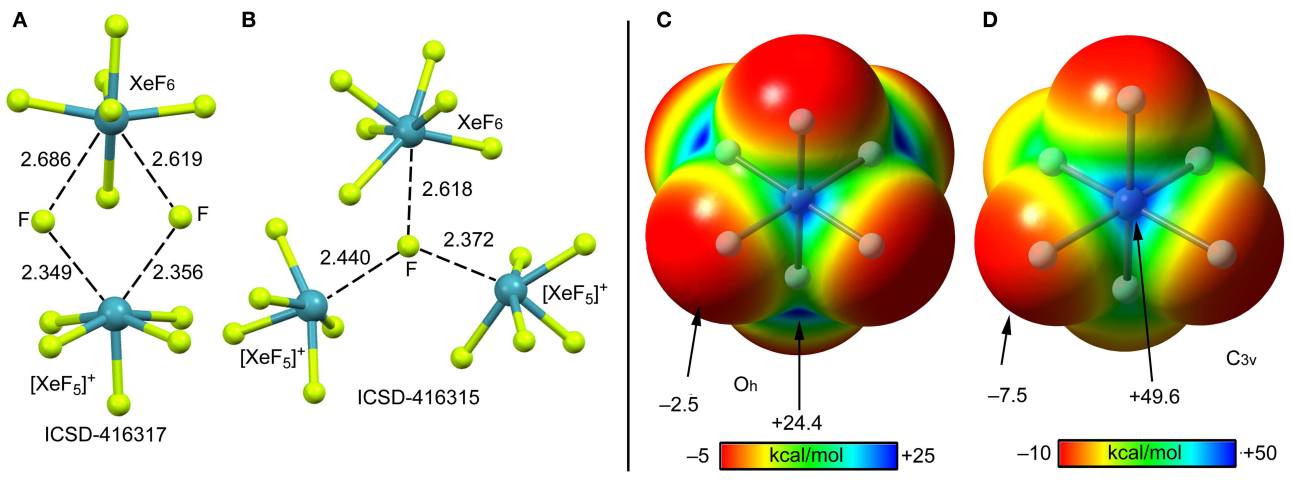

FIGURE 13 | Left panel: Partial views of the X-ray structures ICSD-416317 **(A)** and ICSD-416315 **(B)**. Distances in Å. NgBs represented as dashed lines. Right panel: MEP surfaces (0.001 a.u.) of octahedral **(C)** and C_{3v} **(D)** XeF_6 at the PBE1PBE-D3/def2-TZVP level of theory. The MEP energies at selected points are indicated in kcal/mol.

presented a C_{3v} symmetry similar to that proposed for the gas-phase XeF_6. Other studies have shown that the NgBs in these systems are predominantly electrostatic in nature (Haner et al., 2016).

According to several experimental techniques including crystal X-ray diffraction and neutron powder diffraction, among others, XeF_6 exists in at least six different modifications, depending on the temperature (Hoyer et al., 2006). At high temperature XeF_6 forms a tetramer, better described as $(XeF_5^+F^-)_3{\cdot}XeF_6$ assembly. A partial view of this tetramer is represented in **Figure 13A** where only two fluoride anions, one $[XeF_5]^+$ cation and the XeF_6 unit have been represented for clarity. It can be observed that the fluoride anions bridge the $[XeF_5]^+$ cation and the XeF_6 units by means of four NgBs. Those involving the cation are shorter than those involving the neutral XeF_6 that maintains a pseudoctahedral geometry. **Figure 13B** shows the other form of XeF_6 that is stable at high temperature (obtained by sublimation of the other one). The structure is also tetrameric and better described as $(XeF_5^+F^-)_3{\cdot}XeF_6$ assembly. In this case the fluoride anion is stabilized by three NgBs, one with the XeF_6 unit and two with the $[XeF_5]^+$ cation. Again, the NgB distances involving the XeF_6 unit are longer than those with $[XeF_5]^+$ cation. In this X-ray structure the geometry of the XeF_6 unit is approximately C_{3v}.

DFT Calculations

The molecular electrostatic potential (MEP) surface of $[XeF_6]$ is represented in **Figures 13** (right panel) using the octahedral (**C**) and C_{3v} (**D**) symmetries. The MEP value at the F-atoms is −2.5 kcal/mol in the octahedral form and −7.5 kcal/mol in the C_{3v} form, thus revealing a very low fluorobasicity. For the octahedral XeF_6, the MEP surface plot also shows six symmetrically equivalent σ-holes (24.4 kcal/mol) located in the middle of the six octahedral faces. In contrast, for the C_{3v} form of XeF_6, the maximum value of MEP is more than twice the value obtained for the octahedral form (+49.6 kcal/mol) and it is located at one face of the polyhedron.

The minimum structure of XeF_6 is still under discussion (Kaupp et al., 1996; Seppelt, 2015; Gawrilow et al., 2018; Zhao et al., 2019), since most of the theoretical methods suggests that the O_h-form is more stable than the C_{3v} one, which is the one observed experimentally (see **Scheme 1E**). State of the art calculations suggest that both forms are basically isoenergetic (Dixon et al., 2005). The fact that the energies of both structures of XeF_6 are very close in energy suggests that this molecule is highly fluxional. Therefore, the factors governing the stereoactivity of the lone pair in XeF_6 are very subtle and, consequently, the lone pair has a highly fluxional character (Dixon et al., 2005).

The interaction energies and equilibrium distances of NgB complexes **25**–**30** are summarized in **Table 1**. It can be observed that the NgB interaction energies are stronger in XeF_6 complexes than those in XeF_2 and XeF_4 complexes, as predicted by the MEP analysis. **Table 1** shows that complexes **25** (X = CO), **26** (X = HF) and **27** (X = HCN) are the weakest ones and exhibit equilibrium distances that are significantly longer than ΣR_{cov} and shorter than ΣR_{vdw}, thus suggesting the non-covalent nature of the interaction. However, the rest of complexes (**28**–**30**) present quite short equilibrium distances, thus anticipating some covalent character in agreement with the strong binding energies.

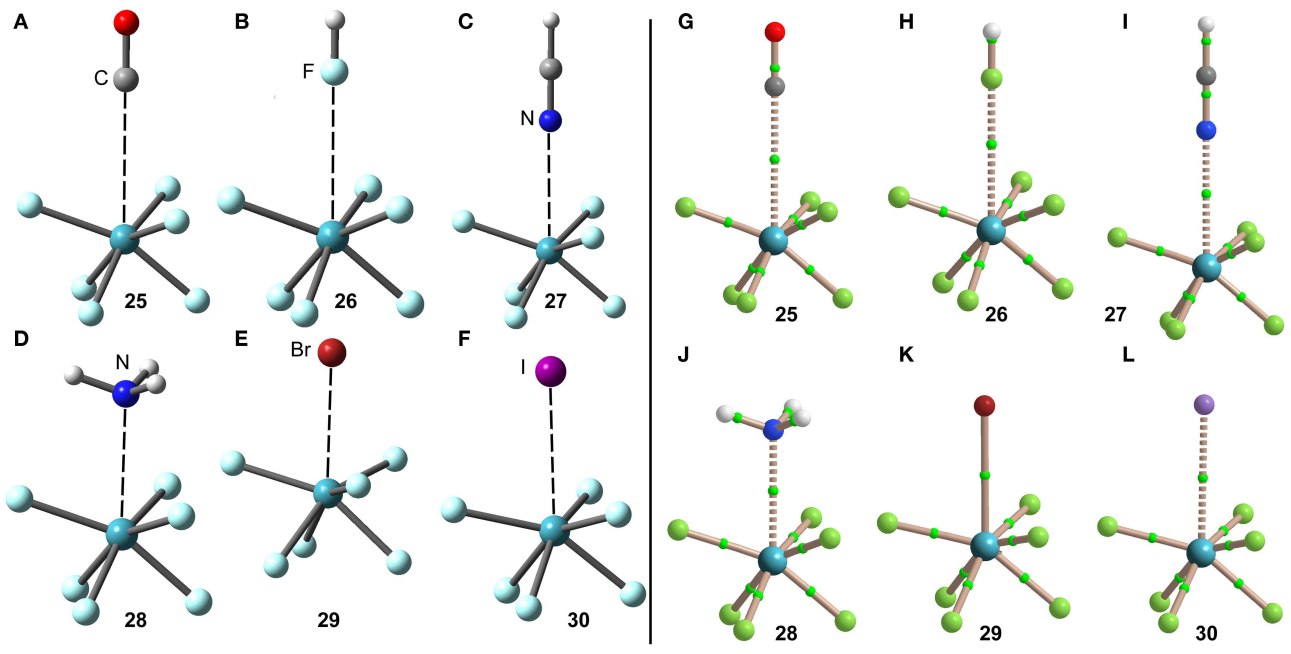

FIGURE 14 | Left panel: PBE1PBE-D3/def2-TZVP Optimized geometries of complexes **25 (A)**, **26 (B)**, **27 (C)**, **28 (D)**, **29 (E)** and **30 (F)**. Distances in **Table 1**. Right panel: QTAIM distribution of bond critical points (green spheres) and bond paths for complexes **25 (G)**, **26 (H)**, **27 (I)**, **28 (J)**, **28 (K)**, and **30 (L)** at the PBE1PBE-D3/def2-TZVP level of theory.

The optimized geometries of the XeF_6 complexes are included in **Figure 14** (left panel), where electron rich atom is located along the C_3 axis. The symmetry of the XeF_6 unit in the complexes is C_{3v} and the Lewis base is located exactly at the position of the σ-hole represented in **Figure 13D**. The C_{3v}-geometry presents a more intense σ-hole thus reinforcing the interaction and compensating the slight deformation energy needed to change from O_h to C_{3v} that is only 0.33 kcal/mol at the level of theory used herein (PBE1PBE-D3/def2-TZVP). The equilibrium distances range from 2.5 to 3.2 Å (see **Table 1**), which are shorter compared to the XeF_2 and XeF_4 complexes, due to the large σ-hole observed in the XeF_6 (C_{3v}-geometry). This behavior is also observed experimentally, since the X-ray structures involving XeF_2 and XeF_4 units exhibit significantly longer distances than those of XeF_6.

The NgB interaction in complexes **25**–**30** has been further characterized using the QTAIM analysis. In agreement with previous observations, the NgB is exclusively characterized by a bond critical point (CP) and bond path that connects the electron rich atom to the Xe atom (see **Figure 14**, right panel). The values of electron charge density ρ(r) at the bond CPs are tabulated in **Table 1** and in line with the rest of complexes, there is good correlation between the values of ρ(r) at the bond CPs that characterize the NgB and the interaction energies by using a logarithmic fitting (regression coefficient, $r = 0.958$, see **Supplementary Material**). It is interesting to highlight that if all complexes **1**–**30** are used in the same representation, a good relationship is also obtained with a $r = 0.928$ (see ESI). It is worthy to emphasize such relationship, since it allows dealing with all complexes in the same plot. The values of the total energy density [H(r)] at the bond CPs are also summarized in **Table 1**, which corroborate the non-covalent nature of the interaction in complexes **25**–**27** and partial covalency in complexes **28**–**30**.

The NBO of the $XeF_6\cdots NH_3$ complex has been computed and it shows the typical LP(N)–σ*(Xe–F) orbital donor acceptor interaction with an associated stabilization energy of $E^{(2)} = -13.8$ kcal/mol, thus revealing a quite strong orbital contribution. significantly stronger than the other two neutral complexes $XeF_2\cdots NH_3$ and $XeF_4\cdots NH_3$. This contribution is even larger than that in the cationic $(XeF_5\cdots NH_3)^+$ complex commented above. This result likely explains the short equilibrium distance and large value of charge density at the bond CP in this complex (larger than the iodide complex). It is also worthy to comment that the three NH bonds of the Lewis base are aligned the Xe–F bonds (see **Figure 14D**), likely contributing to a perfect match between the XeF_6 and NH_3 molecules and a shortening of the Xe···N distance.

CONCLUSIONS

From the results reported in this manuscript, the following conclusions arise:

1. There are numerous examples of X-ray structures of XeF_n (n = 2–6) in the ICSD where non-covalent NgBs play an important role directing the crystal packing and generating interesting supramolecular assemblies, which have been described in detail.
2. The DFT analysis combined with the MEP surfaces show that NgBs are directional and the position of the electron rich atom is determined by the location of the stereo-active lone pair, though the region where the electron pair is located is large and positive.
3. The NgBs in XeF_n (n = 2, 4, 6) are moderately strong with neutral electron donors and quite strong with anions (and NH_3 in some cases). Charge assisted NgBs in $[XeF_3]^+$ and $[XeF_5]^+$ cations are very strong and present high covalent character.
4. The NgBs involving xenon fluorides are characterized by a bond CP and bond path interconnecting the xenon to the electron rich atom. The electron charge density at the bond CP can be used as a measure of the strength of the interaction in the whole set of complexes.
5. Orbital donor acceptor charge transfer effects are important contributors to the NgB interactions in the cationic XeF_3^+, XeF_4^+ and also the neutral XeF_6 molecule, as exemplified by their complexes with NH_3.

DATA AVAILABILITY STATEMENT

The raw data supporting the conclusions of this article will be made available by the authors, without undue reservation, to any qualified researcher.

AUTHOR CONTRIBUTIONS

RG carried out the theoretical calculations and analyzed the data. AF performed the search in the ICSD database, analyzed the data and wrote the manuscript.

FUNDING

Financial support by MICIU/AEI of Spain (project CTQ2017-85821-R FEDER funds) is gratefully acknowledged.

ACKNOWLEDGMENTS

We thank the CTI (Universitat de les Illes Balears) for computational facilities.

SUPPLEMENTARY MATERIAL

The Supplementary Material for this article can be found online at: https://www.frontiersin.org/articles/10.3389/fchem.2020.00395/full#supplementary-material

Supplementary Material 1 | Logarithmic Regression Plots (Energy in kcal/mol, ρ(r) in a.u.).

Supplementary Material 2 | Cartesian coordinates of optimized geometries of all compounds and complexes.

REFERENCES

Adamo, C., and Barone, V. (1999). Toward reliable density functional methods without adjustable parameters: the PBE0 model. *J. Chem. Phys*. 110, 6158–6170. doi: 10.1063/1.478522

Bader, R. F. W. (1985). Atoms in molecules. *Acc. Chem. Res*. 18, 9–15. doi: 10.1021/ar00109a003

Bader, R. F. W. (1990). *Atoms in Molecules, A Quantum Theory*. Clarendon, TX: Oxford.

Bader, R. F. W., Carroll, M. T., Cheeseman, J. R., and Chang, C. (1987). Properties of atoms in molecules: atomic volumes. *J. Am. Chem. Soc*. 109, 7968–7979. doi: 10.1021/ja00260a006

Bartlett, N., and Sladky, F. O. (1968). The relative fluoride ion donor abilities of XeF_2, XeF_4, and XeF_6 and a chemical purification of XeF_4. *J. Am. Chem. Soc*. 90, 5316–5317. doi: 10.1021/ja01021a072

Bartlett, N. (1962). Xenon Hexafluoroplatinate(V) $Xe^{+}[PtF_6]^{-}$. *Proc. Chem. Soc*. 218–220. doi: 10.1039/PS9620000197

Bauzá, A., and Frontera, A. (2015). Aerogen bonding interaction: a new supramolecular force? *Angew. Chem. Int. Ed*. 54, 7340–7343. doi: 10.1002/anie.201502571

Bauzá, A., and Frontera, A. (2020). σ/π-Hole noble gas bonding interactions: insights from theory and experiment. *Coord. Chem. Rev*. 404:213112. doi: 10.1016/j.ccr.2019.213112

Bauzá, A., Mooibroek, T. J., and Frontera, A. (2015). The bright future of unconventional σ/π-hole interactions. *Chem. Phys. Chem*. 16, 2496–2517. doi: 10.1002/cphc.201500314

Bauzá, A., Seth, S. K., and Frontera, A. (2019). Tetrel bonding interactions at work: impact on tin and lead coordination compounds. *Coord. Chem. Rev*. 384, 107–125. doi: 10.1016/j.ccr.2019.01.003

Belpassi, L., Infante, I., Tarantelli, F., and Visscher, L. (2008). The chemical bond between Au(I) and the noble gases. Comparative study of NgAuF and NgAu+ (Ng = Ar, Kr, Xe) by density functional and coupled cluster methods. *J. Am. Chem. Soc*. 130, 1048–1060. doi: 10.1021/ja0772647

Brock, D. S., Mercier, H. P. A., and Schrobilgen, G. J. (2013). $[H(OXeF_2)_n][AsF_6]$ and $[FXe^{II}(OXe^{IV}F_2)_n][AsF_6]$ (n = 1, 2): examples of Xenon(IV) Hydroxide fluoride and oxide fluoride cations and the crystal structures of $[F_3Xe{-}FH][Sb_2F_{11}]$ and $[H_5F_4][SbF_6]{\cdot}2[F_3Xe{-}FH][Sb_2F_{11}]$. *J. Am. Chem. Soc*. 135, 5089–5104. doi: 10.1021/ja312493j

Burns, J. H., Ellison, R. D., and Levy, H. A. (1965). The crystal structure of the molecular addition compound xenon difluoride–xenon tetrafluoride. *Acta Crystallogr*. 18, 11–16. doi: 10.1107/S0365110X65000038

Busschaert, N., Caltagirone, C., Rossom, W., van Gale, P. A. (2015). Applications of supramolecular anion recognition. *Chem. Rev*. 115, 8038–8155. doi: 10.1021/acs.chemrev.5b00099

Cavallo, G., Metrangolo, P., Milani, R., Pilati, T., Priimagi, A., Resnati, G., et al. (2016). The halogen bond. *Chem. Rev*. 116, 2478–2601. doi: 10.1021/acs.chemrev.5b00484

Chernick, C. L., Claassen, H. H., Fields, P. R., Hyman, H. H., Malm, J. G., Manning, W. M., et al. (1962). Fluorine compounds of xenon and radon. *Science* 138, 136–138. doi: 10.1126/science.138.3537.136

Christe, K. O., Curtis, E. C., Dixon, D. A., Mercier, H. P. A., Sanders, J. C. P., and Schrobilgen, G. J. (1991). Crystal structures of [xenon fluoride(+)][ruthenium hexafluoride(–)] and [xenon pentafluoride(+)][ruthenium hexafluoride(–)]. *J. Am. Chem. Soc*. 113, 3351–3361. doi: 10.1021/ja00009a021

Cohen, B., and Peacock, R. D. (1966). Properties of xenon fluoride adducts. *J. Inorg. Nucl. Chem*. 28, 3056–3057. doi: 10.1016/0022-1902(66)80037-4

Cooke, S. A., and Gerry, M. C. L. (2004). XeAuF. *J. Am. Chem. Soc*. 126, 17000–17008. doi: 10.1021/ja044955j

Desiraju, G. R. (2013). Crystal engineering: from molecule to crystal. *J. Am. Chem. Soc*. 135, 9952–9967. doi: 10.1021/ja403264c

Desiraju, G. R., and Steiner, T. (2001). *The Weak Hydrogen Bond in Structural Chemistry and Biology*. Oxford: Oxford University Press.

Dixon, D. A., de Jong, W. A., Peterson, K. A., Christe, K. O., and Schrobilgen, G. J. (2005). Heats of formation of xenon fluorides and the fluxionality of XeF_6 from high level electronic structure calculations. *J. Am. Chem. Soc*. 127, 8627–8634. doi: 10.1021/ja0423116

Edwards, A. J., Holloway, J. H., and Peacock, R. D. (1963). New fluorine compounds of xenon. *Proc. Chem. Soc*. 275–276. doi: 10.1039/ps9630000253

Frisch, M. J., Trucks, G. W., Schlegel, H. B., Scuseria, G. E., Robb, M. A., Cheeseman, J. R., et al. (2016). *Gaussian 16, Revision B.01*. Wallingford, CT: Gaussian Inc.

Frontera, A., Gamez, P., Mascal, M., Mooibroek, T. J., and Reedijk, J. (2011). Putting anion– π interactions into perspective. *Angew. Chem. Int. Ed*. 50, 9564–9583. doi: 10.1002/anie.201100208

Gawrilow, M., Beckers, H., Riedel, S., and Cheng, L. (2018). Matrix–isolation and quantum–chemical analysis of the C_{3v} conformer of XeF_6, $XeOF_4$, and their acetonitrile adducts. *J. Phys. Chem. A* 122, 119–129. doi: 10.1021/acs.jpca.7b09902

Gillespie, R. J., Martin, D., Schrobilgen, G. J., and Slim, D. R. (1977). The crystal structure of trifluoroxenon(IV) hexafluorobismuthate(V): the fluoride–acceptor strength of bismuth pentafluoride. *J. Chem. Soc. Dalton Trans*. 2234–2237. doi: 10.1039/dt9770002234

Gillespie, R. J., and Pez, G. P. (1969). Fluorosulfuric acid solvent system. VII. The behavior of some extremely weak bases in the superacid system fluorosulfuric acid– antimony pentafluoride–sulfur trioxide. *Inorg. Chem*. 8, 1233–1235. doi: 10.1021/ic50076a006

Grandinetti, F. (2018). *Noble Gas Chemistry: Structure, Bonding, and Gas–Phase Chemistry*. Weinheim: Wiley–VCH.

Grochala, W. (2007). Atypical compounds of gases, which have been called 'noble'. *Chem. Soc. Rev*. 36, 1632–1655. doi: 10.1039/b702109g

Hagiwara, R., Hollander, F., Maines, C., and Bartlett, N. (1991). The crystal–structure of $[Ag(XeF_2)_2]AsF_6$ formed in the oxidation of Xe by $AgFAsF_6$. *Eur. J. Solid State Chem*. 28, 855–866.

Haner, J., Matsumoto, K., Mercier, H. P. A., and Schrobilgen, G. J. (2016). Nature of the Xe^{VI}-N bonds in $F_6XeNCCH_3$ and $F_6Xe(NCCH_3)_2$ and the stereochemical activity of their xenon valence electron lone pairs. *Chem. Eur. J*. 22, 4833–4842. doi: 10.1002/chem.201504904

Haner, J., and Schrobilgen, G. J. (2015). The chemistry of xenon(IV). *Chem. Rev*. 115, 1255–1295. doi: 10.1021/cr500427p

Holloway, J. H. (1968). *Noble–Gas Chemistry*. London: Methuen.

Hoyer, S., Emmler, T., and Seppelt, K. (2006). The structure of xenon hexafluoride in the solid state. *J. Fluorine Chem*. 127, 1415–1422. doi: 10.1016/j.jfluchem.2006.04.014

Hughes, M. J., Brock, D. S., Mercier, H. P. A., and Schrobilgen, G. J. (2011). A Raman spectroscopic study of the $XeOF_4/XeF_2$ system and the X–ray crystal structure of $\alpha-$ $XeOF_4{\cdot}XeF_2$. *J. Fluorine Chem*. 132:660. doi: 10.1016/j.jfluchem.2011.05.010

Ibers, J. A., and Hamilton, W. C. (1963). Xenon tetrafluoride: crystal structure. *Science* 139, 106–107. doi: 10.1126/science.139.3550.106

Jones, G. R., Burbank, R. D., and Bartlett, N. (1970). The crystal structure of the 1:1 molecular addition compound xenon difluoride–iodine pentafluoride, $XeF_2{\cdot}IF_5$. *Inorg. Chem*. 9, 2264. doi: 10.1021/ic50092a011

Kaupp, M., van Wüllen, Ch., Franke, R., Schmitz, F., and Kutzelnigg, W. (1996). The structure of XeF_6 and of compounds isoelectronic with it. A challenge to computational chemistry and to the qualitative theory of the chemical bond. *J. Am. Chem. Soc*. 118, 11939–11950. doi: 10.1021/ja9621556

Keith, T. A. (2013). *AIMAll (Version 13.05.06), TK Gristmill Software*. Kansas City, KS.

Koppe, K., Haner, J., Mercier, H. P. A., Frohn, H.–J., and Schrobilgen, G. J. (2014). Xenon(IV)–carbon bond of $[C_6F_5XeF_2]^{+}$; structural characterization and bonding of $[C_6F_5XeF_2][BF_4]$, $[C_6F_5XeF_2][BF_4]{\cdot}2HF$, and $[C_6F_5XeF_2][BF_4]{\cdot}n$NCCH 3 ($n = 1, 2$); and the fluorinating properties of $[C_6F_5XeF_2][BF_4]$. *Inorg. Chem*. 53, 11640–11661. doi: 10.1021/ic501831j

Legon, A. C. (2017). Tetrel, pnictogen and chalcogen bonds identified in the gas phase before they had names: a systematic look at non–covalent interactions. *Phys. Chem. Chem. Phys*. 19, 14884–14896. doi: 10.1039/C7CP02518A

Lutar, K., Borrmann, H., and Žemva, B. (1998). $XeF_2{\cdot}2CrF_4$and $XeF_5^{+}CrF_5^{-}$: syntheses, crystal structures, and some properties. *Inorg. Chem*. 37, 3002–3006. doi: 10.1021/ic971580c

Lutar, K., Leban, I., Ogrin, T., and Zemva, B. (1992). $XeF_2^{*}CrF_4$ and $[XeF_5(+)CrF_5(-)]_4^{*}XeF_4$: syntheses, crystal structures and some properties. *Eur. J. Solid State Inorg. Chem*. 29, 713–727. doi: 10.1002/chin.199836008

Matsumoto, K., Haner, J., Mercier, H. P. A., and Schrobilgen, G. J. (2015). Syntheses and structures of $F_6XeNCCH_3$ and $F_6Xe(NCCH_3)_2$. *Angew. Chem., Int. Ed*. 54, 14169–14173. doi: 10.1002/anie.201507635

McKee, D. E., Zalkin, A., and Bartlett, N. (1973). Crystal structure of $[XeF_3^+][Sb_2F_{11}^-]$. *Inorg. Chem*. 12, 1713–1717. doi: 10.1021/ic50126a001

Meyer, E. A., Castellano, R. K., and Diederich, F. (2003). Interactions with aromatic rings in chemical and biological recognition. *Angew. Chem. Int. Ed*. 42, 1210–1250. doi: 10.1002/anie.200390319

Munárriz, J., Calatayud, M., and Contreras-García, J. (2019). Valence-shell electron-pair repulsion theory revisited: an explanation for core polarization. *Chem. Eur. J*. 25, 10938–10945. doi: 10.1002/chem.201902244

Reed, A. E., Curtiss, L. A., and Weinhold, F. (1988). Intermolecular interactions from a natural bond orbital, donor–acceptor viewpoint. *Chem. Rev*. 88, 899–926. doi: 10.1021/cr00088a005

Scheiner, S. (2013). The pnicogen bond: its relation to hydrogen, halogen, and other noncovalent bonds. *Acc. Chem. Res*. 46, 280–288. doi: 10.1021/ar3001316

Schneider, H.–J., and Yatsimirski, A. (2000). *Principles and Methods in Supramolecular Chemistry*. Chichester: Wiley.

Schneider, H. J. (2009). Binding mechanisms in supramolecular complexes. *Angew. Chem. Int. Ed*. 48, 3924–3977. doi: 10.1002/anie.200802947

Scilabra, P., Terraneo, G., and Resnati, G. (2019). The chalcogen bond in crystalline solids: a world parallel to halogen bond. *Acc. Chem. Res*. 52, 1313–1324. doi: 10.1021/acs.accounts.9b00037

Seidel, S., and Seppelt, K. (2000). Xenon as a complex ligand: the tetra xenono Gold(II) cation in $AuXe_4^{2+}(Sb_2F_{11}^-)_2$. *Science* 290, 117–118. doi: 10.1126/science.290.5489.117

Seppelt, K. (2015). Molecular hexafluorides. *Chem. Rev*. 115, 1296–1306. doi: 10.1021/cr5001783

Sladky, F. O., Bulliner, P. A., and Bartlett, N. (1969). Xenon difluoride as a fluoride ion donor. evidence for the salts $[Xe_2F_3]^+[MF_6]^-$,$[XeF]^+[MF_6]^-$ and $[XeF]^+[M_2F_{11}]^-$. *J. Chem. Soc. A* 2179–2188. doi: 10.1039/J19690002179

Tavčar, G., and Tramšek, M. (2015). XeF_2 as a ligand to a metal center, an interesting field of noble gas chemistry. *J. Fluorine Chem*. 174, 14–21. doi: 10.1016/j.jfluchem.2014.08.009

Tavčar, G., Tramšek, M., Bunič, T., Benkič, P., and Žemva, B. (2004). New class of coordination compounds with noble gas fluorides as ligands to metal ions. *J. Fluorine Chem*. 125, 1579–1584. doi: 10.1016/j.jfluchem.2004.08.006

Tavčar, G., and Žemva, B. (2009). XeF_4 as a ligand for a metal ion. *Angew. Chem. Int. Ed*. 48, 1432–1434. doi: 10.1002/anie.200803365

Templeton, D. H., Zalkin, A., Forrester, J. D., and Williamson, S. M. (1963). Crystal and molecular structure of xenon tetrafluoride. *J. Am. Chem. Soc*. 85, 242–242. doi: 10.1021/ja00885a038

Tramšek, M., Benkič, P., and Žemva, B. (2002). $[M(XeF_2)_3](AsF_6)_2$ (M=Pb, Sr): the first coordination compounds of M^{2+} with XeF_2 ligand. *Solid State Sci*. 4, 9–14. doi: 10.1016/S1293–2558(01)01206–7

Tramšek, M., and Žemva, B. (2006). Synthesis of novel salts with HF, AsF_3 and XeF_2 as ligands to metal cations. *J. Fluorine Chem*. 127, 1275–1284. doi: 10.1016/j.jfluchem.2006.05.014

Weigend, F. (2006). Accurate coulomb–fitting basis sets for H to Rn. *Phys. Chem. Chem. Phys*. 8, 1057–1065. doi: 10.1039/b515623h

Weigend, F., and Ahlrichs, R. (2005). Balanced basis set of split valence, triple zeta valence and quadrupole zeta valence quality for H to Rn: design and assessment of accuracy. *Phys. Chem. Chem. Phys*. 7, 3297–3305. doi: 10.1039/b508541a

Zhao, L., Pan, S., Holzmann, N., Schwerdtfeger, P., and Frenking, G. (2019). Chemical bonding and bonding models of main–group compounds. *Chem. Rev*. 119, 8781–8845. doi: 10.1021/acs.chemrev.8b00722

Zhao, Y., Benz, S., Sakai, N., and Matile, S. (2015). Selective acceleration of disfavored enolate addition reactions by anion–π interactions. *Chem. Sci*. 6, 6219–6223. doi: 10.1039/C5SC02563J

Conflict of Interest: The authors declare that the research was conducted in the absence of any commercial or financial relationships that could be construed as a potential conflict of interest.

frontiers in Physics

REVIEW
published: 08 May 2020
doi: 10.3389/fphy.2020.00157

Noble Gas Reactivity in Planetary Interiors

*Chrystele Sanloup**

Institut de Minéralogie, Physique des Matériaux et Cosmochimie, Sorbonne Université, CNRS, Paris, France

While the field of noble gas reactivity essentially belongs to chemistry, Earth and planetary sciences have brought a different perspective to the field. Indeed, planetary interiors are natural high pressure (*P*) and high temperature (*T*) laboratories, where conditions exist where bonding of the heaviest noble gases may be induced thermodynamically through volume reduction (Le Châtelier's principle). Earth and planetary sciences besides generate numerous and precise observations such as the depletion of the terrestrial and martian atmospheres in xenon, pointing to the potential for Xe to be sequestered at depth, potentially induced by its reactivity. More generally, this paper will review the advances on noble gas reactivity at the extreme *P-T* conditions found within planetary interiors from experiments and theoretical investigations. This review will cover the synthesis of cage compounds, stoichiometric oxides and metals, and non-stoichiometric compounds where noble gases are only minor or trace elements but could be essential in solving some Earth and planetary puzzles. An apparent trend in noble gas reactivity with *P* emerges. In the case of Xe which is the most documented, metals are synthesized above 150 GPa, i.e., at terrestrial core conditions, stoichiometric Xe-oxides between 50 and 100 GPa, i.e., in the *P-T* range of the Earth's lower mantle, but Xe-O high energy bonds may also form under the modest pressures of the Earth's crust (<1 GPa) in non-stoichiometric compounds. Most planetary relevant noble gas compounds found are with xenon, with only a few predicted helium compounds, the latter having no or very little charge transfer between helium and neighboring atoms.

Keywords: xenon, krypton, argon, neon, helium, planetary interiors, high pressure

OPEN ACCESS

Edited by:
Gabriel Merino, Centro de Investigacion y de Estudios Avanzados - Unidad Mérida, Mexico

Reviewed by:
Michael Ward Broadley, UMR7358 Centre de Recherches Pétrographiques et Géochimiques (CRPG), France
Guochun Yang, Northeast Normal University, China

***Correspondence:**
Chrystele Sanloup
chrystele.sanloup@sorbonne-universite.fr

Specialty section:
This article was submitted to Physical Chemistry and Chemical Physics, a section of the journal Frontiers in Physics

Received: *10 March 2020*
Accepted: *15 April 2020*
Published: *08 May 2020*

Citation:
Sanloup C (2020) Noble Gas Reactivity in Planetary Interiors. Front. Phys. 8:157. doi: 10.3389/fphy.2020.00157

1. INTRODUCTION

The inertness of noble gases is the cornerstone of noble gas geochemistry. Helium (He), neon (Ne), argon (Ar), krypton (Kr), and xenon (Xe) are all important markers of a variety of planetary processes, ranging from Earth's accretion, degassing of the atmosphere, vigor of mantle convection, to tracking underground nuclear tests. Noble gas abundances and isotopic ratios have thus been measured in a large variety of samples (atmosphere, fluids, rocks) and from different geological contexts, from Archean rocks over 2.5 Gy old [1, 2] to Martian meteorites [3] and comets [4]. Besides the Earth and Mars, the only other planetary atmosphere probed so far is that of Jupiter [5]. Future missions are targeted at measuring noble gases in other atmospheres with pre-selected NASA DAVINCI+ mission to Venus and SPRITE mission to Saturn, noble gases being presented as critical to understanding the formation and evolution of giant planets.

From these measurements, planetary accretion reservoirs and processes may be traced. Only Ne has preserved a solar signature in some terrestrial samples, a signature interpreted as a proof for the existence of a deep magma ocean (i.e., partially or fully molten Earth in equilibrium with a primary solar-like atmosphere) within the first hundred My of the Earth's formation [6, 7]. Heavier Kr and Xe noble gases overall have a chondritic signature in terrestrial and martian samples, with a minor cometary contribution [4, 8]. Jupiter is the only other planet who's atmosphere has been studied in detail. It is slightly depleted in He, strongly in Ne [5], and enriched by a factor of 2.5–2.7 in heavy noble gases (Ar, Kr, Xe) compared to solar abundances [9], as expected from trapping in amorphous ice and pointing to a major cometary contribution to Jupiter.

Noble gases are also widely used to trace planetary processes. For instance, the iodine-plutonium-xenon system is used to date the formation of the atmosphere [10, 11] due to the very short half-lifes of ^{129}I (17 My) and ^{244}Pu (82 My). Helium and Ar isotopes constrain mantle degassing and convection over much longer time scales [12–14] owing to the longer half-life of their parent isotopes (for instance 1.25 Ga for ^{40}K). None of Kr stable isotopes is purely radiogenic, preventing its use to constrain chronology of the atmosphere evolution. It was pointed out as early as 1970 that Xe is under abundant in the atmospheres of the Earth and Mars relative to the chondritic abundance pattern [15], a depletion of up to 90% [10] and known as the "missing Xe" problem. Atmospheric Xe is furthermore strongly depleted in light isotopes [16], and this depletion in light Xe isotopes was progressive throughout the Archean [17]. The case is more debated for Ar, but the classical double-layered convection model [12] precisely required two separated layers in the mantle on the basis that an unsampled reservoir, such as the lower mantle, must be enriched in Ar to satisfy radiogenic ^{40}Ar mass balance. Seismic tomography later showed that there is a mass flow from the upper to the lower mantle, but the need for an Ar-rich reservoir remains.

The most striking fact emerging from the current data set of noble gas analyses in natural samples remains the "missing Xe." This paradox has launched a search for either ways to lose Xe to space [17–20] or to trap Xe at depth. The interiors of the Earth are indeed characterized by extreme *P*-*T* conditions, with a six-order magnitude increase in *P* and 3-order magnitude increase in *T* between the surface (10^5 Pa–287 K) and the core of the planet (365 GPa–5,000 K). Such conditions may induce chemical reactivity as negative reaction volume change under increased *P* may overcome enthalpic effects of otherwise prohibited reactions at ambient *P*. Natural samples do indicate higher Xe retention in particular contexts. Xe concentrations in near surface rocks are ∼0.05 ppt (part per trillion) in basalts [21] and up to 0.2 ppb (part per billion) in deep sea siliceous fossils [22]. The latter samples have ^{132}Xe/^{36}Ar ratios of up to 0.05, i.e., about thirty times higher than in mid-ocean ridge basalts [23, 24]. Xe enrichment over other noble gases is also reported in high *P* contexts such as mantle xenoliths exhumed by volcanism [25–28] and impact craters [29] by two orders of magnitude with the highest excess (^{132}Xe/^{36}Ar = 0.170) being reported in excavated lunar crustal rocks [30].

The initiation of high *P* solid-state chemistry of Xe was triggered by the discovery of its metallization at 135 GPa [31], yet the potential link to the missing Xe paradox took a decade to be established. Since then, there has been a continuous feedback between high *P* mineral physics and condensed matter physics in the search for new noble gas compounds. Foreseen as promising by Grochala [32] but then still experimentally unexplored, the high *P* chemistry of noble gases now extends to several atoms, an effort largely led by the perspective to understand noble gas reactivity at deep Earth's conditions. Interestingly, noble gases are archetypical pressure-transmitting media used in laser heated diamond-anvil cell experiments to reproduce hydrostatic deep Earth's conditions in an otherwise rather uniaxial compression apparatus, and thermally insulate the sample from the diamond anvils. This technical aspect has doubtless been a positive factor in elucidating some of the high *P* noble gas reactivity reviewed here, and that covers first retention of noble gases in rings, channels and cage structures, second noble gas oxides, third noble gas compounds with metals, and finally other types of high *P* noble gas compounds relevant of planetary interiors.

2. RETENTION OF NOBLE GASES IN RING, CHANNEL, AND CAGE STRUCTURES

2.1. Clathrates and Other Cage Compounds

Water ice is one of the most prevalent substances in the Solar System, with the majority of it existing at high *P* and *T* conditions in the interiors of giant planets. While clathrates hydrates have long been considered as carriers of nobles gases to the giant planets, a consensus emerges now for simple adsorption on amorphous ice [9]. On Earth, clathrate hydrates are found in pergelisols and oceanic margins. Noble gases are among the gases that stabilize clathrate hydrate structures through van der Waals interactions. $Ar_6{\cdot}H_2O$ was actually the first compound of a noble gas discovered in Villard [33]. All noble gases form clathrates by combination with water, with *P*-*T* stability field extending from He to Xe [34]. However, even Xe hydrates are stable only up to 2.5 GPa [35].

Cyclo-silicates can host large amount of noble gases in the channels and ring sites of their crystal structures. These minerals are not occurrences of noble gas reactivity at depth, but are essential carriers of noble gas recycling via subduction of lithospheric plates [36, 37], from the surface reservoirs (atmosphere, oceans) to the deep Earth where reactions may take place. Natural occurrences of He and Ar in cyclo-silicates are abnormally high [38]. He, Ne and Ar occupy ring sites in amphibole [37], a mineral formed in the altered oceanic crust, and experimentally measured solubilities are up to four orders of magnitude higher than for other silicates at similar run *P* (0.17 GPa). Ring sites are formed by a pair of opposing six-membered $(Si,Al)O_4^{4-}$ tetrahedra rings, with a ring inner diameter circa 5 Å. Noble gases sitting in these sites are thus surrounded by 12 neighboring oxygens at approximately 2.5 Å. Kr and Xe solubilities have not been investigated in amphibole, but are even higher than Ar solubility in serpentine (×2 for Kr, ×10

for Xe), another important mineral from the altered oceanic crust [39].

The very first attempts at testing Xe reactivity with silica [40] were guided by the fact that SiO_2 high T phase cristobalite has large cages that could trap Xe atoms and favor chemical reactivity. However, when SiO_2 was loaded as cristobalite, it systematically transformed to quartz, with the latter efficiently trapping Xe (cf. section 3). Xenon, far form stabilizing cristobalite, in fact destabilizes it. Instead, He proved much more interesting in this respect as cristobalite loaded in He as a diamond-anvil cell P-transmitting medium was shown to convert to He-cristobalite at 8 GPa instead of transforming to cristobalite-II at 1.6 GPa [41], its structure and stoichiometry (SiO_2He) were solved (**Figure 2**).

2.2. Stuffed Amorphous Silicates

Noble gas solubility in molten silicates depend on their composition. In fact, noble gas solubility in vitreous silica has been used to characterize glass network geometry [44]. Noble gas retention in silicate melts has long been postulated as occurring by insertion in the interstitial voids [45], with the abundance depending on the melt's polymerization, itself constrained by the SiO_2 content as SiO_4^{4-} tetrahedra polymerize as rings (see below). Silicate melts may accommodate larger amounts of dissolved noble gases under increased P until solubility reaches a plateau circa 5 GPa with for instance a maximum of 3 mol% Ar in silica-rich melts [46, 47]. Note that solubility drops at higher P were reported [48, 49] but these results were not reproduced [50], possibly due to incomplete melting of the samples at higher P in the first studies.

Noble gases affect the behavior of non-crystalline silicates under pressure. Up to 1–2 mol% He may dissolve into the interstitial voids in SiO_2 glass under pressure [51, 52], resulting in a much less compressible glass [52], with a spatial scale of the medium-range order almost independent on P compared to SiO_2 glass compressed in solid P-medium or compressed in H_2. Similarly to He in compressed SiO_2 glass, Xe was also found to affect the medium-range order with a sharpening of the first sharp diffraction peak on x-ray diffraction data, indicative of a stronger medium-range order [53]. More importantly, Xe-O bonds with a bond length of 2.05–2.10 Å and a coordination number of 12 were reported, indicative of the Xe insertion in six-membered rings (i.e., rings formed of six SiO_4^{4-} tetrahedra) rather than in interstitial voids. This ring structure of molten and glassy silicates is similar to that of cyclo-silicates, except that there is a statistical distribution of ring sizes, mostly from 4 to 10 tetrahedra depending on melt composition [54]. This distribution has been recently quantified in vitreous silica by neutron diffraction [55], the six-membered ring being the most prominent and having an inner diameter of 4.30 Å, consistent with the Xe-O bond length reported above. Krypton local environment in compressed melts, as investigated using x-ray absorption spectroscopy [56], is a shell of oxygen atoms located at 2.49 Å. This relatively short distance indicates some degree of covalency albeit less than for Xe-O bonds. It is however difficult to reach further conclusions, as the coordination number could not be calculated due to the lack of Kr oxide references that are necessary to process x-ray absorption spectroscopy data.

3. NOBLE GAS OXIDES

The mineralogical constituents of the crust and mantle of terrestrial planets are silicates, with a predominance of framework silicates in the continental crust such as quartz and feldspars, and a predominance of olivine in the mantle that undergo phase transitions at depth, and decomposes into bridgmanite and magnesiowustite below 660 km. First steps toward establishing noble gas reactivity in planetary crust and mantle have been the synthesis of noble gas oxides, keeping in mind that it can only be firmly established between silicates and noble gases as trace elements for realistic implications to planetary interiors.

3.1. Stoichiometric Oxides

Xenon oxides have been known since the sixties with the synthesis of tetrahedral forms (XeO_3 by Templeton et al. [57], XeO_4 by Huston et al. [58]) by hydrolysis of xenon fluorides at cryogenic T, and more recently with the synthesis of XeO_2 that has a different geometry with local square planar oxygen environment [59]. Although the local structure of XeO_2 is square planar, Xe being bonded to four oxygens, its full crystallographic structure has not yet been resolved.

The first Xe oxide experimentally synthesized by use of high P was $Xe_2O_6H_6$ (**Figure 1**), obtained by reaction between superionic ice and Xe above 50 GPa and 1,500 K upon laser heating in diamond-anvil cells [60], with platinum used as a laser coupler. Superionic ice is a high P-T phase forming at 50 GPa and characterized by a full mobility of the hydrogen atoms [62], while the oxygen lattice is identical to that of lower T phase X. $Xe_2O_6H_6$ is metallic due to the Xe and O atoms, however the diffusivity of hydrogen atoms is similar to that of superionic ice. Pure Xe oxides were predicted to be stable against decomposition above 83 GPa by *ab initio* calculations: XeO, XeO_2, and XeO_3 [63], followed by Xe_2O_3 and more Xe-rich phases at even higher P [64]. Only Xe_2O_3 was observed experimentally albeit at slightly higher P (87 GPa instead of the predicted 75 GPa), along with Xe_2O_5 at 83 GPa [61]. Interesting fact: Xe may exist at different oxidation states in the same structure. That Xe oxidation is induced at significantly lower P with superionic ice compared to pure oxygen could be due to the reactivity of the very diffusive hydrogen with platinum, the formation of platinum hydride contributing to a larger volume reduction of the global reaction. In addition, the oxygen and xenon sublattices in $Xe_2O_6H_6$ bears remarkable resemblance to those of η-O_2 [65] and pure Xe, both having hexagonal closed-packed structures and the η-O_2 being characterized by a high degree of charge transfer.

For krypton, only KrO has been predicted to be stable against decomposition above 300 GPa [66], and no Kr-compound has been synthesized experimentally. No argon oxide nor neon oxide have yet been documented to form at the conditions of planetary interiors, despite the visionary editorial by Abelson [67] citing ArH_4 and ArO_6 as examples of P-induced chemistry. But surprisingly, one helium oxide has been reported. On the basis of *ab initio* calculations, FeO_2He, is predicted to be stable at core-mantle boundary conditions [68]. Unlike Xe-oxides and KrO discussed above, there is almost no charge transfer

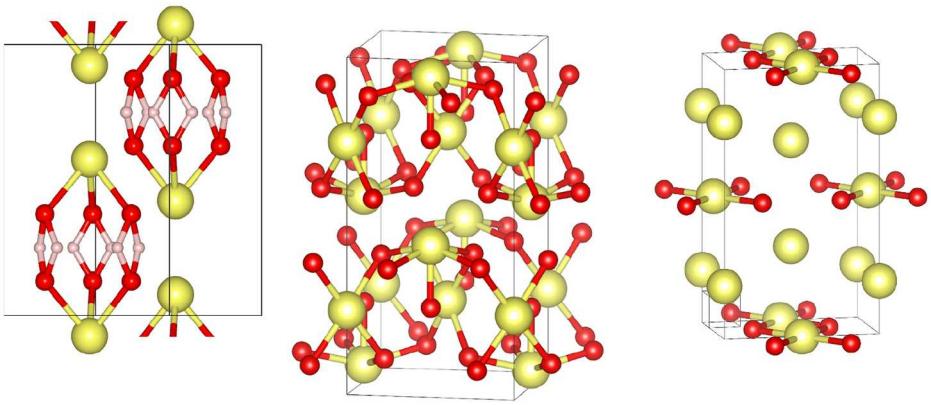

FIGURE 1 | Experimentally observed and theoretically predicted xenon oxides. From left to right: $Xe_2O_6H_6$ [60], Xe_2O_5, Xe_2O_3 [61]. Color code for atoms: xenon (yellow), oxygen (red), hydrogen atoms (light pink).

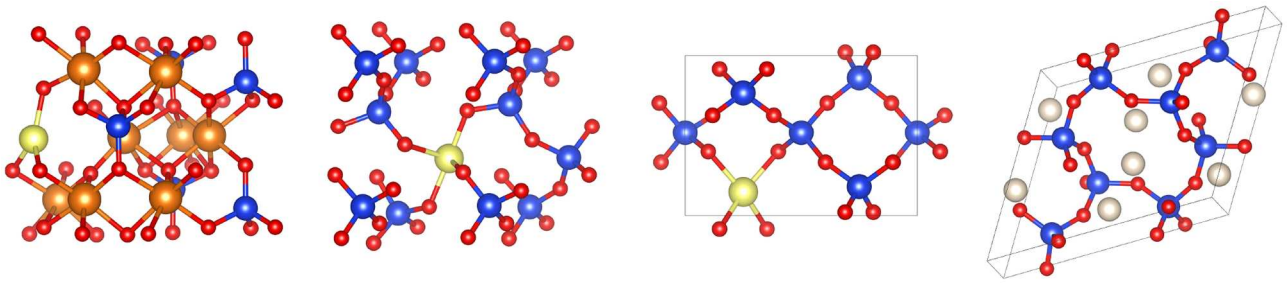

FIGURE 2 | Experimentally synthesized noble gas-silicates. From left to right: Xe-doped olivine Mg_2SiO_4 [42], Xe-doped β-quartz [43], $(Xe,Si)O_2$ phase for which Xe site occupancy is unknown [43], cristobalite-He [41]. Color code for atoms: magnesium (orange), xenon (yellow), oxygen (red), silicon (dark blue), helium (white).

from He to surrounding atoms. Excess primordial He (i.e., ^{3}He, while ^{4}He has been produced throughout Earth's history by radioactive decay) are found in some basalts which rock source is identified as originating from very deep in the mantle [69]. Thermochemical piles are domes of both thermal and chemical origin in the deep mantle, rooted above the core-mantle boundary below central Pacific and south Atlantic-Africa [70], with locally partially molten zones (ultra-low velocity zones) at their very base. These piles might have been preserved during a large part if not all of Earth's history and could indeed by He-rich, providing a reasonable context for the formation of FeO_2He. Besides, hydrogen bearing iron peroxide FeO_2H [71] is also stable at the corresponding *P-T* conditions, or as partially dehydrogenated $FeOOH_x$ postulated as an important component of the ultra-low velocity zones [72]. Both FeO_2He and FeO_2H have a cubic structure with identical cell parameter of, respectively 4.32 Å at 135 GPa [68] and 4.33 Å at 133.5 GPa [73], but with different symmetries, Fm-3m vs. Pa-3.

3.2. Xenon as a Minor/Trace Element in Oxides

That Xe reacts with oxides at the conditions of the deep crust and mantle is a strong indication that it can be stored at depth. However, Xe is a trace element in planetary interiors (cf. section 1), therefore the relevant reactions are not those producing stoichiometric compounds but those where Xe retention occurs as a trace or minor element. This aspect considerably changes the energetics of the reaction, and consequently the *P-T* conditions at which they may occur. Xe trapping in the deep crust and mantle could solve the Xe paradox, and this occurs by Xe substitution to Si (cf. **Figure 2**) whereby Xe gets oxidized such as in hot compressed SiO_2 quartz [74] or $(Mg,Fe)_2SiO_4$ olivine [75]. Xe-O bonds are best evidenced by new Raman and infra-red vibrational modes (cf. **Figure 3**) that appear under *P* upon heating above the melting curve of Xe, the reaction being thermodynamically favored by the volume reduction between reactants (i.e., liquid Xe and quartz or olivine) and products (i.e., Xe-doped quartz or Xe-doped olivine). Theoretical calculations have confirmed this mechanism for quartz [43, 76, 77] and olivine [42], and helped refine the crystal-chemistry of Xe in these minerals. Volume and cell-parameters vs. *P* relationships as well as Raman signature of Xe-doped silicates could be theoretically reproduced by substituting Xe to Si albeit in different geometries depending on the mineral: quasi-planar three-fold in olivine vs. linear two-fold (2 nearest O atoms at 1.99 Å) with 2 next nearest O neighbors in orthogonal plan at 2.27 Å in quartz [43]. Theoretically-derived solubility is up to 0.4 at% Xe in both phases [42, 43].

Xe-doped quartz transforms into a new $(Xe,Si)O_2$ phase upon increased heating above 1,700 K at 1 GPa [43]. $(Xe,Si)O_2$ structure bears similarities to the predicted XeO_2 structure [64]

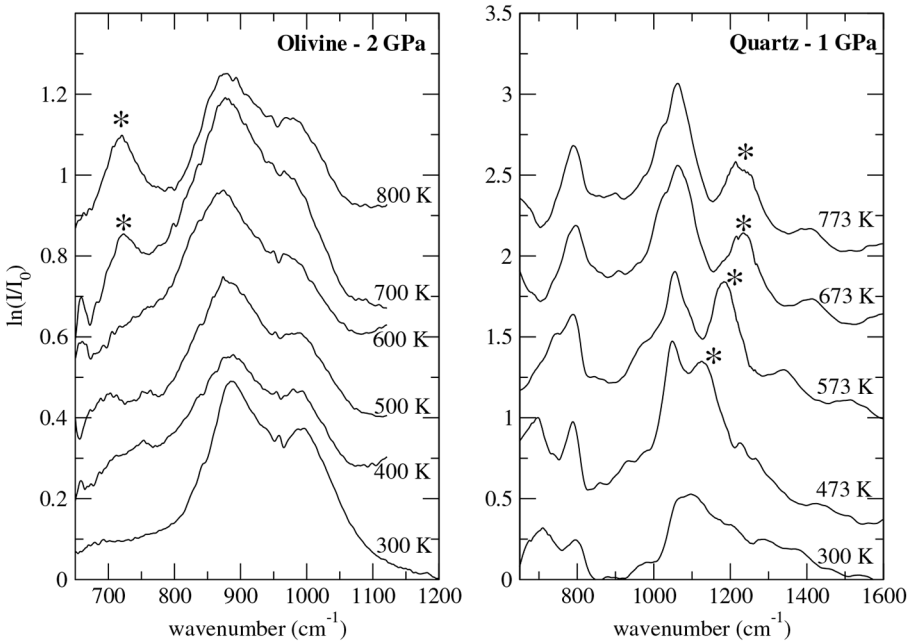

FIGURE 3 | Infrared spectra on Xe-doped silicates under high *P-T* conditions generated using resistive-heating diamond-anvil cells. Left: olivine, right: quartz [43]. The asterisk sign designs new vibrational mode observed only upon heating and assigned to Xe-O bond.

that is not stable at any of the *P* investigated but admittedly the best candidate for the ambient *P* XeO_2 phase [59] as characterized by Raman spectroscopy. Both phases are orthorhombic with cell parameters within 10% difference, and have a square planar Xe local environment.

Xe reactivity with lower mantle minerals such as bridgmanite and ferropericlase has not been tested yet. At lower mantle conditions, silicon bonds to six nearest oxygen atoms in a octahedral geometry. It is therefore a promising area of research as Xe substitution to six-fold Si could lead to structures similar to ambient *P* Xe perovskites whereby Xe bonds to oxygens in octahedral sites [78].

4. OTHER HIGH *P* NOBLE GAS COMPOUNDS RELEVANT OF PLANETARY INTERIORS

4.1. Noble Gas Compounds Relevant to Planetary Fe Cores

The search for Xe reactivity with metals was initiated by the report of Xe metallization at 135 GPa [31], later refined to 155 GPa by means of electrical resistivity measurements [79]. Iron-xenon reactivity received most attention since the first paper by Caldwell et al. [80], showing no tendency from Xe to form a metal with Fe up to 150 GPa. Xe-metals reactivity was later shown to occur at higher *P* with Fe and Ni, first by alloying with Fe with up to 0.8 mol% Xe at the conditions of the terrestrial inner core [81]. Later, Xe-metal compounds were predicted from theoretical predictions [82] and observed in experiments with $XeFe_3$ stable above 200 GPa and 2,000 K [83], conditions that are significantly reduced for $XeNi_3$ to 150 GPa and 1,500 K [83, 84]. In these compounds, Fe and Ni act as oxidants, gaining electrons, and forming anions. This is yet another illustration of pressure-induced noble gas chemistry. Implications for Xe sequestration at depth within planetary cores are less convincing however, as Xe is missing from both martian and terrestrial atmospheres while the martian core extends to <40 GPa [85], i.e., far below the *P*-threshold required to induce Xe-Fe chemistry.

The latest development in this direction is the ArNi compound synthesized above 140 GPa upon laser heating (T>1,500 K) [86]. If such reaction extends to Fe, the Earth's core could be a deep Ar reservoir. ArNi is an intermetallic Laves phase, so there is no bonding but significant electron transfer between Ar and Ni atoms.

4.2. Noble Gas Compounds Relevant to Giant Planets Interiors

The range of applications in this subsection covers giant planets, which main constituents are H and He for Jupiter and Saturn, and planetary ices for Uranus and Neptune [87]. *P-T* conditions reach up to 4,000 GPa–20,000 K inside Jupiter [87], and 510 GPa–5,800 K inside smaller Uranus [88].

Helium is depleted from the atmosphere of Jupiter, and more importantly from that of Saturn, a depletion due to heavier He sedimenting inside the planets at *P-T* conditions where H_2 and He are immiscible. Helium sedimentation may have sequestered Ne, which dissolves preferentially in He rather than in H_2 [89]. Going beyond simple noble gas solubility in giant planets materials, other processes might sequester noble gases

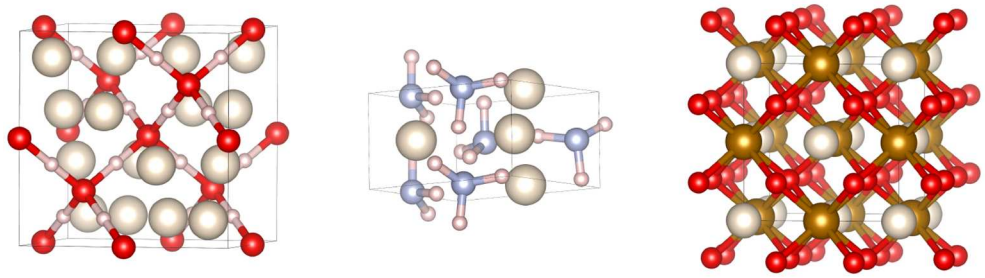

FIGURE 4 | Noble gas compounds potentially relevant for giant planets interiors. From left to right: He_2H_2O [94], NH_3He [95], and FeOOHe [68]. Color code for atoms: helium (white), oxygen (red), nitrogen (light blue), iron (gold), hydrogen (light pink).

at depth. Van der Waals noble gas compounds with hydrogen have been synthesized: $Ar(H_2)_2$ [90] at 4.3 GPa and stable to at least 358 GPa [91], $Kr(H_2)_4$ at 5.3 GPa and stable to at least 50 GPa [92], and $Xe(H_2)_8$ at 4.8 GPa and stable to at least 255 GPa [93]. Raman and/or infra-red spectroscopies have shown that hydrogen is molecular (H_2) in these compounds, freely rotating, with no indication of H-noble gas bonding.

Potential planetary He-compounds were predicted (**Figure 4**): NH_3He above 45 GPa [95], HeH_2O, and He_2H_2O [94] stable against decomposition at 2–8 and 8–92 GPa, respectively, and $(H_2O)_2He$ above 296 GPa [96]. In none of these compounds does He form bond with other atoms. The propension of He to from compounds under high *P* without forming chemical bonds is explained by its insertion with ionic compounds and consequent stabilization of Coulomb interactions [94], besides the volume reduction associated with the reaction. Interestingly, like $Xe_2O_6H_6$, He_2H_2O is superionic at high *T* above 40 GPa [94], with free mobility of He and protons. However, this occurs at 40 GPa only, 10 GPa lower than for pure ice. The presence of He therefore lowers the *P* at which superionicity occurs compared to pure water. This effect should be considered in modeling Uranus and Neptune interiors, superionic ices being the most likely candidates as the carriers of the internal planetary magnetic field.

5. LIMITATIONS AND FUTURE DIRECTIONS IN INVESTIGATING NOBLE GAS REACTIVITY IN PLANETARY PROCESSES

5.1. Current Limitations

Two important limitations of the study of noble gas retention mechanisms in minerals are conceptual. First, most measurements are carried out on samples synthesized at high *P-T* conditions but quenched to ambient conditions, i.e., far from thermodynamic equilibrium, potentially causing noble gases to exsolve. Second, solubility studies still assume neutral speciation and propose retention in defects with similar size as zero charge noble gas radii [97] such as oxygen vacancies [98, 99]. This is however unrealistic for noble gas solubilities above 1 at% as reported at lower mantle conditions for Ar in bridgmanite [98] and Kr in ferropericlase [99], oxygen defects concentrations being at least two orders of magnitude smaller [100, 101].

Even if these conceptual biases are lifted, technical limitations remain. For a chondritic Earth including 1.5% of volatile-rich late veneer [102], 90% of missing Xe [10] represents roughly 7.10^{13} kg of Xe. This translates into concentrations of 10 ppb if all that Xe is stored in the lower continental crust, and 0.05 ppb if stored in the upper mantle. These values are much smaller than the 0.4 at% Xe solubility in olivine and quartz [42, 43], which means that the missing Xe problem is easily solved by storage in silicates at depth. But these values are also much smaller than the detection limit of 0.1 at% for both x-ray diffraction and Raman spectroscopy [42], which is also the minimum concentration that can be handled by theoretical *ab initio* calculations. Neither experimental nor theoretical approaches can therefore be applied to natural levels of concentrations. Henry's law might nonetheless still be obeyed as *ab initio* study on Xe incorporation mechanisms in olivine [42] shows no change in the configuration of Xe with dilution ranging from 0.9 at% down to 0.1 at%; the presence of Xe is only felt locally as expected for a diluted defect and Xe atoms do not interact with each other. This argument justifies the relevance of theoretical calculations and experiments done with 0.1–1 wt% noble gas content to natural abundances.

5.2. Future Directions

Much more efforts have been devoted to understand Xe retention at depth than for lighter noble gases. However, the "missing Xe problem" requires a solution that only applies to Xe. Kr retention mechanism as a minor element has so far only been elucidated in compressed silicate melts [56], with the detection of Kr-O bonds having a lower degree of covalency than Xe-O bonds. Ar and Ne retention mechanisms will be very challenging to solve experimentally due to their lighter mass and consequent weak contribution to x-ray based signals. This could explain why these topics were so far never covered despite Ar and Ne being widely used *P*-transmitting media for x-ray diffraction measurements using laser-heated diamond anvil cells. Spectroscopic methods might be more straightforward to probe any noble gas induced vibration, although their use at combined high *P* and high *T* is still difficult.

Major x-ray synchrotron facilities are undergoing upgrades in this decade in order to build extremely brilliant sources

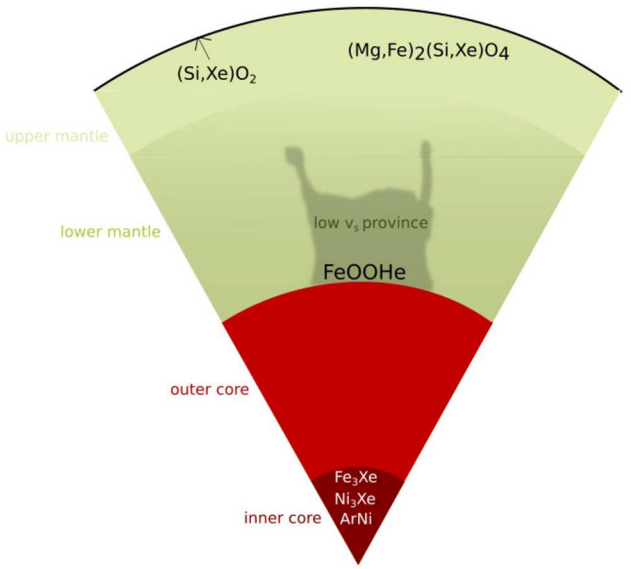

FIGURE 5 | Cartoon of Earth's interiors and potential occurrence of noble gas-compounds at depth. Note that the Earth's crust (black crust) is too thin to be represented at scale.

with improved coherence by a factor of hundred. That should prove highly beneficial to the study of noble gas reactivity with planetary materials at more realistic conditions. This will for instance open the prospect of x-ray absorption spectroscopy measurements at below 0.1 at% concentrations. Increased photon flux will furthermore considerably shorten data collection times, allowing count-limited measurements (e.g., local structure by x-ray absorption or pdf analyses) on these diluted systems for smaller samples at lower mantle conditions using laser heated diamond-anvil cell experiments.

Last but not least, it will be crucial to evaluate the consequences of noble gas chemical reactivity at depth on isotopic fractionation during planetary differentiation processes in order to properly interpret the wealth of high precision isotopic data on natural samples.

6. CONCLUSION

A variety of noble gas compounds may form inside planets, and those potentially found in the Earth are summarized in **Figure 5**. If most of them are with Xe, even the most inert element of the periodic table, He, reacts at the extreme *P-T* conditions found in planetary interiors. While He-compounds do not involve He bonding to other atoms, different types of bonding are found in Xe-compounds, from covalent with Xe as an oxidizing agent (i.e., electron donner), to metallic with Xe as a reducing agent (i.e., electron taker). The main take-away message of this review is therefore that noble gas abundances measured in planetary atmospheres and rocks are certainly a very rich source of information, but they reflect not only planetary formation processes, origins and dynamics, but also *P*-induced noble gas chemistry at depth.

As detailed in section 3, Xe trapping in the deep crust and upper mantle could solve the "missing Xe" problem in the atmospheres of the Earth and Mars, and this occurs by Xe substitution to Si whereby Xe gets oxidized such as in compressed SiO_2 quartz [74]. This report stimulated further work in noble gas chemistry including the synthesis of the Graal compound XeO_2 [59]. Earth sciences have thus brought a different perspective to the field, as Xe-O high energy bonds can be formed under the modest pressures of the Earth's crust in natural minerals. Reciprocally, the synthesis of Xe-water compounds by UV radiation [103] has motivated the investigation of Xe reactivity with water at extreme conditions [60], and the discovery of the $Xe_2O_6H_6$ oxide stable at the conditions of the interiors of Uranus and Neptune. The search for new noble-gases compounds at high *P-T* conditions has also been fueled by the search for high energy compounds in condensed matter physics. The synergy between Earth and planetary sciences, high *P* condensed matter physics, and chemistry has been fruitful and should be pursued, in the perspective to discover new synthesis pathways and new types of noble gas compounds, with the wealth of potential societal benefits that follow such as storage of energy or better anesthetics in medicine [104]. A main effort will be to find ways to preserve the newly found compounds metastably back to room conditions, as none of these high *P* compounds is yet recoverable.

Future research perspectives could be directed at pursuing the synthesis of noble gas-doped phases instead of stoichiometric compounds, which proved to considerably lower the *P*-threshold of Xe bonding to O from 83 GPa in pure Xe-O system [61] down to 1 GPa in more complex silicate systems [43, 74]. Not only is this the mandatory way to adequately reproduce the chemistry of naturally very weakly abundant noble gases in terrestrial planets, but this is also a potential solution to recover metastable phases back to room *P*. In the opposite direction, the discovery of very large exoplanets (super Earths, super Neptunes, super Jupiters) opens the perspective to expand the exploratory *P*-range for noble gas chemistry at depth, as illustrated by the FeHe compound stable above 4,000 GPa, i.e., *P* greater than at the center of Jupiter [105].

AUTHOR CONTRIBUTIONS

The author confirms being the sole contributor of this work and has approved it for publication.

ACKNOWLEDGMENTS

SOLEIL synchrotron is acknowledged for provision of synchrotron radiation facilities at SMIS beamline, as well as Céline Crépisson and Francesco Capitani for collecting the data.

REFERENCES

1. Pujol M, Marty B, Burgess R. Chondritic-like xenon trapped in Archean rocks: a possible signature of the ancient atmosphere. *Earth Planet Sci Lett*. (2011) **308**:298–306. doi: 10.1016/j.epsl.2011.05.053
2. Pujol M, Marty B, Burgess R, Turner G, Philippot P. Argon isotopic composition of Archaean atmosphere probes early Earth geodynamics. *Nature*. (2013) **498**:87–90. doi: 10.1038/nature12152
3. Gilmour JD, Whitby JA, Turner G. Xenon isotopes in irradiated ALH84001: evidence for shock-induced trapping of ancient Martian atmosphere. *Geochim Cosmochim Acta*. (1998) **62**:2555–71. doi: 10.1016/S0016-7037(98)00165-3
4. Marty B, Altwegg K, Balsiger H, Bar-Nun A, Bekaert DV, Berthelier JJ, et al. Xenon isotopes in 67P/Churyumov-Gerasimenko show that comets contributed to Earth's atmosphere. *Science*. (2017) **356**:1069–72. doi: 10.1126/science.aal3496
5. Niemann HB, Atreya SK, Carignan GR, Donahue TM, Haberman JA, Harpold DN, et al. The Galileo probe mass spectrometer: composition of jupiter's atmospheres. *Science*. (1996) **272**:846–9. doi: 10.1126/science.272.5263.846
6. Harper CL. Evidence for $^{9}2g$Nb in the early solar system and evaluation of a new *p*-process cosmochronometer from $^{9}2g$Nb/$^{9}2$Mo. *ApJ*. (1996) **466**:437–56. doi: 10.1086/177523
7. Williams CD, Mukhopadhyay S. Capture of nebular gases during Earth's accretion is preserved in deep-mantle neon. *Nature*. (2019) **565**:78–81. doi: 10.1038/s41586-018-0771-1
8. Holland G, Cassidy M, Ballentine CJ. Meteorite Kr in Earth's Mantle suggests a late accretionary source for the atmosphere. *Science*. (2009) **326**:1522–5. doi: 10.1126/science.1179518
9. Mahaffy PR, Niemann HB, Alpert A, Atreya SK, Demick J, Donahue TM, et al. Noble gas abundance and isotope ratios in the of Jupiter from the Galileo Probe Mass Spectrometer atmosphere. *J Geophys Res*. (2000) **105**:15061–71. doi: 10.1029/1999JE001224
10. Ozima M, Podosek FA. Formation age of Earth from $^{1}29$I/$^{1}27$I and $^{2}44$Pu/$^{2}38$U systematics and the missing Xe. *J Geophys Res*. (1999) **104**:25493–9. doi: 10.1029/1999JB900257
11. Avice G, Marty B. The iodine-plutonium-xenon age of the Moon-Earth system revisited. *Philos Trans R Soc A*. (2014) **372**:20130260. doi: 10.1098/rsta.2013.0260
12. Allégre CJ, Staudacher T, Sarda P. Rare gas systematics: formation of the atmosphere, evolution and structure of the Earth's mantle. *Earth Planet Sci Lett*. (1986) **81**:127–50. doi: 10.1016/0012-821X(87)90151-8
13. Allégre CJ, Hofmann AW, O'Nions RK. The Argon constraints on mantle structure. *Geophys Res Lett*. (1996) **23**:3555–7. doi: 10.1029/96GL03373
14. Gonnermann HM, Mukhopadhyay S. Preserving noble gases in a convecting mantle. *Nature*. (2009) **459**:560-U88. doi: 10.1038/nature 08018
15. Anders E, Owen T. Mars and Earth: origin and abundance of volatiles. *Science*. (1977) **198**:453–65. doi: 10.1126/science.198.4316.453
16. Krummenacher D, Merrihue CM, Pepin RO, Reynolds JH. Meteoritic krypton and barium versus the general isotopic anomalies in xenon. *Geochim Cosmochim Acta*. (1962) **26**:231–49. doi: 10.1016/0016-7037(62) 90014-5
17. Avice G, Marty B, Burgess R, Hofmann A, Philippot P, Zahnle K, et al. Evolution of atmospheric xenon and other noble gases inferred from Archean to Paleoproterozoic rocks. *Geochim Cosmochim Acta*. (2018) **232**:82–100. doi: 10.1016/j.gca.2018.04.018
18. Pepin RO. Atmospheres on the terrestrial planets: clues to origin and evolution. *Earth Planet Sci Lett*. (2006) **252**:1–14. doi: 10.1016/j.epsl.2006.09.014
19. Bekaert DV, Broadley MW, Delarue F, Avice G, Robert F, Marty B. Archean kerogen as a new tracer of atmospheric evolution: Implications for dating the widespread nature of early life. *Sci Adv*. (2018) **4**:eaar2091. doi: 10.1126/sciadv.aar2091
20. Zahnle KJ, Gaseca M, Catling DC. Strange messenger: a new history of hydrogen on Earth, as told by xenon. *Geochim Cosmochim Acta*. (2018) **244**:56–85. doi: 10.1016/j.gca.2018. 09.017
21. Ozima, M. and Podosek, F. A. (2002). *Noble Gas Geochemistry, 2nd ed.*, Vol. 140, Cambridge, New York, NY, Melbourne, VIC: Cambridge University Press.
22. Matsuda JI, Matsubara K. Noble gases in silica and their implication for the terrestrial 'missing' Xe. *Geophys Res Lett*. (1989) **16**:81–4. doi: 10.1029/GL016i001p00081
23. Kunz J, Staudacher T, Allegre CJ. Plutonium-fission xenon found in earth's mantle. *Science*. (1998) **280**:877–80. doi: 10.1126/science.280.5365.877
24. Moreira M, Kunz J, Allégre C. Rare gas systematics in popping rock: isotopic and elemental compositions in the upper mantle. *Science*. (1998) **279**:1178–81. doi: 10.1126/science.279.5354.1178
25. Hennecke EW, Manuel OK. Noble gases in Hawaiian xenolith. *Nature*. (1975) **257**:778–80. doi: 10.1038/257778b0
26. Kaneoka I, Takaoka N, Aoki KI. Rare gases in a phlogopite nodule and a phlogopite-bearing peridotite in South African kimberlites. *Earth Planet. Sci. Lett.* (1977) 136:181–6.
27. Poreda RJ, Farley KA. Rare gases in Samoan xenoliths. *Earth Planet Sci Lett*. (1992) **113**:129–44. doi: 10.1016/0012-821X(92)90215-H
28. Czuppon G, Matsumoto T, Handler MR, Matsuda JI. Noble gases in spinel peridotite xenoliths from Mt Quincan, North Queensland, Australia: undisturbed MORB-type noble gases in the subcontinental lithospheric mantle. *Chem* Geol. (2009) **266**:19–28. doi: 10.1016/j.chemgeo.2009.03.029
29. Kuroda PK, Sherrill RD, Jackson KC. Abundances and isotopic compositions of rare gases in granites. *Geochem J*. (1977) **11**:75–90. doi: 10.2343/geochemj.11.75
30. Bekaert DV, Avice G, Marty B, Henderson B. Stepwise heating of lunar anorthosites 60025, 60215, 65315 possibly reveals an indigenous noble gas component on the Moon. *Geochim Cosmochim Acta*. (2017) **218**:114–1315. doi: 10.1016/j.gca.2017.08.041
31. Goettel KA, Eggert JH, Silvera IF. Optical evidence for the metallization of xenon at 132(5) GPa. *Phys Rev Lett*. (1989) **62**:665–8. doi: 10.1103/PhysRevLett.62.665
32. Grochala W. Atypical compounds of gases, which have been called noble. *Chem Soc Rev*. (2007) **36**:1632–55. doi: 10.1039/b702109g
33. Villard P. Combination of argon with water. *C R Hebd Seances Acad Sci*. (1896) **123**:377.
34. Dyadin YA, Aladko EY, Manakov AY, Zhurko FV, Mikina TV, Komarov VY, et al. Clathrate formation in water-noble gas (hydrogen) systems at high pressures. *J Struct Chem*. (1999) **40**:790–5. doi: 10.1007/BF02903454
35. Sanloup C, Hemley RJ, Mao HK. Evidence for xenon silicates at high pressure and temperature. *Geophys Res Lett*. (2002) **29**:1883. doi: 10.1029/2002GL014973
36. Holland G, Ballentine CJ. Seawater subduction controls the heavy noble gas composition of the mantle. *Nature*. (2006) **441**:186–91. doi: 10.1038/nature04761
37. Jackson CRM, Parman SW, Kelley SP, Cooper RF. Noble gas transport into the mantle facilitated by high solubility in amphibole. *Nat Geosci*. (2013) **6**:562–5. doi: 10.1038/ngeo1851
38. Saito K Jr, Dragon JC. Rare gases in cyclosilicates and cogenetic minerals. *Chem Geol*. (1984) **89**:7891–901. doi: 10.1029/JB089iB09p07891
39. Krantz JA, Parman SW, Kelley SP. Recycling of heavy noble gases by subduction of serpentinite. *Earth Planet Sci Lett*. (2019) **521**:120–7. doi: 10.1016/j.epsl.2019.06.007
40. Sanloup C, Mao HK, Hemley RJ. High-pressure transformations in xenon hydrates. *Proc Natl Acad Sci USA*. (2002) **99**:25–8. doi: 10.1073/pnas.221602698
41. Matsui M, Tomoko S, Funamori N. Crystal structures and stabilities of cristobalite-helium phases at high pressures. *Am Miner*. (2014) **99**:184–9. doi: 10.2138/am.2014.4637
42. Crépisson C, Blanchard M, Lazzeri M, Balan E, Sanloup C. New constraints on Xe incorporation mechanisms in olivine from first-principles calculations. *Geochim Cosmochim Acta*. (2018) **222**:146–55. doi: 10.1016/j.gca.2017.10.028
43. Crépisson C, Sanloup C, Blanchard M, Hudspeth J, Glazyrin K, Capitani F. The Xe-SiO_2 system at moderate pressure and high temperature. *Geochem Geophys Geosyst*. (2019) **20**:992–1003. doi: 10.1029/2018GC007779
44. Shackelford JF, Mazaryk A. The interstitial structure of vitreous silica. *J NonCryst Solids*. (1978) **30**:127–39. doi: 10.1016/0022-3093(78)90061-3

45. Carroll MR, Stolper EM. Noble gas solubilities in silicate melts and glasses: new experimental results for argon and the relationship between solubility and ionic porosity. *Geochim Cosmochim Acta*. (1993) **57**:5039–51. doi: 10.1016/0016-7037(93)90606-W
46. Schmidt B, Keppler H. Experimental evidence for high noble gas solubilities in silicate melts under mantle pressures. *Earth Planet Sci Lett*. (2002) **195**:277–90. doi: 10.1016/S0012-821X(01)00584-2
47. Sarda P, Guillot B. Breaking of Henry's law for noble gas and CO_2 solubility in silicate melt under pressure. *Nature*. (2005) **436**:95–8. doi: 10.1038/nature03636
48. Chamorro-Perez EM, Gillet P, Jambon A, MacMillan PF, Badro J. Low argon solubility in silicate melts at high pressure. *Nature*. (1998) **393**:352–5. doi: 10.1038/30706
49. Bouhifd MA, Jephcoat A. Aluminium control of argon solubility in silicate melts under pressure. *Nature*. (2006) **439**:961–4. doi: 10.1038/nature04583
50. Niwa K, Miyakawa C, Yagi T, Matsuda J. Argon solubility in SiO_2 melt under high pressures: a new experimental result using laser-heated diamond anvil cell. *Earth Planet Sci Lett*. (2013) **363**:1–8. doi: 10.1016/j.epsl.2012.12.014
51. Sato T, Funamori N, Yagi T. Helium penetrates into silica glass and reduces its compressibility. *Nat Commun*. (2011) **2**:345. doi: 10.1038/ncomms1343
52. Shen G, Mei Q, Prakapenka VB, Lazor P, Sinogeikin S, Meng Y, et al. Effect of helium on structure and compression behavior of SiO_2 glass. *Proc Natl Acad Sci USA*. (2011) **108**:6004. doi: 10.1073/pnas.1102361108
53. Leroy C, Sanloup C, Bureau H, Schmidt BC, Konôpková Z, Raepsaet C. Bonding of xenon to oxygen in magmas at depth. *Earth Planet Sci Lett*. (2018) **484**:103–10. doi: 10.1016/j.epsl.2017.12.019
54. Kohara S, Akola J, Morita H, Suzuya K, Weber JKR, Wilding MC, et al. Relationship between topological order and glass forming ability in densely packed enstatite and forsterite composition glasses. *Proc Natl Acad Sci USA*. (2011) **108**:14780–5. doi: 10.1073/pnas.1104692108
55. Shi Y, Neuefeind J, Ma D, Page K, Lamberson LA, Smith NJ, et al. Ring size distribution in silicate glasses revealed by neutron scattering first sharp diffraction peak analysis. *J Non-Cryst Sol*. (2019) **516**:71–81. doi: 10.1016/j.jnoncrysol.2019.03.037
56. Crépisson C, Sanloup C, Cormier L, Blanchard M, Hudspeth J, Rosa AD, et al. Kr environment in feldspathic glass and melt: a high pressure, high temperature X-ray absorption study. *Chem Geol*. (2018) **493**:525–31. doi: 10.1016/j.chemgeo.2018.07.008
57. Templeton DH, Zalkin A, Forrester JD, Williamson SM. Crystal and molecular structure of xenon trioxide. *J Am Chem Soc*. (1963) **85**:817. doi: 10.1021/ja00889a037
58. Huston JL, Studier MH, Cloth EN. Xenon tetroxide: mass spectrum. *Science*. (1964) **143**:1161–2. doi: 10.1126/science.143.3611.1161-a
59. Brock DS, Schrobilgen GJ. Synthesis of the missing oxide of xenon, XeO_2, and its implications for Earth's missing xenon. *J Am Chem Soc*. (2011) **133**:6265–9. doi: 10.1021/ja110618g
60. Sanloup C, Bonev SA, Hochlaf M, Maynard-Casely HE. Reactivity of xenon with ice at planetary conditions. *Phys Rev Lett*. (2013) **110**:265501. doi: 10.1103/PhysRevLett.110.265501
61. Dewaele A, Worth N, Pickard CJ, Needs RJ, Pascarelli S, Mathon O, et al. Synthesis and stability of xenon oxides Xe_2O_5 and Xe_3O_2 under pressure. *Nat Chem*. (2016) **8**:784–90. doi: 10.1038/nchem.2528
62. Cavazzoni C, Chiarotti GL, Scandolo S, Tosatti E, Bernasconi M, Parrinello M. Superionic states of water and ammonia at giant planet conditions. *Science*. (1999) **283**:44–6. doi: 10.1126/science.283.5398.44
63. Zhu Q, Jung DY, Oganov AR, Glass CW, Gatti C, Lyakhov AO. Stability of xenon oxides at high pressures. *Nat Chem*. (2013) **5**:61–5. doi: 10.1038/nchem.1497
64. Hermann A, Schwerdtfeger P. Xenon suboxides stable under pressure. *J Phys Chem Lett*. (2014) **5**:4336–42. doi: 10.1021/jz502230b
65. Lundegaard LF, Guillaume C, McMahon MI, Gregoryanz E, Merlini M. On the structure of high-pressure high-temperature η-O_2. *J Chem Phys*. (2009) **130**:164516. doi: 10.1063/1.3118970
66. Zaleski-Ejgierd P, Lata PM. Krypton oxides under pressure. *Sci Rep*. (2016) **6**:18938. doi: 10.1038/srep18938
67. Abelson PH. Experimental technology. *Science*. (1999) **283**:1263. doi: 10.1126/science.283.5406.1263
68. Zhang J, Lv J, Li H, Feng X, Lu C, Redfern SAT, et al. Rare helium-bearing compound FeO_2He stabilized at deep-earth conditions. *Phys Rev Lett*. (2018) **121**:255703. doi: 10.1103/PhysRevLett.121.255703
69. Jackson MG, Konter JG, Becker TW. Primordial helium entrained by the hottest mantle plumes. *Nature*. (2017) **542**:340–3. doi: 10.1038/nature21023
70. Garnero EJ, McNamara AK. Structure and dynamics of earth's lower mantle. *Science*. (2008) **320**:626–8. doi: 10.1126/science.1148028
71. Hu J, Mao H, Guo Q, Hemley RJ. FeO_2 and FeOOH under deep lower-mantle conditions and Earth's oxygen-hydrogen cycles. *Nature*. (2016) **534**:241–4. doi: 10.1038/nature18018
72. Liu J, Hu Q, Kim DY, Wu Z, Wang W, Xiao Y, et al. Hydrogen-bearing iron peroxide and the origin of ultralow-velocity zones. *Nature*. (2017) **551**:494–7. doi: 10.1038/nature24461
73. Hua Q, Kim DY, Liu J, Meng Y, Yang L, Zhange WLM, et al. Dehydrogenation of goethite in Earth's deep lower mantle. *Proc Natl Acad Sci USA*. (2017) **114**:1498–501. doi: 10.1073/pnas.1620644114
74. Sanloup C, Schmidt BC, Perez EC, Jambon A, Gregoryanz E, Mezouar M. Retention of xenon in quartz and Earth's missing xenon. *Science*. (2005) **310**:1174–7. doi: 10.1126/science.1119070
75. Sanloup C, Schmidt BC, Gudfinnsson G, Dewaele A, Mezouar M. Xenon and argon: a contrasting behavior in olivine at depth. *Geochim Cosmochim Acta*. (2011) **75**:6271–84. doi: 10.1016/j.gca.2011.08.023
76. Probert MIJ. An ab initio study of xenon retention in α-quartz. *J Phys*. (2010) **22**:025501. doi: 10.1088/0953-8984/22/2/025501
77. Kalinowski J, Rasanen M, Gerber RB. Chemically-bound xenon in fibrous silica. *Phys Chem Chem Phys*. (2014) **16**:11658–61. doi: 10.1039/C4CP01355G
78. Britvin SN, Kashtanov SA, Krivovichev SV, Chukanov NV. Xenon in rigid oxide frameworks: structure, bonding and explosive properties of layered perovskite $K_4Xe_3O_12$. *J Am Chem Soc*. (2016) **138**:13838–41. doi: 10.1021/jacs.6b09056
79. Eremets MI, Gregoryanz EA, Struzhkin VV, Mao H, Hemley RJ. Electrical conductivity of xenon at megabar pressures. *Phys Rev Lett*. (2000) **85**:2797–800. doi: 10.1103/PhysRevLett.85.2797
80. Caldwell WA, Nguyen JH, Pfrommer BG, Mauri F, Louie SG, Jeanloz R. Structure, bonding and geochemistry of xenon at high pressures. *Science*. (1997) **277**:930–3. doi: 10.1126/science.277.5328.930
81. Lee KM, Steinle-Neumann G. High-pressure alloying of iron and xenon: "Missing" Xe in the Earth's core? *J Geophys Res*. (2006) **111**:B02202. doi: 10.1029/2005JB003781
82. Zhu L, Liu H, Pickard CJ, Zou G, Ma Y. Reactions of xenon with iron and nickel are predicted in the Earth's inner core. *Nat Chem*. (2014) **6**:645–9. doi: 10.1038/nchem.1925
83. Stavrou E, Yao Y, Goncharov AF, Lobanov SS, Zaug JM, Liu H, et al. Synthesis of xenon and iron-nickel intermetallic compounds at earth's core thermodynamic conditions. *Phys Rev Lett*. (2018) **120**:096001. doi: 10.1103/PhysRevLett.120.096001
84. Dewaele A, Ppin CM, Geneste G, Garbarino G. Reaction between nickel or iron and xenon under high pressure. *High Press Res*. (2016) **97**:215504. doi: 10.1080/08957959.2016.1267165
85. Rivoldini A, Hoolst TV, Verhoeven O, Mocquet A, Dehant V. Geodesy constraints on the interior structure and composition of Mars. *Icarus*. (2011) **213**:451–72. doi: 10.1016/j.icarus.2011.03.024
86. Adeleke AA, Kunz M, Greenberg E, Prakapenka VB, Yao Y, Stavrou E. A high-pressure compound of argon and nickel: noble gas in the earth's core? *ACS Earth Space Chem*. (2019) **3**:2517–24. doi: 10.1021/acsearthspacechem.9b00212
87. Guillot T. Interior of giant planets inside and outside the Solar System. *Science*. (1999) **286**:72–7. doi: 10.1126/science.286.5437.72
88. Redmer R, Mattsson TR, Nettelmann N, French M. The phase diagram of water and the magnetic fields of Uranus and Neptune. *Icarus*. (2011) **211**:798–803. doi: 10.1016/j.icarus.2010.08.008
89. Wilson HF, Militzer B. Sequestration of noble gases in giant planet interiors. *Phys Rev Lett*. (2010) **104**:121101. doi: 10.1103/PhysRevLett.104.121101
90. Loubeyre P, LeToullec R, Pinceaux JF. Compresson of $Ar(H_2)$ up to 175 GPa - A new path for the dissociation of molecular hydrogen. *Phys Rev Lett*. (1994) **72**:1360–3. doi: 10.1103/PhysRevLett.72.1360

91. Ji C, Goncharov AF, Shukla V, Jena NK, Popov D, Li B, et al. Stability of $Ar(H_2)_2$ to 358 GPa. *Proc Natl Acad Sci USA*. (2017) **114**:3596–600. doi: 10.1073/pnas.1700049114
92. Kleppe AK, Amboage M, Jephcoat AP. New high-pressure van der Waals compound $Kr(H_2)_4$ discovered in the krypton-hydrogen binary system. *Sci Rep*. (2014) **4989**:4. doi: 10.1038/srep04989
93. Somayazulu M, Dera P, Goncharov AF, Gramsch SA, Liermann P, Yang W, et al. Pressure-induced bonding and compound formation in xenon-hydrogen solids. *Nat Chem*. (2009) **2**:50–3. doi: 10.1038/nchem.445
94. Liu C, Gao H, Wang Y, Needs RJ, Pickard CJ, Sun J, et al. Multiple superionic states in helium-water compounds. *Nat Phys*. (2019) **15**:1065–70. doi: 10.1038/s41567-019-0568-7
95. Bai Y, Liu Z, Botana J, Yan D, Lin HQ, Sun J, et al. Electrostatic force driven helium insertion into ammonia and water crystals under pressure. *Commun Chem*. (2019) **2**:102. doi: 10.1038/s42004-019-0204-6
96. Liu HY, Yao YS, Klug DD. Stable structures of He and H_2O at high pressure. *Phys Rev B*. (2015) **9**:014102. doi: 10.1103/PhysRevB.91.014102
97. Brooker RA, Du Z, Blundy JD, Kelley SP, Allan NL, Wood BJ, et al. The 'zero charge' partitioning behaviour of noble gases during mantle melting. *Nature*. (2003) **423**:738–41. doi: 10.1038/nature01708
98. Shcheka SS, Keppler H. The origin of the terrestrial noble-gas signature. *Nature*. (2012) **490**:531–4. doi: 10.1038/nature11506
99. Rosa AD, Bouhifd MA, Morard G, Briggs R, Garbarino G, Irifune T, et al. Krypton storage capacity of the Earth's lower mantle. *Earth Planet Sci Lett*. (2020) **532**:116032. doi: 10.1016/j.epsl.2019.116032
100. Hirsch LM, Shankland TJ. Equilibrium point defect concentrations in MgO: understanding the mechanisms of conduction and diffusion and the role of Fe impurities. *J Geophys Res*. (1991) **96**:385–403. doi: 10.1029/90JB02175
101. Hirsch LM, Shankland TJ. Point defects in $(Mg,Fe)SiO_3$ perovskite. *Geophys Res Lett*. (1991) **96**:1305–8. doi: 10.1029/91GL01582
102. Dauphas N, Marty B. Inference on the nature and the mass of Earth's late veneer from noble metals and gases. *J Geophys Res Planets*. (2002) **107**:JE001617. doi: 10.1029/2001JE001617
103. Khriachtchev L, Isokoski K, Cohen A, Räsänen M, Gerber RB. A small neutral molecule with two noble-gas atoms: HXeOXeH. *J Am Chem Soc*. (2008) **130**:6114–8. doi: 10.1021/ja077835v
104. Franks NP, Dickinson R, de Sousa SLM, Hall AC, Lieb WR. How does xenon produce anaesthesia? *Nature*. (1998) **396**:324. doi: 10.1038/24525
105. Monserrat B, Martinez-Canales M, Needs RJ, Pickard CJ. Helium-iron compounds at terapascal pressures. *Phys Rev Lett*. (2018) **121**:015301. doi: 10.1103/PhysRevLett.121.015301

Conflict of Interest: The author declares that the research was conducted in the absence of any commercial or financial relationships that could be construed as a potential conflict of interest.

frontiers in Chemistry

MINI REVIEW
published: 19 June 2020
doi: 10.3389/fchem.2020.00462

Cationic Noble-Gas Hydrides: From Ion Sources to Outer Space

Felice Grandinetti[1,2*†]

[1] Dipartimento per la Innovazione nei Sistemi Biologici, Agroalimentari e Forestali (DIBAF), Università della Tuscia, Viterbo, Italy, [2] Istituto per i Sistemi Biologici del CNR, Monterotondo, Italy

Cationic species with noble gas (Ng)-hydrogen bonds play a major role in the gas-phase ion chemistry of the group 18 elements. These species first emerged more than 90 years ago, when the simplest HeH^+ and HeH_2^+ were detected from ionized He/H_2 mixtures. Over the years, the family has considerably expanded and currently includes various bonding motifs that are investigated with intense experimental and theoretical interest. Quite recently, the results of these studies acquired new and fascinating implications. The diatomic ArH^+ and HeH^+ were, in fact, detected in various galactic and extragalactic regions, and this stimulates intriguing questions concerning the actual role in the outer space of the Ng-H cations observed in the laboratory. The aim of this review is to briefly summarize the most relevant information currently available on the structure, stability, and routes of formation of these fascinating systems.

Keywords: noble-gas ions, noble-gas chemistry, interstellar chemistry, gas-phase chemistry, mass spectrometry, theoretical calculations

OPEN ACCESS

Edited by:
Sudip Pan,
University of Marburg, Germany

Reviewed by:
Vladimir Feldman,
Lomonosov Moscow State University, Russia
Antonio Frontera,
University of the Balearic Islands, Spain
Gabriel Merino,
Centro de Investigacion y de Estudios Avanzados - Unidad Mérida, Mexico

***Correspondence:**
Felice Grandinetti
fgrandi@unitus.it

†ORCID:
Felice Grandinetti
orcid.org/0000-0001-7217-9490

Specialty section:
This article was submitted to Physical Chemistry and Chemical Physics, a section of the journal Frontiers in Chemistry

Received: *23 February 2020*
Accepted: *04 May 2020*
Published: *19 June 2020*

Citation:
Grandinetti F (2020) Cationic Noble-Gas Hydrides: From Ion Sources to Outer Space. Front. Chem. 8:462. doi: 10.3389/fchem.2020.00462

About 130 years after the discovery of argon (Rayleigh, 1895), the chemistry of the noble gases currently appears as a fascinating "saga" (Grandinetti, 2018), where combative scientists never tire of using different chemical and physical weapons to challenge and defeat the proverbial inertness of the elements. Exemplary in this regard is the unceasing interest focused on gaseous ionic species. The story began in 1925, when Hogness and Lunn (1925) first detected the simplest HeH^+ and HeH_2^+ from ionized He/H_2 mixtures. With the upsurge of interest in gas-phase ion-molecule reactions (Stevenson, 1957; Giese et al., 1961), it soon emerged that, under ionizing conditions, all the noble gas atoms (Ng) were "forgetting" to be inert, and capable of combining with a huge variety of atoms and molecules. The subsequent studies actually confirmed an exciting ion chemistry of both fundamental and applied interest (Grandinetti, 2011). None could, however, surmise the amazing implications that emerged quite recently, when ArH^+ and HeH^+ were detected in various galactic and extragalactic regions (Barlow et al., 2013; Schilke et al., 2014; Müller et al., 2015; Güsten et al., 2019). This unexpected projection from the ion sources to outer space rejuvenates particular interest in cationic noble-gas hydrides $Ng_mH_n^+$ ($m, n \geq 1$), a well-established family of noble gas ions. The pertinent literature is already vast, and the contributions chosen here wish to illustrate issues of current interest that are also of relevance for the naturally-occurring chemistry. The systems are described so as to give an overview, useful also as a guide for future studies.

NgH^+

The chemistry of the gaseous $Ng_mH_n^+$ plays around four major bonding motifs, namely the NgH^+, the linear centro-symmetric Ng-H-Ng^+, and their Ng-solvated complexes $(NgHNg^+)(Ng)_n$, the $(H_2^+)(Ng)_n$, and the $(H_3^+)(Ng)_n$ ($n \geq 1$). Their formations also benefit from ion sources operated

at ultra-cold temperatures (Jašik et al., 2013), or from ionized helium nanodroplets doped with suitable precursors (Fárník and Toennies, 2005). The connectivities of some exemplary species are shown in **Figure 1**, and some quantitative data are reported in **Table 1**.

The diatomic NgH^+ (Ng = He-Xe), still elusive in any other environment, are quite stable in the gas phase. Their simplest ionic routes of formation given by the equations

$$Ng + H^+ \rightarrow NgH^+ \quad (1)$$

$$Ng^+ + H \rightarrow NgH^+ \quad (2)$$

$$Ng + H_2^+ \rightarrow NgH^+ + H \quad (3)$$

$$Ng^+ + H_2 \rightarrow NgH^+ + H \quad (4)$$

are, invariably, exothermic (National Institute of Standards and Technology, 2020), with the only exception of He and Ne reacting with ground-state H_2^+ (see **Table 1**). The galactic and extragalactic ArH^+ is, in particular, ascribed to reactions (3) and (4) (Barlow et al., 2013; Theis et al., 2015), whereas the HeH^+ observed in the planetary nebulae (Güsten et al., 2019) mainly arises from reaction (2) (Roberge and Dalgarno, 1982; Cecchi-Pestellini and Dalgarno, 1993; Fortenberry, 2019). In keeping with any type of bonding analysis (Borocci et al., 2015), the short bond distances, and high vibrational frequencies of the NgH^+ point to typical covalent species. The experimental values (Rogers et al., 1987, and references cited therein; Coxon and Hajigeorgiou, 1999; Perry et al., 2014; Gruet and Pirali, 2019) (see **Table 1**) range between 0.774 and 1.603 Å, and 2,911 and 2,270 cm^{-1}, respectively, and follow the expected periodic increase/decrease of R/ν when going from HeH^+ to XeH^+.

Ng-H-Ng$^+$ AND (NgHNg$^+$)(Ng)$_n$ ($n \geq 1$)

The addition of another Ng to NgH^+ produces the linear centro-symmetric Ng-H-Ng^+. Their thermochemistry is experimentally unknown, but theoretical calculations (Kim and Lee, 1999; Tan and Kuo, 2019) predict Ng additions that are exothermic by ca. 13–17 kcal mol^{-1}. The alternative conceivable Ng-Ng-H^+ are instead only marginally stable (Bop et al., 2017a,b), and do not play a role in the chemistry and the dynamics of the gaseous $H^+(Ng_m)$ (Ritschel et al., 2004, 2005, 2007). The structural assignment of the Ng-H-Ng^+ is based first on matrix infrared (IR) spectroscopy. Definitive evidence in this regard was obtained, in particular, by Kunttu and his coworkers (Kunttu et al., 1992; Kunttu and Seetula, 1994), who identified the symmetric (ν_1) and anti-symmetric (ν_3) stretching that appear in the IR spectra of the Ng-H-Ng^+ (Ng = Ar, Kr, Xe) as a progression of ($n\nu_1 + \nu_3$), with n up to 4 for Xe-H-Xe^+. The ν_1 and ($\nu_1 + \nu_3$) absorptions of Kr-H-Kr^+ and Xe-H-Xe^+ were subsequently measured in different matrices

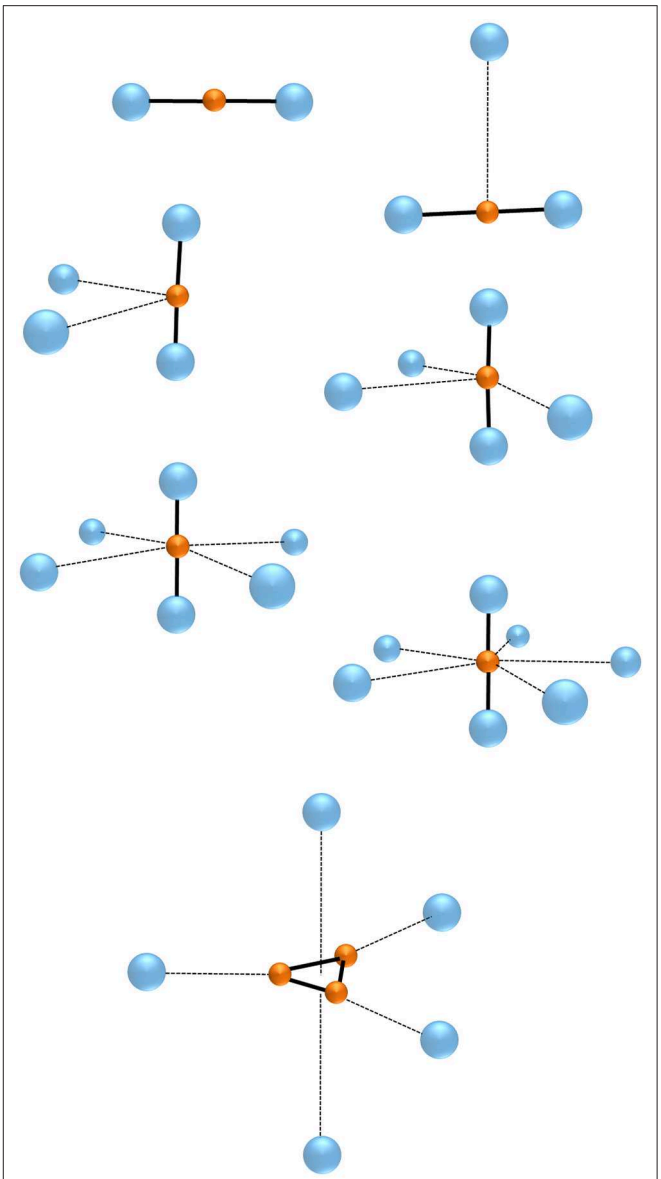

FIGURE 1 | Connectivities of the Ng-H-Ng^+, (Ng-H-Ng^+)(Ng)$_n$ (n = 1–5), and H_3^+(Ng)$_5$.

(Lundell et al., 1999; Tsuge et al., 2015), and found to be sensitive to the environment. As shown in **Table 1**, the comparison with very recent theoretical estimates (Tan and Kuo, 2019) clearly unravels that the "cold" bands are red-shifted by up to 100 cm^{-1} with respect to those of the naked Ng-H-Ng^+. Consistently, the theoretical IR absorptions of Ar-H-Ar^+ are instead quite close to the corresponding gas-phase values obtained by Duncan and his coworkers (McDonald et al., 2016). They produced the entire family of the smallest (Ar-H-Ar^+)Ar_n (n = 1–5), and measured the IR photodissociation spectrum (loss of one Ar atom) of each mass-selected complex. In general, the (Ng-H-Ng^+)Ng_n consist (Giju et al., 2002; Ritschel et al., 2005, 2007; Császár et al., 2019) of Ng atoms weakly bound to a covalent centro-symmetric Ng_2H^+,

TABLE 1 | Energetics (kcal mol^{-1}) of reactions involving the gaseous $Ng_mH_n^+$, and bond distances (R, Å) and vibrational frequencies (ν, cm^{-1}) of the NgH^+ and Ng-H-Ng$^+$.

Reaction[a]	He	Ne	Ar	Kr	Xe
$Ng + H^+ \rightarrow NgH^+$	−42.5	−47.5	−88.2	−101.5	−119.4
$Ng^+ + H \rightarrow NgH^+$	−295.9	−231.2	−138.0	−110.7	−85.5
$Ng + H_2^+ \rightarrow NgH^+ + H$	19.6	14.6	−26.1	−39.4	−57.3
$Ng^+ + H_2 \rightarrow NgH^+ + H$	−191.7	−127.0	−33.8	−6.5	18.7
$Ng + NgH^+ \rightarrow$ Ng-H-Ng$^+$	−13.2[b]	−15.6[c]	−14.8[c]	−14.6[c]	−13.9[c]
$Ng + H_2^+ \rightarrow$ Ng-H-H$^+$	−7.8[d]	−12.9[e]	−42.4[e]		
$2Ng + H_2^+ \rightarrow$ Ng-H-H-Ng$^+$[f]	−5.5	−13.1	−50.0	−66.4	−89.9
$Ng + H_3^+ \rightarrow Ng(H_3^+)$	−0.22 ÷ −0.41[g]	−2.5[h]/−2.6[i]	−6.7[i]/−8.7[h]/-9.0[i]	−13.9[h]	−22.8[h]
NgH^+[k]					
R	0.774[l]	0.991[m]	1.280[m]	1.421[m]	1.603[m]
ν	2911[n]	2904[m]	2711[m]	2495[m]	2270[m]
Ng-H-Ng$^+$					
R	0.926[°]	1.144[p]	1.502[p]	1.661[p]	1.862[p]
ν_3^q	1290 (gas)[r]	1432[s]	1000[s] 989 (gas)[t] 903 (Ar)[u]	927[s] 853 (Kr)[u] 885 (Ar)[v] 871 (p-H_2)[w] 871 (n-H_2)[w]	842[s] 731 (Xe)[u] 828 (Ar)[v] 782 (Kr)[v] 847 (p-H_2)[w] 845 (n-H_2)[w]
$\nu_1^x + \nu_3$		1814[s]	1253[s] 1237 (gas)[t] 1140 (Ar)[u]	1092[s] 1008 (Kr)[u] 974 (p-H_2)[w] 985 (n-H_2)[w]	964[s] 843 (Xe)[u] 953 (Ar)[v] 900 (Kr)[v] 972 (p-H_2)[w] 965 (n-H_2)[w]
$2\nu_1 + \nu_3$		2182[s]	1500[s] 1485 (gas)[t] 1361 (Ar)[u]	1257[s] 1160 (Kr)[u]	1085[s] 953 (Xe)[u]
$3\nu_1 + \nu_3$		2541[s]	1750[s] 1726 (gas)[t]	1428[s] 1309 (Kr)[u]	1213[s] 1062 (Xe)[u]
$4\nu_1 + \nu_3$			2401 (gas)[t]		1168 (Xe)[u]

[a] *Unless stated otherwise, experimental enthalpy changes (ΔH) from National Institute of Standards and Technology (2020).* [b] *CCSD(T)/CBS electronic energy change (ΔE_{el}) from Kim and Lee (1999).* [c] *CCSD(T)/aug-cc-pVQZ//MP2/aug-cc-pVQZ energy change at 0 K [ΔE(0)] from Tan and Kuo (2019).* [d] *FCI/aug-cc-pV5Z ΔE_{el} from Koner et al. (2019).* [e] *CCSD(T)/aug-cc-pVTZ ΔE_{el} from Theis et al. (2015).* [f] *CCSD(T)/def2-TZVPP ΔE(0) from Krapp et al. (2008).* [g] *Range of theoretical values quoted by Savić et al. (2015).* [h] *CCSD(T)/aug-cc-pVQZ ΔE_{el} from Pauzat et al. (2016).* [i] *CCSD(T)/aug-cc-pV5Z ΔE_{el} from Theis and Fortenberry (2015).* [j] *ΔH from Hiraoka and Mori (1989).* [k] *Gas-phase.* [l] *Coxon and Hajigeorgiou (1999).* [m] *Rogers et al. (1987).* [n] *Perry et al. (2014).* [°] *CCSD(T)/aug-cc-pVTZ value from Kim and Lee (1999).* [p] *MP2/aug-cc-pVQZ value from Tan and Kuo (2019).* [q] *Anti-symmetric stretching.* [r] *Gas-phase value from Asvany et al. (2019).* [s] *Discrete variable representation (DVR) theoretical value based on a CCSD(T)/aug-cc-pVQZ//MP2/aug-cc-pVQZ potential from Tan and Kuo (2019).* [t] *Gas-phase value from McDonald et al. (2016).* [u] *Value in Ar, Kr, or Xe matrix from Kunttu and Seetula (1994).* [v] *Value in Ar or Kr matrix from Lundell et al. (1999).* [w] *Value in H_2 matrix from Tsuge et al. (2015).* [x] *Symmetric stretching.*

the (Ng-H-Ng$^+$)Ng_5 growing by the step-by-step addition of five Ng in the plane perpendicular to the Ng-H-Ng$^+$ axis (see **Figure 1**). The IR patterns of the gaseous (Ar-H-Ar$^+$)Ar_n were assigned (McDonald et al., 2016) as the ν_3 and ($n\nu_1 + \nu_3$) progression, with n arriving up to 4 for (Ar-H-Ar$^+$)Ar. As shown in **Table 1**, the ν_3 (989 cm^{-1}), ($\nu_1 + \nu_3$) (1,237 cm^{-1}), and ($2\nu_1 + \nu_3$) (1,485 cm^{-1}) absorptions of the latter species are, invariably, blue-shifted with respect to the corresponding values measured in argon matrix. Consistently, when going from (Ar-H-Ar$^+$)Ar to (Ar-H-Ar$^+$)Ar_5, the ν_3 and ($\nu_1 + \nu_3$) resulted progressively red-shifted up to 965 and 1,207 cm^{-1}, respectively. A strictly similar trend was quite recently noticed by Asvany et al. (2019), who measured the ν_3 of the gaseous (He-H-He$^+$)He_n (n = 1–4) ranging between 1,290 (n = 1) and 1,273 cm^{-1} (n = 4). As for the larger (Ng-H-Ng$^+$)Ng_n ($n > 5$), the available experimental results (Kojima et al., 1992; Bartl et al., 2013; Gatchell et al., 2018, 2019; Lundberg et al., 2020) unravel intriguing differences between the heaviest (Ng-H-Ng$^+$)Ng_n (Ng = Ne, Ar, Kr), and the He congeners. For the former species, the mass-spectrometric abundancies (Gatchell et al., 2018, 2019) indicate the "magic" role of three structures, namely the (Ng-H-Ng$^+$)Ng_5, the (Ng-H-Ng$^+$)Ng_{11}, and the (Ng-H-Ng$^+$)Ng_{17}. Based also on theoretical calculations, these species are identified as the most stable intermediates along a icosahedral growth. Starting from the (Ng-H-Ng$^+$)Ng_5, five Ng atoms progressively bind to one of the two equivalent ends of the Ng-H-Ng$^+$ core, and the ensuing ring is eventually "capped" by a further Ng. A second specular capped ring of six Ng atoms is then obtained

around the other Ng of the core, and the cluster eventually looks like a "roller" made up of an axel with three wheels, the two outside ones having hubcaps (Ritschel et al., 2005). On the other hand, consistent with previous results (Kojima et al., 1992; Bartl et al., 2013), recent experiments (Lundberg et al., 2020) showed that, in the mass spectra of protonated helium clusters, the only observed magic structure associated with the icosahedral motif is the (Ng-H-Ng$^+$)Ng$_{11}$. The (Ng-H-Ng$^+$)Ng$_5$ and (Ng-H-Ng$^+$)Ng$_{17}$ are missing, but there is evidence for peculiarly stable (Ng-H-Ng$^+$)Ng$_4$ and (Ng-H-Ng$^+$)Ng$_9$, the latter being the strongest abundance anomaly. Recent theoretical calculations (Császár et al., 2019) actually suggest the stability of the (Ng-H-Ng$^+$)Ng$_4$, and the (Ng-H-Ng$^+$)Ng$_{11}$, but do not provide evidence for peculiarly stable (Ng-H-Ng$^+$)Ng$_9$. Clearly, there is still room for further investigation.

The Ng-H distances of the Ng-H-Ng$^+$ are experimentally unknown, and **Table 1** quotes accurate available theoretical predictions (Kim and Lee, 1999; Tan and Kuo, 2019). Likewise, the NgH$^+$, the values increase from He-H-He$^+$ to Xe-H-Xe$^+$, but are comparatively longer than those of the diatomic ions. In fact, in the Ng-H-Ng$^+$, the proton is "shared" between two equivalent Ng atoms. In any case, the bonding analysis (Borocci et al., 2011) is again suggestive of covalent bonds.

Mixed ions Ng-H-Ng'$^+$ are still elusive in the gas phase, and the only experimentally-detected species is the Xe-H-Kr$^+$ identified in solid hydrogen by a ν_3 absorption at 1,284 cm^{-1} (Tsuge et al., 2015). Compared with the ν_3 of Kr-H-Kr$^+$ and Xe-H-Xe$^+$ measured in the same environment (see **Table 1**), this value is blue-shifted, and this is in line with previous theoretical predictions (Lundell, 1995) showing that in the Xe-H-Kr$^+$, the proton is more tightly bound to the Xe atom and the ion is best described as a (Xe-H$^+$–Kr) complex with a ν_3 nearer to, but smaller than, the stretching frequency of XeH$^+$ (2270 cm^{-1}). Indeed, an asymmetric structure is a common feature of the mixed Ng-H-Ng'$^+$ (Fridgen and Parnis, 1998a,b; Lundell et al., 1999). The (formal) H$^+$ is more tightly bound to the heaviest Ng, and the resonance structure (Ng-H$^+$–Ng') becomes progressively prevailing by increasing the difference between the proton affinity (PA) of Ng and Ng' (Ng > Ng'). Simplest illustrative examples are the Ne-H-He$^+$, Ar-H-He$^+$, and Ar-H-Ne$^+$ reported by Koner et al. (2012). The Ne-H (1.108 Å) and He-H (0.959 Å) distances of Ne-H-He$^+$ are shorter and longer, respectively, than the bond distances of Ne-H-Ne$^+$ (1.139 Å) and He-H-He$^+$ (0.926 Å), and the loss of Ne from Ne-H-He$^+$ resulted more endothermic than that of He (18.2 vs. 12.0 kcal mol^{-1}). In addition, the ν_3 absorption of Ne-H-He$^+$, 1,644 cm^{-1}, falls in between the value predicted for He-H-He$^+$ (1,717 cm^{-1}) and Ne-H-Ne$^+$ (1,437 cm^{-1}). In the Ar-H-He$^+$ and Ar-H-Ne$^+$, the structural asymmetries are so pronounced to support their description as complexes of ArH$^+$ weakly bound to He and Ne (by ca. 2.0 and 4.1 kcal mol^{-1}, respectively).

Are there prospects to detect the Ng-H-Ng$^+$ and Ng-H-Ng'$^+$ in outer space (Fortenberry, 2017; Stephan and Fortenberry, 2017)? Assuming that the extreme conditions of some dense regions of the interstellar medium and planetary atmospheres may be sufficient to produce not only ArH$^+$ but also NeH$^+$, Fortenberry (2017) suggested the conceivable formation of Ar-H-Ar$^+$, Ne-H-Ne$^+$, and Ar-H-Ne$^+$ from the exothermic reaction of NgH$^+$ with the H_3^+(Ng) (Ng = Ne, Ar) (*vide infra*) or with Ne or Ar atoms absorbed on polycyclic aromatic hydrocarbons (PAHs) (Rodríguez-Cantano et al., 2017). While the former process is probably hampered by the high barriers arising from the positive charges of the colliding partners, the PAHs route seems more plausible, especially in view of the predicted exothermic character of model reactions between NeH$^+$ and $C_{10}H_8$-Ng or $C_{32}H_{14}$-Ng (Ng = Ne, Ar) (Fortenberry, 2017). Other suggestions for conceivable formation routes come from studies performed in cold matrices (Feldman et al., 2016; Saenko and Feldman, 2016), showing that ionized molecules such as H_2O and CH_3OH (quite abundant in the outer space) might protonate Ng atoms so to eventually form the Ng-H-Ng$^+$.

$(H_2^+)(Ng)_n$ ($n \geq 1$)

The NgH$_2^+$, particularly the lightest HeH$_2^+$, NeH$_2^+$, and ArH$_2^+$, have received sustained experimental and theoretical interest, also in connection with their role in reactions (3) and (4). Illustrative in this regard are, for example, the extensive studies on the reaction between H_2^+ and He performed so far by Herman, Zülicke, and their coworkers (Schneider et al., 1976; Havemann et al., 1978, and references cited therein) with crossed-beam experiments and quasi-classical trajectory calculations. The NgH$_2^+$ possess linear Ng-H-H$^+$ connectivities, and their potential wells (see **Table 1**) are deep enough (Theis et al., 2015; Koner et al., 2019) to sustain numerous vibrational and rovibrational states. The latter were accurately estimated even recently (Theis et al., 2015; Papp et al., 2017, 2018; Szidarovszky and Yamanouchi, 2017), also in the intriguing prospect of actual detection of natural NgH$_2^+$. Some general warnings in this regard come, however, from the information already available, in particular on the gas-phase ion chemistry of Ar/H_2 mixtures (Bedford and Smith, 1990; Hvistendahl et al., 1990; Koyanagi et al., 2000). The ArH$_2^+$ was actually detected (Bedford and Smith, 1990) from the ligand-switching between Ar_2^+ and H_2, exothermic by ca. 17 kcal mol^{-1}. However, dynamics calculations on the reaction between Ar and H_2^+ (Liu et al., 2011; Hu et al., 2013) point to a direct reactive mechanism, and the experiments also showed (Bedford and Smith, 1990) that, at least down to 80 K, Ar$^+$ reacts with H_2 to directly from ArH$^+$, with no evidence for ArH$_2^+$. But even assuming stabilization at the lowest temperatures, ArH$_2^+$ could exothermically react with H_2 (by ca. 8 kcal mol^{-1}) to form ArH_3^+. The latter is stable enough to conceivably exist at the lowest temperatures of the interstellar medium (*vide infra*).

The NgH$_2^+$ are the simplest members of the H_2^+(Ng)$_n$ family ($n \geq 1$). The H_2^+(Ng)$_2$ were, in particular, theoretically investigated by Krapp et al. (2008), who obtained evidence for linear symmetric complexes (Ng-H-H-Ng)$^+$, thermochemically bound with respect to H_2^+ and two Ng (see **Table 1**). However, this stability must contend with the rearrangement into Ng—NgH$_2^+$ that resulted exothermic for Ng = Xe, and very fast for Ng = He and Ne. Therefore, the experiments were oriented to

search the argon and krypton congeners; however, no $Ar_2H_2^+$ or $Kr_2H_2^+$ were detected from ionized Ng/H_2 mixtures (Krapp et al., 2008). Somewhat unexpectedly, the lightest $H_2^+(He)_2$ was instead observed by electron ionization of H_2-doped helium droplets soon afterward (Jaksch et al., 2009). Besides the expected dissociation into HeH_2^+ and He, featuring a low kinetic energy release (KER) of 15 ± 4 meV, the mass-analyzed kinetic energy experiments unraveled a not-surmised dissociation into HeH^+ and HeH (or He + H), occurring with a higher probability, and a KER four times larger than that of the loss of He. This behavior was ascribed to a metastable, electronically excited $H_2^+(He)_2$, whose excess energy arising from the ionization event allows the rupture of the stronger H-H^+ bond, the weaker He-H^+ remaining intact. Larger $H_2^+(He)_n$ ($n \leq 30$) were subsequently detected from ionized helium droplets doped with H_2 (Bartl et al., 2013), but their structure is only little explored.

$(H_3^+)(Ng)_n$ ($n \geq 1$)

The $H_3^+(Ng)_n$ generally consist of a H_3^+ covalent ionic core weakly bound to one or more Ng atoms. According to the calculations (Beyer et al., 1999; Kaczorowska et al., 2000), the first three Ng add to the vertices of the equilateral H_3^+, and the fourth and the fifth ones complete the bi-pyramidal structure shown in **Figure 1**. The vertex-coordination of $H_3^+(Ar)$ is also supported by spectroscopic measurements (Bogey et al., 1987, 1988; Bailleux et al., 1998; McCarthy and Thaddeus, 2010). As shown in **Table 1**, the addition of one Ng to H_3^+ is, invariably, exothermic, the stability increasing when going from $H_3^+(He)$ to $H_3^+(Xe)$ (Savić et al., 2015; Pauzat et al., 2016). Interestingly, as shown by the calculations (Beyer et al., 1999; Mousis et al., 2008), this trend mirrors a structure of the $H_3^+(Ng)$ that gradually changes from nearly pure $H_3^+(He)$ and $H_3^+(Ne)$ to a description close to $XeH^+(H_2)$. This parallels a PA of H_2, 100.9 kcal mol^{-1}, that is lower than the PA of Xe (119.4 kcal mol^{-1}). In essence, the periodic increase of the stabilities of the $H_3^+(Ng)$ reflects not only the increase of the polarizability of Ng (with consequent increase of the ensuing charge transfer to H_3^+), but also the onset of covalency in the Kr-H and especially the Xe-H bonds. The calculations indicate also (Pauzat and Ellinger, 2005; Pauzat et al., 2009; Chakraborty et al., 2010) that, when going to the larger $H_3^+(Ng)_n$ ($n \geq 2$), the energy change of the reaction $H_3^+(Ng)_n \rightarrow H_3^+(Ng)_{n-1} + Ng$ tends to decrease by increasing n, appreciable jumps in particular being predicted between $n = 1$ and $n = 2$, and between $n = 3$ and $n = 4$. These trends are well-consistent with the experimental binding energies of $H_3^+(Ar)_n$ (n = 1-7), measured (Hiraoka and Mori, 1989) as 6.7 ($n = 1$), 4.6 ($n = 2$), 4.3 ($n = 3$), 2.5 ($n = 4$), 2.3 ($n = 5$), 2.2 ($n = 6$), and 1.6 kcal mol^{-1} ($n = 7$), and clearly mirror the growing mode of the cluster.

The vibrational and rotational patterns of the $H_3^+(Ar)$ and $H_3^+(Ne)$ were more recently refined by theoretical calculations (Theis and Fortenberry, 2015), performed also to best guide the conceivable detection of these ions in the outer space. The natural role of the $H_3^+(Ng)_n$ was first suggested by Pauzat, Ellinger, and their coworkers, who proposed that the deficit of noble gases observed in planetary objects could be due to the sequestration by H_3^+ during the early stages of the solar nebula (Pauzat and Ellinger, 2005, 2007; Mousis et al., 2008; Pauzat et al., 2009, 2013). According to their recent quantum-dynamics calculations (Pauzat et al., 2016), especially for the heaviest Kr and Xe, the rate constants of the radiative association are indeed large enough to support the sequestration by H_3^+. The helium complexes $H_3^+(He)_n$ are also of potential astrochemical interest. Theoretical calculations (Chakraborty et al., 2010) confirm the planar structure of the $H_3^+(He)_3$, the three He bound to the vertices of H_3^+ featuring nearly constant complexation energies of ca. 1 kcal mol^{-1}. On the experimental side, Gerlich and his coworkers (Savić et al., 2015) recently produced $H_3^+(He)_n$ (n up to 9) in an ion trap cooled down to 3.7 K. Particularly for the simplest $H_3^+(He)$, laser-induced dissociation experiments unraveled almost 100 lines between 2,700 and 2,765 cm^{-1}, whose detailed assignment was, however, hampered by the lack of a sufficiently accurate potential energy surface. Species with higher n are also detected in different ion sources (Kojima et al., 1992; Bartl et al., 2013), the experiments suggesting, in particular, the peculiar stability of the $H_3^+(He)_{12}$, and the "magic" role of $n = 9$ and 10. Further structural assay awaits more detailed theoretical investigations.

Finally, it is worth mentioning a group of complexes of the NgH^+ with simple molecules such as N_2, CO, SiO, CS, BF, N_2, and H_2O investigated by Ghanty and his coworkers (Jayasekharan and Ghanty, 2008, 2012; Ghosh et al., 2013, 2014; Sirohiwal et al., 2013; Sekhar et al., 2015). The $HNgNH_3^+$ were as well-reported (Gao and Sheng, 2015). The most stable complex between NgH^+ and a ligand L is the Ng-H-L^+, the proton being typically more tightly bound to L (the PA of most molecules is, in fact, higher than that of the Ng atoms). In any case, the thermochemically less stable H-Ng-L^+, best described by the limiting resonance structure $(HNg^+)L$, is bound with respect to $NgH^+ + L$, and kinetically protected toward the fast decomposition into $Ng + LH^+$. Whether these conditions are sufficient for their formation in the outer space is another intriguing question related to the fascinating gas-phase chemistry of cationic noble-gas hydrides.

AUTHOR CONTRIBUTIONS

The author made a direct intellectual contribution to the work.

FUNDING

This work was supported by the Departments of Excellence-2018 Program (Dipartimenti di Eccellenza) of the Italian Ministry of Education, University and Research, DIBAF—Department of University of Tuscia, Project Landscape 4.0—food, wellbeing and environment.

REFERENCES

Asvany, O., Schlemmer, S., Szidarovszky, T., and Császár, A. G. (2019). Infrared signatures of the HHe_n^+ and DHe_n^+ ($n = 3$–6) complexes. *J. Phys. Chem. Lett.* 10, 5325–5330. doi: 10.1021/acs.jpclett.9b01911

Bailleux, S., Bogey, M., Bolvin, H., Civiš, S., Cordonnier, M., Krupnov, A. F., et al. (1998). Sub-Millimeter-Wave spectroscopy of the $Ar{\cdot}H_3^+$ and $Ar{\cdot}D_3^+$ ionic complexes. *J. Mol. Spectrosc.* 190, 130–139. doi: 10.1006/jmsp.1998.7564

Barlow, M. J., Swinyard, B. M., Owen, P. J., Cernicharo, J., Gomez, H. L., Ivison, R. J., et al. (2013). Detection of a noble gas molecular ion, $^{36}ArH^+$, in the Crab nebula. *Science* 342, 1343–1345. doi: 10.1126/science.1243582

Bartl, P., Leidlmair, C., Denifl, S., Scheier, P., and Echt, O. (2013). Cationic complexes of hydrogen with helium. *ChemPhysChem* 14, 227–232. doi: 10.1002/cphc.201200664

Bedford, D. K., and Smith, D. (1990). Variable-temperature selected ion flow tube studies of the reactions of $Ar^{+\cdot}$, $Ar_2^{+\cdot}$. and ArH_n^+ (n = 1-3) with H_2, HD and D_2 at 300 K and 80 K. *Int. J. Mass Spectrom. Ion Processes* 98, 179–190. doi: 10.1016/0168-1176(90)85017-V

Beyer, M., Savchenko, E. V., Niedner-Scatteburg, G., and Bondybey, V. E. (1999). Trihydrogen cation solvated by rare gas atoms: $Rg_nH_3^+$. *J. Chem. Phys.* 110, 11950–11957. doi: 10.1063/1.479134

Bogey, M., Bolvin, H., Demuynck, C., and Destombes, J. L. (1987). High-resolution rotational spectroscopy of weakly bound ionic clusters: ArH_3^+, ArD_3^+. *Phys. Rev. Lett.* 58, 988–991. doi: 10.1103/PhysRevLett.58.988

Bogey, M., Bolvin, H., Demuynck, C., Destombes, J. L., and Van Eijck, B. P. (1988). Tunneling motion in ArH_3^+ and isotopomers from the analysis of their rotational spectra. *J. Chem. Phys.* 88, 4120–4126. doi: 10.1063/1.453819

Bop, C. T., Hammami, K., and Faye, N. A. B. (2017b). Collisional rates based on the first potential energy surface of the NeH^+-He system. *Mon. Not. R. Astron. Soc.* 470, 2911–2917. doi: 10.1093/mnras/stx1369

Bop, C. T., Hammami, K., Niane, A., Faye, N. A. B., and Jaïdane, N. (2017a). Rotational excitation of $^{36}ArH^+$ by He at low temperature. *Mon. Not. R. Astron. Soc.* 465, 1137–1143. doi: 10.1093/mnras/stw2809

Borocci, S., Giordani, M., and Grandinetti, F. (2011). Cationic noble gas hydrides-2: a theoretical investigation on $HNgHNgH^+$ (Ng = Ar, Kr, Xe). *Comput. Theor. Chem.* 964, 318–323. doi: 10.1016/j.comptc.2011.01.018

Borocci, S., Giordani, M., and Grandinetti, F. (2015). Bonding motifs of noble-gas compounds as described by the local electron energy density. *J. Phys. Chem. A* 119, 6528–6541. doi: 10.1021/acs.jpca.5b03043

Cecchi-Pestellini, C., and Dalgarno, A. (1993). Emission of HeH^+ in nebulae. *Astrophys. J.* 413, 611–618.

Chakraborty, A., Giri, S., and Chattaraj, P. K. (2010). Trapping of noble gases (He-Kr) by the aromatic H_3^+ and Li_3^+ species: a conceptual DFT approach. *New J. Chem.* 34, 1936–1945. doi: 10.1039/C0NJ00040J

Coxon, J. A., and Hajigeorgiou, P. G. (1999). Experimental Born-Hoppenheimer potential for the $X^1\sum^+$ ground state of HeH^+: comparison with the *Ab Initio* potential. *J. Mol. Spectrosc.* 193, 306–318. doi: 10.1006/jmsp.1998.7740

Császár, A. G., Szidarovszky, T., Asvany, O., and Schlemmer, S. (2019). Fingerprints of microscopic superfluidity in HHe_n^+ clusters. *Mol. Phys.* 117, 1559–1583. doi: 10.1080/00268976.2019.1585984

Fárník, M., and Toennies, J. P. (2005). Ion-molecule reactions in ^{4}He droplets: flying nano-cryo-reactors. *J. Chem. Phys.* 122, 014307. doi: 10.1063/1.1815272

Feldman, V. I., Ryazantsev, S. V., Saenko, E. V., Kameneva, S. V., and Shiryaeva, E. S. (2016). Matrix isolation model studies on the radiation-induced transformations of small molecules of astrochemical and atmospheric interest. *Radiat. Phys. Chem.* 124, 7–13. doi: 10.1016/j.radphyschem.2015.12.005

Fortenberry, R. C. (2017). Rovibrational characterization and interstellar implications of the proton-bound, noble gas complexes: $ArHAr^+$, $NeHNe^+$, and $ArHNe^+$. *ACS Earth Space Chem.* 1, 60–69. doi: 10.1021/acsearthspacechem.7b00003

Fortenberry, R. C. (2019). The oldest molecular ancestor finally brought into the light. *Chem* 5, 1028–1030. doi: 10.1016/j.chempr.2019.04.016

Fridgen, T. D., and Parnis, J. M. (1998a). Electron bombardment matrix isolation of Rg/Rg'/methanol mixtures (Rg = Ar, Kr, Xe): fourier-transform infrared characterization of the proton-bound dimers Kr_2H^+, Xe_2H^+, $(ArHKr)^+$ and $(ArHXe)^+$ in Ar matrixes and $(KrHXe)^+$ and Xe_2H^+ in Kr matrixes. *J. Chem. Phys.* 109, 2155–2161. doi: 10.1063/1.476728

Fridgen, T. D., and Parnis, J. M. (1998b). Density functional theory study of the proton-bound rare-gas dimers Rg_2H^+ and $(RgHRg')^+$ (Rg = Ar, Kr, Xe): interpretation of experimental matrix isolation infrared data. *J. Chem. Phys.* 109, 2162–2168. doi: 10.1063/1.476729

Gao, K., and Sheng, L. (2015). Theoretical investigation of $HNgNH_3^+$ ions (Ng = He, Ne, Ar, Kr, and Xe). *J. Chem. Phys.* 142:144301. doi: 10.1063/1.4916648

Gatchell, M., Martini, P., Kranabetter, L., Rasul, B., and Scheier, P. (2018). Magic sizes of cationic and protonated argon clusters. *Phys. Rev. A* 98:022519. doi: 10.1103/PhysRevA.98.022519

Gatchell, M., Martini, P., Schiller, A., and Scheier, P. (2019). Protonated clusters of neon and krypton. *J. Am. Soc. Mass Spectrom.* 30, 2632–2636. doi: 10.1021/jasms.8b06284

Ghosh, A., Manna, D., and Ghanty, T. K. (2013). Theoretical prediction of rare gas inserted hydronium ions: $HRgOH_2^+$. *J. Chem. Phys.* 138:194308. doi: 10.1063/1.4804623

Ghosh, A., Manna, D., and Ghanty, T. K. (2014). Theoretical prediction of noble gas inserted thioformyl cations: $HNgCS^+$ (Ng = He, Ne, Ar, Kr, and Xe). *J. Phys. Chem. A* 119, 2233–2243. doi: 10.1021/jp5042266

Giese, C. F., and Maier, W. B., II. (1961). Ion-molecule reactions studied with mass analysis of primary ion beam. *J. Chem. Phys.* 35, 1913–1914. doi: 10.1063/1.1732184

Giju, K. T., Roszak, S., and Leszczynski, J. (2002). A theoretical study of protonated argon clusters: Ar_nH^+ (n = 1-7). *J. Chem. Phys.* 117, 4803–4809. doi: 10.1063/1.1485956

Grandinetti, F. (2011). Gas-phase ion chemistry of the noble gases: recent advances and future perspectives. *Eur. J. Mass Spectrom.* 17, 423–463. doi: 10.1255/ejms.1151

Grandinetti, F. (2018). *Noble Gas Chemistry, Structure, Bonding, and Gas-Phase Chemistry*. Weinheim: Wiley, VCH.

Gruet, S., and Pirali, O. (2019). Far-infrared spectroscopy of heavy protonated noble gas species using synchrotron radiation. *Mol. Phys.* 117, 1719–1731. doi: 10.1080/00268976.2018.1564851

Güsten, R., Wiesemeyer, H., Neufeld, D., Menten, K. M., Graf, U. U., Jacobs, K., et al. (2019). Astrophysical detection of the helium hydride ion HeH^+. *Nature* 568, 357–362. doi: 10.1038/s41586-019-1090-x

Havemann, U., Pacák, V., Herman, Z., Schneider, F., Zuhrt, C., and Zülicke, L. (1978). Dissociation in collisions of H_2^+ with He in the eV region. crossed-beam experiments and quasi-classical trajectory calculations. *Chem. Phys.* 28, 147–54. doi: 10.1016/0301-0104(78)85045-9

Hiraoka, K., and Mori, T. (1989). Isotope effect and nature of bonding in the cluster ions $H_3^+(Ar)_n$ and $D_3^+(Ar)_n$. *J. Chem. Phys.* 91, 4821–4826. doi: 10.1063/1.456720

Hogness, T. R., and Lunn, E. G. (1925). The ionization of hydrogen by electron impact as interpreted by positive ray analysis. *Phys. Rev.* 26, 44–55. doi: 10.1103/PhysRev.26.44

Hu, M., Xu, W., Liu, X., Tan, R., and Li, H. (2013). Time-dependent quantum wave packet study of the $Ar + H_2^+ \rightarrow ArH^+ + H$ reaction on a new *ab initio* potential energy surface for the ground electronic state ($^{12}A'$). *J. Chem. Phys.* 138:174305. doi: 10.1063/1.4803116

Hvistendahl, G., Saastad, O. W., and Uggerud, E. (1990). Ion/molecule reactions in a mixture of Ar and H_2: high pressure mass spectrometry and quantum chemical calculations. *Int. J. Mass Spectrom. Ion Processes* 98, 167–177. doi: 10.1016/0168-1176(90)85016-U

Jaksch, S., da Silva, F. F., Denifl, S., Echt, O., Märk, T. D., and Scheier, P. (2009). Experimental evidence for the existence of an electronically excited state of the proposed dihydrogen radical cation He-H-H-He^+. *Chem. Eur. J.* 15, 4190–4194. doi: 10.1002/chem.200802545

Jašik, J., Žabka, J., Roithová, J., and Gerlich, D. (2013). Infrared spectroscopy of trapped molecular dications below 4 K. *Int. J. Mass Spectrom.* 354-355, 204–210. doi: 10.1016/j.ijms.2013.06.007

Jayasekharan, T., and Ghanty, T. K. (2008). Theoretical prediction of $HRgCO^+$ ion (Rg = He, Ne, Ar, Kr, and Xe). *J. Chem. Phys.* 129:184302. doi: 10.1063/1.3008057

Jayasekharan, T., and Ghanty, T. K. (2012). Theoretical investigation of rare gas hydride cations: $HRgN_2^+$ (Rg = He, Ar, Kr, and Xe). *J. Chem. Phys.* 136:164312. doi: 10.1063/1.4704819

Kaczorowska, M., Roszak, S., and Leszczynski, J. (2000). The structure and properties of $H_3^+Ar_n$ (n = 1-9) cations. *J. Chem. Phys*. 113, 3615–3620. doi: 10.1063/1.1287831

Kim, S. T., and Lee, J. S. (1999). *Ab initio* study of He_2H^+ and Ne_2H^+: accurate structure and energetics. *J. Chem. Phys*. 110, 4413–4418. doi: 10.1063/1.478324

Kojima, T. M., Kobayashi, N., and Kaneko, Y. (1992). Formation of helium cluster ions HHe_x^+ ($x \leq 14$) and $H_3He_x^+$ ($x \leq 13$) in a very low temperature drift tube. *Z. Phys. D –Atoms Mol. Clust.* 23, 181–185. doi: 10.1007/BF01436742

Koner, D., Vats, A., Vashishta, M., and Panda, A. N. (2012). Ab initio electronic structure investigation of protonated mixed rare gas dimers $[NeHHe]^+$, $[ArHHe]^+$ and $[ArHNe]^+$. *Comput. Theor. Chem*. 1000, 19–25. doi: 10.1016/j.comptc.2012.09.004

Koner, D., Veliz, J. C. S. V., van der Avoird, A., and Meuwly, M. (2019). Near dissociation states for H_2^+-He on MRCI and FCI potential energy surfaces. *Phys. Chem. Chem. Phys*. 21, 24976–24983. doi: 10.1039/C9CP05259C

Koyanagi, G. K., Lavrov, V. V., Baranov, V., Bandura, D., Tanner, S., McLaren, J. W., et al. (2000). A novel inductively coupled plasma/selected-ion flow tube mass spectrometer for the study of reactions of atomic and atomic oxide ions. *Int. J. Mass Spectrom*. 194, L1–L5. doi: 10.1016/S1387-3806(99)00233-X

Krapp, A., Frenking, G., and Uggerud, E. (2008). Nonpolar dihydrogen bonds - on a gliding scale from weak dihydrogen interaction to covalent H-H in symmetric radical cations $[H_nE\text{-}H\text{-}H\text{-}EH_n]^+$. *Chem. Eur. J.* 14, 4028–2038. doi: 10.1002/chem.200701613

Kunttu, H., Seetula, J., Rasanen, M., and Apkarian, V. A. (1992). Photogeneration of ions via delocalized charge transfer states. I. Xe_2H^+ and Xe_2D^+ in solid Xe. *J. Chem. Phys.* 96, 5630–5635. doi: 10.1063/1.462687

Kunttu, H. M., and Seetula, J. A. (1994). Photogeneration of ionic species in Ar, Kr and Xe matrices doped with HCl, HBr and HI. *Chem. Phys*. 189, 273–292. doi: 10.1016/0301-0104(94)00273-8

Liu, X., Liu, H., and Zhang, Q. (2011). An ab initio potential energy surface and dynamics of the $Ar + H_2^+ \rightarrow ArH(^+) + H$ reaction. *Chem. Phys. Lett*. 507, 24–28. doi: 10.1016/j.cplett.2011.03.021

Lundberg, L., Bartl, P., Leidlmar, C., Scheier, P., and Gatchell, M. (2020). Protonated and cationic helium clusters. *Molecules* 25:1066. doi: 10.3390/molecules25051066

Lundell, J. (1995). Density functional approach on ground state RgH^+ and $RgHRg^+$ (Rg = Ar, Kr, Xe) ions. *J. Mol. Struct*. 355, 291–297. doi: 10.1016/0022-2860(95)08916-J

Lundell, J., Pettersson, M., and Räsänen, M. (1999). The proton-bound rare gas compounds $(RgHRg')^+$ (Rg = Ar, Kr, Xe) - a computational approach. *Phys. Chem. Chem. Phys*. 1, 4151–4155. doi: 10.1039/A904242C

McCarthy, M. C., and Thaddeus, P. (2010). High-resolution rotational spectroscopy of $NNOH^+$, DCS^+, $Ar\cdots D_3^+$, $Ar\cdots DCO^+$, and $Ar\cdots HN_2^+$. *J. Mol. Spectrosc*. 263, 71–77. doi: 10.1016/j.jms.2010.06.006

McDonald, D. C. II, Mauney, D. T., Leicht, D., Marks, J. H., Tan, J. A., Kuo, J.-L., et al. (2016). Communication: trapping a proton in argon: spectroscopy and theory of the proton-bound argon dimer and its solvation. *J. Chem. Phys*. 145:231101. doi: 10.1063/1.4972581

Mousis, O., Pauzat, F., Ellinger, Y., and Ceccarelli, C. (2008). Sequestration of noble gases by H_3^+ in protoplanetary disks and outer solar system composition. *Astrophys. J*. 673, 637–646. doi: 10.1086/523925

Müller, H. S. P., Muller, S., Schilke, P., Bergin, E. A., Black, J. H., Gerin, M., et al. (2015). Detection of extragalactic argonium, ArH^+, toward PKS 1830-211. *Astron. Astrophys*. 582, L4. doi: 10.1051/0004-6361/201527254

National Institute of Standards and Technology (2020) *NIST Chemistry WebBook, NIST Standard Reference Database Number*. eds P. J. Linstrom and W. G. Mallard (Gaithersburg, MD: National Institute of Standards and Technology).

Papp, D., Császár, A. G., Yamanouchi, K., and Szidarovszky, T. (2018). Rovibrational resonances in H_2He^+. *J. Chem. Theory Comput*. 14, 1523–1533. doi: 10.1021/acs.jctc.7b01136

Papp, D., Szidarovszky, T., and Császár, A. G. (2017). A general variational approach for computing rovibrational resonances of polyatomic molecules. application to the weakly bound H_2He^+ and H_2·CO systems. *J. Chem. Phys.* 147:094106. doi: 10.1063/1.5000680

Pauzat, F., Bacchus-Montabonel, M.-C., Ellinger, Y., and Mousis, O. (2016). Trapping of noble gases by radiative association with H_3^+ in the protosolar nebula. *Astrophys. J. Lett*. 821:L33. doi: 10.3847/2041-8205/821/2/L33

Pauzat, F., and Ellinger, Y. (2005). H_3^+ as a trap for noble gases: 1- the case of argon. *Planet. Space Sci*. 53, 1389–1399. doi: 10.1016/j.pss.2005.07.005

Pauzat, F., and Ellinger, Y. (2007). H_3^+ as a trap for noble gases-2: structure and energetics of XH_3^+ complexes from X = neon to xenon. *J. Chem. Phys*. 127:014308. doi: 10.1063/1.2746033

Pauzat, F., Ellinger, Y., Mousis, O., Dib, M. A., and Ozgurel, O. (2013). Gas-phase sequestration of noble gases in the protosolar nebula: possible consequences on the outer solar system composition. *Astrophys. J*. 777:29. doi: 10.1088/0004-637X/777/1/29

Pauzat, F., Ellinger, Y., Pilmé, J., and Mousis, O. (2009). H_3^+ as a trap for noble gases-3: multiple trapping of neon, argon, and krypton in $X_nH_3^+$ (n = 1-3). *J. Chem. Phys*. 130:174313. doi: 10.1063/1.3126777

Perry, A. J., Hodges, J. N., Markus, C. R., Kocheril, G. S., and McCall, B. J. (2014). Communication: high precision sub-Doppler infrared spectroscopy of the HeH^+ ion. *J. Chem. Phys*. 141:101101. doi: 10.1063/1.4895505

Rayleigh, and Ramsay, W. (1895). Argon, a new constituent of the atmosphere. *Philos. Trans. R. Soc. London A* 186, 187–241.

Ritschel, T., Kuntz, P. J., and Zülicke, L. (2005). Structure and dynamics of cationic van-der-Waals clusters. *Eur. Phys J.* 33, 421–432. doi: 10.1140/epjd/e2005-00070-4

Ritschel, T., Zuelicke, L., and Kuntz, P. J. (2004). Cationic van-der-Waals complexes: Theoretical study of Ar_2H^+ structure and stability. *Z. Phys. Chem*. 218, 377–390. doi: 10.1524/zpch.218.4.377.29196

Ritschel, T., Zuhrt, C., Zülicke, L., and Kuntz, P. J. (2007). Structure and dynamics of cationic van-der-Waals clusters. *Eur. Phys J. D* 41, 127–141. doi: 10.1140/epjd/e2006-00191-2

Roberge, W., and Dalgarno, A. (1982). The formation and destruction of HeH^+ in astrophysical plasmas. *Astrophys. J*. 255, 489–496.

Rodríguez-Cantano, R., Bartolomei, M., Hernández, M. I., Campos-Martínez, J., González-Lezana, T., Villarreal, P., et al. (2017). Comparative investigation of pure and mixed rare gas atoms on coronene molecules. *J. Chem. Phys*. 146:034302. doi: 10.1063/1.4973890

Rogers, S. A., Brazier, C. R., and Bernath, P. F. (1987). The infrared spectrum of XeH^+. *J. Chem. Phys*. 87, 159–162. doi: 10.1063/1.453611

Saenko, E. V., and Feldman, V. I. (2016). Radiation-induced transformations of methanol molecules in low-temperature solids: a matrix isolation study. *Phys. Chem. Chem. Phys*. 18, 32503–32513. doi: 10.1039/c6cp06082j

Savić, I., Gerlich, D., Asvany, O., Jusko, P., and Schlemmer, S. (2015). Controlled synthesis and analysis of He-H_3^+ in a 3.7 K ion trap. *Mol. Phys*. 113, 2320–2332. doi: 10.1080/00268976.2015.1037802

Schilke, P., Neufeld, D. A., Müller, H. S. P., Comito, C., Bergin, E. A., Lis, D. C., et al. (2014). Ubiquitous argonium (ArH^+) in the diffuse interstellar medium: a molecular tracer of almost purely atomic gas. *Astron. Astrophys*. 566:A29. doi: 10.1051/0004-6361/201423727

Schneider, F., Havemann, U., Zülicke, L., Pacák, V., Birkinshaw, K., and Herman, Z. (1976). Dynamics of the reaction H_2^+(He;H)HeH^+. comparison of beam experiments with quasi-classical trajectory studies. *Chem. Phys. Lett*. 37, 323–328. doi: 10.1016/0009-2614(76)80225-4

Sekhar, P., Ghosh, A., and Ghanty, T. K. (2015). Noble gas inserted protonated silicon monoxide cations: $HNgOSi^+$ (Ng = He, Ne, Ar, Kr, and Xe). *J. Phys. Chem. A* 119, 11601–11613. doi: 10.1021/acs.jpca.5b09018

Sirohiwal, A., Manna, D., Ghosh, A., Jayasekharan, T., and Ghanty, T. K. (2013). Theoretical prediction of rare gas containing hydride cations: $HRgBF^+$ (Rg = He, Ar, Kr, and Xe). *J. Phys. Chem. A* 117, 10772–10782. doi: 10.1021/jp4064824

Stephan, C. J., and Fortenberry, R. C. (2017). The interstellar formation and spectra of the noble gas, proton-bound $HeHHe^+$, $HeHNe^+$ and $HeHAr^+$ complexes. *Mon. Not. R. Astron. Soc*. 469, 339–346. doi: 10.1093/mnras/stx937

Stevenson, D. P. (1957). Ion-molecule reactions. *J. Phys. Chem*. 61, 1453–1456. doi: 10.1021/j150557a001

Szidarovszky, T., and Yamanouchi, K. (2017). Full-dimensional simulation of the laser-induced alignment dynamics of H_2He^+. *Mol. Phys*. 115, 1916–1926. doi: 10.1080/00268976.2017.1297863

Tan, J. A., and Kuo, J.-L. (2019). A theoretical study on the infrared signatures of proton-bound rare gas dimers (Rg–H^+-Rg), Rg = {Ne, Ar, Kr, and Xe}. *J. Chem. Phys*. 150:124305. doi: 10.1063/1.5090031

Theis, R. A., and Fortenberry, R. C. (2015). Trihydrogen cation with neon and argon: structural, energetic, and spectroscopic data from quartic

force fields. *J. Phys. Chem. A* 119, 4915–4922. doi: 10.1021/acs.jpca.5b03058

Theis, R. A., Morgan, W. J., and Fortenberry, R. C. (2015). ArH_2^+ and NeH_2^+ as global minima in the $Ar^+/Ne^+ + H_2$ reactions: energetic, spectroscopic, and structural data. *Mon. Not. R. Astron. Soc.* 446, 195–204. doi: 10.1093/mnras/stu1785

Tsuge, M., Kalinowski, J., Gerber, R. B., and Lee, Y.-P. (2015). Infrared identification of proton-bound rare-gas dimers $(XeHXe)^+$, $(KrHKr)^+$, and $(KrHXe)^+$ and their deuterated species in solid hydrogen. *J. Phys. Chem. A* 119, 2651–2660. doi: 10.1021/jp5097037

Conflict of Interest: The author declares that the research was conducted in the absence of any commercial or financial relationships that could be construed as a potential conflict of interest.

frontiers in Chemistry

ORIGINAL RESEARCH
published: 03 July 2020
doi: 10.3389/fchem.2020.00566

Changes in Structure and Reactivity of Ng_2 Encapsulated in Fullerenes: A Density Functional Theory Study

Meng Li[1], Xin He[1], Bin Wang[1], Dongbo Zhao[2], Chunying Rong[1], Pratim K. Chattaraj[3] and Shubin Liu[4]**

[1] Department of Chemistry, College of Chemistry and Chemical Engineering, Hunan Normal University, Changsha, China, [2] School of Chemistry and Chemical Engineering, Nanjing University, Nanjing, China, [3] Department of Chemistry and Center for Theoretical Studies, Indian Institute of Technology, Kharagpur, India, [4] Research Computing Centre, University of North Carolina, Chapel Hill, NC, United States

Noble gas can be no noble in certain situations from the perspective of structure, bonding, and reactivity. These situations could be extreme experimental conditions or others. In this contribution, we systematically investigate the impact of fullerene encapsulation on molecular structure and chemical reactivity of noble gas dimers (Ng_2) in a few fullerene molecules. To that end, we consider He_2, Ne_2, and Ar_2 dimers encapsulated in C_{50}, C_{60}, and C_{70} fullerenes. We unveil that bond distances of Ng_2 inside fullerene become substantially smaller and noble gas atoms become more electrophilic. In return, these noble gas dimers make fullerene molecules more nucleophilic. Using analytical tools from density functional theory, conceptual density functional theory, and information-theoretic approach, we appreciate the nature and origin of these structure and reactivity changes. The results and conclusions from this work should provide more new insights from the viewpoint of changing the perspectives of noble gas reactivity.

Keywords: noble gas dimer, fullerene, density functional theory, information-theoretic approach, encapsulation

OPEN ACCESS

Edited by:
Yong Wang,
Ningbo University, China

Reviewed by:
Cina Foroutan-Nejad,
Masaryk University, Czechia
Joshua Schrier,
Fordham University, United States
Said Jalife,
University of Oxford, United Kingdom

***Correspondence:**
Chunying Rong
rongchunying@aliyun.com
Shubin Liu
shubin@email.unc.edu

Specialty section:
This article was submitted to Theoretical and Computational Chemistry, a section of the journal Frontiers in Chemistry

Received: *24 February 2020*
Accepted: *02 June 2020*
Published: *03 July 2020*

Citation:
Li M, He X, Wang B, Zhao D, Rong C, Chattaraj PK and Liu S (2020) Changes in Structure and Reactivity of Ng_2 Encapsulated in Fullerenes: A Density Functional Theory Study. Front. Chem. 8:566. doi: 10.3389/fchem.2020.00566

INTRODUCTION

Regarded as the most unreactive elements in the periodic table, noble gas atoms could indeed be reactive and no noble at all under certain circumstances, [e.g., high temperature, high pressure, special conditions (e.g., confinement, etc.)]. The first successful experimental realization was the synthesis of xenon hexafluoro platinate $XePtF_6$ in 1962 (Bartlett, 1962; Graham et al., 2000). Since then many more compounds with noble gas elements included have been reported (Turner and Pimentel, 1963; Nelson and Pimentel, 1967; Bondybey, 1971; Stein, 1973; Holloway and Hope, 1999) and a brand new discipline of noble gas chemistry has emerged thereafter.

In this contribution, we explore the possibility of fullerene encapsulation as another feasible way to make noble gas elements no longer noble. In specific, we consider the impact of the encapsulation by fullerene molecules on geometrical structure and chemical reactivity for noble gas species. Previously, by heating fullerenes at 650°C under 3,000 atmosphere, helium (Saunders et al., 1993), neon (Saunders et al., 1993), argon (DiCamillo et al., 1996), krypton (Yamamoto et al., 1999), and xenon (Syamala et al., 2002) noble gas atoms were experimentally introduced into the fullerene cage. This experimental realization of fullerene encapsulation demonstrates the feasibility, and there were reports of experimental realization of noble gas dimers encapsulation in fulerenes (Saunders et al., 1996; Laskin et al., 1998; Peres et al., 2001; Popov et al., 2013; Saha et al., 2019).

Also, earlier, Krapp and Frenking performed a computational study on $Ng_2@C_{60}$ (Ng = He, Ne, Ar, Kr, and Xe) systems from the bonding perspective and concluded that $He_2@C_{60}$ and $Ne_2@C_{60}$ were weakly bonded van der Waals complexes (Krapp and Frenking, 2007). On the other hand, Solà et al. explored the same systems from the reactivity perspective and they attributed the changes in reactivity to the stabilized LUMO, increased fullerene strain energy, and compressed Ng_2 unit (Osuna et al., 2009). There are other theoretical and computational studies on the encapsulation of either noble gas or other species in the literature (Osuna et al., 2011; Cheng and Sheng, 2013; Dolgonos and Peslherbe, 2014; Khatua et al., 2014; Bickelhaupt et al., 2015; Kryachko et al., 2015; Nikolaienko and Kryachko, 2015; Jalife et al., 2016; Srivastava et al., 2016; Nikolaienko et al., 2017; Foroutan-Nejad et al., 2018; Jaroš et al., 2018; Gómez and Restrepo, 2019; Das et al., 2020).

In this work, we reconsider the likelihood of these species from the computational perspective using a few newly developed theoretical tools. To that end, we examine noble gas dimers, He_2, Ne_2, and Ar_2, inside a few fullerene systems, C_{50}, C_{60}, and C_{70}, as illustrative examples in this work. In addition, to pinpoint the nature and origin of these structure and reactivity changes, we make use of a few analytical tools available in the literature, including density functional theory, conceptual density functional theory, information-theoretic approach, energy decomposition analysis, bonding energy analysis, natural population analysis, and noncovalent interaction analysis. In information theory, Shannon introduced a measure of information content or a lack of it as an entropy through an analogy with the statistical mechanical variant of thermodynamic entropy as proposed by Boltzmann. Hence the stability of a system and spontaneous evolution toward an equilibrium state can be understood by following the variation of the entropy during the thermodynamic process. These analyses should provide better understanding from the viewpoint of changing the perspectives of noble gas reactivity.

COMPUTATIONAL DETAILS

Models

Nine model systems were built to examine the impact of fullerene encapsulation on structure and reactivity properties for noble gas dimers (Ng_2) using three fullerenes C_{50}, C_{60}, and C_{70} and three Ng_2 species, He_2, Ne_2, and Ar_2. They are represented by following notations: $He_2@C_{50}$, $He_2@C_{60}$, $He_2@C_{70}$, $Ne_2@C_{50}$, $Ne_2@C_{60}$, $Ne_2@C_{70}$, $Ar_2@C_{50}$, $Ar_2@C_{60}$, and $Ar_2@C_{70}$. Also, as the reference, the structural and reactivity properties of these three fullerene molecules and three Ng_2 dimers in vacuum were also simulated and compared.

Analyses

Structure, bonding and reactivity properties for these species were analyzed through a number of well-established analytical tools available in the literature. They include analyses of the total energy decomposition (Parr and Yang, 1989; Liu, 2007), interaction energy decomposition (Bickelhaupt and Baerends, 2000), natural population (Glendening et al., 2012), non-covalent interactions (Johnson et al., 2010), conceptual density functional theory (Geerlings et al., 2003, 2020; Liu, 2009, 2013), and informational-theoretic approach (Liu, 2016; Rong et al., 2019). These analyses enable in-depth understanding about the origin and nature of the changes in structure, bonding, and reactivity. Formulations as well as the details of how to perform these analyses are available elsewhere.

Methodologies

Structure optimizations and natural population analyses were performed with the Gaussian 16 (Frisch et al., 2016) package (versionA03), with ultrafine integration grids and tight self-consistent field (SCF) convergence. To obtain the most stable orientation of Ng_2 dimer in a fullerene cage, quantum molecular dynamics simulations were performed for each species at the DFT B3LYP/3-21G (Lee et al., 1988; Becke, 1993) level of theory at 3,000 K for 300 ps with a step size of 1 fs. A total of 20 structures with the lowest total energy were selected as the possible structure candidates from the trajectory and then optimized at the DFT M06-2X/6-311G(d) (Zhao and Truhlar, 2008) level of theory. The structure with the lowest total energy from these 20 candidates was selected as the global minimum for the species. The full structure optimization was followed by a single-point frequency calculation to ensure that the final optimized structure has no imaginary frequency. As a measure of quality control, we conducted a benchmark test on the impact of different choices of basis sets and approximate DFT functionals (Ma et al., 2014). The Multiwfn 3.6.1 program (Lu and Chen, 2012) was utilized to calculate the information-theoretic quantities by using the checkpoint file from the Gaussian calculations as the input file. The total energy components were obtained from Gaussian calculations with the keyword of iop(5/33 = 1). The ADF (Amsterdam Density Functional) (Lee et al., 1988) package was employed to perform the bond energy decomposition (BED) analysis. The BED analysis was conducted using the previously optimized structure and the DFT BP86 approximate functional with the double zeta basis set, zero order regular approximation for relativistic correction, and Grimme4 dispersion correction (Te Velde et al., 2001).

RESULTS AND DISCUSSION

Table 1 is the benchmark results using $Ar_2@C_{60}$ as an example with 14 basis sets and 14 DFT functionals as well as HF and MP2 methods to examine their impact on the Ar-Ar bond distance. It is compared with Ar-Ar length in vacuum. As can be seen from the table, the bond length in $Ar2@C_{60}$ is not significantly dependent on the choice of basis sets and functionals, which is unsurprising because the Ng_2 molecule is confined. As a reference, the experimental Ar-Ar length in vacuum is 3.758 Å (Computational Chemistry Comparison Benchmark DataBase, 2019). There are a handful of computational results for the Ar-Ar length (Colburn and Douglas, 1976). In all analyses below, we chose M06-2X/6-311G(d).

Figure 1 shows the final structure obtained for $Ng_2@C_{50}$, $Ng_2@C_{60}$, and $Ng_2@C_{70}$ with both top and side views. With a given fullerene, the binding mode is the same for different

Ng_2 dimers, but for different fullerenes, as shown in **Figure 1**, the same Ng_2 dimer prefers to bind differently. This is not surprising either. This is because, for instance, C_{70} is elongated so the dimer aligns with the long axis, as one would expect from a simple steric argument. These similarity and difference illustrate the fact that the size and nature of fullerene molecules play more important role during the encapsulation process of Ng_2 dimers.

Table 2 exhibits a few selected structural and electronic properties of these species. As can be seen from the table, the bond length of Ng_2 dimers becomes smaller when encapsulated in fullerenes, and the smaller the fullerene cage the shorter the Ng-Ng distance. This latter trend was resulted from the fact that

TABLE 1 | Benchmark tests for Ar_2@C_{60} with 14 basis sets and 14 functionals/methods to examine the impact of the methodology dependence on the Ar-Ar bond distance in both vacuum and C_{60} fullerene.

Basis set	Vacuum	C_{60}	Functional	Vacuum	C_{60}
STO-3G	3.619	2.381	lsda	3.383	2.356
3-21G	3.395	2.388	blyp	5.709	2.376
6-31G(d)	3.971	2.353	b3lyp	6.481	2.359
6-311G(d)	4.039	2.353	pw91pw91	3.835	2.370
6-311G(d,p)	4.039	2.353	cAM-b3lyp	3.823	2.351
6-311+G(d)	4.174	2.352	b3pw91	6.198	2.357
6-311++G(d,p)	4.174	2.352	pbepbe	3.878	2.372
Def2SVPP	3.360	2.352	hseh1pbe	3.905	2.355
Def2TZVP	4.015	2.347	hcth	3.838	2.354
DGDZVP	4.031	2.355	tpsstpss	4.083	2.374
cc-pVDZ	3.741	2.355	ωb97xd	4.147	2.344
cc-pVTZ	4.029	2.349	m06-2x	3.971	2.353
aug-cc-pVTZ	4.041	2.352	hf	4.525	2.338
CBSB7	4.034	2.350	mp2	4.173	2.352

When basis sets were tested, M06-2X functional was employed. When functionals were tested, 6-31G(d) basis set was employed. Units in Å.

TABLE 2 | A few selected structure and electronic properties at the DFT M06-2X/6-311G(d) level of theory for Ng_2 (Ng = He, Ne, and Ar) dimers encapsulated in C_{50}, C_{60}, and C_{70} fullerenes[a].

Ng-Ng	Property	Vacuum	C_{50}	C_{60}	C_{70}
He-He	R (Å)	2.862	1.835	1.984	2.559
	Point group		C_{2v}	D_{3d}	D_{5h}
	E_{int}^{BSSE} (kcal/mol)		−1.47	−4.36	−6.73
	E_{int} (kcal/mol)		−2.42	−5.13	−7.39
	Hirshfeld charge on Ng		0.073	0.056	0.047
	NPA charge on Ng		0.002	0.002	0.002
Ne-Ne	Distance (Å)	2.685	1.971	2.090	2.557
	Point group		C_{2v}	D_{3d}	D_{5h}
	E_{int}^{BSSE} (kcal/mol)		15.12	1.31	−8.13
	E_{int} (kcal/mol)		4.71	−7.15	−15.36
	Hirshfeld charge on Ng		0.127	0.091	0.067
	NPA charge on Ng		0.010	0.009	0.008
Ar-Ar	Distance (Å)	4.041	2.235	2.352	2.667
	Point group		C_{2v}	D_{3d}	D_{5h}
	E_{int}^{BSSE} (kcal/mol)		131.41	53.81	−7.06
	E_{int} (kcal/mol)		126.52	49.91	−10.17
	Hirshfeld charge on Ng		0.180	0.168	0.161
	NPA charge on Ng		−0.047	−0.007	0.003

[a] *R is the bond distance between Ng atoms; E_{int}^{BSSE} and E_{int} are the interaction energy between Ng_2 dimer and the fullerene molecule with and without the BSSE (basis set superposition error) correction considered, respectively; Hirshfeld is the Hirshfeld charge based on the stockholder partition of atoms in molecules; and NPA charge is the electron charged based on the natural population analysis.*

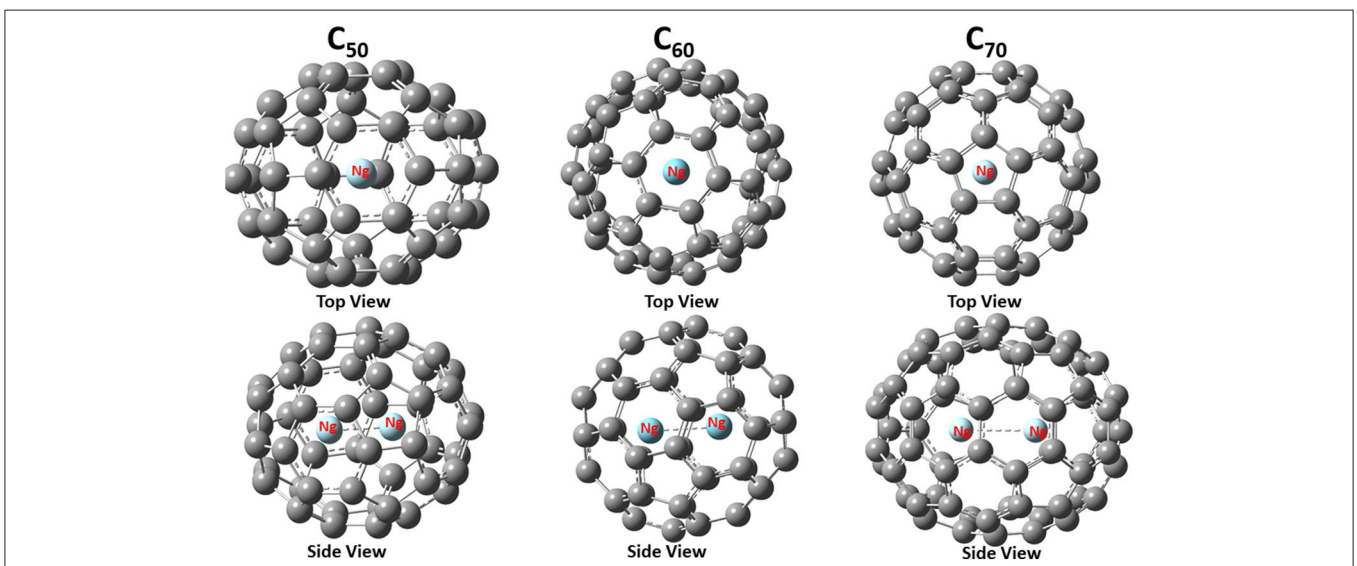

FIGURE 1 | Optimized structures of noble gas dimers encapsulated in fullerene cages with Ng = Ar as an illustrative example. The point group for these three encapsulated systems are C_{2v}, D_{3d}, and D_{5h}, respectively.

a smaller fullerene has a smaller cage inside so Ng_2 dimers are forced to have shorter bond distance. Energetically, both BSSE (basis set superposition error; Boys and Bernardi, 1970; Simon et al., 1996)-corrected and uncorrected interaction energy results show that for He_2, all three fullerene molecules yield negative (favorable) interaction energies, whereas for larger Ng_2 dimers, (e.g., Ne_2 and Ar_2, it appears that only larger-sized fullerenes such as C_{70} are able to yield attractive interactions between Ng_2 and fullerene, albeit with the limitations of the method of computation used). This is because larger Ng_2 dimers tend to occupy more space within the fullerene molecule, making it harder for smaller-sized fullerenes to compensate the energetic cost from electrostatic and other repulsions. We are, however, interested in analyzing the qualitative trends only.

Shown in **Table 2** are two charge results for Ng atoms encapsulated in fullerene molecules. The first one is the NPA (natural population analysis) charge from NBO (natural bond orbital) analysis (Glendening et al., 2012), and the other is the Hirshfeld charge based on the shareholder partition of atoms in molecules (Hirshfeld, 1977). NPA charges for Ng atoms could be either positive or negative, but the Hirshfeld charge value is always positive for Ng atoms. According to the reference literature on the Hirshfeld charge (Liu et al., 2014), which is a good descriptor of electrophilicity and nucleophilicity, a positive Hirshfeld charge is an indication that the atom is electrophilic. The larger value of a positive Hirshfeld charge indicates that it is more electrophilic, able to accept more electrons from a nucleophile. Hirshfeld charge results in **Table 2** displays that Ng_2 in smaller fullerenes tend to be more electrophilic.

Shown in **Figure 2** are frontier molecular orbitals from both top and side views for Ar_2@C_{70} as an illustrative example,

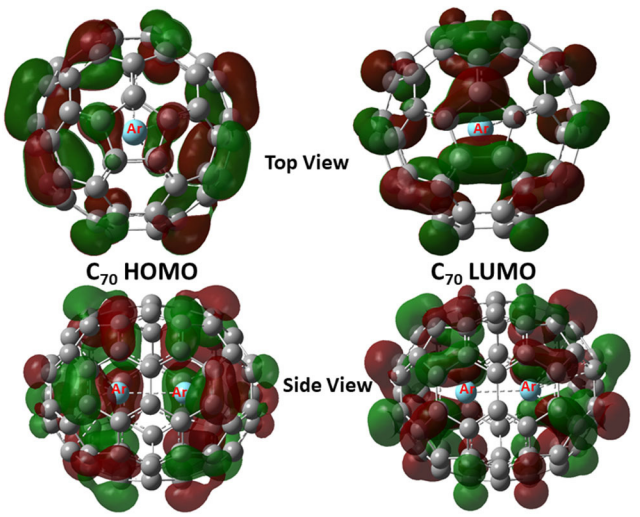

FIGURE 2 | HOMO and LUMO contour surfaces of Ar_2@C_{70} molecule.

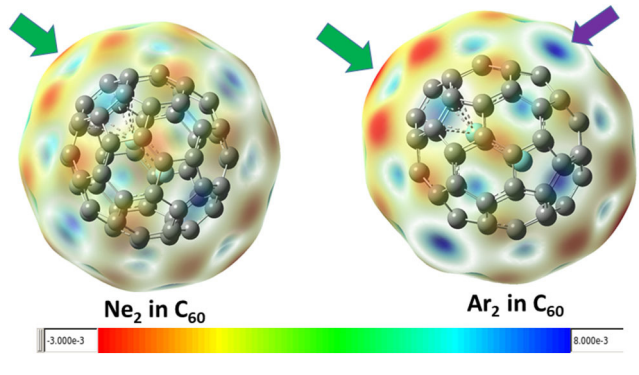

FIGURE 3 | The mapped contour surface of the molecular electrostatic potential onto the van der Waals surface for Ne_2 and Ar_2 dimers encapsulated in C_{60} fullerene.

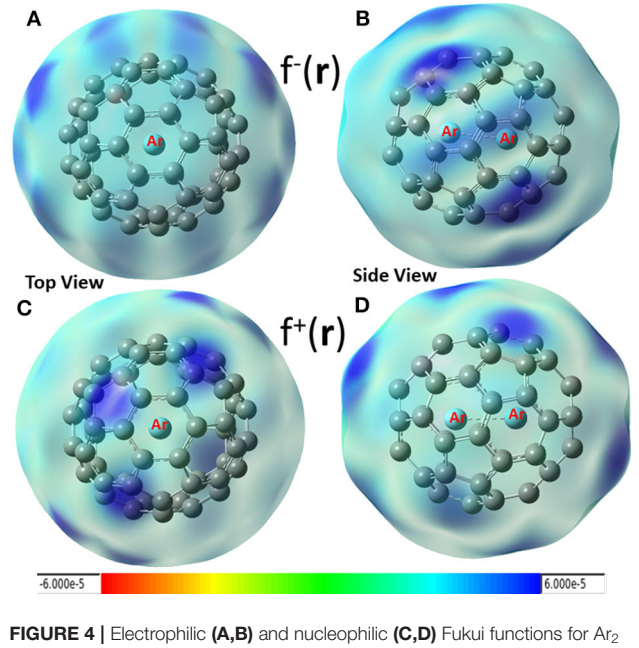

FIGURE 4 | Electrophilic **(A,B)** and nucleophilic **(C,D)** Fukui functions for Ar_2 dimer encapsulated in C_{60} fullerene.

TABLE 3 | Global descriptors from Conceptual DFT, including HOMO, LUMO, chemical potential μ, chemical hardness η, and electrophilicity index ω for the systems studied in this work.

Ng_2	Fullerene	HOMO	LUMO	μ	η	ω
	C_{50}	−0.263	−0.150	−0.206	0.114	0.375
He_2	C_{50}	−0.251	−0.135	−0.193	0.115	0.324
Ne_2	C_{50}	−0.252	−0.136	−0.194	0.116	0.324
Ar_2	C_{50}	−0.256	−0.140	−0.198	0.116	0.337
	C_{60}	−0.280	−0.114	−0.197	0.166	0.234
He_2	C_{60}	−0.266	−0.100	−0.183	0.166	0.201
Ne_2	C_{60}	−0.265	−0.101	−0.183	0.165	0.203
Ar_2	C_{60}	−0.263	−0.105	−0.184	0.158	0.215
	C_{70}	−0.275	−0.116	−0.195	0.158	0.241
He_2	C_{70}	−0.261	−0.102	−0.182	0.159	0.207
Ne_2	C_{70}	−0.261	−0.102	−0.182	0.159	0.207
Ar_2	C_{70}	−0.262	−0.104	−0.183	0.159	0.211

Atomic units.

from which one can see that they are both delocalized over the entire molecule. Notice that in both orbitals, we do not see discernible contributions from the Ng_2 dimer overlapping with any of the atomic orbitals from the fullerene, suggesting that atomic orbitals from Ng atoms are not involved in the frontier molecular orbital delocalization. In **Table 3**, using the information from these frontier orbitals, we calculated a few global reactivity descriptors from conceptual DFT, including chemical potential μ (Parr et al., 1978), chemical hardness η (Parr and Pearson, 1983), and electrophilicity index ω (Parr et al., 1999) for the nine systems studied in this work. A larger value in hardness is usually an indication of being more stable, while a larger value in electrophilicity index suggests that the species is more reactive. From the results in **Table 2**, we can see that numerical values of these reactivity indices are slightly changed after Ng_2 encapsulation. This should be mainly due to the charge transfer between Ng_2 and fullerene. Ng_2 in smaller fullerenes are more reactive with a larger ω value, whereas in larger fullerenes it becomes often more stable with a larger η value. These results agree well with the conventional chemical wisdom.

Figure 3 shows the contour surface of the molecular electrostatic potential mapped onto the van der Waals surface for Ne_2 and Ar_2 dimers encapsulated in C_{60} fullerene. It shows that the carbon atoms perpendicular to the Ng-Ng bond is more electronegative. This result is consistent with our Hirshfeld charge result, showing that Ng atoms become more positive and the neighboring carbon atoms in fullerene become more negative. Since Hirshfeld charges are reliable descriptors of electrophilicity and nucleophilicity, **Figure 3** also shows that carbon atoms of the fullerene molecule become more nucleophilic, capable of donating more electrons to an electrophile.

In conceptual DFT, Fukui functions (Yang et al., 1984) can also be employed as local descriptors to predict nucleophilic and electrophilic attacks. Shown in **Figure 4** are these local functions, where both electrophilic (**Figures 4A,B**) and nucleophilic (**Figures 4C,D**) Fukui functions for Ar_2 dimer encapsulated in C_{60} fullerene are exhibited. From the figure, we found that (i) carbon atoms in fullerene can be both electrophilic (dark blue areas in **Figures 4A,B**) and nucleophilic (dark blue regions in

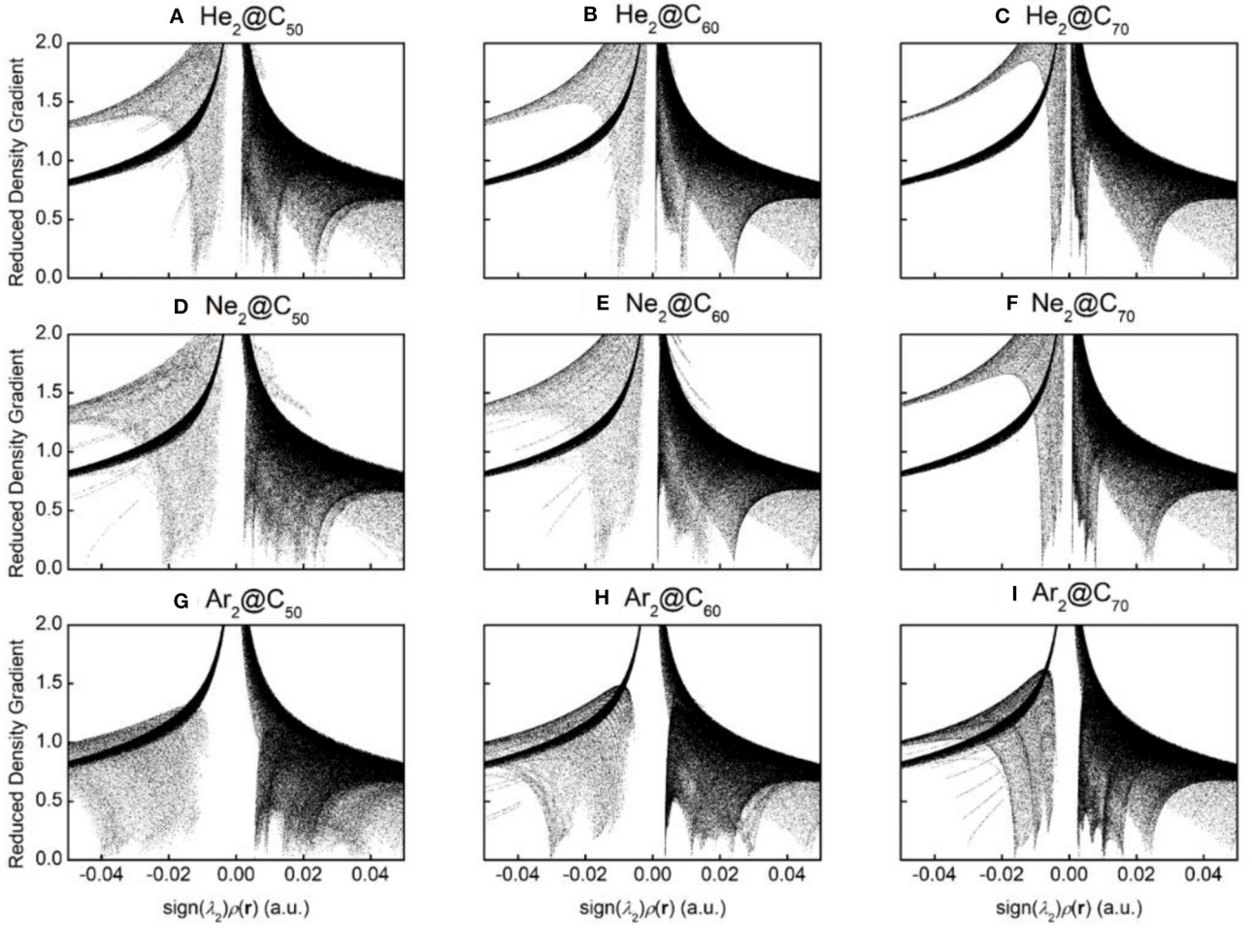

FIGURE 5 | Diagrams of the reduced density gradient (RDG) vs. sign(λ_2)ρ(r) for nine endohedral fullerenes: **(A)** He_2@C50; **(B)** He_2@C60; **(C)** He_2@C70; **(D)** Ne_2@C50; **(E)** Ne_2@C60; **(F)** Ne_2@C70; **(G)** Ar_2@C50; **(H)** Ar_2C60; and **(I)** Ar_2@C70.

Figures 4C,D), and (ii) nucleophilic regions in **Figures 4C,D** are drastically different from those of **Figure 3** (red areas), suggesting that using Hirshfeld charge and Fukui charge, we obtain different results. According our recent findings, this discrepancy is not unusual. As our recent study demonstrated (Wang et al., 2019), results from the Hirshfeld charge should be more robust and reliable. Notice that Krapp and Frenking (2007) also observed that Ng_2 molecules were oxidized inside fullerenes, implying that Ng_2 became more electrophilic in return as electrons were transferred to C_{60}, and this also made fullerenes more nucleophilic. This result was confirmed by Solà et al. (Osuna et al., 2009, 2011), also who unveiled that the combination of the LUMO stabilization, increased fullerene strain energy, and greater compression of the encapsulated Ng_2 contributed to the reactivity change.

To qualitatively identify and distinguish weak interactions between Ng_2 and fullerene molecules, noncovalent interaction (NCI) analysis (Johnson et al., 2010) was employed, whose results are shown in **Figure 5**. The reduced density gradient is large and positive in the regions far from the molecule, but it becomes small in the vicinity of both covalent and non-covalent interactions. To identify different types of interactions, the sign of Laplacian of the density is utilized and compared. Plotting low-gradient isosurfaces subject to a further low-density constraint enables real-space visualization of non-covalent interactions. Results in **Figure 5** show that when He_2 encapsulated from C_{50} to C_{70}, a "spike" area becomes more apparent from −0.02 to 0 a.u., indicating that there existed more attractive interactions within the complexes as the fullerene cage becomes larger. The same trend is also observed for Ne_2 and Ar_2. These results are also in qualitative agreement with the total energy difference result as shown in **Table 2**.

Table 4 is the results from the two schemes (Parr and Yang, 1989; Liu, 2007) of the total energy partition for the nine Ng_2-fullerene systems studied in this work. Different from the traditional binding energy or interaction energy partition, the total energy partition decomposes the total energy E of a molecular system in terms of a few components that are physiochemically meaningful. In DFT (Parr and Yang, 1989), we have $E = T_S + E_{xc} + E_e$, where T_S, E_{xc}, and E_e are the non-interacting kinetic energy, exchange-correlation energy, and electrostatic interaction energy, respectively. An alternative scheme was proposed by one of us (Liu, 2007), where $E = E_S + E_e + E_q$, where E_S, E_e, and E_q stand for the energetic contribution from three physiochemical effects, steric, electrostatic, and quantum (due to the exchange-correlation effects). There is a common component in these two partition schemes, the electrostatic energy E_e. Considering the energy difference ΔE between two chemical processes sharing the same molecular fragments, we have $\Delta E = \Delta T_S + \Delta E_{xc} + \Delta E_e$, and $\Delta E = \Delta E_S + \Delta E_e + \Delta E_q$. **Table 4** shows the values of these five components from the above two partition schemes using Ng_2 and fullerene in vacuum as the reference. From the table, we found that in the first scheme (Parr and Yang, 1989; Liu, 2007), both ΔT_s and ΔE_{xc} contribute positively to $\Delta E < 0$, and it is the electrostatic contribution ΔE_e that contributes negatively to their stability, in order to make $\Delta E < 0$. Since E_e itself is negative in value (Liu, 2007), this result suggests that to put Ng_2 dimer in the fullerene cage, one has to overcome the large electrostatic repulsion between Ng_2 and fullerene. This result is further verified by the second total energy partition scheme (Liu, 2007), where we found that in this case both electrostatic and quantum (due to exchange-correlation effects) contribute negatively to $\Delta E < 0$ but the steric contribution ΔE_S is positive. This result shows that after Ng_2 dimer is put into the cage, smaller space is occupied, but to do so, large electrostatic and Fermionic quantum repulsions have to be overcome. Notice that this total energy difference is different from the BSSE corrected interaction energy in **Table 2** and our present results are consistent with what we observed elsewhere for other systems.

Figure 6 illustrates the total energy partition analysis to elucidate which energy component is dominant over others in contributing to the total energy difference. A strong linear correlation of the total energy difference ΔE with the electrostatic

TABLE 4 | Numerical results of the two total energy partition schemes using Ng_2 and fullerene in vacuum as the references for the nine Ng_2-fullerene systems studied in this work.

Ng_2	Fullerene	ΔE	ΔT_s	ΔE_{xc}	ΔE_e	ΔE_s	ΔE_q
He_2	C_{50}	0.44	−73.19	−11.90	85.57	−357.75	272.66
He_2	C_{60}	−3.66	−56.13	−7.91	60.37	−270.58	206.54
He_2	C_{70}	−7.33	−47.92	−5.54	46.09	−205.288	151.82
Ne_2	C_{50}	14.04	−184.03	−15.31	213.37	−709.51	510.17
Ne_2	C_{60}	−2.50	−125.76	−12.07	135.38	−531.19	393.36
Ne_2	C_{70}	−15.28	−62.23	−11.40	58.32	−379.22	305.59
Ar_2	C_{50}	202.08	−356.45	−11.79	570.33	−1018.14	649.90
Ar_2	C_{60}	97.83	−241.92	−27.79	367.51	−916.08	646.36
Ar_2	C_{70}	0.77	−142.95	−43.29	187.01	−838.78	652.54

Units in kcal/mol.

TABLE 5 | The chemical bonding analysis results using the ADF package to analyze the bond energy between the Ng_2dimer and fullerene fragments.

Ng	Fullerene	ΔE_{Pauli}	ΔE_{steric}	ΔE_{orb}	ΔE_{disp}	ΔE_{elstat}	ΔE_{bond}
He_2	C_{50}	29.65	16.71	−6.10	−5.99	−29.65	4.62
He_2	C_{60}	16.40	8.87	−4.30	−5.55	−16.40	−0.98
He_2	C_{70}	8.25	4.24	−3.03	−5.24	−8.25	−4.03
Ne_2	C_{50}	95.01	43.64	−7.62	−11.36	−95.01	24.66
Ne_2	C_{60}	50.91	21.36	−4.72	−10.98	−50.91	5.66
Ne_2	C_{70}	22.02	7.41	−2.94	−10.60	−22.02	−6.13
Ar_2	C_{50}	431.50	197.82	−31.52	−33.92	−431.49	132.39
Ar_2	C_{60}	244.49	103.07	−19.37	−34.79	−244.50	48.90
Ar_2	C_{70}	103.18	33.17	−11.53	−34.85	−103.18	−13.21

Units in kcal/mol.

The energy decomposition analysis (EDA) in ADF dissects the interactions that constitute a chemical bond between fragments in a molecule. The total bonding energy ΔE_{bond} consists of contributions from the Pauli repulsion ΔE_{Pauli}, steric interaction ΔE_{steric}, electrostatic attraction ΔE_{elstat}, orbital interactions ΔE_{orb}, and dispersion Pauli repulsion ΔE_{disp}, $\Delta E_{bond} = \Delta E_{Pauli} + \Delta E_{steric} + \Delta E_{orb} + \Delta E_{disp} + \Delta E_{elstat}$.

energy difference ΔE_e is shown in **Figure 6A**, suggesting that it is the electrostatic repulsion that dominates the energetic contribution, which agrees well with the numerical results in **Table 4**. If the strategy of two-variable fitting is employed, shown in **Figures 6B,C**, we found that ΔE_e combining with either ΔE_{xc} and ΔE_S yields even stronger correlations, indicating that contributions from the exchange-correlation and steric effects are minor yet indispensable.

To confirm the results in **Tables 4**, **5** shows the total bonding energy ΔE_{bond} analysis (Bickelhaupt and Baerends, 2000) results using the ADF package. In this analysis, ΔE_{bond} consists of contributions from the Pauli repulsion ΔE_{Pauli}, steric interaction ΔE_{steric}, electrostatic attraction ΔE_{elstat}, orbital interactions ΔE_{orb}, and dispersion Pauli repulsion ΔE_{disp}, $\Delta E_{bond} = \Delta E_{Pauli} + \Delta E_{steric} + \Delta E_{orb} + \Delta E_{disp} + \Delta E_{elstat}$. From the results in **Table 5**, it can be seen that the steric effect (even though its definition is substantially different) contributes favorably and the major opposite contribution is from the electrostatic interaction, agreeing well with our results in **Table 4**.

Lastly, we examine the results of eight quantities from the information-theoretic approach, which are shown in **Table 6**, including Shannon entropy (Shannon, 1948), Fisher information (Fisher, 1925), Ghosh-Berkowitz-Parr entropy (Ghosh et al., 1984), information gain (Kullback and Leibler, 1951), 2nd and 3rd orders of absolute Rényi and relative Rényi entropy (Rényi, 1970; Nagy and Romera, 2015). These quantities each have their own physio-chemical meaning and thus representing different

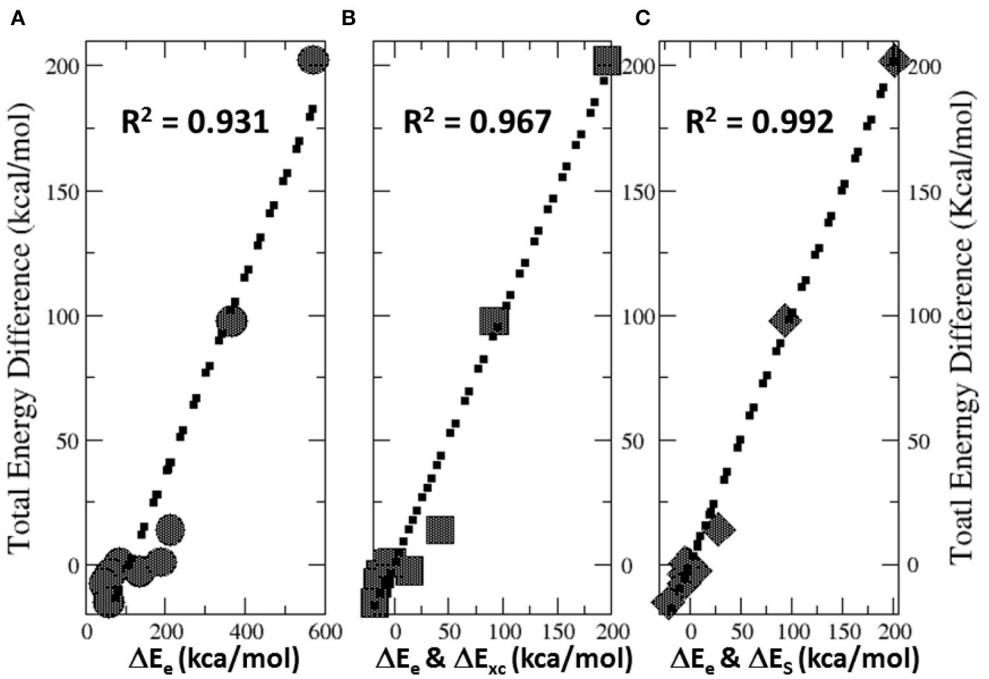

FIGURE 6 | Strong linear correlations of the total energy difference ΔE with **(A)** the electrostatic energy difference ΔE_e, **(B)** two-variable fitting with ΔE_e and ΔE_{xc}, and **(C)** two-variable fitting with ΔE_e and ΔE_S.

TABLE 6 | Numerical results of eight ITA quantities.

Ng	Fullerene	ΔS_s	ΔI_F	ΔS_{GBP}	ΔI_G	ΔR_2	ΔR_3	$\Delta^r R_2$	$\Delta^r R_3$
He_2	C_{50}	−0.674	−4.561	−0.658	−0.035	0.183	0.096	0.596	0.597
He_2	C_{60}	−0.470	−3.450	−0.509	−0.027	0.183	0.096	0.597	0.598
He_2	C_{70}	−0.293	−2.617	−0.390	−0.024	0.183	0.096	0.598	0.598
Ne_2	C_{50}	−0.773	−9.045	−1.003	−0.067	2.448	2.227	1.274	1.275
Ne_2	C_{60}	−0.596	−6.772	−0.774	−0.053	2.461	2.246	1.278	1.279
Ne_2	C_{70}	−0.456	−4.835	−0.573	−0.043	2.470	2.261	1.281	1.282
Ar_2	C_{50}	−1.777	−12.980	−1.943	−0.118	2.979	2.370	1.508	1.510
Ar_2	C_{60}	−1.891	−11.679	−1.864	−0.099	3.025	2.408	1.516	1.517
Ar_2	C_{70}	−1.991	−10.694	−1.848	−0.084	3.062	2.441	1.521	1.523

Atomic units.

TABLE 7 | Correlation coefficients R^2 values between ΔE and eight ITA quantities for three Ng_2 dimers with different fullerene systems (first three rows) and for three fullerenes with different Ng_2 dimers (last three rows).

R^2	ΔS_s	ΔI_F	ΔS_{GBP}	ΔI_G	ΔR_2	ΔR_3	$\Delta^r R_2$	$\Delta^r R_3$
He_2	1.000	0.998	0.999	0.964	0.999	0.874	0.996	0.997
Ne_2	1.000	0.999	0.999	0.999	1.000	1.000	1.000	1.000
Ar_2	0.998	0.997	0.890	0.999	0.998	0.999	0.995	0.995
C_{50}	1.000	0.769	0.960	0.896	0.479	0.357	0.549	0.549
C_{60}	0.995	0.846	0.970	0.888	0.437	0.316	0.500	0.501
C_{70}	0.676	0.498	0.649	0.443	0.040	0.006	0.065	0.066

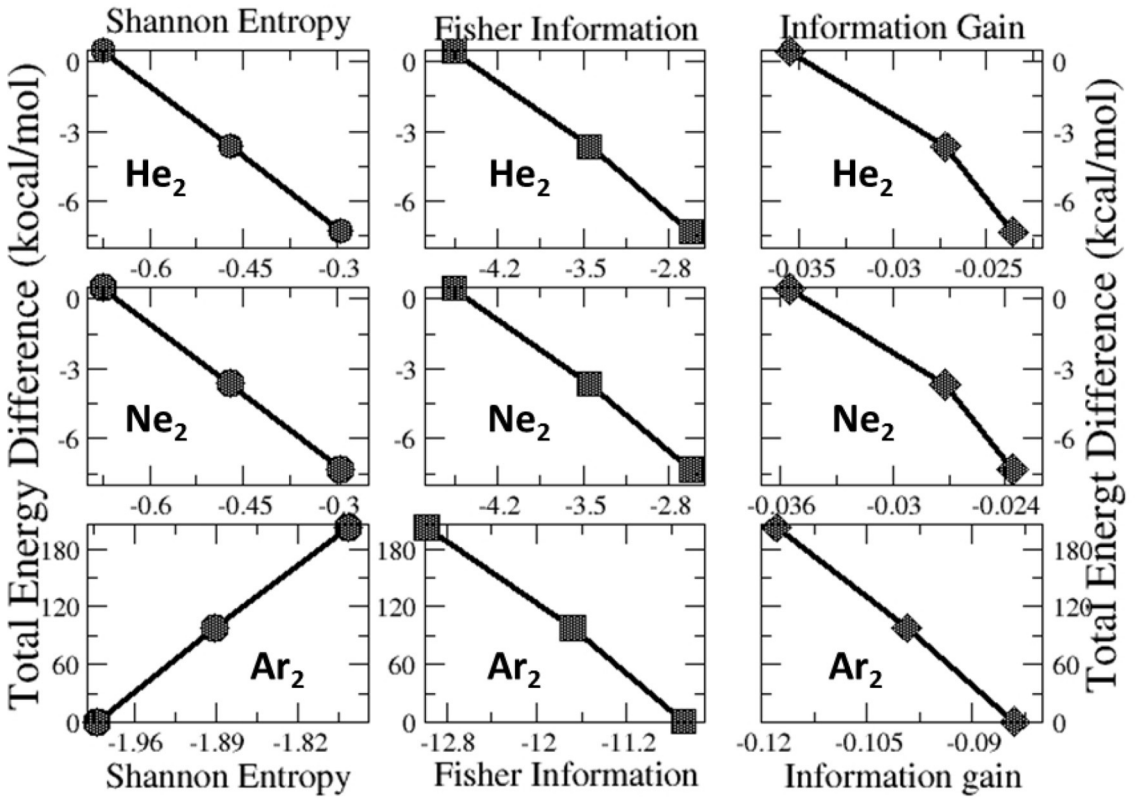

FIGURE 7 | Strong linear relationships of the total energy difference ΔE with ITA quantities such as Shannon entropy, Fisher information, and information gain for He_2, Ne_2, and Ar_2 encapsulated in C_{50}, C_{60}, and C_{70} fullerenes.

yet intrinsic properties of molecular systems. For example, Shannon entropy is a measure of the electron density distribution uniformity, Fisher information gauges the heterogeneity of the same electron density distribution, and information gain is a robust measurement of regioselectivity, electrophilicity, and nucleophilicity, with its first-order approximation yielding the Hirshfeld charge (Liu et al., 2014). To make sense of these ITA results, **Table 7** lists the correlation coefficient of these quantities with respect to either Ng_2 or fullerene types, and **Figure 7** displays illustrative example of strong linear relationships of the total energy difference ΔE with Shannon entropy, Fisher information, and information gain for He_2, Ne_2, and Ar_2 encapsulated in three fullerenes. Strong correlations are seen in most cases, as shown in the figure, but as highlighted in **Table 7**, these strong correlations are true only for Ng_2 dimers cross different fullerenes. If one fits a fullerene with three Ng_2 dimers, no such strong correlation is often observed. Also, we tried to put all data points in one plot, and no significant correlation was observed either. Strong correlations in **Figure 7** show that ITA quantities could be good descriptors of change trends for Ng_2 dimers encapsulated in fullerene cages. For instance, for He_2 encapsulated in from C_{50} to C_{70}, binding energy increases, so does the Shannon entropy, due to the more delocalization of the electron density distribution. Another example is the information gain, which is a direct measure of the Hirshfeld charge. Again, for He_2 dimer, from C_{50} to C_{70},

the difference in information gain decreases, leading to the decrease in Hirshfeld charge, which is in good agreement with the result in **Table 2**. We noticed the abnormality of Shannon entropy for Ar_2 dimer in **Figure 7**, whose trend is opposite to that of He_2 and Ne_2. The reason is unknown. More studies are in need.

CONCLUSIONS

To summarize, in this work, we investigated the possibility of making noble gas reactive through the means of fullerene encapsulation. To that end, we built a total of nine model systems, with three Ng_2 dimers (He_2, Ne_2, and Ar_2) encapsulated in three fullerene (C_{50}, C_{60}, and C_{70}) cages. Quantum molecular dynamics simulations were employed to explore the potential energy surface of Ng_2 inside the fullerene molecule. To obtain the lowest energy structure it was further examined through a few well-established analytical tools such as conceptual density functional theory, information-theoretic approach, total energy decomposition, bonding energy decomposition, and others. Our results show that bond distances of Ng_2 inside fullerene become substantially smaller and noble gas atoms become more electrophilic. In return, these noble gas dimers make fullerene molecules more nucleophilic. Using these analytical tools, we appreciate the nature and origin of these structure and reactivity changes. Our results and conclusions drawn from the present study should provide more understanding and new insights from the viewpoint of changing the perspectives of noble gas reactivity.

DATA AVAILABILITY STATEMENT

The raw data supporting the conclusions of this article will be made available by the authors, without undue reservation, to any qualified researcher.

AUTHOR CONTRIBUTIONS

ML performed the calculations and analyses and prepared the draft. XH and BW helped in calculations and analyses. DZ and CR managed progression of the project. PC initiated the project and revised the draft. SL worked on the plan, assisted the calculations and analyses, and revised the manuscript. All authors contributed to the article and approved the submitted version.

ACKNOWLEDGMENTS

ML and CR acknowledge support from the Excellent Undergraduate Research Fund of Haoqing Experimental Class, Hunan Normal University and the National Natural Science Foundation of China (No. 21503076). PC would like to thank the DST, New Delhi for the J. C. Bose National Fellowship.

REFERENCES

Bartlett, N. (1962). Xenon hexafluoroplatinate(V) Xe+[PtF 6]-. *Proc. Chem. Soc.* 115:218. doi: 10.1039/ps9620000197

Becke, A. D. (1993). Density-functional thermochemistry. III. The role of exact exchange. *J. Chem. Phys*. 98, 5648–5652. doi: 10.1063/1.464913

Bickelhaupt, F. M., and Baerends, E. J. (2000). "Kohn-Sham density functional theory: predicting and understanding chemistry," in *Rev. Comput. Chem.*, eds K. B. Lipkowitz and D. B. Boyd (New York, Ny: Wiley-VCH), 1–86. doi: 10.1002/9780470125922.ch1

Bickelhaupt, F. M., Solà, M., and Fernández, I. (2015). Understanding the reactivity of endohedral metallofullerenes: C_{78} versus $Sc_3N@C_{78}$. *Chem. Eur. J.* 21, 5760–5768. doi: 10.1002/chem.201500067

Bondybey, V. E. (1971). *Matrix Isolation Search for Transient Species*. (Thesis). University of California, Berkeley, CA, United States.

Boys, S. F., and Bernardi, F. (1970). Calculation of small molecular interactions by differences of separate total energies—some procedures with reduced errors. *Mol. Phys*. 19, 553–566. doi: 10.1080/00268977000101561

Cheng, C., and Sheng, L. (2013). Ab-Initio study of Helium-small carbon cage systems. *Int. J. Quantum Chem*. 113, 35–38. doi: 10.1002/qua.24303

Colburn, E. Q., and Douglas, A. E. (1976). The spectrum and ground state potential curve of Ar2. *J. Chem. Phys*. 65:1741. doi: 10.1063/1.433319

Computational Chemistry Comparison and Benchmark DataBase (2019). *NIST Chemistry Webbook*. Available online at: https://cccbdb.nist.gov/exp2x.asp?casno=12595594, https://cccbdb.nist.gov/geom2x.asp (accessed June 23, 2020).

Das, P., Saha, R., and Chattaraj, P. K. (2020). Encapsulation of Mg_2 inside a C_{60} cage forms an electride. *J. Comput. Chem*. 41, 1645–1653. doi: 10.1002/jcc.26207

DiCamillo, B. A., Hettich, R. L., Guiochon, G., Compton, R. N., Saunders, M., Jimenez-Vazquez, H. A., et al. (1996). Enrichment and characterization of a noble gas fullerene: $Ar@C_{60}$. *J. Phys. Chem*. 100, 9197–9201. doi: 10.1021/jp960049k

Dolgonos, G. A., and Peslherbe, G. H. (2014). Encapsulation of diatomic molecules in fullerene C_{60}: implications for their main properties. *Phys. Chem. Chem. Phys.* 16, 26294–26305. doi: 10.1039/C4CP04069D

Fisher, R. A. (1925). Theory of statistical estimation. *Proc. Cambridge Philos. Soc.* 22, 700–725. doi: 10.1017/S0305004100009580

Foroutan-Nejad, C., Straka, M., Fernández, I., and Frenking, G. (2018). Buckyball difluoride $F_2^-@C_{60}^+$–a single-molecule crystal. *Angew. Chem. Int. Ed.* 57, 13931–13934. doi: 10.1002/anie.201809699

Frisch, M. J., Trucks, G. W., Schlegel, H. B., Scuseria, G. E., Robb, M. A., Cheeseman, J. R., et al. (2016). *Gaussian Inc.*, Wallingford, CT.

Geerlings, P., Chamorro, E., Chattaraj, P. K., De Proft, F., Gazquez, J. L., Liu, S. B., et al. (2020). Conceptual density functional theory: status, prospects, issues. *Theor. Chem. Acc*. 139:36. doi: 10.1007/s00214-020-2546-7

Geerlings, P., De Proft, F., and Langenaeker, W. (2003). Conceptual density functional theory. *Chem. Rev*. 103, 1793–1847. doi: 10.1021/cr990029p

Ghosh, S. K., Berkowitz, M., and Parr, R. G. (1984). Transcription of ground-state density-functional theory into a local thermodynamics. *Proc. Natl. Acad. Sci. U. S. A*. 81, 8028–8031. doi: 10.1073/pnas.81.24.8028

Glendening, E. D., Landis, C. R., and Weinhold, F. (2012). Natural bond orbital methods. *WIREs Comput. Mol. Sci*. 2, 1–42. doi: 10.1002/wcms.51

Gómez, S., and Restrepo, A. (2019). Noble gas dimers confined inside C_{70}. *Phys. Chem. Chem. Phys*. 21, 15815–15822. doi: 10.1039/C9CP03015H

Graham, L., Graudejus, O., Jha, N. K., and Bartlett, N. (2000). Concerning the nature of $XePtF_6$. *Coord. Chem. Rev*. 197, 321–334. doi: 10.1016/S0010-8545(99)00190-3

Hirshfeld, F. (1977). Bonded-atom fragments for describing molecular charge densities. *Theor. Chim. Acc*. 44, 129–138. doi: 10.1007/BF00549096

Holloway, J. H., and Hope, E. G. (1999). Recent advances in noble-gas chemistry. *Adv. Inorg. Chem*. 46, 51–100. doi: 10.1016/S0898-8838(08)60149-X

Jalife, S., Mondal, S., Cabellos, J. L., Pan, S., Méndez-Rojas, M. Á., Fernández, I., et al. (2016). Breaking the isolated pentagon rule by encapsulating Xe_2 in C_{60}: the guest defines the shape of the host. *Chemistry Select* 1, 2405–2408. doi: 10.1002/slct.201600525

Jaroš, A., Badri, Z., Bora, P. L., Bonab, E. F., Marek, R., Straka, M., et al. (2018). How does a container affect acidity of its content: charge-depletion bonding inside fullerenes. *Chem. Eur. J.* 24, 4245–4249. doi: 10.1002/chem.201706017

Johnson, E. R., Keinan, S., Mori-Sánchez, P., Contreras-García, J., Cohen, A. J., and Yang, W. (2010). Revealing noncovalent interactions. *J. Am. Chem. Soc.* 132, 6498–6506. doi: 10.1021/ja100936w

Khatua, M., Pan, S., and Chattaraj, P. K. (2014). Movement of Ng_2 molecules confined in a C_{60} cage: an ab initio molecular dynamics study. *Chem. Phys. Lett.* 610–611, 351–356. doi: 10.1016/j.cplett.2014.06.052

Krapp, A., and Frenking, G. (2007). Is this a chemical bond? A theoretical study of $Ng_2@C_{60}$ (Ng=He, Ne, Ar, Ke, Xe). *Chem. Eur. J.* 13, 8256–8270. doi: 10.1002/chem.200700467

Kryachko, E. S., and Nikolaienko, T., Yu. (2015). $He_2@C_{60}$: thoughts of the concept of a molecule and of the concept of a bond in quantum chemistry. *Int. J. Quantum Chem.* 115, 859–867. doi: 10.1002/qua.24916

Kullback, S., and Leibler, R. A. (1951). On information and sufficiency. *Ann. Math. Stat.* 22, 79–86. doi: 10.1214/aoms/1177729694

Laskin, J., Peres, T., Lifshitz, C., Saunders, M., Cross, R. J., and Khong, A. (1998). An artificial molecule of Ne_2 inside C_{70}. *Chem. Phys. Lett.* 285, 7–9. doi: 10.1016/S0009-2614(97)01473-5

Lee, C., Yang, W., and Parr, R. G. (1988). Density-functional exchange-energy approximation with correct asymptotic behavior. *Phys. Rev. B* 37, 785–789. doi: 10.1103/PhysRevB.37.785

Liu, S. B. (2007). Steric effect: a quantitative description from density functional theory. *J. Chem. Phys.* 126:244103. doi: 10.1063/1.2747247

Liu, S. B. (2009). Conceptual density functional theory and some recent developments. *Acta Phys. Chim. Sin.* 25, 590–600. doi: 10.3866/PKU.WHXB20090332

Liu, S. B. (2013). Origin and nature of bond rotation barriers: a unified view. *J. Phys. Chem. A* 17, 962–965. doi: 10.1021/jp312521z

Liu, S. B. (2016). Information-theoretic approach in density functional reactivity theory. *Acta Phys. Chim. Sin.* 32, 98–118. doi: 10.3866/PKU.WHXB201510302

Liu, S. B., Rong, C. Y., and Lu, T. (2014). Information conservation principle determines electrophilicity, nucleophilicity, and regioselectivity. *J. Phys. Chem. A* 118, 3698–3704. doi: 10.1021/jp5032702

Lu, T., and Chen, F. (2012). Multiwfn: a multifunctional wavefunction analyzer. *J. Comput. Chem.* 33, 580–592. doi: 10.1002/jcc.22885

Ma, Y., Ai, Y., Song, X., Wang, C., and Luo, Y. (2014). The equilibrium geometry of $A@C_{60}$: a test case for conventional density functional theory. *Chem. Phys. Lett.* 591, 312–316. doi: 10.1016/j.cplett.2013.11.050

Nagy, Á., and Romera, E. (2015). Relative Rényi entropy and fidelity susceptibility. *Europhys. Lett.* 109:60002. doi: 10.1209/0295-5075/109/60002

Nelson, L. Y., and Pimentel, G. C. (1967). Infrared detection of xenon dichloride. *Inorg. Chem.* 6, 1758–1759. doi: 10.1021/ic50055a038

Nikolaienko, T., Yu., Kryachko, E. S., and Dolgonos, G. A. (2017). On the existence of He–He bond in the endohedral fullerene $H?_2@C_{60}$. *J. Comput. Chem.* 39, 1090–1102. doi: 10.1002/jcc.25061

Nikolaienko, T. Y., and Kryachko, E. S. (2015). Formation of dimers of light noble atoms under encapsulation within fullerene's voids. *Nanoscale Res. Lett.* 30:185. doi: 10.1186/s11671-015-0871-x

Osuna, S., Swart, M., and Solà, M. (2009). Reactivity and regioselectivity of noble gas endohedral fullerenes $Ng@C_{60}$ and $Ng_2@C_{60}$ (Ng=He–Xe). *Chem. Eur. J.* 15, 13111–13123. doi: 10.1002/chem.200901224

Osuna, S., Swart, M., and Solà, M. (2011). The reactivity of endohedral fullerenes. What can be learnt from computational studies? *Phys. Chem. Chem. Phys.* 13, 3585–3603. doi: 10.1039/C0CP01594F

Parr, R. G., Donnelly, R. A., Levy, M., and Palke, W. E. (1978). Electronegativity: the density functional viewpoint. *J. Chem. Phys.* 68, 3801–3807. doi: 10.1063/1.436185

Parr, R. G., and Pearson, R. G. (1983). Absolute hardness: companion parameter to absolute electronegativity. *J. Am. Chem. Soc.* 105, 7512–7516. doi: 10.1021/ja00364a005

Parr, R. G., Szentpaly, L. V., and Liu, S. B. (1999). Electrophilicity index. *J. Am. Chem. Soc.* 121, 1922–1924. doi: 10.1021/ja983494x

Parr, R. G., and Yang, W. (1989). *Density Functional Theory of Atoms and Molecules*. Oxford: Oxford University Press.

Peres, T., Cao, B., Cui, W., Khong, A., Cross, R. J. Jr., Saunders, M., et al. (2001). Some new diatomic molecule containing endohedral fullerenes. *Int. J. Mass Spec.* 210–211, 241–247. doi: 10.1016/S1387-3806(01)00420-1

Popov, A. A., Yang, S., and Dunsch, L. (2013). Endohedral fullerenes. *Chem. Rev.* 113, 5989–6113. doi: 10.1021/cr300297r

Rényi, A. (1970). *Probability Theory*. Amsterdam: North-Holland.

Rong, C., Wang, B., Zhao, D., and Liu, S. (2019). Information-theoretic approach in density functional theory and its recent applications to chemical problems. *WIREs Comput. Mol. Sci.* 10:e1461. doi: 10.1002/wcms.1461

Saha, R., Jana, G., Pan, S., Merino, G., and Chattaraj, P. K. (2019). How far can one push the noble gases towards bonding?: a personal account. *Molecules* 24:2933. doi: 10.3390/molecules24162933

Saunders, M., Cross, R. J., Jiménez-Vázquez, H. A., Shimshi, R., and Khong, A. (1996). Noble gas atoms inside fullerenes. *Science* 271, 1693–1697. doi: 10.1126/science.271.5256.1693

Saunders, M., Jiménez-Vázquez, H. A., Cross, R. J., and Poreda, R. J. (1993). Stable compounds of helium and neon: $He@C_{60}$ and $Ne@C_{60}$. *Science* 259, 1428–1430. doi: 10.1126/science.259.5100.1428

Shannon, C. E. (1948). A mathematical theory of communication. *Bell Syst. Tech. J.* 27, 379–423. doi: 10.1002/j.1538-7305.1948.tb01338.x

Simon, S., Duran, M., and Dannenberg, J. J. (1996). How does basis set superposition error change the potential surfaces for hydrogen bonded dimers? *J. Chem. Phys.* 105, 11024–11031. doi: 10.1063/1.472902

Srivastava, A. K., Pandey, S. K., and Misra, N. (2016). $(CH_3Br?NH_3)@C_{60}$: the effect of nanoconfinement on halogen bonding. *Chem. Phys. Lett.* 662, 240–243. doi: 10.1016/j.cplett.2016.09.036

Stein, L. (1973). Removal of xenon and radon from contaminated atmospheres with dioxygenyl hexafluoroantimonate, O_2SbF_6. *Nature* 243, 30–32. doi: 10.1038/243030a0

Syamala, M. S., Cross, R. J., and Saunders, M. (2002). ^{129}Xe NMR spectrum of Xenon inside C_{60}. *J. Am. Chem. Soc.* 124, 6216–6219. doi: 10.1021/ja012676f

Te Velde, G. T., Bickelhaupt, F. M., Baerends, E. J., Fonseca Guerra, C., van Gisbergen, S. J., Snijders, J. G., et al. (2001). Chemistry with ADF. *J. Comput. Chem.* 22, 931–967. doi: 10.1002/jcc.1056

Turner, J. J., and Pimentel, G. C. (1963). Krypton fluoride: preparation by the matrix isolation technique. *Science* 140, 974–975. doi: 10.1126/science.140.3570.974-a

Wang, B., Rong, C. Y., Chattaraj, P. K., and Liu, S. B. (2019). A comparative study to predict regioselectivity, electrophilicity and nucleophilicity with Fukui function and Hirshfeld charge. *Theor. Chem. Acc.* 138:124. doi: 10.1007/s00214-019-2515-1

Yamamoto, K., Saunders, M., Khong, A., Cross, R. J., Grayson, M., Gross, M. L., et al. (1999). Isolation and spectral properties of $Kr@C_{60}$, a stable van der Waals molecule. *J. Am. Chem. Soc.* 121, 1591–1596. doi: 10.1021/ja9831498

Yang, W., Parr, R. G., and Pucci, R. (1984). Electron density, Kohn–Sham frontier orbitals, and Fukui functions. *J. Chem. Phys.* 81, 2862–2863. doi: 10.1063/1.447964

Zhao, Y., and Truhlar, D. G. (2008). The M06 suite of density functionals for main group thermochemistry, thermochemical kinetics, noncovalent interactions, excited states, and transition elements: two new functionals and systematic testing of four M06-class functionals and 12 other functionals. *Theor. Chem. Acc.* 120, 215–241. doi: 10.1007/s00214-007-0310-x

Conflict of Interest: The authors declare that the research was conducted in the absence of any commercial or financial relationships that could be construed as a potential conflict of interest.

frontiers in Chemistry

ORIGINAL RESEARCH
published: 21 July 2020
doi: 10.3389/fchem.2020.00616

Noble Gas Binding Ability of an Au(I) Cation Stabilized by a Frustrated Lewis Pair: A DFT Study

Manas Ghara[1] *and Pratim Kumar Chattaraj*[1,2]*

[1] Department of Chemistry and Center for Theoretical Studies, Indian Institute of Technology, Kharagpur, India, [2] Department of Chemistry, Indian Institute of Technology Bombay, Mumbai, India

The noble gas (Ng) binding ability of a monocationic $[(FLP)Au]^+$ species has been investigated by a computational study. Here, the monocationic $[(FLP)Au]^+$ species is formed by coordination of Au(I) cation with the phosphorous (Lewis base) and the boron (Lewis acid) centers of a frustrated Lewis pair (FLP). The bonds involving Au and P, and Au and B atoms in $[(FLP)Au]^+$ are partially covalent in nature as revealed by Wiberg bond index (WBI) values, electron density analysis and energy decomposition analysis (EDA). The zero point energy corrected bond dissociation energy (D_0), enthalpy and free energy changes are computed for the dissociation of Au-Ng bonds to assess the Ng binding ability of $[(FLP)Au]^+$ species. The D_0 ranges from 6.0 to 13.3 kcal/mol, which increases from Ar to Rn. Moreover, the dissociation of Au-Ng bonds is endothermic as well as endergonic for Ng = Kr-Rn, whereas the same for Ng = Ar is endothermic but exergonic at room temperature. The partial covalent character of the bonds between Au and Ng atoms is demonstrated by their WBI values and electron density analysis. The Ng atoms get slight positive charges of 0.11–0.23 |e|, which indicates some amount of charge transfer takes place from it. EDA demonstrates that electrostatic and orbital interactions have equal contributions to stabilize the Ng-Au bonds in the $[(FLP)AuNg]^+$ complex.

Keywords: frustrated lewis pair, noble gas binding, noble gas-noble metal bond, bond dissociation energy, energy decomposition analysis

OPEN ACCESS

Edited by:
Nino Russo,
University of Calabria, Italy

Reviewed by:
Michele Pavone,
University of Naples Federico II, Italy
Jordi Poater,
University of Barcelona, Spain

****Correspondence:***
Pratim Kumar Chattaraj
pkc@chem.iitkgp.ac.in

Specialty section:
This article was submitted to Theoretical and Computational Chemistry, a section of the journal Frontiers in Chemistry

Received: *14 May 2020*
Accepted: *11 June 2020*
Published: *21 July 2020*

Citation:
Ghara M and Chattaraj PK (2020) Noble Gas Binding Ability of an Au(I) Cation Stabilized by a Frustrated Lewis Pair: A DFT Study. Front. Chem. 8:616. doi: 10.3389/fchem.2020.00616

INTRODUCTION

The noble gas (Ng) elements (He, Ne, Ar, Kr, Xe, and Rn) were have been supposed to be non-reactive in forming chemical bonds with other elements in the periodic table. Their inertness arises because the s and p orbitals are totally occupied. However, Pauling (1933), predicted the possibility of bond formation by the heavier Ng elements. Since the core electrons will exhibit larger screening effect for the valence electrons on moving down the group, the valence electrons would be in a relatively loosely bound state and hence they can be easily ionized. However, it took long time to convert it into reality when xenon hexafluoro platinate $[Xe^+(PtF_6)^-]$ was synthesized by Bartlett (1962). This discovery opened a new chapter in the Ng chemistry refuting the prejudice regarding the chemical inertness of Ngs. After this finding, a vast series of Ng compounds were either characterized experimentally or predicted to be viable *in silico* (Thompson and Andrews, 1994; Pettersson et al., 1995, 1997, 1998a,b; Evans and Gerry, 2000a,b; Evans et al., 2000a,b; Khriachtchev et al., 2000, 2001, 2003a,b; Li et al., 2002; Feldman et al., 2003; Tanskanen et al., 2003; Cooke and Gerry, 2004a,b; Wang et al., 2004, 2012; Smith et al., 2007; Chakraborty et al., 2010; Pan et al., 2013a,b, 2014;

Debackere et al., 2014; Khatua et al., 2014; Mondal and Chattaraj, 2014; Chakraborty and Chattaraj, 2015a,b; Pan et al., 2015a,b,c,d, 2016a,b, 2018a,b; Saha et al., 2015, 2016, 2017, 2019; Jana et al., 2018a). Similarly, the noble metals (M = Cu, Ag, Au) are known to be comparatively less reactive that allows their use in day-to-day life. Following the successful synthesis of different types of compounds containing Ng atoms, the possible union of noble metal and Ng atoms acquired appreciable attention. In Pyykkö (1995) showed the possibility of $NgAu^+$ and $NgAuNg^+$ through coupled-cluster based technique and in a subsequent study these species were characterized employing mass spectroscopic study (Schröder et al., 1998). Thereafter, a series of Ng complexes with Ng-Au bonds have been studied both experimentally and theoretically (Pan et al., 2015e, 2016c,d; Ghara et al., 2016; Jana et al., 2016, 2018b,c). The experimental and theoretical advancement in the complexes having Ng-Au bond has been summarized in a recent review paper (Pan et al., 2019).

In recent times, frustrated Lewis pairs (FLP) (Stephan, 2008) have seen an upsurge of interest since they can be used as metal-free catalysts, which can also activate some small molecules. The FLP skeleton is constructed by a pair of Lewis acid and base. These acidic and basic centers may be located in two separate molecules or in one particular molecule. Due to steric hindrance those centers are not allowed to form the usual dative bonds. Accordingly, further reactivity is exhibited by the unquenched Lewis acid and base centers. Welch et al. (2006) and Welch and Stephan (2007) reported the reversible activation of molecular hydrogen by an intramolecular boron/phosphorous FLP for the first time in 2006. After that several theoretical (Rokob et al., 2008, 2009; Hamza et al., 2009; Mueck-Lichtenfeld and Grimme, 2012; Ghara et al., 2019) studies were performed to understand the function of FLP in the cleavage of H-H bond in H_2 molecule. Two different models of H_2 activation by FLPs are proposed viz., electron transfer (ET) model as given by Rokob et al. (2008) and electric field (EF) model as given by Mueck-Lichtenfeld and Grimme (2012). Various imines, nitriles, enamens, alkenes, ketone, CO_2, etc., have been catalytically hydrogenated by exploiting the hydrogen activating ability of FLPs (Chase et al., 2007, 2008; Spies et al., 2008; Sumerin et al., 2008; Ashley et al., 2009; Mahdi and Stephan, 2014, 2015; Stephan and Erker, 2015; Ghara and Chattaraj, 2019; Ghara et al., 2019). FLPs may also activate other molecules such as NO, SO_2, CO_2, N_2O, CO, C_2H_4, C_2H_2 etc. (Mc Cahill et al., 2007; Moemming et al., 2009; Dureen and Stephan, 2010; Appelt et al., 2011; Cardenas et al., 2011; Kolychev et al., 2012; Sajid et al., 2014; Stephan and Erker, 2014; Ghara and Chattaraj, 2018a,b). FLP assisted small molecule activation thereby offers new synthetic opportunities. This performance of FLPs has rendered it as a highly attractive species being inexpensive and environment friendly. Recently, Erker et al. have shown that an intramolecular vicinal P/B FLP stabilized AuCl and $AuNTf_2$ may surve as catalysts for the hydroamination of alkynes (Ueno et al., 2019). An active catalytic species $[(FLP)Au]^+$ is generated in the reaction medium. As the Lewis acidic boron center interacts with the Au center it enhances the electrophilicity of the Au center, which in turn improves the catalytic activity of $[(FLP)Au]^+$ species as suggested by Erker.

In the present study, the Ng (Ng = Ar-Rn) binding ability at the Au center of $[(FLP)Au]^+$ is computationally investigated. Bond dissociation energy (D_0), enthalpy (ΔH) and Gibbs free energy changes (ΔG) are calculated to evaluate how the $[(FLP)Au]^+$ species can bind the Ng atoms. Topology of the electron density (Bader, 1990), natural bond orbital (NBO) (Reed and Weinhold, 1983), and energy decomposition (EDA) are analyzed and natural orbital for chemical valence (NOCV) (Morokuma, 1977; Mitoraj and Michalak, 2007; Mitoraj et al., 2009; Hopffgarten and Frenking, 2012) theory is to analyze the type of the bond formed connecting the Ng and the Au centers.

COMPUTATIONAL DETAILS

Geometries of all the molecules have been optimized in the gas phase at the M06-2X-D3 (Zhao and Truhlar, 2008; Grimme et al., 2010)/def2-TZVP level and not applying any symmetry constraint. The functional M06-2X performs well in describing the FLP chemistry as reported previously (Huang et al., 2014). Effective core potential (Peterson et al., 2003) was used in order to take care of the relativistic effect in Au, Xe and Rn. It may be noted that the presence of the dispersion term is just adding a semi-empirical correction to the total Kohn-Sham energy and is important when the long-range interactions are strong (Grimme et al., 2010). It is expected to increase the contribution of the dispersion term and hence the overall interaction energy. Effectiveness of the MO6-2X-D3 in certain cases has been shown earlier albeit with the presence of some amount of medium range interaction in MO6-2X (Burns et al., 2011) Vibrational frequencies are calculated to confirm whether the stationary points belong to a minimum on the potential energy surface (PES) or a higher order saddle point. This techniques also provides the zero point energy (ZPE) and the thermodynamic corrections at 298.15 K temperature. Natural bond orbitals(NBO) were analyzed to obtain the partial natural charges on each atomic site and the Wiberg bond index (WBI) (Wiberg, 1968) value. All the calculations were done using Gaussian 16 suit of program (Frisch et al., 2016). Quantum theory of atoms in a molecule (QTAIM) is used to analyze the distribution of the electron density by using a Multiwfn software (Lu and Chen, 2012). An all electron basis set WTBS was made use of for Au, Xe and Rn for this computation.

The bonding situations were further analyzed by means of the EDA-NOCV method as provided in the (ADF, 2018).105 program package. The EDA-NOCV calculations have been carried out at the BP86-D3(BJ)/TZ2P-ZORA level with the M06-2X-D3/def2-TZVP optimized geometries. BP86 functional is selected since D3 or D3(BJ) is not compatible with M06-2X functional as used in ADF to get the dispersion contribution. In this analysis, the interaction energy (ΔE_{int}) within two fragments may be decomposed into different energy components like:

$$\Delta E_{int} = \Delta E_{elstat} + \Delta E_{Pauli} + \Delta E_{orb} + \Delta E_{disp} \quad (1)$$

Since we have used D3(BJ), it provides extra dispersion contribution between two interacting fragments. The term ΔE_{orb} comes from orbital mixing. It may be devided into individual

components belonging to separate irreducible representations

$$\Delta E_{orb} = \sum_{r} \Delta E_r \tag{2}$$

An analysis containing the EDA and the NOCV allows one to partition the net orbital interactions into the corresponding pairwise contributions. The deformation in charge density $\Delta\rho_k(r)$, with orbital pairs $\Delta\rho_k(r)$ and $\psi_{-k}(r)$ get mixed up provides the amount and the direction of the charge flow (Equation 3), and the related energy term ΔE_{orb} gives the amount of stabilization in orbital energy (Equation 4).

$$\Delta\rho_{orb}(r) = \sum \Delta\rho_k(r) = \sum_{k=1}^{N/2} \nu_k[-\varphi_{-k}^2(r)+\varphi_k^2(r)] \tag{3}$$

$$\Delta E_{orb} = \sum_{k} \Delta E_k^{orb} = \sum_{k=1}^{N/2} \nu_k[-F_{-k,-k}^{TS} + F_{k,k}^{TS}] \tag{4}$$

RESULTS AND DISCUSSION

The optimized geometries of the bare $[(FLP)Au]^+$ complex and the Ng bound $[(FLP)AuNg]^+$ complexes are displayed in **Figure 1**. The bare $[(FLP)Au]^+$ complex corresponds to the C_1 point group with ^1A electronic state. The computed Au-P and Au-B bond distances are 2.29 and 2.38 Å respectively, whereas the experimental bond distances of these bonds are 2.27 and 2.35 Å respectively when a chloride ion is attached to the Au center of the complex (Ueno et al., 2019). The Au center posseses a natural charge of 0.42 $|e|$, and the P and B centers possess the NBO charge of 1.17 $|e|$ and 0.60 $|e|$, respectively in this complex. Low positive charge on Au center is a consequence of P→ Au donation and B→ Au and P→ Au backdonation (vide infra). The WBI values of Au-P and Au-B bonds are 0.69 and 0.32, respectively, implying partial covalent character of these bonds. The Au-P and Au-B bonds are further examined by electron density and EDA-NOCV analyses (*vide infra*).

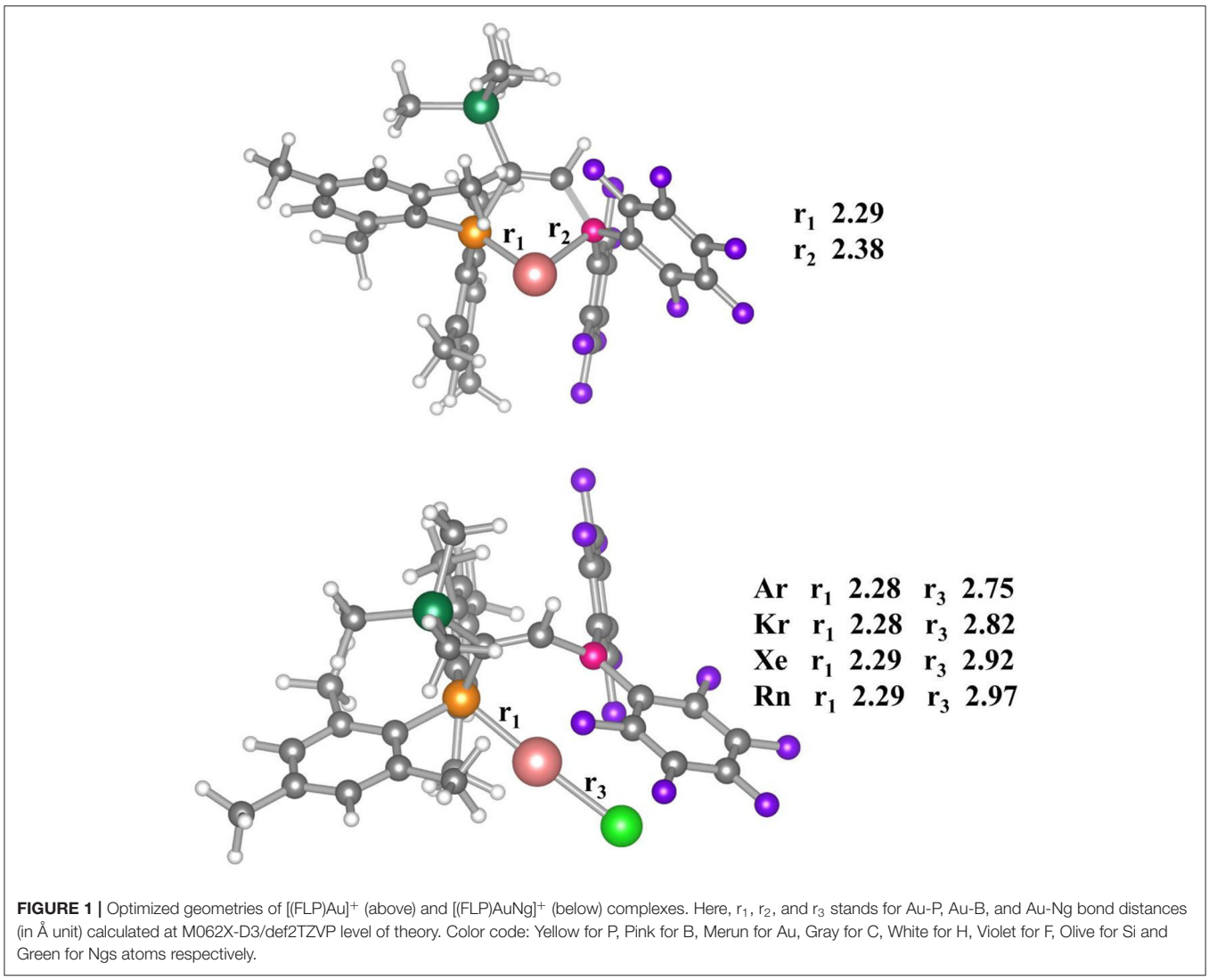

FIGURE 1 | Optimized geometries of $[(FLP)Au]^+$ (above) and $[(FLP)AuNg]^+$ (below) complexes. Here, r_1, r_2, and r_3 stands for Au-P, Au-B, and Au-Ng bond distances (in Å unit) calculated at M062X-D3/def2TZVP level of theory. Color code: Yellow for P, Pink for B, Merun for Au, Gray for C, White for H, Violet for F, Olive for Si and Green for Ngs atoms respectively.

Thus, any anionic/neutral ligand near the Au center may be polarized fascilitated by Au and can form chemical bond with Au. Accordingly, the $[(FLP)Au]^+$ complex is enable to bind Ng atoms (Kr-Rn) effectively as discussed in this study. The $[(FLP)AuNg]^+$ (Ng = Ar-Rn) complexes do not change the same electronic state and point group as that of the bare $[(FLP)Au]^+$ complex. The Ng-Au bond dissociation energy (ZPE corrected, D_0) values become 6.0–13.3 kcal/mol (see **Table 1**). Note that, the D_0 values are gradually increasing down the group from Ar to Rn and it was expected as the polarizabilities of the Ng atoms are increasing down the group which help the Au center to deform the electron cloud of Ngs. Further, the thermochemical stabilities of the Ng bound $[(FLP)Au]^+$ complexes are explored by calculating ΔH and ΔG associated with the dissociation of $[(FLP)AuNg]^+$ into $[(FLP)Au]^+$ and the respective Ng atoms at 298 K. The computed ΔH of all the dissociation processes is positive implying all these dissociation processes are endothermic and it also increases gradually down the group. The computed ΔG of dissociation is also positive for Kr-Rn bound cases implying endergonic dissociation of these Ng atoms from $[(FLP)AuNg]^+$ (Ng = Kr-Rn) systems except the dissociation of Ar from $[(FLP)AuAr]^+$ which is exergonic. Note that, all the dissociation processes are entropy driven and this is the reason for the observed exergonicity in the dissociation of $[(FLP)AuAr]^+$ into $[(FLP)Au]^+$ and the Ar atom. However, this dissociation could be frozen by slightly lowering the temperature. The HOMO-LUMO energy difference where HOMO and LUMO are the highest occupied and lowest unoccupied molecular orbitals respectively, is related to the global hardness (Parr and Chattaraj, 1991) can also be used to describe the stability of a molecular system. If the HOMO-LUMO gap (ΔE_{H-L}) of a molecule is high, then it will not like to give or take electron. It means the system is relatively more stable. Since, the ΔE_{H-L} of $[(FLP)Au]^+$ was 5.21 eV and after the Ng binding it increases to 5.45–5.59 eV which shows that the stability of the complex is increased upon Ng binding.

The NPA charges of the atoms in the complexes as provided by the NBO analysis are also listed in **Table 1**. In $[(FLP)AuNg]^+$ complexes the Ng centers gain some positive NPA charges and at the same time the positive charge of the Au center decreases from 0.42 $|e|$ to 0.25-0.16 $|e|$ as a result of Ng binding. This shows that some charge transfer takes place from Ng to the Au center and also to the complex and the amount of charge transfer gets increased as the size of the Ng atoms. The WBI value of a chemical bond gives the idea about the degree of covalency of that bond. A smaller value of WBI of a chemical bond implies non-covalent type of interaction like electrostatic or van der Waals interaction. Conversely, a higher value of WBI of a chemical bond implies dominant covalent character of that bond. In our case, the WBI values of the Au-Ng bonds are gradually increasing from 0.187 (of Ar) to 0.366 (of Rn) implying a partial covalent character of the bonds. However, the WBI value of the Au-P bond increases slightly after Ng binding to the Au center, whereas it is not found between the Au and B centers of the FLP and these are evident from the Au-P and Au-B bond distances. Since, the Au-P bond distances remain almost same and the Au-B distance increase ∼0.54–0.63 Å after the Ng binding.

The type of Au-P and Au-B bonds in the $[(FLP)Au]^+$ complexes and the Au-P and Au-Ng bonds in the $[(FLP)AuNg]^+$ complexes is understood through a topological electron density analysis and the results are given in **Table 2**. If the Laplacian of electron density $[\nabla^2\rho(r_c)]$ is negative at the bond critical point (BCP) of a chemical bond it implies that the electron density is accumulated in between the two bonded atoms and thus a covalent bond is present between them. Conversely,

TABLE 1 | ZPE corrected dissociation energy (D_0, kcal/mol), enthalpy (ΔH, kcal/mol) and free energy (ΔG, kcal/mol) changes at 298 K for the dissociation process $[(FLP)AuNg]^+ \rightarrow Ng + [(FLP)Au]^+$ (Ng = Ar-Rn), HOMO-LUMO energy differences (ΔE_{H-L}, eV), NPA charges at Au and Ng centers (q, au), WBI of Au-P (WBI_{Au-P}) and Au-Ng (WBI_{Au-Ng}) bonds calculated at M062X-D3/def2TZVP level.

Complex	D_0	ΔH	ΔG	ΔE_{H-L}	q(Au)	q(Ng)	WBI_{Au-P}	WBI_{Au-Ng}
$[(FLP)Au]^+$				5.21	0.42		0.692	
$[(FLP)AuAr]^+$	6.0	6.1	−1.6	5.58	0.25	0.11	0.752	0.187
$[(FLP)AuKr]^+$	8.8	8.9	1.2	5.59	0.21	0.16	0.735	0.256
$[(FLP)AuXe]^+$	11.9	12.0	4.2	5.58	0.17	0.22	0.710	0.348
$[(FLP)AuRn]^+$	13.3	13.3	5.8	5.58	0.16	0.23	0.705	0.366

TABLE 2 | Electron density descriptors at the bond critical points (BCP) of P-Au and B-Au bonds in $[(FLP)Au]^+$ and of P-Au and Ng-Au bonds in $[(FLP)AuNg]^+$ complexes (Ng = Ar-Rn) obtained at the M062X-D3/def2TZVP/WTBS level.

Complex	BCP	$\rho(r_c)$	$\nabla^2\rho(r_c)$	$G(r_c)$	$V(r_c)$	$H(r_c)$	$-G(r_c)/V(r_c)$
$[(FLP)Au]^+$	P-Au	0.107	0.135	0.081	−0.129	−0.048	0.630
	B-Au	0.050	0.049	0.028	−0.045	−0.016	0.638
$[(FLP)AuAr]^+$	P-Au	0.111	0.137	0.085	−0.136	−0.051	0.626
	Ar-Au	0.027	0.136	0.032	−0.030	0.002	1.067
$[(FLP)AuKr]^+$	P-Au	0.110	0.140	0.085	−0.135	−0.050	0.629
	Kr-Au	0.032	0.128	0.033	−0.033	−0.001	0.983
$[(FLP)AuXe]^+$	P-Au	0.109	0.141	0.084	−0.133	−0.049	0.633
	Xe-Au	0.031	0.117	0.030	−0.030	−0.001	0.981
$[(FLP)AuRn]^+$	P-Au	0.109	0.142	0.084	−0.133	−0.049	0.634
	Rn-Au	0.032	0.111	0.029	−0.031	−0.001	0.954

a positive $\nabla^2\rho(r_c)$ value at the BCP of a bond implies non-covalent interaction between the two bonded atoms. Although, this hypothesis can provide an explanation of the nature of bonding in most of the cases, it cannot properly interpret the bond involving heavier transition metals (Macchi et al., 1998) It also fails to interprit the bond in some typical covalent molecules like CO and F_2 (Cremer and Kraka, 1984). In that case, if the total electron energy density [$H(r_c)$] is negative at the BCP of a chemical bond, then the bond may contain some short of shaired interaction as suggested by Cramer. Here, $H(r_c)$ is the sum of the local kinetic energy density [$G(r_c)$] and the local potential energy density [$V(r_c)$].

In the bare $[(FLP)Au]^+$ complex, although the $\nabla^2\rho(r_c)$ is positive at the BCPs of P-Au and B-Au bonds, the negative $H(r_c)$ values of the same indicate the partially shared bonding interactions. Furthermore, the value of $-G(r_c)/V(r_c)$ is also a usefull quantity to describe the nature of a chemical bond. If the value of $-G(r_c)/V(r_c)$ at the BCP of a chemical bond ranges in between 0.5 and 1 then it contains some degree of shared interaction (Ziolkowski et al., 2006). Conversely, for a purely non-covalent interaction the value of $-G(r_c)/V(r_c)$ will be >1. Since, the value of $-G(r_c)/V(r_c)$ lies within 0.5 and 1 for both the P-Au and B-Au bonds, some degree of shared interactions is present in these bonds. Now, in $[(FLP)AuAr]^+$ complex, both the $\nabla^2\rho(r_c)$ and $H(r_c)$ are positive at the BCP of Au-Ar bond and so it may be classicified as non-covalent. Moreover, the value of $-G(r_c)/V(r_c)$ is >1 at the BCP implying a purely non-covalent interaction between them. On the other hand, in $[(FLP)AuNg]^+$ complexes (Ng = Kr-Rn) at the BCPs of Au-Kr, Au-Xe and Au-Rn bonds although $\nabla^2\rho(r_c)$ is positive, the negative $H(r_c)$ values indicate the partially shared bonding interactions. In addition, the value of $-G(r_c)/V(r_c)$ lies in between 0.5 and 1 which also implies some degree of shared interactions in these bonds. Moreover, the values of $\nabla^2\rho(r_c)$, $H(r_c)$ and $-G(r_c)/V(r_c)$ of the P-Au bond remain as in the bare complex after Ng binding exhibiting a partially covalent nature of the bond. Although, the $\nabla^2\rho(r_c)$, $H(r_c)$ and $-G(r_c)/V(r_c)$ values of the B-Au bond in the bare complex indicate a partial covalent character of this bond, no BCP was found in between the Au and B centers in the $[(FLP)AuNg]^+$ complexes.

The contour plots of $\nabla^2\rho(r)$ of P-Au and B-Au bonds in the bare complex $[(FLP)Au]^+$ and P-Au and Au-Ng bonds in the Ng bound complexes are provided in **Figure 2**. In these figures solid pink lines depict the portion with positive $\nabla^2\rho(r)$, the dotted green lines depict the region with negative $\nabla^2\rho(r)$ and the blue solid lines represent the interbasin paths between the two atomic basins. It is apparent from all these plots that there is no green region which belongs to the interbasin path. Only, the valence orbitals are slightly deformed in shape.

The nature of the Au-P and Au-B bonds present in the $[(FLP)Au]^+$ complex is further analyzed by EDA and the results are depicted in **Table S1** in the Supportion information (SI). The contributions of ΔE_{elstat} and ΔE_{orb} toward the total attractive interaction between the FLP and the Au^+ cation become 53.1 and 41.5% respectively, whereas the ΔE_{disp} has a very less contribution (5.4%). Hence, the complex is mostly stabilized by electrostatic interaction followed by the orbital interactions between the FLP and the Au^+ cation. Decomposition of ΔE_{orb} into pair-wise orbital interactions shows that there exist two major contributing orbital interactions $\Delta E_{orb(1)}$ and $\Delta E_{orb(2)}$, and four minor contributing orbital interactions $\Delta E_{orb(3)}$ to $\Delta E_{orb(6)}$. The deformation densities associated with these orbital interaction channels are also depicted in **Figure S1** in the SI to understand the origin of these orbital interactions. The deformation density $\Delta\rho(1)$ (associated with $\Delta E_{orb(1)}$) refers to the amount of electron density donated from the Lewis basic P center to the Au^+ cation, whereas $\Delta\rho(2)$ (associated with $\Delta E_{orb(2)}$) refers to the amount of electron density donated backward from the Au^+ cation to both the LA and LB centers of the FLP. The remaining four deformation densities $\Delta\rho(3)$ to $\Delta\rho(6)$ also refer to the backward donation of electron density from the Au^+ cation to the FLP and these are very small.

The nature of Au-Ng bonds present in the $[(FLP)AuNg]^+$ complexes is also analyzed by EDA and the results are given in **Table 3**. In these Au-Ng bonds, the contribution of the ΔE_{elstat} and ΔE_{orb} are almost equal (∼40%) to the total attractive interaction between the Ng and the $[(FLP)Au]^+$ complex, and the contribution from the ΔE_{disp} is less but not negligible (18–19%). However, the total attractive interaction made by these three interactions is sufficient to overcome the repulsive Pauli interaction and therefore the ΔE_{int} becomes negative. Further, decomposing ΔE_{orb} into pair-wise orbital interactions by NOCV method we get four different orbital interaction channels $\Delta E_{orb(1)}$ to $\Delta E_{orb(4)}$. Among them, the $\Delta E_{orb(1)}$ has the maximum contribution (68–73%) to the total ΔE_{orb} of all the Au-Ng bonds. The deformation densities viz., $\Delta\rho(1)$, $\Delta\rho(2)$, $\Delta\rho(3)$, and $\Delta\rho(4)$ associated with the $\Delta E_{orb(n)}$ (n = 1–4) of the $[(FLP)AuXe]^+$ complex are also depicted in **Figure 3**. Here, the $\Delta\rho(1)$ (corresponding to the major contributing $\Delta E_{orb(1)}$) refers to the donation of σ-electron density from the Xe atom to the Au center. Conversly, the $\Delta\rho(2)$ refers to the back donation of σ-electron density from the Au center to the Xe atom. Moreover, the $\Delta\rho(3)$ and $\Delta\rho(4)$ refer to the back donation of π-electron density from the Ng to the Au center. However, the donation of σ-electron density from the Xe atom to the Au center is not fully compensated by the sum of the back donations of electron density from the Au center to the Xe atom which leads to the observed positive NPA charge on the Xe center in the $[(FLP)AuXe]^+$ complex.

CONCLUSION

The noble gas (Ng) binding ability of a monocationic $[(FLP)Au]^+$ species has been assessed. Here, the monocationic $[(FLP)Au]^+$ species is formed by coordinating Au(I) cation with the LA and LB centers of a FLP. The Au-P and Au-B bonds in $[(FLP)Au]^+$ are partially covalent in nature as revealed by electron density and energy decomposition analyses. The Au center possesses an NPA charge of 0.42 $|e|$ as obtained from NBO analysis.

The bond dissociation energy values (ZPE corrected, D_0) for the dissociation of Au-Ng bonds (Ng = Ar-Rn) get increased and range between 6.0 and 13.3 kcal/mol from Ar to Rn. It is apparent

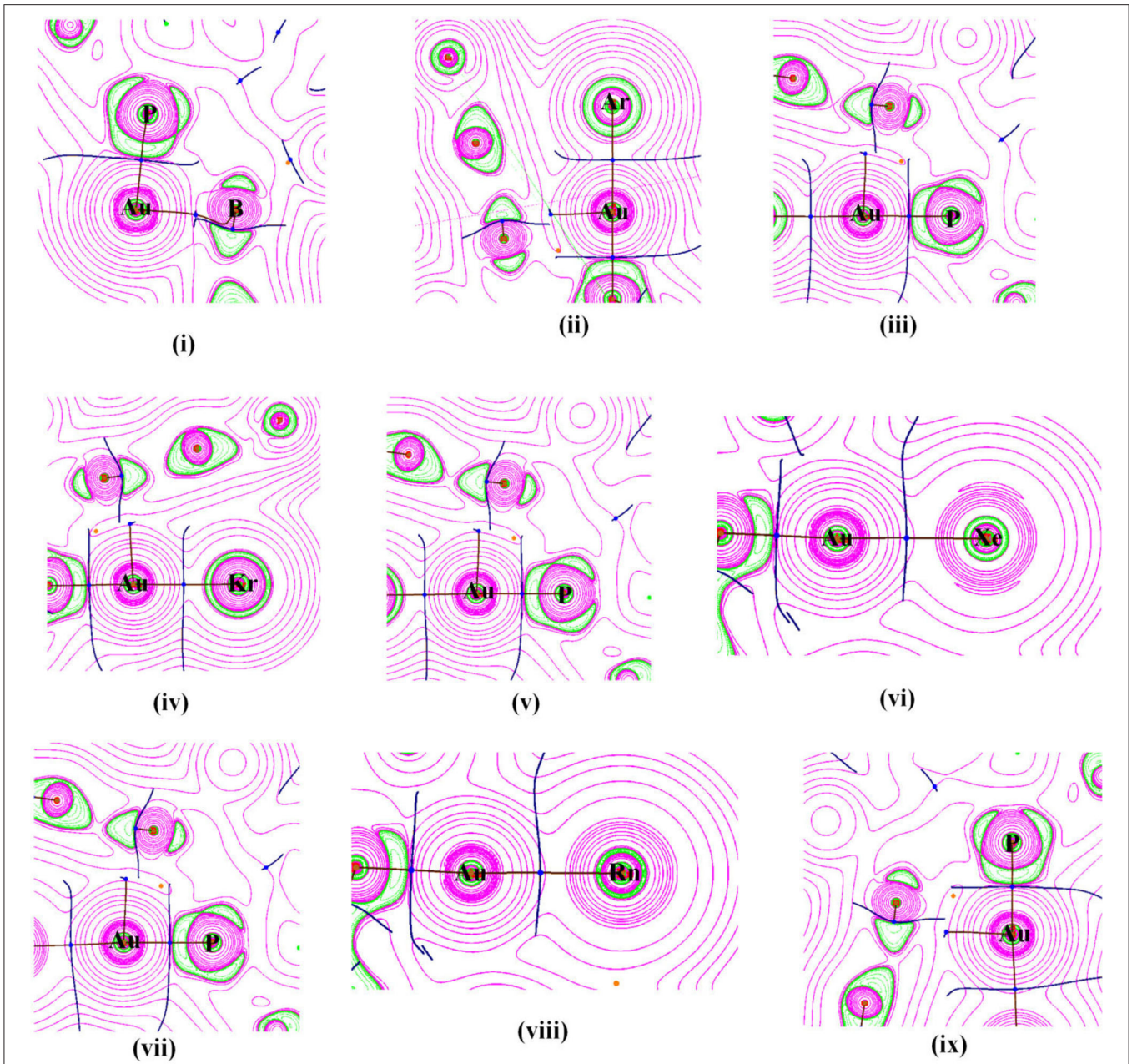

FIGURE 2 | Contour plots of Laplacian of electron density [$\nabla^2\rho(r)$] of (i) Au-P and Au-B bonds in $[(FLP)Au]^+$, (ii) Au-Ar and (iii) Au-P bonds in $[(FLP)AuAr]^+$, (iv) Au-Kr and (v) Au-P bonds in $[(FLP)AuKr]^+$, (vi) Au-Xe and (vii) Au-P bonds in $[(FLP)AuXe]^+$, (viii) Au-Rn and (ix) Au-P bonds in $[(FLP)AuRn]^+$ at the M06-2X-D3/def2-TZVP/WTBS level. [Pink solid lines stand for $\nabla^2\rho(r) > 0$ and the green dotted lines stand for $\nabla^2\rho(r) < 0$].

that the dissociation of Au-Ng bonds is endothermic as well as endergonic for Ng = Kr-Rn, whereas the same for Ng = Ar is endothermic but exergonic at room temperature.

The stability of the complex is increased upon Ng binding as highlighted through an increase in the HOMO-LUMO gap (ΔE_{H-L}) of $[(FLP)Au]^+$, as a result of Ng binding. The partial covalent character of the Au-Ng bonds is indicated by the WBI values as well as through an electron density analysis at the BCP of these bonds. The Ng atoms get a slightly positive charge of 0.11–0.23 $|e|$, which indicates some amount of charge transfer from it. EDA demonstrates that both electrostatic and orbital interactions contribute almost equally to the total interaction energy between the Ng and the $[(FLP)Au]^+$ complex, and the dispersion interaction has a very less contribution. Further, decomposing the orbital interaction (ΔE_{orb}), we obtained four different interaction channels ($\Delta E_{orb(n)}$, n = 1–4), which are the results of donation and back donation of electron

TABLE 3 | Energy decomposition analysis (EDA) results for the $[(FLP)AuNg]^+$ complexes by taking Ng as one fragment and $[(FLP)Au]^+$ as another, studied at the BP86-D3(BJ)/TZ2P//M06-2X-D3/ def2TZVP level. All energy values are given in kcal/mol.

Energy	$[(FLP)AuAr]^+$	$[(FLP)AuKr]^+$	$[(FLP)AuXe]^+$	$[(FLP)AuRn]^+$
ΔE_{int}	−6.0	−11.3	−16.7	−19.4
ΔE_{Pauli}	18.9	24.8	32.5	36.1
ΔE_{disp}[a]	−4.9 (19.8%)	−6.6(18.2%)	−8.9 (18.0%)	−10.1 (18.2%)
ΔE_{elstat}[a]	−10.0 (40.3%)	−14.4 (40.0%)	−20.3 (41.3%)	−23.3 (41.9%)
ΔE_{orb}[a]	−9.9 (39.8%)	−15.1 (41.7%)	−20.1 (40.7%)	−22.2 (39.9%)
$\Delta E_{orb(1)}$[b]	−6.8 (68.7%)	−9.7 (64.2%)	−13.9 (69.3%)	−16.2 (73.0%)
$\Delta E_{orb(2)}$[b]	−1.0 (10.4%)	−1.4 (9.3%)	−1.8 (9.1%)	−1.8 (7.9%)
$\Delta E_{orb(3)}$[b]	−0.8 (8.2%)	−1.2 (7.6%)	−1.5 (7.6%)	−1.6 (7.0%)
$\Delta E_{orb(4)}$[b]	−0.8 (7.9%)	−1.1 (7.5%)	−1.5 (7.7%)	−1.6 (7.1%)

[a] *The values inside parentheses refer to the percentage contributions toward the total attractive interactions* $\Delta E_{elstat} + \Delta E_{orb} + \Delta E_{disp}$.
[b] *The values inside parentheses correspond to the percentage contributions toward the total orbital interactions,* ΔE_{orb}.

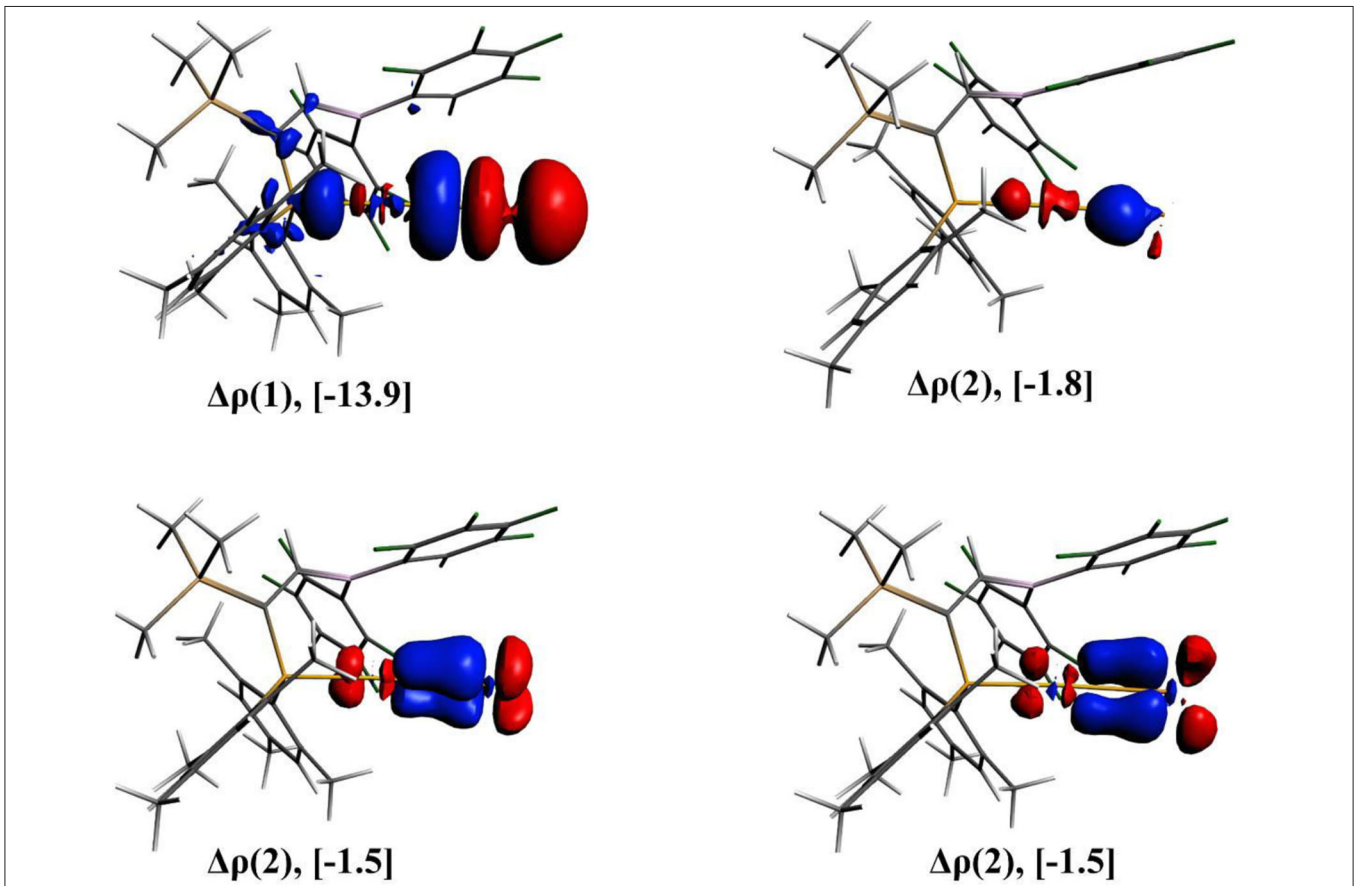

FIGURE 3 | The plots of deformation densities ($\Delta\rho$) of the pair-wise orbital interactions and the associated ΔE_{orb} energies obtained from the EDA-NOCV calculation on $[(FLP)AuXe]^+$. The color code of charge flow is red → blue.

densities between Ng and Au centers as obtained from the EDA-NOCV calculation.

DATA AVAILABILITY STATEMENT

The raw data supporting the conclusions of this article will be made available by the authors, without undue reservation.

AUTHOR CONTRIBUTIONS

MG has done the computation and has written the first draft of the manuscript. PC has critically examined the project and has made the final corrections. Both authors contributed to the article and approved the submitted version.

ACKNOWLEDGMENTS

PC thanks the DST, New Delhi for his J. C. Bose National Fellowship (JBF Grant no. SR/S2/JCB-09/2009). We would like to thank Dr. Sudip Pan for his help in various ways.

SUPPLEMENTARY MATERIAL

The Supplementary Material for this article can be found online at: https://www.frontiersin.org/articles/10.3389/fchem.2020.00616/full#supplementary-material

REFERENCES

ADF (2018). *SCM, Theoretical Chemistry*. Amsterdam: Vrije Universiteit. Available online at: http://www.scm.com

Appelt, C., Westenberg, H., Bertini, F., Ehlers, A. W., Slootweg, J. C., Lammertsma, K., et al. (2011). Geminal phosphorus/aluminum-based frustrated Lewis pairs: C-H versus C-C activation and CO_2 fixation. *Angew. Chem. Int. Ed.* 50:3925. doi: 10.1002/anie.201006901

Ashley, A. E., Thompson, A. L., and Hare, D. O. (2009). Non-metal-mediated homogeneous hydrogenation of CO_2 to CH_3OH. *Angew. Chem. Int. Ed.* 48:9839. doi: 10.1002/anie.200905466

Bader, R. F. W. (1990). *Atoms in Molecules: A Quantum Theory*. Oxford: Oxford University Press.

Bartlett, N. (1962). Xenon hexafluoroplatinate(V) $Xe^{+}[PtF_6]^{-}$. *Proc. Chem. Soc*. 6:197.

Burns, L. A., Vázquez- Mayagoitia, Á., Sumpter, B. G., and Sherrill, C. D. (2011). Density-functional approaches to noncovalent interactions: a comparison of dispersion corrections (DFT-D), exchange-hole dipole moment (XDM) theory, and specialized functionals. *J. Chem. Phys.* 134:084107. doi: 10.1063/1.3545971

Cardenas, A. J. P., Culotta, B. J., Warren, T. H., Grimme, S., Stute, A., Froehlich, R., et al. (2011). Capture of NO by a frustrated Lewis pair: a new type of persistent N-Oxyl radical. *Angew. Chem. Int. Ed.* 50:7567. doi: 10.1002/anie.201101622

Chakraborty, A., Giri, S., and Chattaraj, P. K. (2010). Trapping of noble gases (He-Kr) by the aromatic H_3^+ and Li_3^+ species: a conceptual DFT approach. *New J. Chem*. 34:1936. doi: 10.1039/c0nj00040j

Chakraborty, D., and Chattaraj, P. K. (2015a). Confinement induced binding in noble gas atoms within a BN-doped carbon nanotube. *Chem. Phys. Lett*. 621:29. doi: 10.1016/j.cplett.2014.12.053

Chakraborty, D., and Chattaraj, P. K. (2015b). In Quest of a superhalogen supported covalent bond involving a noble gas atom. *J. Phys. Chem. A* 119:3064. doi: 10.1021/jp513018v

Chase, P. A., Welch, G. C., Jurca, T., and Stephan, D. W. (2007). Metal-free catalytic hydrogenation. *Angew. Chem. Int. Ed.* 46:8050. doi: 10.1002/anie.200702908

Chase, P. A., Jurca, T., and Stephan, D. W. (2008). Lewis acid-catalyzed hydrogenation: $B(C_6F_5)_3$-mediated reduction of imines and nitriles with H_2. *Chem. Commun*. 1701. doi: 10.1039/b718598g

Cooke, S. A., and Gerry, M. C. L. (2004a). Insights into the xenon–silver halide interaction from a rotational spectroscopic study of XeAgF and XeAgCl. *Phys. Chem. Chem. Phys*. 6:3248. doi: 10.1039/B404953P

Cooke, S. A., and Gerry, M. C. L. (2004b). XeAuF. *J. Am. Chem. Soc*. 126:17000. doi: 10.1021/ja044955j

Cremer, D., and Kraka, E. (1984). Chemical bonds without bonding electron density — does the difference electron-density analysis suffice for a description of the chemical bond? *Angew. Chem. Int. Ed. Engl.* 23:627. doi: 10.1002/anie.198406271

Debackere, J. R., Mercier, H. P. A., and Schrobilgen, G. J. (2014). Noble-gas difluoride complexes of mercury(II): the syntheses and structures of $Hg(OTeF_5)_2{\cdot}1.5NgF_2$ (Ng = Xe, Kr) and $Hg(OTeF_5)_2$. *J. Am. Chem. Soc.* 136:3888. doi: 10.1021/ja412193z

Dureen, M. A., and Stephan, D. W. (2010). Reactions of boron amidinates with CO_2 and CO and other small molecules. *J. Am. Chem. Soc*. 132:13559. doi: 10.1021/ja1064153

Evans, C. J., and Gerry, M. C. L. (2000a). Noble gas–metal chemical bonding? The microwave spectra, structures, and hyperfine constants of Ar–CuX(X=F, Cl, Br). *J. Chem. Phys*. 112:9363. doi: 10.1063/1.481557

Evans, C. J., and Gerry, M. C. L. (2000b). The microwave spectra and structures of Ar–AgX (X=F,Cl,Br). *J. Chem. Phys*. 112:1321. doi: 10.1063/1.480684

Evans, C. J., Lesarri, A., and Gerry, M. C. L. (2000a). Noble gas–metal chemical bonds. Microwave spectra, geometries, and nuclear quadrupole coupling constants of Ar–AuCl and Kr–AuCl. *J. Am. Chem. Soc*. 122:6100. doi: 10.1021/ja000874l

Evans, C. J., Rubinoff, D. S., and Gerry, M. C. L. (2000b). Noble gas–metal chemical bonding: the microwave spectra, structures and hyperfine constants of Ar–AuF and Ar–AuBr. *Phys. Chem. Chem. Phys*. 2:3943. doi: 10.1039/b004352o

Feldman, V. I., Sukhov, F. F., Orlov, A. Y., and Tyulpina, I. V. (2003). Experimental evidence for the formation of HXeCCH: the first hydrocarbon with an inserted rare-gas atom. *J. Am. Chem. Soc*. 125:4698. doi: 10.1021/ja034585j

Frisch, M. J., Trucks, G. W., Schlegel, H. B., Scuseria, G. E., Robb, M. A., Cheeseman, J. R., et al. (2016). *Gaussian 16, Revision B.01*. Wallingford, CT: Gaussian, Inc.

Ghara, M., and Chattaraj, P. K. (2018a). A DFT study on trapping of nitric oxide by 1,3,2,5-diazadiborinine, a frustrated Lewis pair. *J. Indian Chem. Soc*. 95:1019.

Ghara, M., and Chattaraj, P. K. (2018b). Fixation of nitrous oxide (N_2O) by 1, 4, 2, 5-diazadiborinine: a DFT study. *Int. J. Quantum Chem*. 118:e25593. doi: 10.1002/qua.25593

Ghara, M., and Chattaraj, P. K. (2019). A computational study on hydrogenation of CO_2, catalyzed by a bridged B/N frustrated Lewis pair. *Struct. Chem*. 30:1067. doi: 10.1007/s11224-018-1264-4

Ghara, M., Pan, S., and Chattaraj, P. K. (2019). A theoretical investigation on boron-ligand cooperation to activate molecular hydrogen by a frustrated Lewis pair and subsequent reduction of carbon dioxide. *Phys. Chem. Chem. Phys*. 21:21267. doi: 10.1039/C9CP03756J

Ghara, M., Pan, S., Kumar, A., Deb, J., Sarkar, U., and Chattaraj, P. K. (2016). A computational study on structure, stability and bonding in noble gas bound metal nitrates, sulfates and carbonates (Metal = Cu, Ag, Au). *J. Chem. Sci*. 128:1537. doi: 10.1007/s12039-016-1150-9

Grimme, S., Antony, J., Ehrlich, S., and Krieg, H. (2010). A consistent and accurate ab initio parametrization of density functional dispersion correction (DFT-D) for the 94 elements H-Pu. *J. Chem. Phys*. 132:154104. doi: 10.1063/1.3382344

Hamza, A., Stirling, A., Rokob, T. A., and Pápai, I. (2009). Mechanism of hydrogen activation by frustrated Lewis pairs: a molecular orbital approach. *Int. J. Quantum Chem*. 109:2416. doi: 10.1002/qua.22203

Hopffgarten, M. V., and Frenking, G. (2012). Energy decomposition analysis. *Wiley Interdiscip. Rev. Comput. Mol. Sci*. 2:43. doi: 10.1002/wcms.71

Huang, F., Jiang, J., Wen, M., and Wang, Z.-X. (2014). Assessing the performance of commonly used DFT functionals in studying the chemistry of frustrated Lewis pairs. *Theor. Comput. Chem*. 13:1350074. doi: 10.1142/S0219633613500740

Jana, G., Pan, S., Merino, G., and Chattaraj, P. K. (2018a). Noble gas inserted metal acetylides (Metal = Cu, Ag, Au). *J. Phys. Chem. A* 122:7391. doi: 10.1021/acs.jpca.8b05404

Jana, G., Pan, S., Osorio, E., Zhao, L., Merino, G., and Chattaraj, P. K. (2018b). Cyanide-isocyanide isomerization: stability and bonding in noble gas inserted metal cyanides (Metal = Cu, Ag, Au). *Phys. Chem. Chem. Phys*. 20:18491. doi: 10.1039/C8CP02837K

Jana, G., Pan, S., Ravell, E., Zarate, X., Osorio, E., Merino, G., et al. (2018c). Stable NCNgNSi (Ng = Kr, Xe, Rn) compounds with covalently bound C-Ng-N unit: possible isomerization of NCNSi through the release of the noble gas atom. *Chem. Eur. J*. 24:2879. doi: 10.1002/chem.201705112

Jana, G., Saha, R., Pan, S., Kumar, A., Merino, G., and Chattaraj, P. K. (2016). Noble gas binding ability of metal-bipyridine monocationic complexes (Metal = Cu, Ag, Au): a computational study. *Chem. Select* 18:5842. doi: 10.1002/slct.201601245

Khatua, M., Pan, S., and Chattaraj, P. K. (2014). Confinement induced binding of noble gas atoms. *J. Chem. Phys.* 140:164306. doi: 10.1063/1.4871800

Khriachtchev, L., Pettersson, M., Lignell, A., and Rasanen, M. (2001). A more stable configuration of HArF in solid argon. *J. Am. Chem. Soc.* 123:8610. doi: 10.1021/ja016197s

Khriachtchev, L., Pettersson, M., Lundell, J., Tanskanen, H., Kiviniemi, T., Runeberg, N., et al. (2003a). A neutral xenon-containing radical, HXeO. *J. Am. Chem. Soc.* 125:1454. doi: 10.1021/ja029024r

Khriachtchev, L., Pettersson, M., Runeberg, N., Lundell, J., and Rasanen, M. (2000). A stable argon compound. *Nature* 406:874. doi: 10.1038/35022551

Khriachtchev, L., Tanskanen, H., Cohen, A., Gerber, R. B., Lundell, J., Pettersson, M., et al. (2003b). A gate to organokrypton chemistry: HKrCCH. *J. Am. Chem. Soc.* 125:6876. doi: 10.1021/ja0355269

Kolychev, E. L., Bannenberg, T., Freytag, M., Daniliuc, C. G., Jones, P. G., and Tamm, M. (2012). Reactivity of a frustrated Lewis pair and small-molecule activation by an isolable arduengo carbene-B{3,5-$(CF_3)_2C_6H_3$}$_3$ complex. *Chem. Eur. J.* 18:16938. doi: 10.1002/chem.201202840

Li, J., Bursten, B. E., Liang, B., and Andrews, L. (2002). Noble gas-actinide compounds: complexation of the CUO molecule by Ar, Kr, and Xe Atoms in Noble Gas Matrices. *Science* 295:2242. doi: 10.1126/science.1069342

Lu, T., and Chen, F. (2012). Multiwfn: a multifunctional wavefunction analyzer. *J. Comput. Chem.* 33:580. doi: 10.1002/jcc.22885

Macchi, P., Proserpio, D. M., and Sironi, A. (1998). Experimental electron density in a transition metal dimer: Metal–metal and metal–ligand bonds. *J. Am. Chem. Soc.* 120:13429. doi: 10.1021/ja982903m

Mahdi, T., and Stephan, D. W. (2014). Enabling catalytic ketone hydrogenation by frustrated Lewis pairs. *J. Am. Chem. Soc.* 136:15809. doi: 10.1021/ja508829x

Mahdi, T., and Stephan, D. W. (2015). Facile protocol for catalytic frustrated Lewis pair hydrogenation and reductive deoxygenation of ketones and aldehydes. *Angew. Chem. Int. Ed.* 54:8511. doi: 10.1002/anie.201503087

Mc Cahill, J. S. J., Welch, G. C., and Stephan, D. W. (2007). Reactivity of "Frustrated Lewis Pairs": three-component reactions of phosphines, a borane, and olefins. *Angew. Chem. Int. Ed.* 46:4968. doi: 10.1002/anie.200701215

Mitoraj, M. P., and Michalak, A. (2007). Donor–acceptor properties of ligands from the natural orbitals for chemical valence. *Organometallics* 26:6576. doi: 10.1021/om700754n

Mitoraj, M. P., Michalak, A., and Ziegler, T. A. (2009). A combined charge and energy decomposition scheme for bond analysis. *J. Chem. Theory Comput.* 5:962. doi: 10.1021/ct800503d

Moemming, C. M., Otten, E., Kehr, G., Froehlich, R., Grimme, S., Stephan, D. W., et al. (2009). Reversible metal-free carbon dioxide binding by frustrated Lewis pairs. *Angew. Chem. Int. Ed.* 48:6643. doi: 10.1002/anie.200901636

Mondal, S., and Chattaraj, P. K. (2014). Noble gas encapsulation: clathrate hydrates and their HF doped analogues. *Phys. Chem. Chem. Phys.* 16:17943. doi: 10.1039/C4CP02062F

Morokuma, K. (1977). Why do molecules interact? The origin of electron donor-acceptor complexes, hydrogen bonding and proton affinity. *Acc. Chem. Res.* 10:294. doi: 10.1021/ar50116a004

Mueck-Lichtenfeld, C., and Grimme, S. (2012). Theoretical analysis of cooperative effects of small molecule activation by frustrated Lewis pairs. *Dalton Trans.* 41:9111. doi: 10.1039/c2dt30562c

Pan, S., Contreras, M., Romero, J., Reyes, A., Merino, G., and Chattaraj, P. K. (2013a). $C_5L_{17}^+$ and $O_2Li_5^+$ as noble gas trapping agents. *Chem. Eur. J.* 19:2322. doi: 10.1002/chem.201203245

Pan, S., Ghara, M., Ghosh, S., and Chattaraj, P. K. (2016a). Noble gas bound beryllium chromate and beryllium hydrogen phosphate: a comparison with noble gas bound beryllium oxide. *RSC Adv.* 6:92786. doi: 10.1039/C6RA20232B

Pan, S., Ghara, M., Kar, S., Zarate, X., Merino, G., and Chattaraj, P. K. (2018a). Noble gas encapsulated B_{40} cage. *Phys. Chem. Chem. Phys.* 20:1953. doi: 10.1039/C7CP07890K

Pan, S., Gupta, A., Mandal, S., Moreno, D., Merino, G., and Chattaraj, P. K. (2015a). Metastable behavior of noble gas inserted tin and lead fluorides. *Phys. Chem. Chem. Phys.* 17:972. doi: 10.1039/C4CP03856H

Pan, S., Gupta, A., Saha, R., Merino, G., and Chattaraj, P. K. (2015b). A coupled-cluster study on the noble gas binding ability of metal cyanides versus metal halides (Metal = Cu, Ag, Au). *J. Comp. Chem.* 36:2168. doi: 10.1002/jcc.24190

Pan, S., Jalife, S., Kumar, M., Subramanian, V., Merino, G., and Chattaraj, P. K. (2013b). Structure and stability of $(NG)_nCN_3Be_3^+$ clusters and comparison with (NG)$BeY^{0/+}$ (Ng=Noble Gas and Y=O, S, Se, Te). *Chem. Phys. Chem.* 14:2511. doi: 10.1002/cphc.201300357

Pan, S., Jana, G., Merino, G., and Chattaraj, P. K. (2019). Noble-noble strong union: gold at its best to make a bond with a noble gas atom. *Chem. Open* 8:173. doi: 10.1002/open.201800257

Pan, S., Kar, S., Saha, R., Osorio, E., Zarate, X., and Zhao, L. (2018b). Boron nanowheel with an axle containing noble gas atoms: viable noble gas bound $M@B_{10}^-$ Clusters (M = Nb, Ta). *Chem. Eur. J.* 24:3590. doi: 10.1002/chem.201705790

Pan, S., Mandal, S., and Chattaraj, P. K. (2015c). Cucurbit[6]uril: a possible host for noble gas atoms. *J. Phys. Chem. B* 119:10962. doi: 10.1021/acs.jpcb.5b01396

Pan, S., Moreno, D., Ghosh, S., Merino, G., and Chattaraj, P. K. (2016b). Structure and stability of noble gas bound EX_3^+ compounds (E = C, Ge, Sn, Pb; X = H, F, Cl, Br). *J. Comp. Chem.* 37:226. doi: 10.1002/jcc.23986

Pan, S., Moreno, D., Merino, G., and Chattaraj, P. K. (2014). Stability of the noble gas bound SiH_3^+ clusters. *Chem. Phys. Chem.* 15:3554. doi: 10.1002/cphc.201402370

Pan, S., Saha, R., and Chattaraj, P. K. (2015d). Exploring the nature of silicon-noble gas bonds in $H_3SiNgNSi$ and HSiNgNSi compounds (Ng = Xe, Rn). *Int. J. Mol. Sci.* 16:6402. doi: 10.3390/ijms16036402

Pan, S., Saha, R., and Chattaraj, P. K. (2015e). On the stability of noble gas bound 1-tris(pyrazolyl)borate beryllium and magnesium complexes. *New J. Chem.* 39:6778. doi: 10.1039/C5NJ00983A

Pan, S., Saha, R., Kumar, A., Gupta, A., Merino, G., and Chattaraj, P. K. (2016c). A noble interaction: an assessment of noble gas binding ability of metal oxides (Metal = Cu, Ag, Au). *Int. J. Quantum Chem.* 116:1016. doi: 10.1002/qua.25121

Pan, S., Saha, R., Mandal, S., and Chattaraj, P. K. (2016d). σ-Aromatic cyclic M_3^+ (M = Cu, Ag, Au) clusters and their complexation with dimethyl imidazol-2-ylidene, pyridine, isoxazole, furan, noble gases and carbon monoxide. *Phys. Chem. Chem. Phys.* 18:11661. doi: 10.1039/C5CP06282A

Parr, R. G., and Chattaraj, P. K. (1991). Principle of maximum hardness. *J. Am. Chem. Soc.* 113:1854. doi: 10.1021/ja00005a072

Pauling, L. (1933). The formulas of antimonic acid and the antimonates. *J. Am. Chem. Soc.* 55:1895. doi: 10.1021/ja01332a016

Peterson, K. A., Figgen, D., Goll, E., Stoll, H., and Dolg, M. (2003). Systematically convergent basis sets with relativistic pseudopotentials. II. Small-core pseudopotentials and correlation consistent basis sets for the post-d group 16–18 elements. *J. Chem. Phys.* 119:11113. doi: 10.1063/1.1622924

Pettersson, M., Lundell, J., Isamieni, L., and Rasanen, M. (1998a). HXeSH the first example of a xenon-sulfur bond. *J. Am. Chem. Soc.* 120:7979. doi: 10.1021/ja981032d

Pettersson, M., Lundell, J., Khriachtchev, L., and Rasanen, M. (1998b). Neutral rare-gas containing charge-transfer molecules in solid matrices. III. HXeCN, HXeNC, and HKrCN in Kr and Xe. *J. Chem. Phys.* 109:618. doi: 10.1063/1.476599

Pettersson, M., Lundell, J., and Rasanen, M. (1995). Neutral rare-gas containing charge-transfer molecules in solid matrices. II. HXeH, HXeD, and DXeD in Xe. *J. Chem. Phys.* 103:205. doi: 10.1063/1.469632

Pettersson, M., Nieminen, J., Khriachtchev, L., and Rasanen, M. (1997). The mechanism of formation and infrared-induced decomposition of HXeI in solid Xe. *J. Chem. Phys.* 107:8423. doi: 10.1063/1.475042

Pyykkö, P. (1995). Predicted chemical bonds between rare gases and Au+. *J. Am. Chem. Soc.* 117:2067. doi: 10.1021/ja00112a021

Reed, A. E., and Weinhold, F. (1983). Natural bond orbital analysis of near-Hartree–Fock water dimer. *J. Chem. Phys.* 78:4066. doi: 10.1063/1.445134

Rokob, T. A., Hamza, A., and Pápai, I. (2009). Rationalizing the reactivity of frustrated Lewis pairs: thermodynamics of H_2 activation and the role of acid–base properties. *J. Am. Chem. Soc.* 131:10701. doi: 10.1021/ja903878z

Rokob, T. A., Hamza, A., Stirling, A., Soos, T., and Papai, I. (2008). Turning frustration into bond activation: a theoretical mechanistic study on heterolytic hydrogen splitting by frustrated Lewis pairs. *Angew. Chem. Int. Ed.* 47:2435. doi: 10.1002/anie.200705586

Saha, R., Jana, G., Pan, S., Merino, G., and Chattaraj, P. K. (2019). How far can one push the noble gases towards bonding?: a personal account. *Molecules* 24:2933. doi: 10.3390/molecules24162933

Saha, R., Pan, S., and Chattaraj, P. K. (2015). A comparative study on the noble gas binding ability of BeX clusters (X = SO4, CO3, O). *J. Phys. Chem. A* 119:6746. doi: 10.1021/acs.jpca.5b03888

Saha, R., Pan, S., and Chattaraj, P. K. (2017). $NgMC_p^+$: noble gas bound half-sandwich complexes (Ng = He-Rn, M = Be-Ba, $C_p = \eta^5$-C_5H_5). *J. Phys. Chem. A* 121:3526. doi: 10.1021/acs.jpca.7b00389

Saha, R., Pan, S., Mandal, S., Orozco, M., Merino, G., and Chattaraj, P. K. (2016). Noble gas supported B_3^+ cluster: formation of strong covalent noble gas–boron bonds. *RSC Adv.* 6:78611. doi: 10.1039/C6RA16188J

Sajid, M., Kehr, G., Daniliuc, C. G., and Erker, G. (2014). Formylborane formation with frustrated Lewis pair templates. *Angew. Chem. Int. Ed.* 53:1118. doi: 10.1002/anie.201307551

Schröder, D., Schwarz, H., Hrusak, J., and Pyykk,ö, P. (1998). Cationic Gold(I) complexes of xenon and of ligands containing the donor atoms oxygen, nitrogen, phosphorus, and sulfur. *Inorg. Chem.* 37:624. doi: 10.1021/ic970986m

Smith, G. L., Mercier, H. P., and Schrobilgen, G. J. (2007). Synthesis of $[F_3S{:}NXeF][AsF_6]$ and structural study by multi-NMR and raman spectroscopy, electronic structure calculations, and X-ray crystallography. *Inorg. Chem.* 46:1369. doi: 10.1021/ic061899+

Spies, P., Schwendemann, S., Lange, S., Kehr, G., Frhlich, R., and Erker, G. (2008). Metal-free catalytic hydrogenation of enamines, imines, and conjugated phosphinoalkenylboranes. *Angew. Chem. Int. Ed.* 47:7543. doi: 10.1002/anie.200801432

Stephan, D. W. (2008). "Frustrated Lewis pairs": a concept for new reactivity and catalysis. *Org. Biomol. Chem.* 6:1535. doi: 10.1039/b802575b

Stephan, D. W., and Erker, G. (2014). Frustrated Lewis pair chemistry of carbon, nitrogen and sulfur oxides. *Chem. Sci.* 5:2625. doi: 10.1039/C4SC00395K

Stephan, D. W., and Erker, G. (2015). Frustrated Lewis pair chemistry: development and perspectives. *Angew. Chem. Int. Ed.* 54:6400. doi: 10.1002/anie.201409800

Sumerin, V., Schulz, F., Atsumi, M., Wang, C., Nieger, M., Leskela, M., et al. (2008). Molecular tweezers for hydrogen: synthesis, characterization, and reactivity. *J. Am. Chem. Soc.* 130:14117. doi: 10.1021/ja806627s

Tanskanen, H., Khriachtchev, L., Lundell, J., Kiljunen, H., and Rasanen, M. (2003). Chemical compounds formed from diacetylene and rare-gas atoms: $HKrC_4H$ and $HXeC_4H$. *J. Am. Chem. Soc.* 125:16361. doi: 10.1021/ja038610x

Thompson, C. A., and Andrews, L. (1994). Noble gas complexes with BeO: infrared spectra of NG-BeO (NG = Ar, Kr, Xe). *J. Am. Chem. Soc.* 116:423. doi: 10.1021/ja00080a069

Ueno, A., Watanabe, K., Daniliuc, C. G., Kehr, G., and Erker, G. (2019). Unsaturated vicinal frustrated phosphane/borane Lewis pairs as ligands in gold(I) chemistry. *Chem. Commun.* 55:4367. doi: 10.1039/C9CC01136F

Wang, X., Andrews, L., Li, J., and Bursten, B. E. (2004). Significant interactions between uranium and noble-gas atoms: coordination of the UO_2^+ cation by Ne, Ar, Kr, and Xe atoms. *Angew. Chem. Int. Ed.* 43:2554. doi: 10.1002/anie.200453790

Wang, X., Andrews, L., Willmann, K., Brosi, F., and Riedel, S. (2012). Investigation of gold fluorides and noble gas complexes by matrix-isolation spectroscopy and quantum-chemical calculations. *Angew. Chem. Int. Ed.* 51:10628. doi: 10.1002/anie.201205072

Welch, G. C., Juan, R. R. S., Masuda, J. D., and Stephan, D. W. (2006). Reversible, metal-free hydrogen activation. *Science* 314:1124. doi: 10.1126/science.1134230

Welch, G. C., and Stephan, D. W. (2007). Facile heterolytic cleavage of dihydrogen by phosphines and boranes. *J. Am. Chem. Soc.* 129:1880. doi: 10.1021/ja067961j

Wiberg, K. B. (1968). Application of the pople-santry-segal CNDO method to the cyclopropylcarbinyl and cyclobutyl cation and to bicyclobutane. *Tetrahedron* 24:1083. doi: 10.1016/0040-4020(68)88057-3

Zhao, Y., and Truhlar, D. G. (2008). The M06 suite of density functionals for main group thermochemistry, thermochemical kinetics, noncovalent interactions, excited states, and transition elements: two new functionals and systematic testing of four M06-class functionals and 12 other functionals. *Theor. Chem. Acc.* 120:215. doi: 10.1007/s00214-007-0310-x

Ziolkowski, M., Grabowski, S. J., and Leszczynski, J. (2006). Cooperativity in hydrogen-bonded interactions: Ab Initio and "Atoms in Molecules" analyses. *J. Phys. Chem. A* 110:6514. doi: 10.1021/jp06 0537k

Conflict of Interest: The authors declare that the research was conducted in the absence of any commercial or financial relationships that could be construed as a potential conflict of interest.

frontiers in Chemistry

ORIGINAL RESEARCH
published: 06 August 2020
doi: 10.3389/fchem.2020.00621

Confinement Effects of a Noble Gas Dimer Inside a Fullerene Cage: Can It Be Used as an Acceptor in a DSSC?

*Debolina Paul, Harkishan Dua and Utpal Sarkar**

Department of Physics, Assam University, Silchar, India

A detailed density functional theory investigation of He_2-encapsulated fullerene C_{36} and C_{40} has been presented here. When confinement takes place, He-He bond length shortens and a non-covalent type of interaction exists between two He atoms. Energy decomposition analysis shows that though an attractive interaction exists in free He_2, when it is confined inside the fullerenes, repulsive interaction is observed due to the presence of dominant repulsive energy term. Fullerene C_{40}, with greater size, makes the incorporation of He_2 much easier than C_{36} as confirmed from the study of boundary crossing barrier. In addition, we have studied the possibility of using He_2-incorporated fullerene as acceptor material in dye-sensitized solar cell (DSSC). Based on the highest energy gap, $He_2@C_{40}$ and bare C_{40} fullerenes are chosen for this purpose. Dye constructed with $He_2@C_{40}$ as an acceptor has the highest light-harvesting efficiency and correspondingly will possess the maximum short circuit current as compared to pure C_{40} acceptor.

Keywords: noble gas dimer, fullerene, encapsulation, DFT, solar cell

OPEN ACCESS

Edited by:
Sudip Pan,
University of Marburg, Germany

Reviewed by:
Shubin Liu,
University of North Carolina at Chapel Hill, United States
Santanab Giri,
Haldia Institute of Technology, India

****Correspondence:***
Utpal Sarkar
utpalchemiitkgp@yahoo.com

Specialty section:
This article was submitted to Physical Chemistry and Chemical Physics, a section of the journal Frontiers in Chemistry

Received: *27 April 2020*
Accepted: *15 June 2020*
Published: *06 August 2020*

Citation:
Paul D, Dua H and Sarkar U (2020) Confinement Effects of a Noble Gas Dimer Inside a Fullerene Cage: Can It Be Used as an Acceptor in a DSSC? Front. Chem. 8:621. doi: 10.3389/fchem.2020.00621

INTRODUCTION

Ever since the discovery of fullerene (Kroto et al., 1985), it has been studied extensively due to its fascinating properties, leading to versatile applications in various fields of nano and opto-electronics (Bhusal et al., 2016; Paul et al., 2017, 2018a,b; Qu et al., 2019), besides being used as sensors (Jaroš et al., 2019; Parey et al., 2019) and hydrogen storage devices (Chandrakumar and Ghosh, 2008; Srinivasu and Ghosh, 2012). Fullerenes are also known to exist in different isomeric forms (Małolepsza et al., 2007; Zhao et al., 2018). Insertion of various atoms and molecules into the fullerene cage has attracted a lot of interest in the scientific community and is designated as the endohedral fullerenes. It is believed that the endohedrally trapped species can manipulate different properties and affect the reactivities of the fullerene cage as well (Ravinder and Subramanian, 2011, 2012). Thus, this class of fullerenes is studied both theoretically and experimentally, having their extensive use in the field of electronics, medicine, and nanotechnology (Guha and Nakamoto, 2005; Martín, 2006; Yamada et al., 2010). They can also serve the purpose of being an acceptor in photovoltaic devices (Osuna et al., 2011). Reactivity pattern of a system (atoms and molecules) significantly changes due to confinement (Chattaraj and Sarkar, 2003; Sarkar et al., 2009, 2012; Khatua et al., 2014c; Deb et al., 2016a,b); as a result, stability increases and reduces the activation barrier. The encapsulated atoms or molecules can be either metal, non-metal, or noble gas (Ng). Noble gases, due to their closed electronic shell configuration, are generally reluctant of forming any chemical compound. However, it is possible to successfully encapsulate them inside fullerenes

using techniques, such as ion bombardment (Weiske et al., 1991), molecular surgery (Saunders et al., 1994), and involving high pressure and high-temperature methods. Synthesis of the first xenon-containing molecule opened a way and interest for the researchers that noble gases are eligible to take part in chemical reactions (Bartlett, 1962). Ng-containing compound HNgY (Ng = Ar, Kr, Xe; Y = electron-withdrawing group) has been successfully synthesized by Pettersson et al. (1998). Literature survey also reveals that Feldman et al. has prepared hydrides and other Ng-related compounds (Feldman and Sukhov, 1996; Feldman et al., 1997). A number of theoretical studies on Ng have also been done apart from experimental investigations (Pan et al., 2013a,b,c, 2014a,b,c, 2015a,b,c; Saha et al., 2015; Ghara et al., 2016; Ayub, 2017). Inclusion and exclusion of Ng inside fullerene cages have been reported (Saunders et al., 1993; Hummelen et al., 1995), where an intermediate is formed by the rupture of one or more bonds, thus making an open window for the encapsulation of these noble gas atoms, although some disagreement is also set forth (Haaland et al., 2004). Experimental studies show that noble gases put inside the hollow cavity of C_{60} acquire an activation barrier energy as high as 90 kcal/mol^{-1} during its dissociation (Becker et al., 1996). Ng atoms are not only encapsulated inside larger fullerene cages (C_{60}, C_{70}), but they can also be successfully trapped inside much smaller cages such as $C_{10}H_{10}$, $C_{20}H_{20}$, C_{32}, etc. (Darzynkiewicz and Scuseria, 1997; Jiménez-Vázquez et al., 2001; Zou et al., 2010; Chakraborty et al., 2016; Sekhar et al., 2017). Further studies on trapping two Ng atoms forming an Ng dimer (Ng_2) inside fullerene have been first theoretically predicted by Giblin et al. (1997) and just after a year, He and Ne dimers are experimentally spotted into C_{70} fullerene (Khong et al., 1998; Laskin et al., 1998). Confinement of Ng dimers in C_{60} fullerene starting from He to Xe atoms have been studied theoretically by some groups (Krapp and Frenking, 2007; Fernández et al., 2014; Khatua et al., 2014b), where it was found that the Ng-Ng bond distances relatively get smaller when the Ng_2 molecule is trapped inside the cage as compared to the bond distances of the isolated dimer (Krapp and Frenking, 2007). However, as a whole, these systems are thermodynamically not stable owing to the exclusion of the Ng atoms. In a study as reported by Krapp and Frenking (2007) a genuine chemical bond is found to exist between the two Xe atoms when its dimer is confined inside the C_{60} cage, while for its lighter analogs, i.e., He and Ne, the presence of weak van der Waals interaction is detected. Cerpa et al. (2009) have studied the effect of confinement on the electronic interaction between He-He bond in the host $C_{20}H_{20}$ and their results followed that a shorter He-He bond does not always indicate a chemical bond. Not only are the carbon related compounds considered as the hosts for entrapping the Ng atoms and their dimers, but hosts constituted with other elements such as B_{40} cage (Pan et al., 2018), $B_{12}N_{12}$ (Khatua et al., 2014a; Paul et al., 2019), $B_{16}N_{16}$ (Khatua et al., 2014a), Sn_{12}^{2-}, and Pb_{12}^{2-} (Sekhar et al., 2017) are also reported. Encapsulation of Ng and Ng_2 in $B_{12}N_{12}$ and $B_{16}N_{16}$ fullerenes show that the dimer He_2 undergoes not only vibration and translation, but also rotation inside the cage. These investigations on noble gases encourage further comprehensive study on their confinement with different host materials.

Fullerenes possessed with electron-deficient characteristics are used as electron acceptors in a solar cell device (Liu and Troisi, 2011; Eom et al., 2014; Leng et al., 2014; Shimata et al., 2016). Dye-sensitized solar cell (DSSC) (O'Regan and Grätzel, 1991) is one of the widely used organic solar cells because it offers the possibility to convert light photons to electrical energy at a low cost. A dye in a DSSC consists of three parts: an electron-rich donor, a spacer, and an electron-deficient acceptor. Among the acceptors, [6,6]-phenyl-C_{61}-butyric acid methyl ester (PCBM) has been widely investigated (Liu and Troisi, 2011). Apart from fullerene C_{60} in PCBM, C_{70} cage is also used (Leng et al., 2014). Endohedral fullerenes can be used in designing solar cells (Ross et al., 2009) where the confined atoms are supposedly contributing to the efficiencies of the carrier transport (Yamada et al., 2010).

Inspired by all these works on noble gas, herein, we have investigated the influence of He_2 molecule when trapped inside C_{36} and C_{40} fullerenes by calculating the energetic stability, bonding analysis, energy decomposition analysis, distortion energy, and boundary-crossing barrier energy of $He_2@C_X$ (X = 36, 40). A glimpse of the UV-visible absorption spectra of $He_2@C_X$ is presented. Finally, considering the energetically most stable fullerene among the two ($He_2@C_{40}$), various parameters associated with the study of a dye-sensitized solar cell have been investigated. To make a comparison, pristine C_{40} fullerene is considered for this particular case study.

COMPUTATIONAL DETAILS

All the structures have been optimized using density functional theory (DFT) methodology as implemented in Gaussian 09 program package (Frisch et al., 2009), using M05-2X functional (Hohenstein et al., 2008). We have used 6-31+g(d,p) basis set for the C atoms and def2-TZVP basis set for the He atoms.

Dissociation energy (D_e) and distortion energy (E_d) are calculated using the relations:

$$D_e = \left[\left(E_{C_X} + E_{He_2}\right) - E_{He_2@C_X}\right] \quad (1)$$

$$E_d = E_{C_X(expanded)} - E_{C_X} \quad (2)$$

where E_{C_X} is the total energy of pristine C_X fullerenes, $E_{He_2@C_X}$ is the total energy of the He_2 encapsulated fullerenes (i.e., $He_2@C_{36}$ and $He_2@C_{40}$), $E_{C_X(expanded)}$ is the energy calculated by removing the He_2 dimer and evaluating single point energy of the expanded C_X fullerenes, and E_{He_2} is the energy of He_2 dimer.

The boundary-crossing barrier of the He_2 dimer through one hexagonal face of the fullerenes has been obtained by scanning the potential energy surface at different distances from the center of the fullerene cages. GAMESS software (Schmidt et al., 1993) has been implemented in calculation of energy decomposition analysis. Multiwfn software (Lu and Chen, 2011) is used to perform the topological analysis of electron density. Time-dependent density functional theory (TDDFT) has been employed to check the absorption spectra for the first 40 excited state transitions of the fullerenes and GaussSum software (O'Boyle et al., 2008) has been used for plotting. For calculating

solar cell parameters, we have considered B3LYP functional and 6–31 g basis set for all the atoms.

RESULTS AND DISCUSSION

The optimized structure of He_2 dimer encapsulated fullerenes are shown in **Figure 1** below.

Upon optimization, He_2 dimer orients itself in the middle of the fullerene cage in such a way that it can move through the midpoint of a six-membered ring easily when put inside C_{36} and C_{40} cages. In the beginning, empty C_{36} and C_{40} fullerenes (**Figure S1**) possess D_{2d} and D_2 symmetry, respectively. On enclosing He_2 inside them, the symmetry of C_{36} (i.e., $He_2@C_{36}$) changes to C_2 but C_{40} (i.e., $He_2@C_{40}$) successfully retains its original symmetry D_2. The highest dissociation energy is found when He_2 is encapsulated inside C_{36} cage (−53.1 kcal/mol) and naturally, the least is found for C_{40} fullerene, having a value of −45.6 kcal/mol. Negative values of dissociation energy reveal that He_2 encapsulation in them is not favorable. It should be noted that cage distortion and Pauli repulsion plays an important role in destabilization. However, with the increase in the size of the fullerene cage ($C_{36} < C_{40}$), destabilization decreases due to enlargement of space inside the cavity. Hence, it may be inferred that larger cages may lead toward favoring He_2 encapsulation in them. This result is also supported by the values of energy gap of He_2-incorporated C_{36} and C_{40} fullerenes. The larger fullerene C_{40} records a value of 3.980 eV, whereas C_{36} has 3.028 eV energy gap when they both hold the He_2 dimer inside them, indicating that $He_2@C_{40}$ is more stable than $He_2@C_{36}$ owing to its greater energy gap in comparison.

Distortion Energy

The encapsulation of the He_2 dimer inside the fullerene cages expands the surface area of the fullerene cage and this expansion may increase the binding energy of the system. The calculated distortion energy for $He_2@C_{36}$ is 1.6 kcal/mol and for $He_2@C_{40}$ is 1.7 kcal/mol. Thus, He_2 dimer has to expend this amount of energy barriers to get encapsulated inside the fullerene cages, as can be seen from the distortion energy values.

Structural Properties and Bonding Analysis

In order to get an idea about how the confinement of He_2 affects itself as well as the fullerene encaging it, we have calculated the bond lengths of the He_2 dimer both in unconfined and confined state. We have also performed electron density analysis, which will further strengthen the results. The equilibrium bond length for an isolated He_2 is calculated to be 2.666 Å, which is exactly same as that of Khatua et al. (2014a). As expected, confinement reduces the bond length of He_2 dimer, which is found from the investigation. More specifically, when He_2 is entrapped inside C_{36}, its bond length diminishes to 1.520 Å, while with the larger C_{40} cage, it has a value of 1.546 Å.

To understand the nature of interaction between the two He atoms both inside and outside fullerene C_{36} and C_{40} and surrounding C atoms when He_2 is placed inside the cages, the electron density analysis at the bond critical point (BCP) was performed (Deb et al., 2018) by employing the Bader's atoms-in-molecules theory (Bader, 1990). The corresponding topological descriptors are tabulated in **Table 1** and the contour plot of the Laplacian of electron densities at the BCPs are shown in **Figure 2**. At the BCP, depletion and accumulation of electron density $[\rho(r_c)]$ can be well understood from the positive and negative values of the Laplacian of electron density ($\nabla^2\rho_{BCP}$), respectively. Thus, when the magnitude of $\nabla^2\rho_{BCP} < 0$, a covalent or shared bond is formed between two atoms while a non-covalent bond is expected when $\nabla^2\rho_{BCP} > 0$. This criterion is helpful in explaining the bonding nature in many systems, but for the systems involving heavier atoms or with 3d orbitals, considering only $[\nabla^2\rho(r_c)]$ is not adequate to describe the nature of bonding connecting the heavier atoms. Therefore, some more topological descriptors like the local kinetic energy density $[G(r_c)]$, local potential energy density $[V(r_c)]$, and local electron energy density $[H(r_c)]$, including two ratios $-G(r_c)/V(r_c)$ and $G(r_c)/\rho(r_c)$, become essential to knowing the bonding nature. Based on these parameters, Cremer and Kraka (1984) proposed that if $\nabla^2\rho(r_c) > 0$ and $H(r_c) < 0$, then the nature of bonding is partially covalent. It is also stated that if the ratio $-G(r_c)/V(r_c)$ falls in the range 0.5–1, then there exists some degree of covalent character (partial covalent type) and if $-G(r_c)/V(r_c) > 1$, a purely non-covalent type of interaction is formed. Further, the magnitude of $G(r_c)/\rho(r_c) < 1$ is also indicative of the presence of covalency in any bond.

Present case deals with two types of bonds, i.e., one between He-He (in He_2 and $He_2@C_{36}$, $He_2@C_{40}$) and another between He-C (in $He_2@C_{36}$ and $He_2@C_{40}$); corresponding labeled figure is provided in **Figure S2**. From **Table 1**, it is seen that both $\nabla^2\rho(r_c)$ and $H(r_c)$ have values > 0, which means that a non-covalent type of bonding exists between them. The ratios $-G(r_c)/V(r_c)$ and $G(r_c)/\rho(r_c)$ both have a value > 1, which again emphasizes the finding that a non-covalent type of interaction is present between both He-He and He-C bonds. It should be mentioned here that along with positive $\nabla^2\rho(r_c)$, the magnitude of $\rho(r_c)$ at the BCP is also lower than 0.1 au, which is the threshold value for $\rho(r_c)$ considered here, and again confirms that the studied bonds are not of covalent type. Now examining the He-He bonds in the two host fullerenes C_{36} and C_{40}, one can find that the $\rho(r_c)$ value of He-He bond present in C_{36} is the highest between the two hosts, recording a value of 0.045 au. However, it may be noted that for unconfined He_2, the values of $\rho(r_c)$, $\nabla^2\rho(r_c)$, $G(r_c)$, $V(r_c)$, and $H(r_c)$ are very small and almost close to zero, but when it gets confined inside the cages, the values are considerably increased. This indicates that confinement of He_2 inside fullerene C_{36} and C_{40} has affected its various parameters.

Energy Decomposition Analysis

To examine the interdependence of He_2 inside C_{36} and C_{40} fullerene cages, we studied the interaction energy and the different contributing energy terms in connection with the total interaction obtained from all-electron calculations using localized molecular orbital energy decomposition analysis (LMO-EDA). To make a comparison, we also checked the

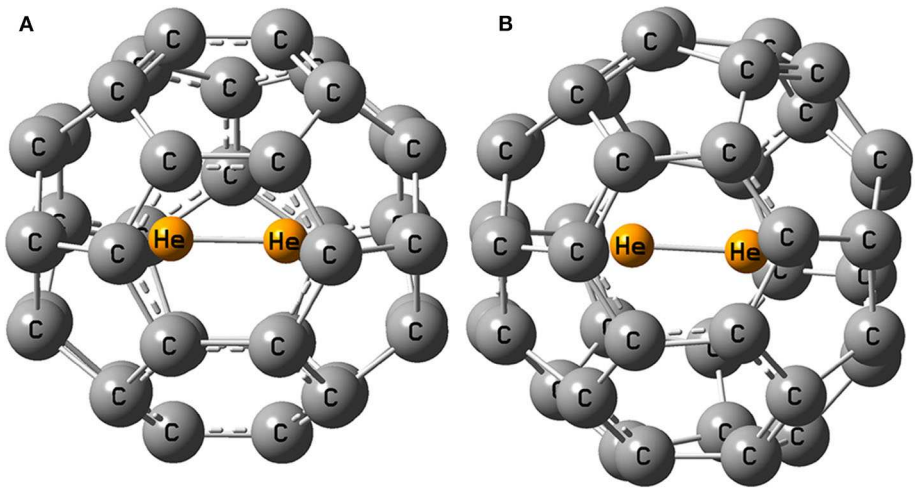

FIGURE 1 | Optimized geometry of **(A)** $He_2@C_{36}$ and **(B)** $He_2@C_{40}$.

TABLE 1 | Electron density descriptors (in au) at the bond critical points (BCPs) in between some selected bonds of He_2, $He_2@C_X$ ($X = 36, 40$).

System	BCP	$\rho(r_c)$	$\nabla^2\rho(r_c)$	$G(r_c)$	$V(r_c)$	$H(r_c)$	$-G(r_c)/V(r_c)$	$G(r_c)/\rho(r_c)$
He_2	He(1)-He(2)	0.002	0.012	0.002	−0.001	0.001	−2.000	1.000
$He_2@C_{36}$	He(37)-He(38)	0.045	0.276	0.066	−0.062	0.003	−1.065	1.467
	He(37)-C(6)	0.026	0.142	0.031	−0.026	0.005	−1.192	1.192
$He_2@C_{40}$	He(41)-He(42)	0.042	0.257	0.060	−0.055	0.005	−1.091	1.429
	He(41)-C(20)	0.025	0.133	0.029	−0.024	0.005	−1.208	1.160

interaction energy for an unconfined He_2 dimer. The interaction energy (E_{int}) can be decomposed into five energy components: electrostatic (E_{elec}), exchange (E_{exc}), repulsion (E_{rep}), polarization (E_{pol}), and dispersion (E_{disp}). This particular study will shed light into the attractive (negative E_{int}) or repulsive (positive E_{int}) nature of interaction between the He_2 molecule and the concerned fullerene cages. For the He_2-entrapped C_{36} and C_{40} fullerenes, He_2 molecule is considered as one fragment and the associated fullerene as the other. Here, the electrostatic energy represents the classical Coulomb interaction, the exchange energy includes the Pauli repulsion. The repulsion energy deals with the contribution coming from the exchange of parallel spin electrons between the two fragments. The energy gained due to the orbital relaxation of one fragment because of the existence of other fragment having undistorted charge distribution in the former fragment's proximity is accounted for the polarization energy. Lastly, the dispersion energy comes from the instantaneous correlation of fluctuating electron density distribution between the two fragments. From **Table 2**, we may find that attractive nature of interaction is found when two He atoms form a He_2 dimer, which is clear from its negative interaction energy. However, the situation is changed as soon as the dimer gets confined inside the two fullerene cages and records a positive value of interaction energy. In case of free He_2 dimer, all the energy components are less in magnitude, with zero contribution coming from the polarization energy. Now, coming to the confined He_2 inside the cages, it can be seen that E_{elec}, E_{exc}, E_{pol}, and E_{disp} energies are attractive in nature. Of all the attractive terms, E_{exc} contributes the most toward the total attraction energy, the second leading contributor being E_{disp} for both the systems. The electrostatic energy makes the third-highest attractive contribution and the polarization term with a smaller value (as compared to other attractive terms) is put in the last of all. However, the Pauli repulsion energy component, E_{rep}, is so repulsive with the highest magnitude (positive) among all other energy terms that it makes the net interaction energy term positive and thus overall repulsive interaction energy is found for He_2 incorporated fullerenes. The highest repulsive energy is found for $He_2@C_{36}$ (149.05 kcal/mol), whereas $He_2@C_{40}$ records much less repulsive energy than $He_2@C_{36}$, with a value 120.18 kcal/mol. It may be noted here that the steep rise in the destabilizing Pauli repulsive energy term in the case of He_2-entrapped C_{36} and C_{40} fullerene and a positive interaction energy is due to the compression of bond distance in He_2 dimer confined inside the cages in comparison to the isolated He_2 dimer. One important finding is that when compared to He_2 entrapped in $B_{12}N_{12}$ and $B_{16}N_{16}$ cages (Khatua et al., 2014a), the total interaction energy is much lowered in the present study owing to the increase in the size of the fullerene cages. This may indicate that larger cages can accommodate He_2 dimer easily and may at some point stabilize the whole system.

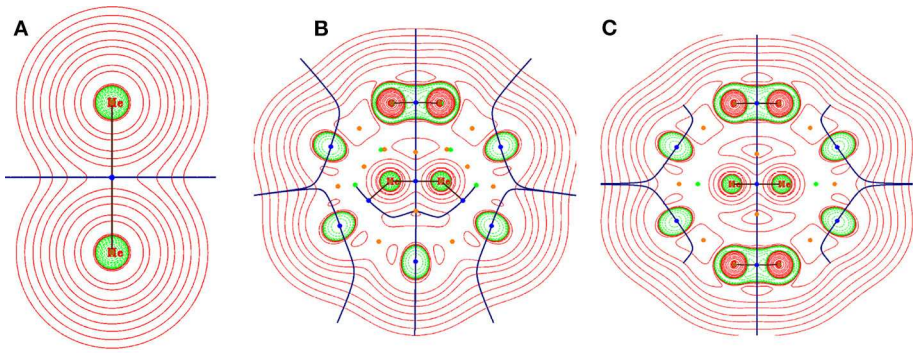

FIGURE 2 | Contour plot representation of Laplacian of electron density at a particular plane of **(A)** He_2, **(B)** $He_2@C_{36}$, and **(C)** $He_2@C_{40}$. Red region depicts the area having $\nabla^2 \rho(r_c) > 0$ and green region depicts the area having $\nabla^2 \rho(r_c) < 0$.

TABLE 2 | Energy decomposition analysis of He_2 and $He_2@C_X$ ($X = 36, 40$).

System	E_{int}	E_{elec}	E_{exc}	E_{rep}	E_{pol}	E_{disp}
He_2	−0.02	−0.02	−0.07	0.20	−0.00	−0.12
$C_{36}@He_2$	28.98	−25.02	−48.98	149.05	−7.54	−38.52
$C_{40}@He_2$	21.29	−19.74	−38.21	120.18	−5.89	−35.06

All the values are in kcal/mol.

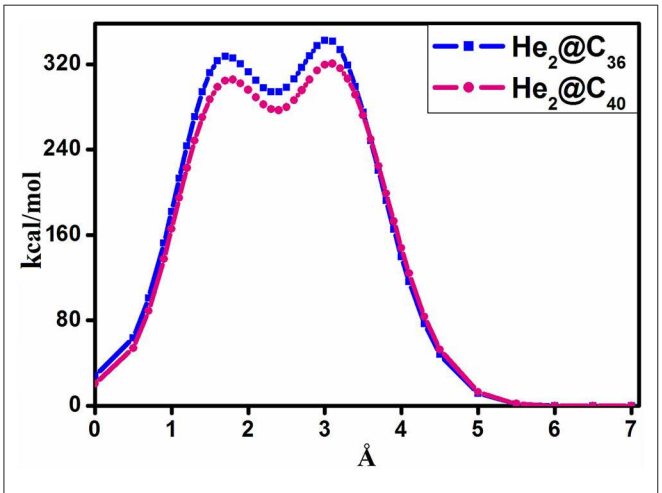

FIGURE 3 | Boundary-crossing barrier of $He_2@C_X$ ($X = 36, 40$).

Barrier Crossing Energy

The barrier crossing energy of $He_2@C_{36}$ and $He_2@C_{40}$ fullerenes have been depicted in **Figure 3**. The potential of an atom or a molecule to enter/exit into/from a fullerene cage is measured by speculating the boundary-crossing barriers. The corresponding energies provide information about the permeability and kinetic barrier of the atom or the molecule for crossing the boundary of the fullerene cage. Thus, to observe the movement of He_2 through C_{36} and C_{40} fullerenes, the boundary-crossing barrier has been studied. Also, five pictures of He_2 encapsulation in fullerenes are shown in **Figure 4**. Now, since an easy translation of the dimer into the cage can be done through a six-membered ring (instead of five-membered ring), the scanning process for its barrier crossing is calculated through a hexagon only. From **Figure 3**, we may observe that there are two peaks for each of the curves, with the second one (2nd maxima) from left much steeper than the first one (1st maxima). The barrier crossing energy is calculated in such a way that at the beginning the He_2 dimer is put at a distance of 7 Å from the center and then it is moved toward the cage to finally get placed in the center of the fullerene cage. The energy along this path is noted and the resulting curve is shown in **Figure 3**. The presence of two peaks is due to the two He atoms, which enter through the cage. The first peak from right (2nd maxima) corresponds to the energy when the first He atom passes through the cage, then the energy comes down slightly corresponding to the valley between two peaks, where the two He atoms are equally placed, one inside and another outside the surface of the cage. After that, when the second He atom just reaches the surface of the fullerene cage, the corresponding energy again rises (1st maxima), but with a relatively lower magnitude than that of the former peak value. Thereafter the energy value gradually decreases as the He_2 dimer reaches the center of the cage, where it takes the minimum energy position. Among the two cages, namely fullerene C_{36} and C_{40}, it is clear from **Figure 3** that He_2 dimer possesses lower barrier crossing energy when it enters the C_{40} fullerene as compared to C_{36}. Thus, it is obvious that with increase in the size of the cage, it becomes comparatively easier for the He_2 dimer to be encapsulated inside it. Moreover, high energy barrier for the encapsulation process of any atom/molecule to be confined inside any closed complex suggests their kinetic stability, and once these encapsulated clusters are formed, they cannot dissociate into fragments owing to higher kinetic barrier (Sekhar et al., 2017). Here in this study, both the He_2 encapsulated fullerenes, $He_2@C_{36}$ (327. 3 kcal/mol at 1st maxima and 342.2 kcal/mol at 2nd maxima) and $He_2@C_{40}$ (305.4 kcal/mol at 1st maxima and 320.4 kcal/mol at 2nd maxima), have a much higher energy barrier when the two He atoms of the constituting He_2 dimer cross the surface of the fullerene cages. Thus, they may be considered as kinetically stable systems.

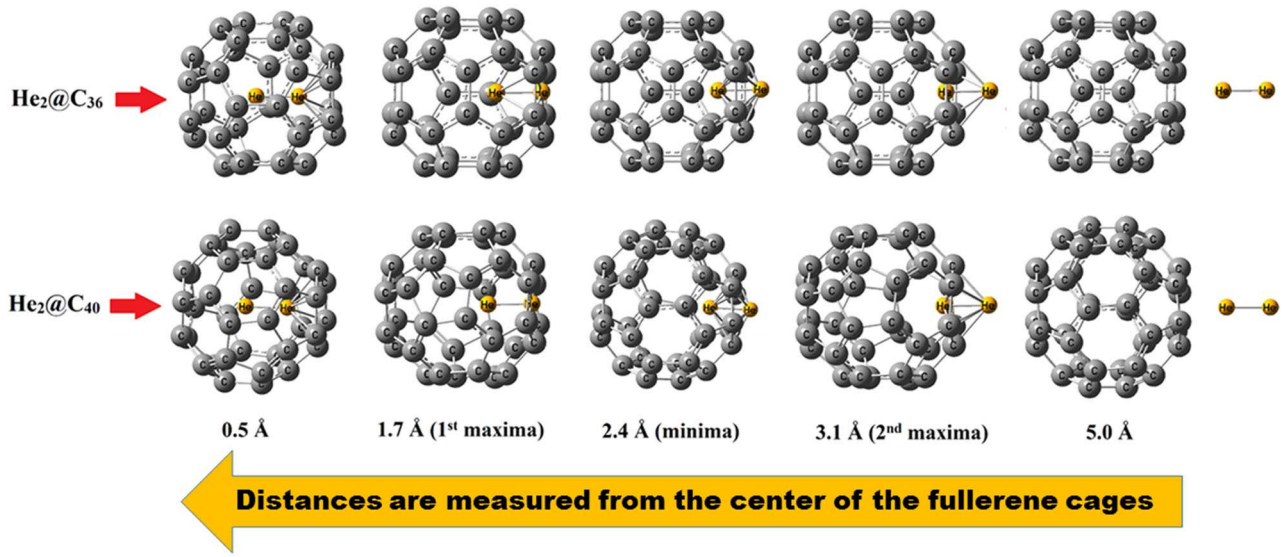

FIGURE 4 | Different pictures during the encapsulation of He_2 inside fullerene C_{36} and C_{40}.

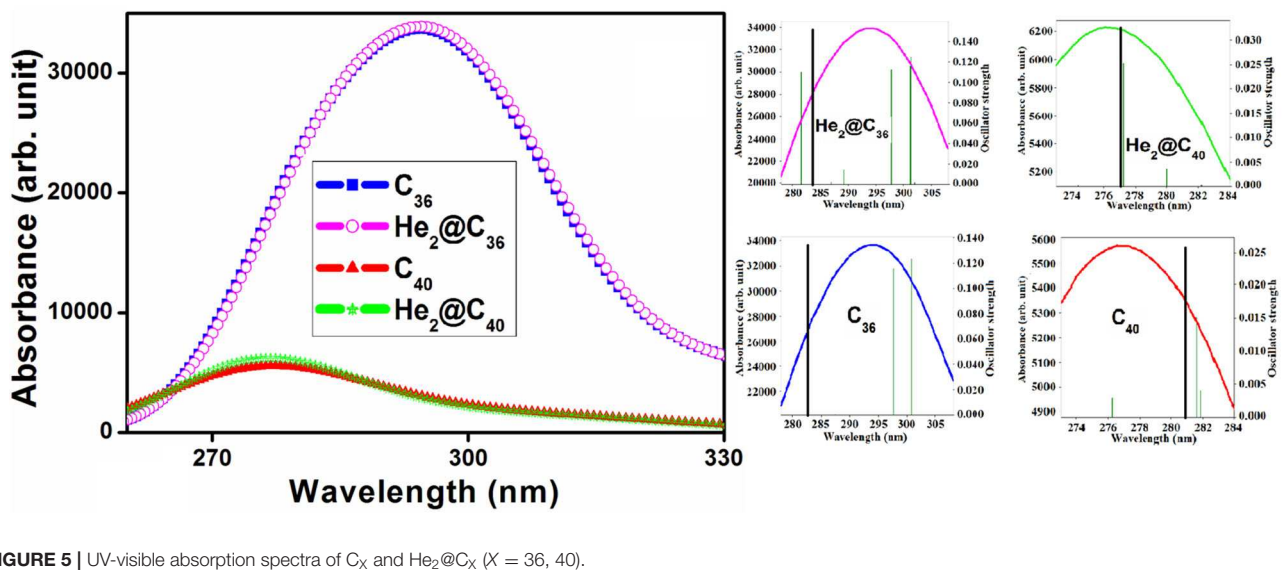

FIGURE 5 | UV-visible absorption spectra of C_X and $He_2@C_X$ ($X = 36, 40$).

Absorption Spectra

Table S1 provides the maximum absorption wavelength (λ_{max}), corresponding transition energy (E_0), highest oscillator strength (f_{max}), and the major electronic transitions of the He_2 encapsulated C_{36} and C_{40} fullerenes along with their empty counterparts. The associated absorption spectra are provided in **Figure 5**. Also, to get a clear view of the highest absorption peak and highest oscillator strength of both bare and He_2-encapsulated fullerenes, a zoom plot is provided. We may see that both the He_2-encaged fullerenes possess absorption maxima in the ultraviolet (UV) region of the spectra with their λ_{max} values of 283.652 and 277.090 nm for $He_2@C_{36}$ and $He_2@C_{40}$, respectively. One may observe that the highest oscillator strength of He_2 confined C_{36} cage (0.1521) is much higher than that of C_{40} cage (0.0324). In addition, the corresponding λ_{max} of $He_2@C_{36}$ is red-shifted toward a higher wavelength compared to $He_2@C_{40}$. Again, from the absorption spectra, it should be pointed out that the maximum absorption of the empty fullerenes, i.e., C_{36} (282.572 nm) and C_{40} (280.669 nm), also occur in the UV region, having slight displacement of the peaks with respect to their He_2-confined analogs. C_{36}, $He_2@C_{36}$ has higher intensity of absorption compared to C_{40}, $He_2@C_{40}$. This is because the former set (C_{36} and $He_2@C_{36}$) has recorded a much higher value of oscillator strength, which significantly increased its absorption maxima with respect to the later set (C_{40} and $He_2@C_{40}$). In addition, the increment in the oscillator strength of C_{36} and

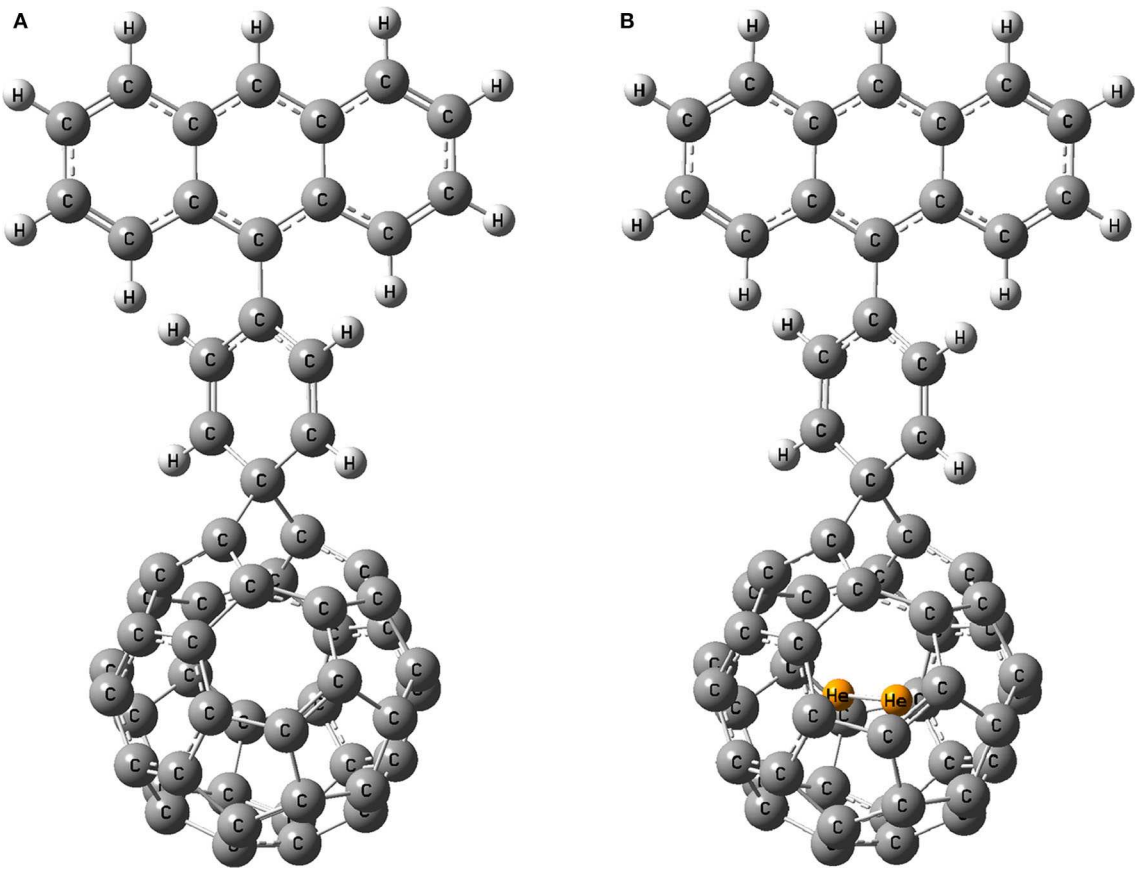

FIGURE 6 | Optimized geometry of dyes **(A)** D1 and **(B)** D1@He_2.

He_2@C_{36} occurs may be due to higher value of transition dipole moment, which ultimately puts an impact on the intensity of the highest electronic transition (Wang et al., 2015).

The shift in the absorption maxima (either blue or red) depends on various factors; for example, the electronic structure (Yanagisawa et al., 2013; Giri et al., 2014), implementation of gas or solvent phase (Giri et al., 2014), orientation of embedded molecule inside any closed cage (Wang et al., 2018), substitution of donor or acceptors (Ma et al., 2019), and sometimes dependency on the method of calculation is also observed (Cárdenas-Jirón et al., 2017). Here, in this case, may be the electronic structure (symmetry, orientation of He_2 inside the fullerenes) plays an important role in this shift. In addition, red shift of the absorption spectra is also associated with a smaller energy gap (HOMO-LUMO gap) (Giri et al., 2014). Thus, He_2@C_{36} (3.028 eV) with comparatively lower value of energy gap than He_2@C_{40} (3.980 eV), has its absorption maxima red shifted toward the greater wavelength region. These systems with their maximum absorption peak falling in the UV region are usable in designing UV light protection devices.

Solar Cell Parameters

The most stable He_2 encapsulated fullerene (He_2@C_{40}) among the two hosts is chosen as the acceptor for designing a solar cell device. To make a comparison, its free counterpart, pristine C_{40}, is also taken as another acceptor. For the study, anthracene as donor and benzene as spacer are being used. For simplicity, we name the dye with acceptor as pristine C_{40} as D1 and that with He_2@C_{40} as D1@He_2. The optimized dyes are shown in **Figure 6**.

The energy levels of a dye molecule, which primarily indicates its HOMO and LUMO, play a very important role in its performance as a solar cell and the corresponding energy level diagram of the dyes is shown in **Figure 7** (HOMO level of the dyes is zoomed). Eventually, the HOMO level of the dye must lie below the redox potential of I_3^-/I^-couple ($\mu_{redox} = -4.80$ eV), while the LUMO level must be placed above the conduction band (CB) edge of TiO_2 semiconductor ($E_{CB} = -4.00$ eV) (Qin et al., 2007). We found that the HOMO level of both the dyes lie just below the redox potential of I_3^-/I^-couple, with a magnitude of −4.821 eV (for D1) and −4.816 eV (for D1@He_2), which confirms that charge regeneration of the dyes is possible. The LUMO value of dye, D1, is calculated to be −3.736 eV, while that of D1@He_2 is −3.795 eV. This means the LUMO levels of both the dyes lie above the conduction band of TiO_2, and thus electron injection from the excited dyes to the conduction band of the semiconductor (TiO_2) will become easier. However, on comparing the HOMO and LUMO values of both the dyes, one may observe that the LUMO of D1 acquires

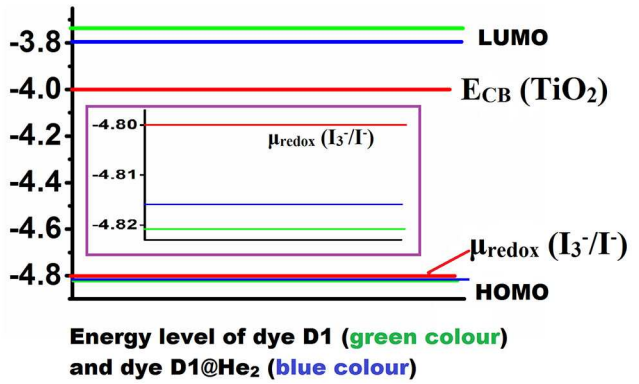

FIGURE 7 | Energy level diagram of dyes D1 and D1@He_2.

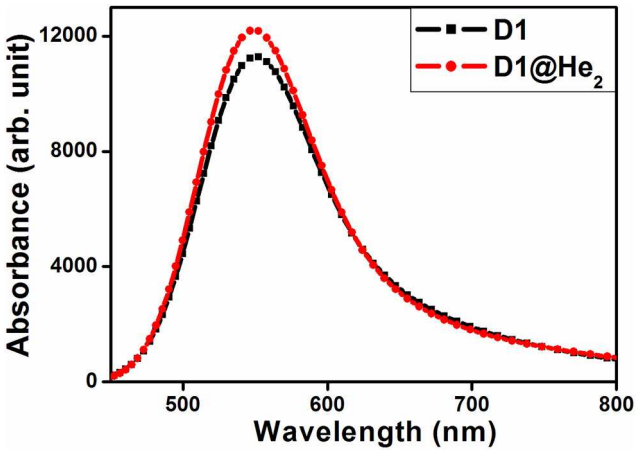

FIGURE 8 | UV-visible absorption spectra of dyes D1 and D1@He_2.

some appreciable changes when He_2 dimer is inserted in the acceptor (i.e., D1@He_2 dye), but there is very less change in the HOMO energy. Therefore, it can be inferred that changing the acceptor can only affect the LUMO energy level of the dye. Moreover, dye D1 with comparatively higher LUMO value than D1@He_2 will help to increase the open-circuit voltage, opening a path to improve the efficiency of the dye-sensitized solar cell. The energy gap of dyes D1 and D1@He_2 are calculated to be 1.085 and 1.021 eV, respectively. Thus, dye D1@He_2 with a relatively smaller energy gap and a comparatively higher light-harvesting efficiency will show a better result.

Absorption Properties

Here we have calculated the UV-visible absorption spectra of both the dyes (**Figure 8**) considering the lowest 40 transitions and results are provided in **Table S2**. One may observe that the maximum absorption wavelength corresponding to the highest oscillator strength (0.1456) of D1 dye falls at 547.126 nm with major transitions from HOMO → LUMO+3 (55%), HOMO → LUMO+5 (20%). For dye D1@He_2, the highest oscillator strength increases to 0.1570 and there is a blue shift of the maximum absorption peak as compared to dye D1, located at 545.897 nm. There are two major transitions found for D1@He_2 dye that take place from HOMO → LUMO+3 (53%) and HOMO → LUMO+5 (20%). Both the dyes show absorption in the visible region occurring at around 550 nm. From this study, we can infer that He_2 dimer incorporation inside C_{40} increases the oscillator strength of dye D1. Thus, based on the study of absorption spectra, it is found that dye D1@He_2 possesses a comparatively higher light-harvesting efficiency resulting a greater photocurrent response.

Short-Circuit Current and Open-Circuit Voltage

The short circuit current (J_{SC}) (Zhang et al., 2012) is given by the relation

$$J_{SC} = \int_{\lambda} LHE(\lambda)\phi_{inject}\eta_{collect}d\lambda \tag{3}$$

It greatly depends on the light-harvesting efficiency (*LHE*) and electron injection efficiency (ϕ_{inject}). For the systems differing only in the choice of dyes, $\eta_{collect}$ can be assumed constant.

$$LHE \text{ may be determined using } LHE = 1 - 10^{-f_{\max}} \tag{4}$$

On the other hand, ϕ_{inject} is related to the free energy of electron injection from the excited states of dye to the semiconductor surface (ΔG_{inject}), which can be expressed as

$$\phi_{inject} \propto f\left(\Delta G_{inject}\right) \tag{5}$$

ΔG_{inject} can be estimated using the following equation (Katoh et al., 2004),

$$\Delta G_{inject} = E_{ox}^{dye*} - E_{CB} = E_{ox}^{dye} + E_0 - E_{CB} \tag{6}$$

where E_{ox}^{dye*} represents the excited state oxidation potential of the dye, E_{ox}^{dye} represents the ground state oxidation potential of the dye, E_0 is the vertical transition energy corresponding to the maximum absorption wavelength of the dye, and E_{CB} refers to the conduction band edge of the semiconductor (TiO_2).

The computed results of various quantities involved in the calculation of J_{SC} are provided in **Table 3** for both the dyes. With the increase in the magnitude of E_{ox}^{dye*}, ΔG_{inject} increases, which ultimately increases the ϕ_{inject}. Out of the two dyes, dye with the He_2 dimer records the highest LHE value and thus will have a tendency to absorb more photons, which will lead to a higher magnitude of the short circuit current in comparison to dye D1. Also, according to a study (Islam et al., 2003), the electron injection efficiency of a dye is approximately equal to 1 when $|\Delta G_{inject}| > 0.2$. Here, we can see that both the dyes have a value of ΔG_{inject}, which are much higher than 0.2. Thus, both of them possess sufficient driving force for electron injection to the semiconductor TiO_2.

The open-circuit voltage (V_{OC}) of a dye molecule can be evaluated approximately by finding the difference in

TABLE 3 | Calculated solar cell parameters of dyes D1 and D1@He_2.

Dye	E_{ox}^{dye} (eV)	E_0 (eV)	E_{ox}^{dye*} (eV)	ΔG_{inject} (eV)	(f_{max})	*LHE*	eV_{OC} (eV)
D1	−4.821	2.266	−2.555	1.445	0.1456	0.2848	0.264
D1@He_2	−4.816	2.271	−2.545	1.455	0.1570	0.3034	0.205

energy between the LUMO energy level of the dye and the conduction band edge E_{CB} of the semiconductor substrate, which may be represented by the mathematical relation (Sang-aroon et al., 2012),

$$eV_{OC} = E_{LUMO} - E_{CB} \quad (7)$$

The eV_{OC} values of the dyes are given in **Table 3**. The equation indicates that higher the magnitude of the LUMO level of the dye, the higher open-circuit voltage (V_{OC}) it will generate. From **Table 3** we can see that dye D1 records greater value of eV_{OC} than its He_2 dimer encapsulated counterpart, which has a comparatively higher value of ΔG_{inject}. This may be due to the fact that too high value of ΔG_{inject} leads to energy redundancy, making a fall in the value of V_{OC} (Li et al., 2017). Hence though the dye D1@He_2 has a higher ΔG_{inject}, but it possesses a smaller value of V_{OC} than dye D1.

Non-linear Optical Properties

To explore the relationship between the efficiency of the dye molecules and their non-linear optical (NLO) properties, the isotropic polarizability of the dyes has been calculated. The response of any system when it is subjected to an external electric field is characterized by the study of NLO properties of that system (Deb et al., 2020). In case of dye D1, the isotropic polarizability is found to be 574.045 au, while for the dye D1@He_2 the value increases to 577.945 au. This means that inclusion of a He_2 dimer inside C_{40} acceptor improves the dye's polarizability. In addition, dyes having higher magnitudes of polarizability possibly will create strong interaction with its surroundings and will increase the local concentration of acceptor. Thus, the local concentration of the acceptor of the dye D1@He_2, i.e., C_{40}@He_2 is increased on the semiconductor surface, which in turn will increase the possibility of this acceptor to perforate into the dye adsorption layer.

CONCLUSION

Density functional theory has been implemented to assess the various properties of He_2 dimer when encaged inside two fullerene cages, C_{36} and C_{40}. Our study shows that when He_2 is confined in the cages, its bond length considerably decreases. The compression in bond length is more when C_{36} holds the dimer as compared to that of its relatively larger counterpart, C_{40} fullerene. Non-covalent type of interaction exists between the He-He bond, whether in isolated or confined inside the cages, which is confirmed from the electron density analysis. From energy decomposition analysis it is observed that attractive interaction is found for He_2 dimer, but after being encapsulated in the fullerenes, the interaction becomes repulsive. The presence of larger repulsive energy compared to the other attractive energy terms may be responsible for this change in the case of He_2@C_{36} and He_2@C_{40}. Fullerene C_{40} bearing a larger cavity makes He_2 incorporation energetically much easier than that of C_{36} as observed from the investigation of barrier crossing energy. Absorption spectra analysis of both the He_2@C_X shows that they can be potentially used as UV light protectors since they possess absorption maxima in the UV region. Next, we designed a DSSC with free C_{40} and He_2 confined C_{40} as acceptors. Charge regeneration and electron injection, which are the two most important qualities, are being fulfilled here by the dyes. In addition, both the dyes show an absorption peak in the visible region, which is another criterion for a DSSC. He_2@C_{40}, when used as acceptor, records the highest LHE value and thus will have a higher magnitude of J_{SC}. NLO properties of the dyes are also calculated, and we found that the dye with He_2-confined C_{40} acceptor has greater polarizability and thus will have higher possibility to perforate into the dye adsorption layer. This indicates that He_2 incorporation inside fullerene really has a good effect on different properties.

DATA AVAILABILITY STATEMENT

The raw data supporting the conclusions of this article will be made available by the authors, without undue reservation.

AUTHOR CONTRIBUTIONS

DP has played the lead role in data collection, analysis, visualization, and writing original draft. HD has played a supporting role in data extraction and formal analysis. US has a lead role in supervision, funding and software, and supporting role in conceptualization. All authors contributed to the article and approved the submitted version.

ACKNOWLEDGMENTS

DP thanks, University Grant Commission for her fellowship. US would like to thank DST, New Delhi, India for providing the financial support from SERB project (File No. EMR/2016/006764).

SUPPLEMENTARY MATERIAL

The Supplementary Material for this article can be found online at: https://www.frontiersin.org/articles/10.3389/fchem.2020.00621/full#supplementary-material

REFERENCES

Ayub, K. (2017). Binding affinity and permeation of $X_{12}Y_{12}$ nanoclusters for helium and neon. *J. Mol. Liquids* 244, 124–134. doi: 10.1016/j.molliq.2017.08.118

Bader, R. F. W. (1990). *Atoms in Molecules: A Quantum Theory*. Clarendon: Oxford.

Bartlett, N. (1962). Xenon hexafluoroplatinate (V) $Xe^{+}[PtF_6]^{-}$. *Proc. Chem. Soc.* 6:218.

Becker, L., Poreda, R. J., and Bada, J. L. (1996). Extraterrestrial helium trapped in fullerenes in the sudbury impact structure. *Science* 272, 249–252. doi: 10.1126/science.272.5259.249

Bhusal, S., Zope, R. R., Bhatta, S., and Baruah, T. (2016). Electronic and optical properties of $VSc_2N@C_{68}$ fullerene. *J. Phys. Chem. C* 120, 27813–27819. doi: 10.1021/acs.jpcc.6b08904

Cárdenas-Jirón, G., Borges-Martínez, M., Sikorski, E., and Baruah, T. (2017). Excited states of light-harvesting systems based on fullerene/graphene oxide and porphyrin/smaragdyrin. *J. Phys. Chem. C* 121, 4859–4872. doi: 10.1021/acs.jpcc.6b12452

Cerpa, E., Krapp, A., Flores-Moreno, R., Donald, K. J., and Merino, G. (2009). Influence of endohedral confinement on the electronic interaction between He atoms: a $He_2@C_{20}H_{20}$ case study. *Chem. Eur. J.* 15, 1985–1990. doi: 10.1002/chem.200801399

Chakraborty, D., Pan, S., and Chattaraj, P. K. (2016). Encapsulation of small gas molecules and rare gas atoms inside the octa acid cavitand. *Theor. Chem. Acc.* 135:119. doi: 10.1007/s00214-016-1876-y

Chandrakumar, K. R. S., and Ghosh, S. K. (2008). Alkali-metal-induced enhancement of hydrogen adsorption in C_{60} fullerene: an *ab initio* study. *Nano Lett.* 8, 13–19. doi: 10.1021/nl071456i

Chattaraj, P. K., and Sarkar, U. (2003). Effect of spherical confinement on chemical reactivity. *J. Phys. Chem. A* 107, 4877–4882. doi: 10.1021/jp034321j

Cremer, D., and Kraka, E. (1984). Chemical bonds without bonding electron density? Does the difference electron-density analysis suffice for a description of the chemical bond? *Angew. Chem. Int. Ed. Engl.* 23, 627–628. doi: 10.1002/anie.198406271

Darzynkiewicz, R. B., and Scuseria, G. E. (1997). Noble gas endohedral complexes of C_{60} buckminsterfullerene. *J. Phys. Chem. A* 101, 7141–7144. doi: 10.1021/jp971323t

Deb, J., Bhattacharya, B., Paul, D., and Sarkar, U. (2016b). Interaction of nitrogen molecule with pristine and doped graphyne nanotube. *Phys. E* 84, 330–339. doi: 10.1016/j.physe.2016.08.006

Deb, J., Bhattacharya, B., and Sarkar, U. (2016a). Confinement of water molecule inside (2, 2) graphyne nanotube. *AIP Conf. Proc.* 1731:050081. doi: 10.1063/1.4947735

Deb, J., Paul, D., and Sarkar, U. (2020). Density functional theory investigation of nonlinear optical properties of T-graphene quantum dots. *J. Phys. Chem. A* 124, 1312–1320. doi: 10.1021/acs.jpca.9b10241

Deb, J., Paul, D., Sarkar, U., and Ayers, P. W. (2018). Characterizing the sensitivity of bonds to the curvature of carbon nanotubes. *J. Mol. Model.* 24:249. doi: 10.1007/s00894-018-3793-6

Eom, S. H., Baek, M.-J., Park, H., Yan, L., Liu, S., You, W., et al. (2014). Roles of interfacial modifiers in hybrid solar cells: inorganic/polymer bilayer vs inorganic/polymer: fullerene bulk heterojunction. *ACS Appl. Mater. Interfaces* 6, 803–810. doi: 10.1021/am402684w

Feldman, V., Sukhov, F., and Orlov, A. Y. (1997). Further evidence for formation of xenon dihydride from neutral hydrogen atoms: a comparison of ESR and IR spectroscopic results. *Chem. Phys. Lett.* 280, 507–512. doi: 10.1016/S0009-2614(97)01208-6

Feldman, V. I., and Sukhov, F. F. (1996). Formation and decay of transient xenon dihydride resulting from hydrocarbon radiolysis in a xenon matrix. *Chem. Phys. Lett.* 255, 425–430. doi: 10.1016/0009-2614(96)00346-6

Fernández, I., Solà, M., and Bickelhaupt, F. M. (2014). Origin of reactivity trends of noble gas endohedral fullerenes $Ng_2@C_{60}$ (Ng = He to Xe). *J. Chem. Theory Comput.* 10, 3863–3870. doi: 10.1021/ct500444z

Frisch, M. J., Trucks, G. W., Schlegel, H. B., Scuseria, G. E., Robb, M. A., Cheeseman, J. R., et al. (2009). *Gaussian 09, Revision D.01*. Wallingford, CT: Gaussian, Inc.

Ghara, M., Pan, S., Deb, J., Kumar, A., Sarkar, U., and Chattaraj, P. K. (2016). A computational study on structure, stability and bonding in noble gas bound metal nitrates, sulfates and carbonates (Metal = Cu, Ag, Au). *J. Chem. Sci.* 128, 1537–1548. doi: 10.1007/s12039-016-1150-9

Giblin, D. E., Gross, M. L., Saunders, M., Jiménez-Vázquez, H., and Cross, R. J. (1997). Incorporation of helium into endohedral complexes of C_{60} and C_{70} containing noble-gas atoms: a tandem mass spectrometry study. *J. Am. Chem. Soc.* 119, 9883–9890. doi: 10.1021/ja971104l

Giri, S., Moore, C. H., Mcleskey, J. T., and Jena, P. (2014). Origin of red shift in the photoabsorption peak in MEH-PPV polymer. *J. Phys. Chem. C* 118, 13444–13450. doi: 10.1021/jp5030069

Guha, S., and Nakamoto, K. (2005). Electronic structures and spectral properties of endohedral fullerenes. *Coord. Chem. Rev.* 249, 1111–1132. doi: 10.1016/j.ccr.2004.11.017

Haaland, A., Shorokhov, D. J., and Tverdova, N. V. (2004). Topological analysis of electron densities: is the presence of an atomic interaction line in an equilibrium geometry a sufficient condition for the existence of a chemical bond? *Chem. Eur. J.* 10, 4416–4421. doi: 10.1002/chem.200400663

Hohenstein, E. G., Chill, S. T., and Sherrill, C. D. (2008). Assessment of the performance of the M05-2X and M06-2X exchange-correlation functionals for noncovalent interactions in biomolecules. *J. Chem. Theory Comput.* 4, 1996–2000. doi: 10.1021/ct800308k

Hummelen, J. C., Prato, M., and Wudl, F. (1995). There is a hole in my bucky. *J. Am. Chem. Soc.* 117, 7003–7004. doi: 10.1021/ja00131a024

Islam, A., Sugihara, H., and Arakawa, H. (2003). Molecular design of ruthenium(II) polypyridyl photosensitizers for efficient nanocrystalline TiO_2 solar cells. *J. Photochem. Photobiol. A* 158, 131–138. doi: 10.1016/S1010-6030(03)00027-3

Jaroš, A., Bonab, E. F., Straka, M., and Foroutan-Nejad, C. (2019). Fullerene-based switching molecular diodes controlled by oriented external electric fields. *J. Am. Chem. Soc.* 141, 19644–19654. doi: 10.1021/jacs.9b07215

Jiménez-Vázquez, H. A., Tamariz, J., and Cross, R. J. (2001). Binding energy in and equilibrium constant of formation for the dodecahedrane compounds $He@C_{20}H_{20}$ and $Ne@C_{20}H_{20}$. *J. Phys. Chem. A* 105, 1315–1319. doi: 10.1021/jp0027243

Katoh, R., Furube, A., Yoshihara, T., Hara, K., Fujihashi, G., Takano, S., et al. (2004). Efficiencies of electron injection from excited N3 dye into nanocrystalline semiconductor (ZrO_2, TiO_2, ZnO, Nb_2O_5, SnO_2, In_2O_3) films. *J. Phys. Chem. B* 108, 4818–4822. doi: 10.1021/jp031260g

Khatua, M., Pan, S., and Chattaraj, P. K. (2014a). Confinement induced binding of noble gas atoms. *J. Chem. Phys.* 140:164306. doi: 10.1063/1.4871800

Khatua, M., Pan, S., and Chattaraj, P. K. (2014b). Movement of Ng_2 molecules confined in a C_{60} cage: an *ab initio* molecular dynamics study. *Chem. Phys. Lett.* 610-611, 351–356. doi: 10.1016/j.cplett.2014.06.052

Khatua, M., Sarkar, U., and Chattaraj, P. K. (2014c). Reactivity dynamics of a confined molecule in presence of an external magnetic field. *Int. J. Quantum Chem.* 115, 144–157. doi: 10.1002/qua.24801

Khong, A., Jiménez-Vázquez, H. A., Saunders, M., Cross, R. J., Laskin, J., Peres, T., et al. (1998). An NMR study of He_2 inside C_{70}. *J. Am. Chem. Soc.* 120, 6380–6383. doi: 10.1021/ja980142h

Krapp, A., and Frenking, G. (2007). Is this a chemical bond? a theoretical study of $Ng_2@C_{60}$ (Ng = He, Ne, Ar, Kr, Xe). *Chem. Eur. J.* 13, 8256–8270. doi: 10.1002/chem.200700467

Kroto, H. W., Heath, J. R., O'Brien, S. C., Curl, R. F., and Smalley, R. E. (1985). C_{60}: buckminsterfullerene. *Nature* 318, 162–163. doi: 10.1038/318162a0

Laskin, J., Peres, T., Lifshitz, C., Saunders, M., Cross, R. J., and Khong, A. (1998). An artificial molecule of Ne_2 inside C_{70}. *Chem. Phys. Lett.* 285, 7–9. doi: 10.1016/S0009-2614(97)01473-5

Leng, C., Qin, H., Si, Y., and Zhao, Y. (2014). Theoretical prediction of the rate constants for exciton dissociation and charge recombination to a triplet state in PCPDTBT with different fullerene derivatives. *J. Phys. Chem. C* 118, 1843–1855. doi: 10.1021/jp410562u

Li, Y., Li, Y., Song, P., Ma, F., Liang, J., and Sun, M. (2017). Screening and design of high-performance indoline-based dyes for DSSCs. *RSC Adv.* 7, 20520–20536. doi: 10.1039/C6RA28396A

Liu, T., and Troisi, A. (2011). Absolute rate of charge separation and recombination in a molecular model of the P3HT/PCBM interface. *J. Phys. Chem. C* 115, 2406–2415. doi: 10.1021/jp109130y

Lu, T., and Chen, F. (2011). Multiwfn: a multifunctional wavefunction analyzer. *J. Comput. Chem.* 33, 580–592. doi: 10.1002/jcc.22885

Ma, N., Lv, M., Liu, T., Song, M., Liu, Y., and Zhang, G. (2019). Second-order nonlinear optical properties of [60] fullerene-fused dihydrocarboline derivates: a theoretical study on switch effect. *J. Mater. Chem. C* 7, 13052–13058. doi: 10.1039/C9TC04126E

Małolepsza, E., Witek, H. A., and Irle, S. (2007). Comparison of geometric, electronic, and vibrational properties for isomers of small fullerenes C_{20}-C_{36}. *J. Phys. Chem. A* 111, 6649–6657. doi: 10.1021/jp068529r

Martín, N. (2006). New challenges in fullerene chemistry. *Chem. Commun.* 20, 2093–2104. doi: 10.1039/B601582B

O'Boyle, N. M., Tenderholt, A. L., and Langner, K. M. (2008). cclib: a library for package-independent computational chemistry algorithms. *J. Comput. Chem.* 29, 839–845. doi: 10.1002/jcc.20823

O'Regan, B., and Grätzel, M. (1991). A low-cost, high-efficiency solar cell based on dye-sensitized colloidal TiO_2 films. *Nature* 353, 737–740. doi: 10.1038/353737a0

Osuna, S., Swart, M., and Solà, M. (2011). The reactivity of endohedral fullerenes. What can be learnt from computational studies? *Phys. Chem. Chem. Phys.* 13, 3585–3603. doi: 10.1039/C0CP01594F

Pan, S., Contreras, M., Romero, J., Reyes, A., Merino, G., and Chattaraj, P. K. (2013a). $C_5Li_7^+$ and $O_2Li_5^+$ as noble gas trapping agents. *Chem. Eur. J.* 19, 2322–2329. doi: 10.1002/chem.201203245

Pan, S., Ghara, M., Kar, S., Zarate, X., Merino, G., and Chattaraj, P. K. (2018). Noble gas encapsulated B_{40} cage. *Phys. Chem. Chem. Phys.* 20, 1953–1963. doi: 10.1039/C7CP07890K

Pan, S., Gupta, A., Mandal, S., Moreno, D., Merino, G., and Chattaraj, P. K. (2015a). Metastable behavior of noble gas inserted tin and lead fluorides. *Phys. Chem. Chem. Phys.* 17, 972–982. doi: 10.1039/C4CP03856H

Pan, S., Gupta, A., Saha, R., Merino, G., and Chattaraj, P. K. (2015b). A coupled-cluster study on the noble gas binding ability of metal cyanides versus metal halides (Metal = Cu, Ag, Au). *J. Comp. Chem.* 36, 2168–2176. doi: 10.1002/jcc.24190

Pan, S., Jalife, S., Kumar, R. M., Subramanian, V., Merino, G., and Chattaraj, P. K. (2013b). Structure and stability of $(NG)_n$ $CN_3Be_3^+$ clusters and comparison with $(NG)BeY^{0/+}$. *ChemPhysChem* 15, 2511–2517. doi: 10.1002/cphc.201300357

Pan, S., Jalife, S., Romero, J., Reyes, A., Merino, G., and Chattaraj, P. K. (2013c). Attractive Xe-Li interaction in Li-decorated clusters. *Comput. Theor. Chem.* 1021, 62–69. doi: 10.1016/j.comptc.2013.06.026

Pan, S., Mandal, S., and Chattaraj, P. K. (2015c). Cucurbit[6]uril: a possible host for noble gas atoms. *J. Phys. Chem. B* 119, 10962–10974. doi: 10.1021/acs.jpcb.5b01396

Pan, S., Moreno, D., Cabellos, J. L., Merino, G., and Chattaraj, P. K. (2014a). An *ab initio* study on the stability of $Ng_nBe_2N_2$, $Ng_nBe_3N_2$, and $NgBeSiN_2$ clusters (Ng = He-Rn). *ChemPhysChem* 15, 2618–2625. doi: 10.1002/cphc.201402101

Pan, S., Moreno, D., Cabellos, J. L., Romero, J., Reyes, A., Merino, G., and Chattaraj, P. K. (2014b). In quest of strong Be-Ng bonds among the neutral Ng-Be complexes. *J. Phys. Chem. A* 118, 487–494. doi: 10.1021/jp409941v

Pan, S., Moreno, D., Merino, G., and Chattaraj, P. K. (2014c). Stability of noble-gas-bound SiH_3^+ clusters. *ChemPhysChem* 15, 3554–3564. doi: 10.1002/cphc.201402370

Parey, V., Jyothirmai, M. V., Kumar, E. M., Saha, B., Gaur, N. K., and Thapa, R. (2019). Homonuclear B_2/B_3 doped carbon allotropes as a universal gas sensor: possibility of CO oxidation and CO_2 hydrogenation. *Carbon* 143, 38–50. doi: 10.1016/j.carbon.2018.10.060

Paul, D., Deb, J., Bhattacharya, B., and Sarkar, U. (2017). Density functional theory study of pristine and transition metal doped fullerene. *AIP Conf. Proc.* 1832:050107. doi: 10.1063/1.4980340

Paul, D., Deb, J., Bhattacharya, B., and Sarkar, U. (2018a). Electronic and optical properties of C_{24}, $C_{12}X_6Y_6$, and $X_{12}Y_{12}$ (X = B, Al and Y = N, P). *J. Mol. Model.* 24:204. doi: 10.1007/s00894-018-3735-3

Paul, D., Deb, J., Bhattacharya, B., and Sarkar, U. (2018b). The influence of the substitution of transition metals on pristine C_{20}: a DFT study. *Int. J. Nano. Sci.* 16:1760026. doi: 10.1142/S0219581X17600262

Paul, D., Deb, J., and Sarkar, U. (2019). Influence of noble gas atoms on $B_{12}N_{12}$ fullerene: a DFT study. *AIP Conf. Proc.* 2115:030171. doi: 10.1063/1.5113010

Pettersson, M., Lundell, J., Khriachtchev, L., Isoniemi, E., and Räsänen, M. (1998). HXeSH, the first example of a xenon-sulfur bond. *J. Am. Chem. Soc.* 120, 7979–7980. doi: 10.1021/ja981032d

Qin, P., Yang, X., Chen, R., Sun, L., Marinado, T., Edvinsson, T., et al. (2007). Influence of π-conjugation units in organic dyes for dye-sensitized solar cells. *J. Phys. Chem. C* 111, 1853–1860. doi: 10.1021/jp065550j

Qu, M., Qin, G., Du, A., Fan, J., and Sun, Q. (2019). B_{80} fullerene: a promising metal-free photocatalyst for efficient conversion of CO_2 to HCOOH. *J. Phys. Chem. C* 123, 24193–24199. doi: 10.1021/acs.jpcc.9b07562

Ravinder, P., and Subramanian, V. (2011). Studies on the encapsulation of various anions in different fullerenes using density functional theory calculations and Born-Oppenheimer molecular dynamics simulation. *J. Phys. Chem. A* 115, 11723–11733. doi: 10.1021/jp203421v

Ravinder, P., and Subramanian, V. (2012). Role of encapsulation of Na^+ and F^- ions on the Diels-Alder reactivity of C_{32}. *J. Phys. Chem. A* 116, 6870–6878. doi: 10.1021/jp3015244

Ross, R. B., Cardona, C. M., Guldi, D. M., Sankaranarayanan, S. G., Reese, M. O., Kopidakis, N., et al. (2009). Endohedral fullerenes for organic photovoltaic devices. *Nat. Mater.* 8, 208–212. doi: 10.1038/nmat2379

Saha, R., Pan, S., Merino, G., and Chattaraj, P. K. (2015). Comparative study on the noble-gas binding ability of BeX clusters (X = SO_4, CO_3, O). *J. Phys. Chem. A* 119, 6746–6752. doi: 10.1021/acs.jpca.5b03888

Sang-aroon, W., Saekow, S., and Amornkitbamrung, V. (2012). Density functional theory study on the electronic structure of monascus dyes as photosensitizer for dye-sensitized solar cells. *J. Photochem. Photobiol. A* 236, 35–40. doi: 10.1016/j.jphotochem.2012.03.014

Sarkar, U., Giri, S., and Chattaraj, P. K. (2009). Dirichlet boundary conditions and effect of confinement on chemical reactivity. *J. Phys. Chem. A* 113, 10759–10766. doi: 10.1021/jp902374d

Sarkar, U., Khatua, M., and Chattaraj, P. K. (2012). A tug-of-war between electronic excitation and confinement in a dynamical context. *Phys. Chem. Chem. Phys.* 14, 1716–1727. doi: 10.1039/C1CP22862E

Saunders, M., Jiménez-Vázquez, H. A., Cross, R. J., Mroczkowski, S., Gross, M. L., Giblin, D. E., et al. (1994). Incorporation of helium, neon, argon, krypton, and xenon into fullerenes using high pressure. *J. Am. Chem. Soc.* 116, 2193–2194. doi: 10.1021/ja00084a089

Saunders, M., Jiménez-Vázquez, H. A., Cross, R. J., and Poreda, R. J. (1993). Stable compounds of helium and neon: $He@C_{60}$ and $Ne@C_{60}$. *Science* 259, 1428–1430. doi: 10.1126/science.259.5100.1428

Schmidt, M. W., Baldridge, K. K., Boatz, J. A., Elbert, S. T., Gordon, M. S., Jensen, J. H., et al. (1993). General atomic and molecular electronic structure system. *J. Comput. Chem.* 14, 1347–1363. doi: 10.1002/jcc.540141112

Sekhar, P., Ghosh, A., Joshi, M., and Ghanty, T. K. (2017). Noble gas encapsulated endohedral zintl ions $Ng@Pb_{12}^{2-}$ and $Ng@Sn_{12}^{2}$ (Ng = He, Ne, Ar, and Kr): a theoretical investigation. *J. Phys. Chem. C* 121, 11932–11949. doi: 10.1021/acs.jpcc.7b03294

Shimata, Y., Ide, M., Tashiro, M., Katouda, M., Imamura, Y., and Saeki, A. (2016). Charge dynamics at heterojunction between face-on/edge-on PCPDTBT and PCBM bilayer: interplay of donor/acceptor distance and local charge carrier mobility. *J. Phys. Chem. C* 120, 17887–17897. doi: 10.1021/acs.jpcc.6b04827

Srinivasu, K., and Ghosh, S. K. (2012). Transition metal decorated porphyrin-like porous fullerene: promising materials for molecular hydrogen adsorption. *J. Phys. Chem. C* 116, 25184–25189. doi: 10.1021/jp3047517

Wang, L., Wang, W.-Y., Qiu, Y.-Q., and Lu, H.-Z. (2015). Second-order nonlinear optical response of electron donor-acceptor hybrids formed between corannulene and metallofullerenes. *J. Phys. Chem. C* 119, 24965–24975. doi: 10.1021/acs.jpcc.5b06870

Wang, L., Ye, J.-T., Wang, H.-Q., Xie, H.-M., and Qiu, Y.-Q. (2018). Third-order nonlinear optical properties of endohedral fullerene $(H_2)_2@C_{70}$ and $(H_2O)_2@C_{70}$ accompanied by the prospective of novel $(HF)_2@C_{70}$. *J. Phys. Chem. C* 122, 6835–6845. doi: 10.1021/acs.jpcc.8b00623

Weiske, T., Boehme, D. K., and Schwarz, H. (1991). Injection of helium atoms into doubly and triply charged carbon (C_{60}) cations. *J. Phys. Chem.* 95, 8451–8452. doi: 10.1021/j100175a011

Yamada, M., Akasaka, T., and Nagase, S. (2010). Endohedral metal atoms in pristine and functionalized fullerene cages. *Acc. Chem. Res.* 43, 92–102. doi: 10.1021/ar900140n

Yanagisawa, S., Yasuda, T., Inagaki, K., Morikawa, Y., Manseki, K., and Yanagida, S. (2013). Intermolecular interaction as the origin of red shifts in absorption spectra of zinc-phthalocyanine from first-principles. *J. Phys. Chem. A* 117, 11246–11253. doi: 10.1021/jp407608w

Zhang, J., Li, H.-B., Sun, S.-L., Geng, Y., Wu, Y., and Su, Z.-M. (2012). Density functional theory characterization and design of high-performance diarylamine-fluorenedyes with different π spacers for dye-sensitized solar cells. *J. Mater. Chem.* 22, 568–576. doi: 10.1039/C1JM 13028E

Zhao, D., Liu, S., Rong, C., Zhong, A., and Liu, S. (2018). Toward understanding the isomeric stability of fullerenes with density functional theory and the information-theoretic approach. *ACS Omega* 3, 17986–17990. doi: 10.1021/acsomega.8b02702

Zou, W., Liu, Y., Liu, W., Wang, T., and Boggs, J. E. (2010). He@$Mo_6Cl_8F_6$: a stable complex of helium. *J. Phys. Chem. A* 114, 646–651. doi: 10.1021/jp908254r

Conflict of Interest: The authors declare that the research was conducted in the absence of any commercial or financial relationships that could be construed as a potential conflict of interest.

frontiers in Chemistry

MINI REVIEW
published: 05 November 2020
doi: 10.3389/fchem.2020.570492

Noble Gases in Solid Compounds Show a Rich Display of Chemistry With Enough Pressure

*Maosheng Miao**

Department of Chemistry and Biochemistry, California State University Northridge, Northridge, CA, United States

In this review, we summarize the rapid progress that has been made in the study of noble gas chemistry in solid compounds under high pressure. Thanks to the recent development of first-principles crystal structure search methods, many new noble gas compounds have been predicted and some have been synthesized. Strikingly, almost all types of chemical roles and interactions are found or predicted in these high-pressure noble gas compounds, ranging from cationic and anionic noble gases to covalent bonds between noble gas atoms, and to hydrogen bond-like noble gas bonds. Besides, the recently discovered He insertion reactions reveal a unique chemical force that displays no local chemical bonding, providing evidence that research into noble gas reactions can advance the frontier of chemistry at the very basic level.

Keywords: noble gas anions, NG–NG bonds, noble gas bond, chemistry without chemical bond, DFT—density functional theory, high pressure

OPEN ACCESS

Edited by:
Sudip Pan,
University of Marburg, Germany

Reviewed by:
Wojciech Grochala,
University of Warsaw, Poland
Xiang-Feng Zhou,
Yanshan University, China

***Correspondence:**
Maosheng Miao
mmiao@csun.edu

Specialty section:
This article was submitted to Theoretical and Computational Chemistry, a section of the journal Frontiers in Chemistry

Received: *08 June 2020*
Accepted: *16 September 2020*
Published: *05 November 2020*

Citation:
Miao M (2020) Noble Gases in Solid Compounds Show a Rich Display of Chemistry With Enough Pressure. Front. Chem. 8:570492. doi: 10.3389/fchem.2020.570492

INTRODUCTION

For many years after their discovery, noble gases (NG) were known as elements that do not have any chemistry. This idea was consolidated by the atomic shell structure and the corresponding theory that all elements are destined to a complete shell while forming compounds. Therefore, the noble gases would remain chemically inert (noble) since their valence orbitals are already completely filled. This doctrine was first challenged in 1933 by Pauling who predicted the formation of KrF_6 and XeF_6 compounds (Pauling, 1933). It took almost another 30 years before the first noble gas compound, $XePtF_6$ was synthesized by Bartlett (1962). Soon after, many Xenon binary compounds such as XeF_4, XeF_2 etc. were obtained (Chernick et al., 1962). By now, there are already a few hundred known noble gas compounds and the list continues to grow (Grochala, 2007). The most recent advancements include the first truly bonded Argon compound, HArF (Khriachtchev et al., 2000), and a striking compound $AuXe_4$ (Sb_2F_{11}) (Seidel and Seppelt, 2000) in which Xenon, a noble gas element, bonds with Au, a noble metal, as a weak reducing and coordinating agent.

A scenario of rich chemistry for NG elements has been rolled out gradually over the past decades, especially while locking them in an extreme chemical environment. For example, many NG elements can be coerced to form charged or strongly polarized species, such as HHe^+ (Hogness and Lunn, 1925), $HNGO^-$ (Li et al., 2005), and $HeOLi_2F_2$, etc. (Grochala, 2012). In contrast, a similar chemical environment is difficult to achieve in solid compounds since the charge neutrality needs to be preserved globally and locally. As a result, the chemical roles that NG elements can play in solid compounds are more limited. Lots of noble gas compounds are not formed by local chemical bonds featuring electron sharing or transfer.

In many of these compounds, noble gases are either bonded to other atoms by weak interactions such as van der Waals force or inserted into the voids preexisting in some solid compounds such as clathrates, C_{60}, etc. (Saunders et al., 1994; Guńka et al., 2015). While forming true chemical bonds in compounds, such as XeF_2, XeO_3, etc., noble gases act like reductants (electron donors).

On the other hand, we can drive chemical interactions to an extreme in solid compounds by applying mechanical pressures so that new chemistry can emerge. Due to both the development of first-principles computer simulations (Zhang et al., 2017; Oganov et al., 2019; Miao et al., 2020) and the diamond anvil cell (DAC) experiments (Mao et al., 2018), numerous novel compounds have been predicted and some have been synthesized. These new compounds under pressure, such as Na_mCl_n (Zhang et al., 2013), H_3S (Drozdov et al., 2015), LaH_n (Pickard et al., 2020), CsF_n (Miao, 2013), etc., show a distinct trend of having a large range of compositions, with very different stoichiometries to the ambient condition. Although many unconventional stoichiometries are caused by the formation of homonuclear bonds or species, such as Cl–Cl in $NaCl_3$, some compounds with atypical compositions are formed due to the change of oxidation states of their constituent elements (Miao et al., 2020). In some extreme cases, the core electrons, such as the 5p electrons of Cs, can be coerced to form chemical bonds, leading to the formation of atypical compounds, such as CsF_3 and CsF_5 (Miao, 2013).

For the same reason, pressure can greatly enrich noble gas chemistry. It goes far beyond the known NG compounds formed by sharing their closed-shell electrons with strong oxidants such as F. In contrast to molecular and ionic species, most of the solid NG compounds under pressure are thermodynamically stable. In this review, we will show that NG elements, under high-pressure, can (1) be oxidized by elements such as Fe that usually are not considered as oxidants, (2) become an oxidant themselves and behave like anions in compounds, (3) form strong NG–NG covalent bonds, (4) form intermolecular NG bonds that are similar to hydrogen bonds, and (5) form stable compounds that are not bound by any local chemical bonds.

METHODS AND THE PROGRESS OF HIGH-PRESSURE CHEMISTRY

The progresses of high-pressure chemistry strongly depend on the development of experimental methods. The first leap of this field is triggered by the development of diamond anvil cell (DAC) and the corresponding heating and measurement techniques. However, high-pressure experiments are usually very difficult, expensive, and time-consuming. Recently, the density functional theory (DFT) calculations have been widely used in predicting phase diagrams of binary compounds under pressure, which gave rise to the second leap of high-pressure chemistry. These "complete ab initio" studies neither use any empirical parameters for electronic structure nor take any crystal structures and chemical bonding information as input. Instead, crystal structures are generated and the globally stable structures are searched, using various algorithms, such as random search (RS) (Pickard and Needs, 2011), genetic algorithm (GA) (Glass et al., 2006; Avery et al., 2019) and particle swarm optimization (PSO) (Wang et al., 2012). In the last decade, numerous new compounds have been predicted by this method without any experimental input and many of them have been confirmed by DAC experiments. Many of these compounds assume atypical compositions, such as $NaCl_3$, CsF_3, H_3S, LaH_{10}, etc. The change of the chemistry and the formation of a plethora of atypical compounds can be roughly grouped into two kinds: those caused by the formation of homonuclear bonds and those caused by the change of oxidation states, both of which can be found in high-pressure noble gas compounds (Miao et al., 2020).

NOBLE GAS CHEMISTRY UNDER HIGH PRESSURE

Oxidation of NG Under Pressure

Although most of noble gas chemistry is about the sharing of their closed-shell electrons, oxidizing NG is not an easy task and most of the stable NG compounds contain F, the strongest oxidant element. Several Xenon oxides exist but they are not stable (Brock and Schrobilgen, 2011; Goettel et al., 2016). Pressure can greatly extend the chemistry of NG as a reductant because the energies of their valence orbitals increase rapidly under pressure and become significantly higher than those of the valence orbitals of oxidant elements. For example, DFT/GA simulations showed that XeO, XeO_2, and XeO_3 become stable at pressures above 83, 102, and 114 GPa (Zhu et al., 2013). A study that combined the DAC experiment and DFT simulation work added two new compositions, Xe_3O_2 and Xe_2O_5, in which Xe adopted mixed oxidation states (Dewaele et al., 2016). Similarly, Kr–O (Zaleski-Ejgierd and Lata, 2016), Xe–N (Peng et al., 2015), and Xe–C (Bovornratanaraks et al., 2019) compounds are predicted by DFT/GA, DFT/PSO, and DFT/GA methods respectively. Probably the most striking prediction is the formation of stable Xe–Fe and Xe–Ni compounds under high pressure (Zhu et al., 2014), which has been confirmed by DAC experiments (Dewaele et al., 2017; Stavrou et al., 2018). Especially, the DFT/PSO calculations showed that $XeFe_3$ and $XeNi_3$ become stable at the pressures and temperatures found in the Earth's core, indicating that the iron core of the Earth might be a chemical reservoir of the missing Xe (Zhu et al., 2014). From the chemistry point of view, it is significant that Xe can be oxidized by Fe or Ni under high pressure, as shown by the large calculated charge transfer from Xe to Fe/Ni in these compounds. The alloying of Xe with transition metals such as Hg has been predicted before, but DFT calculations showed only a slight charge transfer from Xe to Hg (Grochala, 2007).

Anionic Noble Gases Under Pressure

Besides extending the range of reductant chemistry, pressure can endow a new role for NG elements. They might oxidize metals such as Li and Mg and become anions in the corresponding compounds (Li et al., 2015; Miao et al., 2015; Liu et al., 2017). The first example was predicted by the DFT/PSO method, which showed that Mg forms stable compounds with Xe, Kr, and Ar under pressures higher than 125, 250, and 250 GPa, respectively (Miao et al., 2015). Among all the calculated compositions,

MgNG and Mg_2NG are stable under high pressure. These compounds adopt very simple structures. For Xe and Kr, MgNG adopts a $Pm\bar{3}m$ (CsCl) structure, whereas Mg_2NG adopts a P_4/nmm structure. In contrast, both MgAr and Mg_2Ar compounds adopt hexagonal $P6_3/mcm$ structures. The most important chemical feature of these compounds is the charge transfer. As calculated by Bader's Quantum Theory of Atoms in Molecules method (Bader, 1990), there are large charges transferred from Mg to NG, which also strongly depend on the pressure (Miao et al., 2015). For example, the charge transfer from Mg to Xe in MgXe under 100 GPa is 1.5 e/Mg, which is comparable to that in MgO under ambient conditions. From the band structures, these compounds are clearly metallic. The projected density of states (PDOS) reveals that the transferred electrons occupy the Xe 5d orbitals (Miao et al., 2015). Therefore, under high pressure, Xe behaves like a 5d transition metal. The electron localization function (ELF) (Silvi and Savin, 1994) calculations also show large values between Mg and NG, which is also the characteristic of intermetallic compounds. A similar phenomenon has not been found or predicted in any case without compression. The closest sign of anionic NG is a theoretical study that shows a positive electron affinity for Oganesson (Gaston et al., 2002), a synthetic element that has a half-life of about 1 ms.

The Mg-rich compounds show another unique feature in their electronic structures. The charges on Mg and NG do not add up to 0. For example, at 50 GPa, the charges on Xe and Mg are −1.03e/Xe and 1.29e/Mg. There are about 1.54e which are not located on either Mg or Xe (Miao et al., 2015). Both the charge distribution and the ELF plots show that these charges locate at the interstitial sites between Mg and NG atoms (**Figures 1A,B**). Therefore, Mg_2NG is a high-pressure electride (HPE). Electrides are compounds in which some electrons detach from all the atoms and locate at the interstitial sites, playing the role of anions (Dawes et al., 1986). The formation of electrides under high pressure can be explained by the energy change of a local orbital constrained at an interstitial site by the surrounding atoms (Miao and Hoffmann, 2014). Although its energy increases due to the reduced volume under increasing pressure, it may change less significantly than the energies of many atomic orbitals. A series of calculations of these orbital energy changes using a He-matrix model showed that the local orbital energy of the interstitial quasi-atoms (ISQ) decreases relative to that of s and p orbitals with a rate that strongly depends on the atom and the orbital (Miao and Hoffmann, 2014). HPE can form while the energy of ISQ becomes significantly lower than the energy of valence orbitals of the atom, for example, Li and Na. Mg metal has been predicted to become an HPE under pressures higher than 800 GPa (Li et al., 2010). The insertion of NG atoms into the Mg lattice while forming Mg–Xe compounds significantly lowers the pressure of forming HPE.

NG–NG Covalent Bonds in Simple Compounds

The examples of chemical bonds between NG atoms are rare. In principle, they do not form bonds because their valence orbitals are completely filled. However, while one or both NG atoms lose electrons, they may form bonds. Examples of this kind include the Xe–Xe bonds in molecules HXeXeR and RXeXeR′ (R,R′ =F, Cl, Br, I) (Fernández and Frenking, 2012), and the Xe^{2+} cations that occur in $Xe_2^+(Sb_4F_{21})^-$. (Drews and Seppelt, 1997) More recently, an example of the Xe–Xe bond was found unexpectedly in novel Xe–F compounds under pressure (Peng et al., 2016). An experimental study of XeF_2 under compression showed that the XeF_2 molecular crystal transformed into 2D and 3D extended solids and become metallic (Kim et al., 2010). However, the later DFT study did not agree with the proposed structure evolution of XeF_2 under pressure, and therefore cannot explain the observed metallization of the compound (Kurzydlowski et al., 2011). This discrepancy was alleviated by a full-scale computation study of the Xe–F compounds with various compositions (Peng et al., 2016). The PSO based structure search revealed that XeF_2 becomes unstable and decomposes to Xe_2F and XeF_4 at 81 GPa (Peng et al., 2016). DFT calculations using HSE functional show that XeF_2 maintains its energy gap at least up to 100 GPa, whereas Xe_2F is metallic. The observed insulator-metal transition of XeF_2 at 70 GPa might be caused by the partial decomposition of the sample. The metallic transition was not observed in a later experiment where pressure is applied up to 80 GPa without heating the sample (Wu et al., 2017). Throughout its stable pressure range (60–200 GPa), Xe_2F adopts an I4/mcm structure (**Figure 1C**) consisting of intercalated Xe graphitic (graphene-like) layers (**Figure 1D**) (Peng et al., 2016). At 200 GPa, the Xe–Xe distances are 2.573 and 2.636 Å (**Figure 1D**), which is close to the summation of the covalent radius of two Xe atoms. The calculated COHP and ELF prove that the two neighboring Xe atoms form covalent bonds (Peng et al., 2016). The appearance of Xe–Xe bonds in a simple binary compound is due to the enhancement of the homonuclear bond strength under pressure (Miao et al., 2020). It causes the instability of XeF_2, a stoichiometric compound consisting of Xe in its typical oxidation state of +2.

Noble Gas Bonds

Another type of chemical interaction that has been missing in noble gas chemistry is the donor-acceptor weak interaction between molecules, which is similar to hydrogen bonds (Pauling, 1960) Although this type of bond is the strongest for hydrogen, especially while H atoms are bonded with strong oxidant elements such as F and O and become very electrophilic, it has been found for other elements. It was extended to halogens where they are named halogen bonds (Cavallo et al., 2016), and then to chalcogens, pnictogens, etc. (Cavallo et al., 2016). Up till recently, almost all groups of elements in the periodic table have been found to form this type of bond, except noble gases. Recently, Bauzá and Frontera (2015) studied the molecular electrostatic potential surface of XeO_3 and showed that there was an unexpectedly positive potential at the position of the lone pair of Xe^{6+}, indicating that Xe are very electrophilic while in a high oxidation state and can form a noble gas bond. Similar bonding features are also found in XeO_3 and alkylnitrile adducts (Goettel et al., 2016).

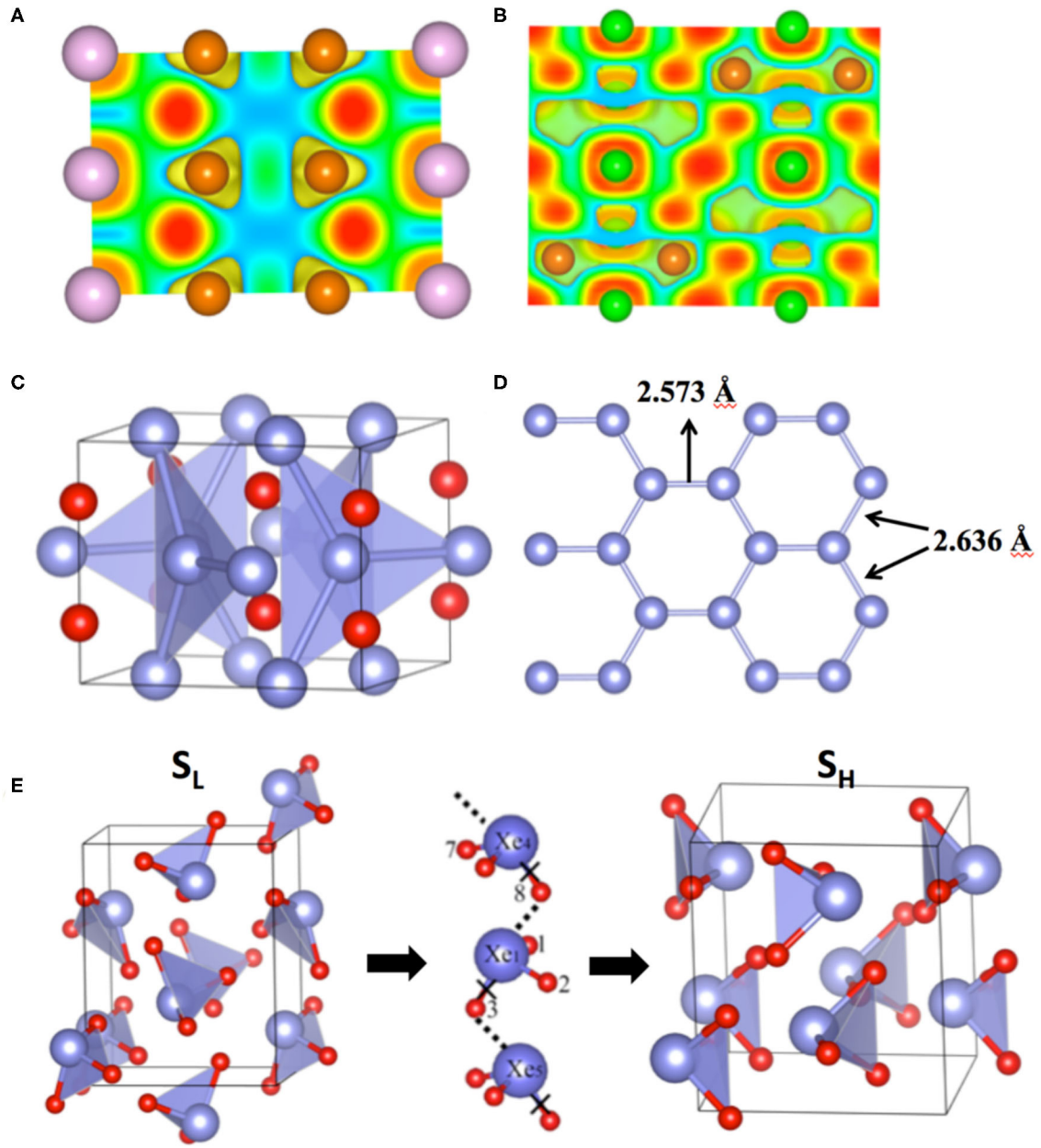

FIGURE 1 | Electronic structure and geometry of compounds containing anionic noble gases, NG–NG covalent bonds and NG bonds. **(A)** Electron localization function (ELF) of Mg_2Kr at 200 GPa; **(B)** ELF of Mg_2Ar at 200 GPa; **(C)** Structure of Xe_2F at 200 GPa; **(D)** The view of one set of Xe atoms in a graphene-like lattice in Xe_2F. The bond lengths are slightly different due to the distortion. **(E)** The low pressure (S_L) and the high pressure (S_H) structures of XeO_3 and the O path for the transition from S_L to S_H or vice versa. Brown, purple and green balls represent Mg, Xe and Ar atoms in **(A)** and **(B)**. Blue and red balls represent Xe and F (or O) atoms in **(C–E)**.

Under increasing pressure, molecular crystals bound by hydrogen bonds behave very differently to molecular crystals without it. In the latter case, the lengths of the covalent intramolecular bonds, such as C–H bonds in CH_4, decrease while the intermolecular distances are reduced by pressure. In contrast, the lengths of some intramolecular bonds, such as H–O in H_2O, increases under compression, if the hydrogen bonds dominate the intermolecular interactions. In accordance with this change, some vibration modes are softened by the external pressure, opposing our chemical intuition that all vibration frequencies should increase while the material is compressed. Therefore, the change of bond lengths and vibration modes

under pressure can be used to demonstrate the presence of hydrogen bonds. The same idea can be applied to noble gas bonds. As shown by a recent computational work of Hou et al. (2017), under increasing pressure, the Xe–O bond lengths of both S_L and S_H increase, and the vibration frequencies of S_H decrease. Furthermore, the strong noble gas bonds between XeO_3 molecules under pressure might provide transition paths for O atoms from one Xe to a neighboring Xe, a process that is essential for the structural transitions between S_L and S_H (**Figure 1E**) (Hou et al., 2015).

Forming Compounds While Keeping Nobility

Being the second most abundant element in the universe, Helium has the highest ionization energy of 24.59 eV and a negative electron affinity. Thus, He shows much less chemistry than most other elements in the periodic table. Yet, several chemical species have been predicted or synthesized by locking He in an unusual chemical environment by exquisitely designed molecular scaffolding (Hogness and Lunn, 1925; Hotokka et al., 1984; Li et al., 2005; Rzepa, 2010; Grochala, 2012). In contrast, the chemistry of He in solid compounds is almost a blank slate except the insertion of He into solid compounds with clathrate or cage structures (Saunders et al., 1994; Guńka et al., 2015). Up till very recently, there is no known reaction of He that can form a stable solid compound. The first example of such is proposed by a thorough structure search study of elements in the periodic table reacting with He under pressure and confirmed by a DAC experiment. Most of the elements were found not to react with He except Na that will form a stable Na_2He compound under pressure higher than 113 GPa (Dong et al., 2017) The enthalpy of formation is as large as a 0.35 eV/atom at a pressure of 350 GPa. Such a large energy gain during the reaction excluded the possibility that Na_2He is bound by weak interactions such as vdW. On the other hand, electronic structure analysis did not show any evidence that He formed chemical bonds with neighboring Na atoms, which immediately give rise to a question: how can He form a stable compound without forming chemical bonds (Miao, 2017)?

The answer to this paradox lies in the unusual behavior of electrons in Na under pressure. At pressures higher than 200 GPa, Na undergoes a structural transition and becomes transparent due to the presence of a large band-gap (Ma et al., 2009). In this double-hexagonal closed-packed structure, the valence electrons of Na detach from all the Na atoms and locate at the interstitial sites and play the role of anions. Electron analysis showed that Na_2He is also an HPE (Dong et al., 2017), although Na atoms form a simple cubic lattice in Na_2He. Therefore, the reaction can be viewed as the insertion of He into the Na_2E ionic compound. Indeed, soon after the discovery of Na_2He, the reaction of He with several other ionic compounds such as Na_2O (Dong et al., 2017), Na_2S (Gao et al., 2019), H_2O (Liu et al., 2015), etc., have been predicted by DFT calculations. Similar to Na_2He, He does not form chemical bonds with neighboring atoms in these compounds.

The driving force of He insertion reactions is electrostatic (Liu et al., 2018; Bai et al., 2019). The key point is that all the above ionic compounds involved in He insertion possess unequal numbers of cations and anions, although the overall charge is neutral. The mechanism can be explained more easily by a one-dimensional model (**Figure 2A**) (Liu et al., 2018). While reacting with the AB type of ionic compounds, He needs to be inserted in between two ions with opposite charges and therefore increase the electrostatic (Madelung) energy. In contrast, if the ionic compound is an A_2B (or AB_2) type, He atoms can choose to stay in between two ions (such as A^+) with the same charge and therefore lower the Madelung energy. The two A^+ ions repel each other, but are forced to stay close by external pressure. The insertion of the He in between two A+ ions alleviates this pressure effect, therefore the insertion of He in this type of ionic compounds becomes favored under increasing pressure. Thus, the reaction does not involve the formation of any local chemical bond, i.e., He can react with ionic compounds while keeping its chemical inertness (nobility). This mechanism has been demonstrated by rigorous energy analysis for He insertion into MgO (AB type) and MgF_2 (AB_2 type) compounds (**Figures 2B–G**) (Liu et al., 2018).

CONCLUSIONS AND PERSPECTIVES

Many recent simulations and experiments showed that noble gases could have very rich chemistry under high pressure. The types of chemical roles and interactions include electron donors (being oxidizing), electron acceptors (being reduced), NG–NG covalent bonds, noble gas bonds, and reliever of repulsive electrostatic interactions. A major effect of pressure is the change of the energies of the atomic orbitals. Although the energies of all local orbitals increase under higher pressure, the effect is more significant to those orbitals with lower principal quantum numbers and higher angular momenta, especially to those having no corresponding core orbitals such as 2p and 3d. As a result of this orbital energy reordering, the electrons are redistributed in different quantum orbitals under pressure. If the energy of the valence np orbital of a noble gas (5p for Xe, 4p for Kr) is close to or higher than the energies of the valence orbitals of an oxidant element such as F, O, or Fe, the noble gas will be oxidized. Conversely, if the unoccupied orbitals of the noble gases such as 5d for Xe become lower in energy than the orbitals of reductants such as Li or Mg, the noble gases will be reduced and become anionic.

The future of the exotic chemistry of noble gases as well as the high-pressure study rely on three signs of progress, the experimental methods that allow us to study the chemistry of materials under higher pressure (>200 GPa), the computer power and the simulation algorithms that can enable us to explore the structures and stability of more complicated materials such as ternary and quaternary compounds, the conceptual framework that can help us in understanding and predicting the change of chemistry under pressure without full-scale

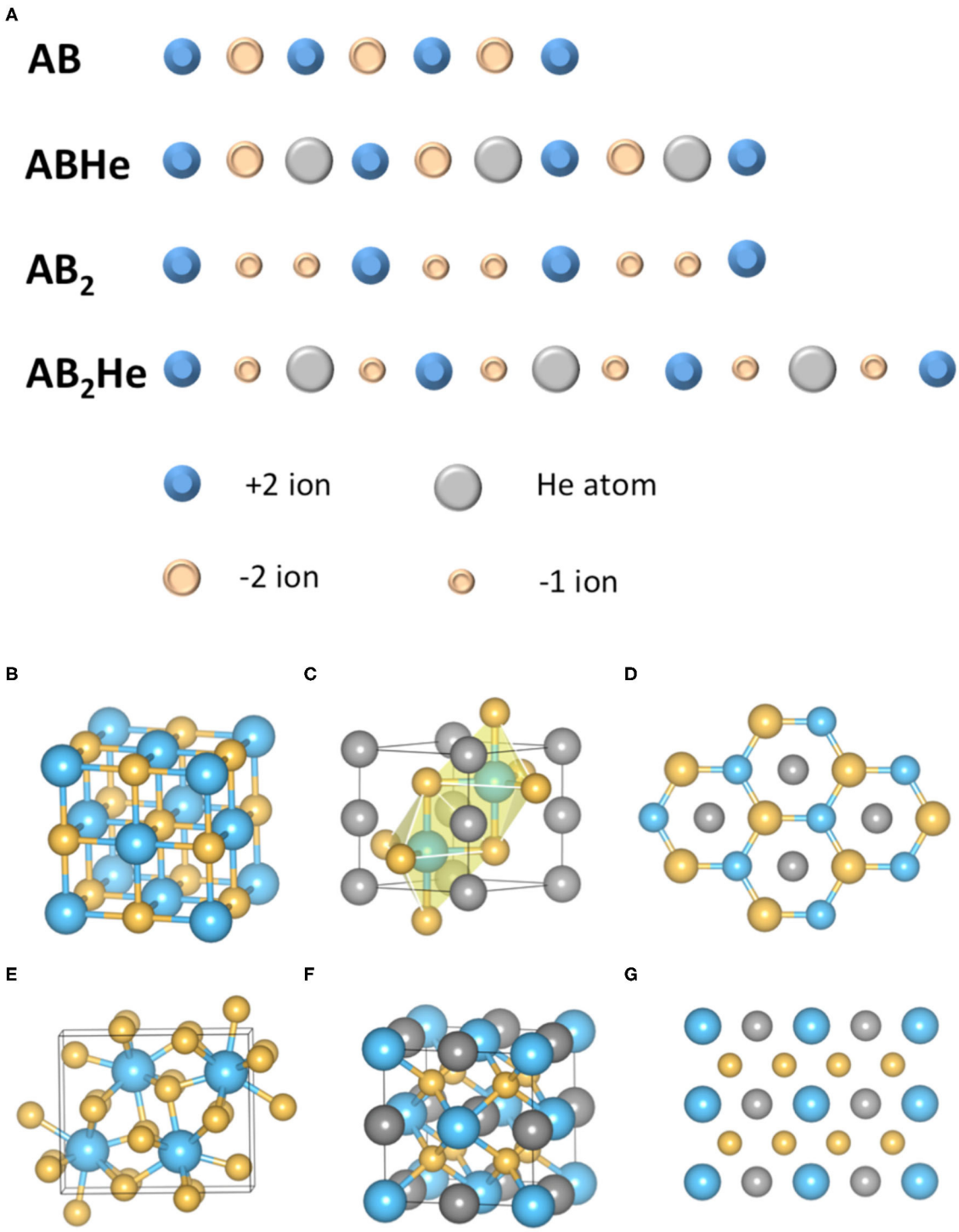

FIGURE 2 | Mechanism of He insertion reaction with ionic compounds. **(A)** The schematics of He insertions into AB and AB_2 types of ionic compounds. The Madelung energy increases in the former case whereas decreases in the latter case; **(B)** The rocksalt structure of MgO under high pressure; **(C)** The lowest energy structure of conceived compound MgOHe; **(D)** The view from (001) direction of MgOHe structure, showing that He chains are inserted between Mg and O atoms; **(E)** The $PbCl_2$ structure of MgF_2 under pressure; **(F)** The structure of stable MgF_2He compound; **(G)** The (110) plane of MgF_2He structure. The He atoms are inserted in between the neighboring F atoms, which further demonstrated the proposed mechanism. The blue, yellow and grey balls represent Mg, O (or F) and He atoms in **(B–G)**.

calculations. Although the recent high-pressure studies have greatly advanced noble gas chemistry, many important questions still remain unanswered. What are the oxidation and reduction limits of noble gases? Can He or Ne be oxidized or reduced under pressure? Can high-pressure noble gas compounds become superconducting or topological? Can high-pressure noble gas bonding be recovered after releasing the pressure? The developments of theoretical, simulation, and experimental methods might help to answer these questions and extend the noble gas chemistry to an unexpected territory.

AUTHOR CONTRIBUTIONS

The author confirms being the sole contributor of this work and has approved it for publication.

FUNDING

The author acknowledges the support of NSF CAREER award 1848141, ACS PRF 59249-UNI6, and computational resources provided by XSEDE (TG-DMR130005).

REFERENCES

Avery, P., Toher, C., Curtarolo, S., and Zurek, E. (2019). XtalOpt Version R12: an open-source evolutionary algorithm for crystal structure prediction. *Comput. Phys. Commun.* 237, 274–275. doi: 10.1016/j.cpc.2018.11.016

Bader, R. (1990). *Atoms in Molecules: A Quantum Theory*. New York, NY: Oxford University Press.

Bai, Y., Liu, Z., Botana, J., Yan, D., Lin, H.-Q., Sun, J., et al. (2019). Electrostatic force driven helium insertion into ammonia and water crystals under pressure. *Commun Chem.* 2, 1–7. doi: 10.1038/s42004-019-0204-6

Bartlett, N. (1962). Xenon Hexafluoroplatinate (V) Xe+PtF6. In: *Proceedings of the Chemical Society of London* (London).

Bauzá, A., and Frontera, A. (2015). Aerogen bonding interaction: a new supramolecular force? *Angew. Chem. Int. Ed.* 54, 7340–7343. doi: 10.1002/anie.201502571

Bovornratanaraks, T., Tsuppayakorn-aek, P., Luo, W., and Ahuja, R. (2019). Ground-state structure of semiconducting and superconducting phases in xenon carbides at high pressure. *Sci. Rep.* 9, 1–6. doi: 10.1038/s41598-019-39176-4

Brock, D. S., and Schrobilgen, G. J. (2011). Synthesis of the missing oxide of xenon, XeO_2, and its implications for earth's missing xenon. *J. Am. Chem. Soc.* 133, 6265–6269. doi: 10.1021/ja110618g

Cavallo, G., Metrangolo, P., Milani, R., Pilati, T., Priimagi, A., Resnati, G., et al. (2016). The halogen bond. *Chem. Rev.* 116, 2478–2601. doi: 10.1021/acs.chemrev.5b00484

Chernick, C. L., Claassen, H. H., Fields, P. R., Hyman, H. H., Malm, J. G., Manning, W. M., et al. (1962). Fluorine compounds of xenon and radon. *Science*. 138, 136–138. doi: 10.1126/science.138.3537.136

Dawes, S. B., Ward, D. L., Huang, R. H., and Dye, J. L. (1986). First electride crystal structure. *J. Am. Chem. Soc.* 108, 3534–3535. doi: 10.1021/ja00272a073

Dewaele, A., Pépin, C. M., Geneste, G., and Garbarino, G. (2017). Reaction between nickel or iron and xenon under high pressure. *High Press. Res.* 37, 137–146. doi: 10.1080/08957959.2016.1267165

Dewaele, A., Worth, N., Pickard, C. J., Needs, R. J., Pascarelli, S., Mathon, O., et al. (2016). Synthesis and stability of xenon oxides Xe_2O_5 and Xe_3O_2 under pressure. *Nat. Chem.* 8, 784–790. doi: 10.1038/nchem.2528

Dong, X., Oganov, A. R., Goncharov, A. F., Stavrou, E., Lobanov, S., Saleh, G., et al. (2017). A stable compound of helium and sodium at high pressure. *Nat. Chem.* 9, 440–445. doi: 10.1038/nchem.2716

Drews, T., and Seppelt, K. (1997). The Xe ion-preparation and structure. *Angew. Chem. Int. Ed. Eng.* 36, 273–274. doi: 10.1002/anie.199702731

Drozdov, A. P., Eremets, M. I., Troyan, I. A., Ksenofontov, V., and Shylin, S. I. (2015). Conventional superconductivity at 203 kelvin at high pressures in the sulfur hydride system. *Nature*. 525, 73–76. doi: 10.1038/nature14964

Fernández, I., and Frenking, G. (2012). Neutral noble gas compounds exhibiting a Xe–Xe bond: structure, stability and bonding situation. *Phys. Chem. Chem. Phys.* 14, 14869–14877. doi: 10.1039/c2cp41244f

Gao, H., Sun, J., Pickard, C. J., and Needs, R. J. (2019). Prediction of pressure-induced stabilization of noble-gas-atom compounds with alkali oxides and alkali sulfides. *Phys. Rev. Mater.* 3, 015002. doi: 10.1103/PhysRevMaterials.3.015002

Gaston, N., Schwerdtfeger, P., and Nazarewicz, W. (2002). Ionization potentials of internal conversion electrons for the superheavy elements 112, 114, 116, and 118. *Phys. Rev.. A.* 66, 062505. doi: 10.1103/PhysRevA.66.062505

Glass, C. W., Oganov, A. R., and Hansen, N. (2006). USPEX - evolutionary crystal structure prediction. *Comput. Phys. Commun.* 175, 713–720. doi: 10.1016/j.cpc.2006.07.020

Goettel, J. T., Matsumoto, K., Mercier, H. P. A., and Schrobilgen, G. J. (2016). Syntheses and structures of xenon trioxide alkylnitrile adducts. *Angew. Chem. Int. Ed.* 55, 13780–13783. doi: 10.1002/anie.201607583

Grochala, W. (2007). Atypical compounds of gases, which have been called "noble." *Chem. Soc. Rev.* 36, 1632–1655. doi: 10.1039/b702109g

Grochala, W. (2012). A metastable He-O bond inside a ferroelectric molecular cavity: (HeO)(LiF)(2). *Phys. Chem. Chem. Phys.* 14, 14860–14868. doi: 10.1039/c2cp42321a

Guńka, P. A., Dziubek, K. F., Gładysiak, A., Dranka, M., Piechota, J., Hanfland, M., et al. (2015). Compressed arsenolite As_4O_6 and its helium clathrate $As_4O_6{\cdot}2He$. *Cryst. Growth Des.* 15, 3740–3745. doi: 10.1021/acs.cgd.5b00390

Hogness, T. R., and Lunn, E. G. (1925). The ionization of hydrogen by electron impact as interpreted by positive ray analysis. *Phys. Rev.* 26, 44–55. doi: 10.1103/PhysRev.26.44

Hotokka, M., Kindstedt, T., Pyykkö, P., and Roos, B. O. (1984). On bonding in transition-metal helide ions. *Mol. Phys.* 52, 23–32. doi: 10.1080/00268978400101031

Hou, C., Wang, X., Botana, J., and Miao, M. (2017). Noble gas bond and the behaviour of XeO_3 under pressure. *Phys. Chem. Chem. Phys.* 19, 27463–27467. doi: 10.1039/C7CP05385A

Hou, P., Tian, F., Li, D., Zhao, Z., Duan, D., Zhang, H., et al. (2015). Ab initio study of germanium-hydride compounds under high pressure. *RSC Adv.* 5, 19432–19438. doi: 10.1039/C4RA13183E

Khriachtchev, L., Pettersson, M., Runeberg, N., Lundell, J., and Rasanen, M. (2000). A stable argon compound. *Nature*. 406, 874–876. doi: 10.1038/35022551

Kim, M., Debessai, M., and Yoo, C. S. (2010). Two- and three-dimensional extended solids and metallization of compressed XeF2. *Nat. Chem.* 2, 784–788. doi: 10.1038/nchem.724

Kurzydlowski, D., Zaleski-Ejgierd, P., Grochala, W., and Hoffmann, R. (2011). Freezing in resonance structures for better packing: XeF_2 becomes (XeF+)(F-) at large compression. *Inorg. Chem.* 50, 3832–3840. doi: 10.1021/ic200371a

Li, P., Gao, G., Wang, Y., and Ma, Y. (2010). Crystal structures and exotic behavior of magnesium under pressure. *J. Phys. Chem. C.* 114, 21745–21749. doi: 10.1021/jp108136r

Li, T. H., Mou, C. H., Chen, H. R., and Hu, W. P. (2005). Theoretical prediction of noble gas containing anions FNgO- (Ng = He, Ar, and Kr). *J. Am. Chem. Soc.* 127, 9241–9245. doi: 10.1021/ja051276f

Li, X., Hermann, A., Peng, F., Lv, J., Wang, Y., Wang, H., et al. (2015). Stable lithium argon compounds under high pressure. *Sci. Rep.* 5, 16675. doi: 10.1038/srep16675

Liu, H. Y., Yao, Y. S., and Klug, D. D. (2015). Stable structures of He and H_2O at high pressure. *Phys. Rev. B.* 91:014102. doi: 10.1103/PhysRevB.91.014102

Liu, Z., Botana, J., Hermann, A., Valdez, S., Zurek, E., Yan, D., et al. (2018). Reactivity of He with ionic compounds under high pressure. *Nat. Commun.* 9, 951. doi: 10.1038/s41467-018-03284-y

Liu, Z., Botana, J., Miao, M. S., and Yan, D. D. (2017). Unexpected Xe Anions in XeLin intermetallic compounds. *Europhys Lett*. 117, 26002. doi: 10.1209/0295-5075/117/26002

Ma, Y., Eremets, M., Oganov, A. R., Xie, Y., Trojan, I., Medvedev, S., et al. (2009). Transparent dense sodium. *Nature*. 458, 182–185. doi: 10.1038/nature07786

Mao, H. K., Chen, X. J., Ding, Y., Li, B., and Wang, L. (2018). Solids, liquids, and gases under high pressure. *Rev. Mod. Phys*. 90, 015007. doi: 10.1103/RevModPhys.90.015007

Miao, M. (2017). Helium chemistry: react with nobility. *Nat. Chem*. 9, 409–410. doi: 10.1038/nchem.2768

Miao, M., Sun, Y., Zurek, E., and Haiqing, L. (2020). Chemistry under high pressure. *Nat. Rev. Chem*. 4, 508–527. doi: 10.1038/s41570-020-0213-0

Miao, M.-S., and Hoffmann, R. (2014). High Pressure electrides: a predictive chemical and physical theory. *Acc. Chem. Res*. 47, 1311–1317. doi: 10.1021/ar4002922

Miao, M. S. (2013). Caesium in high oxidation states and as a P-block element. *Nat. Chem*. 5, 846–852. doi: 10.1038/nchem.1754

Miao, M. S., Wang, X. L., Brgoch, J., Spera, F., Jackson, M. G., Kresse, G., et al. (2015). Anionic chemistry of noble gases: formation of Mg-NG (NG = Xe, Kr, Ar) compounds under pressure. *J. Am. Chem. Soc*. 137, 14122–14128. doi: 10.1021/jacs.5b08162

Oganov, A. R., Pickard, C. J., Zhu, Q., and Needs, R. J. (2019). Structure prediction drives materials discovery. *Nature Reviews Materials*. 4, 331–348. doi: 10.1038/s41578-019-0101-8

Pauling, L. (1933). The formulas of antimonic acid and the antimonates. *J. Am. Chem. Soc*. 55, 1895–1900. doi: 10.1021/ja01332a016

Pauling, L. (1960). *The Nature of the Chemical Bond*. Ithaca, NY: Cornell University Press.

Peng, F., Botana, J., Wang, Y., Ma, Y., and Miao, M. (2016). unexpected trend in stability of Xe-F compounds under pressure driven by Xe-Xe covalent bonds. *J. Phys. Chem. Lett*. 7, 4562–4567. doi: 10.1021/acs.jpclett.6b01922

Peng, F., Wang, Y. C., Wang, H., Zhang, Y. W., and Ma, Y. M. (2015). Stable xenon nitride at high pressures. *Phys. Rev. B*. 92, 094104. doi: 10.1103/PhysRevB.92.094104

Pickard, C. J., Errea, I., and Eremets, M. I. (2020). Superconducting hydrides under pressure. *Annu. Rev. Condens. Matter Phys*. 11, 57–76. doi: 10.1146/annurev-conmatphys-031218-013413

Pickard, C. J., and Needs, R. J. (2011). Ab initio random structure searching. *J. Phys. Condens. Matter*. 23, 053201. doi: 10.1088/0953-8984/23/5/053201

Rzepa, H. S. (2010). The rational design of helium bonds. *Nat. Chem*. 2, 390–393. doi: 10.1038/nchem.596

Saunders, M., Jimenez-Vazquez, H. A., Cross, R. J., Mroczkowski, S., Gross, M. L., Giblin, D. E., et al. (1994). Incorporation of helium, neon, argon, krypton,and xenon into fullerenes using high pressure. *J. Am. Chem. Soc*. 116, 2193–2194. doi: 10.1021/ja00084a089

Seidel, S., and Seppelt, K. (2000). Xenon as a complex ligand: the tetra xenono gold(II) cation in $AuXe_4^{2+}(Sb_2F_{11}^-)_2$. *Science*. 290, 117–118. doi: 10.1126/science.290.5489.117

Silvi, B., and Savin, A. (1994). Classification of chemical bonds based on topological analysis of electron localization functions. *Nature*. 371, 683–686. doi: 10.1038/371683a0

Stavrou, E., Yao, Y., Goncharov, A. F., Lobanov, S. S., Zaug, J. M., Liu, H., et al. (2018). Synthesis of xenon and iron-nickel intermetallic compounds at earth's core thermodynamic conditions. *Phys. Rev. Lett*. 120, 096001. doi: 10.1103/PhysRevLett.120.096001

Wang, Y., Lv, J., Zhu, L., and Ma, Y. (2012). CALYPSO: a method for crystal structure prediction. *Comput. Phys. Commun*. 183, 2063–2070. doi: 10.1016/j.cpc.2012.05.008

Wu, G., Huang, X., Huang, Y., Pan, L., Li, F., Li, X., et al. (2017). Confirmation of the structural phase transitions in XeF_2 under high pressure. *J. Phys. Chem. C*. 121, 6264–6271. doi: 10.1021/acs.jpcc.6b11558

Zaleski-Ejgierd, P., and Lata, P. M. (2016). Krypton oxides under pressure. *Sci. Rep*. 6, 18938. doi: 10.1038/srep18938

Zhang, L., Wang, Y., Lv, J., and Ma, Y. (2017). Materials Discovery at high pressures. *Nat. Rev. Mater*. 2. doi: 10.1038/natrevmats.2017.5

Zhang, W., Oganov, A. R., Goncharov, A. F., Zhu, Q., Boulfelfel, S. E., Lyakhov, A. O., et al. (2013). Unexpected stable stoichiometries of sodium chlorides. *Science*. 342, 1502–1505.

Zhu, L., Liu, H., Pickard, C. J., Zou, G., and Ma, Y. (2014). Reactions of xenon with iron and nickel are predicted in the earth's inner core. *Nat. Chem*. 6, 644–648. doi: 10.1038/nchem.1925

Zhu, Q., Jung, D. Y., Oganov, A. R., Glass, C. W., Gatti, C., and Lyakhov, A. O. (2013). Stability of xenon oxides at high pressures. *Nat. Chem*. 5, 61–65. doi: 10.1038/nchem.1497

Conflict of Interest: The author declares that the research was conducted in the absence of any commercial or financial relationships that could be construed as a potential conflict of interest.

frontiers in Chemistry

ORIGINAL RESEARCH
published: 13 November 2020
doi: 10.3389/fchem.2020.580295

New Perspectives in the Noble Gas Chemistry Opened by Electrophilic Anions

Markus Rohdenburg[1], *Vladimir A. Azov*[2*] *and Jonas Warneke*[3,4*]

[1] Fachbereich 2-Biologie/Chemie, Institut für Angewandte und Physikalische Chemie, Universität Bremen, Bremen, Germany, [2] Department of Chemistry, University of the Free State, Bloemfontein, South Africa, [3] Wilhelm-Ostwald-Institut für Physikalische und Theoretische Chemie, Universität Leipzig, Leipzig, Germany, [4] Leibniz Institute of Surface Engineering (IOM), Leipzig, Germany

Binding of noble gases (NGs) is commonly considered to be the realm of highly reactive electophiles with cationic or at least non-charged character. Herein, we summarize our latest results evidencing that the incorporation of a strongly electrophilic site within a rigid cage-like anionic structure offers several advantages that facilitate the binding of noble gases and stabilize the formed NG adducts. The anionic superelectrophiles investigated by us are based on the *closo*-dodecaborate dianion scaffold. The record holder $[B_{12}(CN)_{11}]^-$ binds spontaneously almost all members of the NG family, including the very inert argon at room temperature and neon at 50 K in the gas phase of mass spectrometers. In this perspective, we summarize the argumentation for the advantages of anionic electrophiles in binding of noble gases and explain them in detail using several examples. Then we discuss the next steps necessary to obtain a comprehensive understanding of the binding properties of electrophilic anions with NGs. Finally, we discuss the perspective to prepare bulk ionic materials containing NG derivatives of the anionic superelectophiles. In particular, we explore the role of counterions using computational methods and discuss the methodology, which may be used for the actual preparation of such salts.

Keywords: noble gas compounds, *closo*-dodecaborates, anionic electrophiles, mass spectrometry, collision induced dissociation, weakly coordinating cations, soft landing, DFT calculations

OPEN ACCESS

Edited by:
Sudip Pan,
University of Marburg, Germany

Reviewed by:
Purusottam Jena,
Virginia Commonwealth University, United States
Felice Grandinetti,
University of Tuscia, Italy
Gabriel Merino,
Center for Research and Advanced Studies - Mérida Unit, Mexico

***Correspondence:**
Vladimir A. Azov
AzovV@ufs.ac.za
Jonas Warneke
jonas.warneke@uni-leipzig.de

Specialty section:
This article was submitted to Physical Chemistry and Chemical Physics, a section of the journal Frontiers in Chemistry

Received: *05 July 2020*
Accepted: *05 October 2020*
Published: *13 November 2020*

Citation:
Rohdenburg M, Azov VA and Warneke J (2020) New Perspectives in the Noble Gas Chemistry Opened by Electrophilic Anions. Front. Chem. 8:580295. doi: 10.3389/fchem.2020.580295

INTRODUCTION

The spontaneous binding of a noble gas (NG) at room temperature remains the privilege of the strongest electrophiles (Brock et al., 2013; Pan et al., 2019). Due to the closed electron shell of NGs, their electron affinities are negative and a NG atom cannot be chemically attacked by any type of nucleophile. Therefore, the only possibility to form a bond is to abstract electron density from the NG. A number of NG adducts with electrophiles have been characterized in cryogenic matrices (Khriachtchev et al., 2000; Wang and Wang, 2013; Wang X. et al., 2013) where even very weak bonds can hold these compounds together. Under these reaction conditions, it was even possible to observe the first neutral argon compound (Khriachtchev et al., 2000; Bochenkova et al., 2009). In contrast, room temperature NG chemistry is mainly limited to the heavier NGs, mainly xenon (Malm et al., 1965; Haner and Schrobilgen, 2015) and, on a much more limited basis, krypton (Lehmann et al., 2002). The majority of NG compounds contains fluorine or oxygen (Liebman and Deakyne, 2003; Samanta, 2014) since these elements have very

high electronegativities and are strongly electron withdrawing. Also, compounds with vacant boron and beryllium atoms were often proposed as suitable NG binders due to their exceptional electron deficiency (Pan et al., 2014; Saha et al., 2016, 2019). It is also well understandable that strong NG bonds have been frequently reported for highly reactive isolated cations (Grandinetti, 2011), which satisfy their demand for electrons with almost everything that comes into reach—even a NG. However, other molecules or atoms, which are more nucleophilic, tend to substitute the NG and bind the electrophilic cations. Using cationic NG derivatives for the generation of a condensed phase compound is therefore hindered by a fundamental problem: a cation needs to be paired with a counteranion. Anions are typically much stronger nucleophiles than the NG itself and, therefore, immediately substitute the NG by forming a bond with the electrophilic binding site. Experimental access to most reported molecular NG cations, which are stable at room temperature, remains limited to the low-pressure gas phase of a mass spectrometer.

Recently, we discovered that the electrophilic anion $[B_{12}Cl_{11}]^-$ is able to bind spontaneously xenon and krypton at room temperature in the gas phase (Rohdenburg et al., 2017). Later, aiming at further increase of reactivity, we prepared and investigated the cyanated derivative $[B_{12}(CN)_{11}]^-$, which was found to be much more electrophilic than its predecessor. It is able to bind argon at room temperature (Mayer et al., 2019) and can even form a stable adduct with extremely unreactive neon (Mayer et al., 2020) at temperatures up to 50 K. High level computational studies and investigations of the weak complexes in the cold matrix have shown that the binding energies for Ne are often even smaller than for He in similar adducts and, therefore, Ne was discussed to be the most inert NG (Frenking et al., 1990; Grandinetti, 2013; Grochala, 2018). These electrophilic anions are generated by collision induced dissociation (CID) of their gaseous precursors *closo*-dodecaborate dianions $[B_{12}X_{12}]^{2-}$ (X=halogen, CN), which constitute a class of very stable and inert weakly coordinating anions (WCAs) (Knapp, 2013). The discussed experimental results inspired further theoretical investigations on the NG binding properties of similar compounds, even with higher negative charge (Joshi and Ghanty, 2019, 2020).

In the first section of this perspective, we summarize and explain the binding concepts of electrophilic anions with NGs and their advantages when compared with "common" cationic electrophiles. Then, we discuss open questions that still need to be clarified to obtain a comprehensive and quantitative understanding of the binding between electrophilic anions and NGs. Finally, we deepen the insights on the effect of counterions on the NG bond with electrophilic anions and discuss the possibilities and limitations for the preparation of salts using $[B_{12}X_{11}NG]^-$ anions as precursors.

RESULTS AND DISCUSSION

Remark: If not stated otherwise, calculations were performed using the B3LYP DFT functional and, in most cases, results have not been confirmed using high-level correlated methods. Reported numbers are given for the purpose of qualitative comparison of reactions and should not be interpreted as quantitative thermochemistry values. More details can be found in the methods section and in the **Supplementary Material**.

Fundamental Concepts of Electrophilic Anions and Their Reactivity

Several fundamental concepts underline the formation and binding traits of electrophilic anions. We will discuss them below on the example of *closo*-dodecaborate dianions $[B_{12}X_{12}]^{2-}$, which have been the objects of our detailed investigations. However, related molecular systems, for example so called anionic "super atomic clusters" (Jena and Sun, 2018) or other *closo*-borate anions may show similar features (Rohdenburg et al., 2020).

(i) Breaking the Most Stable Generates the Most Reactive

An exceptionally reactive electrophilic site within an ion is required to bind a NG atom. In our search for very reactive molecular ions we were following a simple idea: breaking bonds in very stable molecular ions should result in the most reactive fragments. A large driving force should be present in the fragment to recover the original highly stable structural and electronic configuration of the precursor. The *closo*-dodecaborate dianions $[B_{12}X_{12}]^{2-}$ (**Figure 1A**) possess very high icosahedral (I_h) molecular symmetry, a 3D-aromatic σ-electron system and exceptional electronic stability (Warneke et al., 2017). As first predicted theoretically (Zhao et al., 2016) and later confirmed experimentally (Mayer et al., 2019), the $[B_{12}(CN)_{12}]^{2-}$ dianion has the highest second electron binding energy (the energy necessary to detach an electron from the doubly charged anion) known for small multiply charged anions synthesized so far (>5 eV). The $[B_{12}Cl_{12}]^{2-}$ dianion has been used to stabilize extremely reactive countercations in the condensed phase, including methyl (Bolli et al., 2010) and silyl (Kessler et al., 2010) cations, thus evidencing its exceptional chemical inertness. These facts demonstrate the outstanding electronic, structural, and chemical stability of *closo*-dodecaborate dianions and make them ideal precursors for the generation of highly reactive fragments by breaking a B-X bond.

(ii) Positive, Strong Electrophilic Site Within an Anion

Since only strong electrophiles, but not nucleophiles, are able to bind a NG by forming a bond with significant covalent character, anions have raised limited attention as potential strong NG binders. However, the fragment $[B_{12}X_{11}]^-$ possess a special charge distribution: although the ion is overall negatively charged, the vacant boron atom exhibits a strong positive partial charge (**Figure 1B**), very electrophilic in nature and, therefore, can bind a NG atom. Experimentally, the positive site was probed by infrared photodissociation spectroscopy [for details on the used instrument and method, see Heine and Asmis (2015)] of its CO adduct (Gruene et al., 2008). The CO stretching frequency is a sensitive probe for the charge state of a binding site. Thus, a CO molecule was allowed to bind to the anion and IR spectra

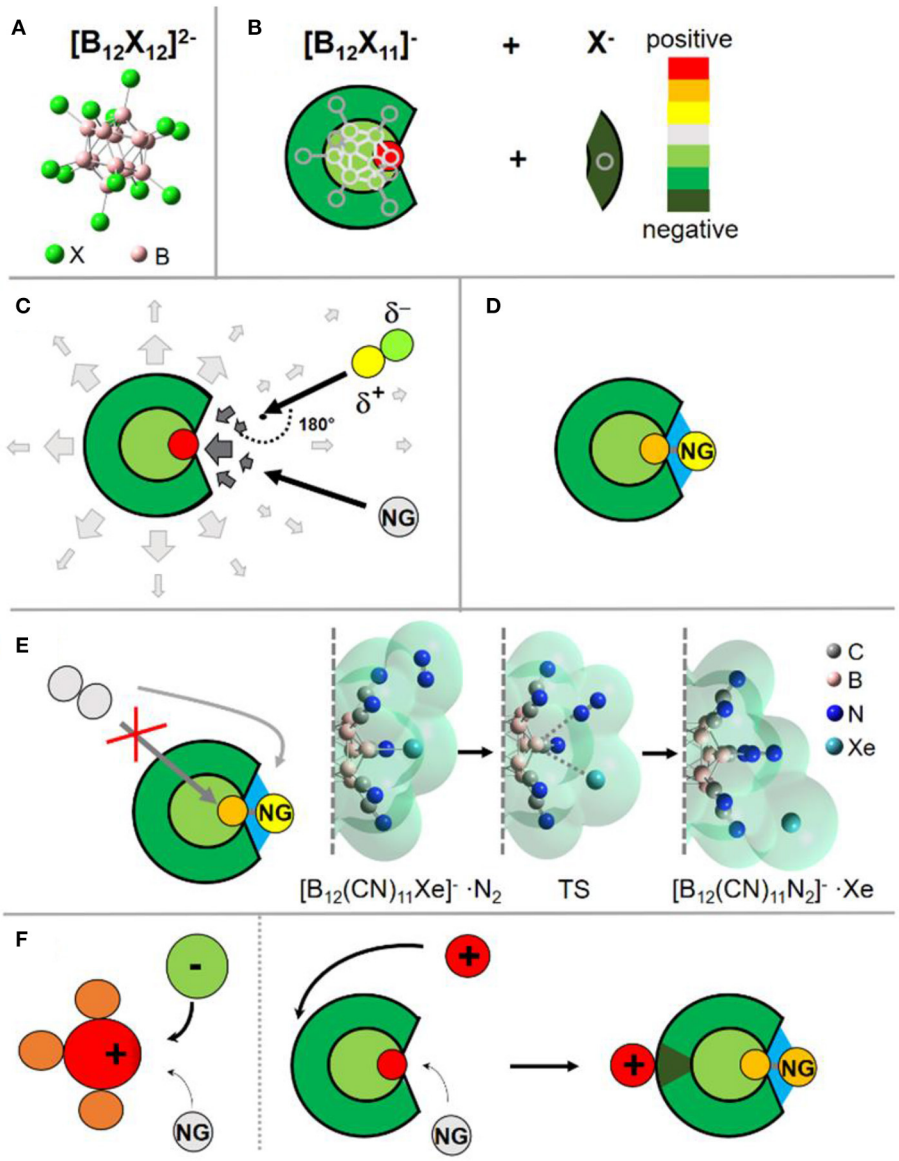

FIGURE 1 | Visualization of the discussed binding concept. **(A)** Structure of the *closo*-dodecaborate dianions. **(B)** Simplified scheme to show the charge distribution in the fragment $[B_{12}X_{11}]^-$ after abstraction of a negatively charged substituent X^- from the doubly charged precursor. **(C)** Schematic visualization of the electric field near the ion. Close to the binding site the field changes its direction, leading to the change of the preferred orientation for a polar reaction partner. **(D)** Schematic visualization of the ion-NG interaction. Next to the dative bond to the boron (gray), interactions with the surrounding substituents (electrostatics, dispersion) are shown in blue. **(E)** S_N2 substitution by another nucleophile is blocked from the back; a nucleophile must attack from the side, as shown on an example of the substitution reaction of Xe with N_2 in $[B_{12}(CN)_{11}Xe]^-$ adduct. The molecular surface is plotted semitransparent to show the steric demand of the reaction partners. The start and end structures are true minima. For detailed discussion, see Concept (vi). **(F)** Schematic explaining the different effect of counterions on NG binding in an electrophilic cation and an electrophilic anion. While the case of an electrophilic cation NG and counterion compete for one binding site, they target different binding sites in the case of the electrophilic anion. The countercation increases the strength of the formed B-NG bond, see discussion in Concept (vii). Images are partially based on our previous illustrations (Rohdenburg et al., 2017; Mayer et al., 2019, 2020).

of $[B_{12}X_{11}CO]^-$ were measured in the gas phase. A strong blue shift of the CO stretching frequency, typically observed for very electrophilic cations (Saha et al., 2017) like, for example, the phenyl cation (Winkler and Sander, 2006), was measured for the $[B_{12}X_{11}CO]^-$ ions. Computationally, the picture of a positive vacant boron atom was confirmed by calculated atomic charges, the electrostatic potential and the electric field. The calculated charge distributions of $[B_{12}X_{11}]^-$ suggests that, from a qualitative point of view, this anion could better be described as a reactive cation embedded into an inert dianionic framework. The leaving X^-, which is disconnected from the $[B_{12}X_{12}]^{2-}$ precursor, takes the electron density almost exclusively from the boron atom to which it was bound and very limited charge redistribution occurs in the formed fragment ion. The analysis

of the electron localizability indicator (ELI-D) evidenced that the vacant boron site of $[B_{12}X_{11}]^-$ is electronically separated from the delocalized σ-electron system, which gives an explanation to the strong electrophilic and cationic nature of this vacant boron site (**Figure 1B**) (Rohdenburg et al., 2017).

(iii) Preserving the Reactive Site Within a Large Molecular Framework

Large ion sizes are an advantage for the observation of weakly bound adducts in the gas phase. Upon collision of the ion with a NG, a "hot collision complex" is formed. If the collisional energy can be efficiently redistributed into many vibrational degrees of freedom, the complex can survive until further collisions with background gases cool the adduct. Collision complexes of smaller ions have much less chances to survive long enough for experimental observation, even if the NG bond may have a similar strength. However, most highly reactive isolated cations which exhibit NG binding at room temperature are small (<10 atoms). Often, a highly reactive positively charged site embedded into a large molecular framework results in structural rearrangement of the molecular ion. For example, electrophilicity of the phenyl cation can be increased by the substitution of all five hydrogens by fluorine, raising its binding energy with Xe theoretically from around 70 to 150 kJ/mol. However, it has been experimentally and theoretically shown that, unlike the phenyl cation $[C_6H_5]^+$, the pentafluorinated phenyl cation $[C_6F_5]^+$ is unstable in the gas phase and spontaneously fragments by expulsion of difluorocarbene. This rearrangement results in a more stable cationic species containing an aromatic cyclopropenium moiety (Wang H.-Y. et al., 2013), which has only a small Xe binding enthalpy of around 15 kJ/mol. Though pentafluorinated phenyl cations cannot be generated in a gas phase reaction, the preparation of its xenon derivative, the $[C_6F_5Xe]^+$ cation, was possible in a reaction between XeF_2 and $B(C_6F_5)$, proceeding via a concerted substitution mechanism, at low temperature in an inert organic solvent, such as CH_2Cl_2 or MeCN (Frohn and Jakobs, 1989; Naumann and Tyrra, 1989). In our case, the rigid B_{12} framework does not allow for any intramolecular rearrangements of the $[B_{12}X_{11}]^-$ anion, independent on the nature of the substituent X, and can be used as a non-solvated, isolated ion for binding of NG atoms. Comprising 23 atoms, $[B_{12}X_{11}]^-$ is large in comparison to most experimentally observed NG binding ions, thus affording efficient stabilization of collisional complexes.

(iv) Preference for Binding of Non-polar Nucleophiles

A cationic binding site within an anion results in a special distribution of the electric field near this site. Reaction partners located far away from the ions are only affected by the anionic negative charge, while close to the positive binding site, the electric field changes its direction. Polar molecules such as water, which are usually stronger nucleophiles than NGs, change their preferred orientation upon approach to the binding site (**Figure 1C**). This situation may result in substantial centrifugal barriers. In contrast, a NG atom can just repolarize and may have an advantage in the competition with polar nucleophiles for the binding site. Thus, such electrophilic anions should show relative selectivity in binding to non-polar nucleophilic species.

(v) Large Interaction Surface Between Ion and NG

The binding site of an electrophilic anion $[B_{12}X_{11}]^-$ is located within a "crater" of five substituents X. Therefore, beside the dative bond formed by the shift of electron density from the NG to the electrophilic boron, a large surface for additional electrostatic forces and dispersion interactions between the anion and a NG atom strengthens the total interaction (**Figure 1D**). Upon formation of the dative bond with $[B_{12}X_{11}]^-$, the NG atom becomes partially positively charged, which affords additional attractive electrostatic interaction with the negatively charged $[B_{12}X_{11}]^-$ residue. Dispersion interactions (Wagner and Schreiner, 2015) are in particular strong for the heavier and more polarizable NGs, but they also make a significant contribution in the case of Ar and Ne binding (Mayer et al., 2019, 2020).

(vi) Protection of the Adducts Against Substitution

The cage structure of the borate anion protects the B-Ng bond against a typical back-side nucleophilic attack following the S_N2 mechanism. Therefore, only a side attack of the B-NG bond by a nucleophile is possible. A significant elongation of the B-NG bond is required before such a nucleophile will be able to interact with the vacant boron atom. Therefore, we expect the energy of the transition state (TS) for substitution to be strongly correlated with the B-NG dissociation enthalpy (DE). As an example, we have computationally investigated the substitution of Xe in $[B_{12}(CN)_{11}Xe]^-$ by the stronger nucleophile N_2. Xe is bound to $[B_{12}(CN)_{11}]^-$ with a 0 K DE of 114 kJ/mol. We started with a $\{[B_{12}(CN)_{11}Xe]^-\cdots N_2\}$ complex, in which N_2 is only weakly bound to the ion (**Figure 1E**). Then, we simulated the attack by systematically reducing the B-N distance. The optimized TS was found to be 90 kJ/mol higher in enthalpy than the initial minimum with a B-Xe bond significantly elongated by 1.3 Å. The product of the favorable substitution was found at $\Delta H_{0K} = -52$ kJ/mol. For direct comparison, we choose the adduct between Xe and CH_3^+, which binds Xe even stronger (see details in **Supplementary Material**, section Substitution of Xe by N_2 in $[H_3CXe]^+$). Although the substitution of Xe in $[H_3CXe]^+$ with N_2 is less exothermic ($\Delta H_{0K} = -20$ kJ/mol), the TS was calculated to be considerably lower in enthalpy with $\Delta H_{0K} = 17$ kJ/mol and a C-Xe bond length elongation by 0.5 Å was found. This demonstrates that the TS for substitution reactions in $[B_{12}(CN)_{11}NG]^-$ is comparatively high. We note that the same argumentation qualitatively holds when repeating the calculations on the BMK-GD3BJ/aug-cc-pVTZ (SDD) level of theory (see details in **Supplementary Material**, section Substitution of Xe by N_2 on BMK-GD3BJ/aug-cc-pVTZ (SDD) Level of Theory). It has been reported that the BMK functional yields better quantitative thermochemistry values for NG compounds compared to our standard approach relying on the dispersion-corrected B3LYP DFT functional (Grandinetti, 2018). The dispersion-corrected B3LYP functional showed sufficient accord with high-level post-Hartree Fock methods like SCS-MPS or CCSD(T) in our former studies (Rohdenburg et al., 2017; Mayer et al., 2019, 2020) of similar Ng compounds as discussed herein.

(vii) Stabilization of Adducts With Counterions

There exists an intrinsic thermodynamic problem for highly reactive cations to form stable NG adducts in the condensed phase, since they demand the presence of counterions. These counterions are anions that have commonly nucleophilic nature. Usually, anionic counterions will be by far stronger competitors for the positive electrophilic binding site of a reactive cation than NGs and a substitution of the NG by the anion's nucleophilic site will be energetically preferred. The existence of a salt consisting of a NG binding cation and a counteranion is only possible if strong kinetic barriers hinder this substitution reaction. In contrast, $[B_{12}X_{11}NG]^-$ requires a countercation. Simple counterions like alkali cations do not show any tendency to bind to the electrophilic boron site. Instead, the most preferred position of a cation is the backside of the $[B_{12}X_{11}NG]^-$ ion, which constitutes its most negative region (**Figure 1F**). In order to demonstrate this concept on an example, we compare the $[B_5O_7Xe]^+$ cation (Jin et al., 2017), and the $[B_{12}(CN)_{11}Xe]^-$ anion (see **Figures 2A,B**, respectively) using computational methods. $[B_5O_7]^+$ belongs to the strongest singly charged cationic NG binders observed experimentally, and its binding strength toward NGs is comparable with $[B_{12}(CN)_{11}]^-$. The 0 K DE for Xe is calculated to be around 115 kJ/mol for the $[B_5O_7Xe]^+$ cation. If a chloride, a "simple" atomic anion, is placed close to the $[B_5O_7Xe]^+$ cation, geometry optimization of the ion pair results in the substitution of the Xe atom from the adduct, and no other minimum can be found. Previously, the stabilization of highly labile cations has been performed using extremely weakly coordinating anions (Strauss, 1993; Krossing and Raabe, 2004; Riddlestone et al., 2018). One of the most prominent and successful examples of them is the carba-*closo*-dodecaborate anion $[HCB_{11}Cl_{11}]^-$ (Juhasz et al., 2004). However, placing even this very inert anion next to the $[B_5O_7Xe]^+$ cation also resulted in elimination of Xe upon geometry optimization (**Figure 2A**). The electrophilic boron in $[B_5O_7]^+$ attaches to a halogen substituent and the resulting neutral unit $[B_5O_7$-$HCB_{11}Cl_{11}]$ has no vacant site and, thus, a small Xe binding strength. Therefore, it appears extremely difficult to stabilize cationic NG adducts like $[B_5O_7Xe]^+$ in the condensed phase, even using the most weakly coordinating anions known today. If instead a simple monoatomic Li^+ cation is combined with $[B_{12}(CN)_{11}Xe]^-$, ion pairing does not result in the elimination of the Xe from its adduct. On the contrary, the B-NG bond is additionally stabilized against dissociation by 25 kJ/mol in comparison to the isolated $[B_{12}(CN)_{11}Xe]^-$ anion (see **Figure 2B**). The Coulomb attraction of the cation on the electron cloud of the anion results in further polarization and strengthens the cationic character of the vacant boron site that binds to the NG atom. The calculated NPA charge of Xe increases from +0.70 *e* in $[B_{12}(CN)_{11}Xe]^-$ to +0.74 *e* in $Li[B_{12}(CN)_{11}Xe]^-$, showing the enhanced electrophilic character of the anion upon ion pairing.

The stabilization of the B-NG bond upon ion pairing with a cation is based on the electron withdrawing effect of a cation. Therefore, it may be suggested that an even more electrophilic cation should have a stronger stabilizing effect on the B-NG bond.

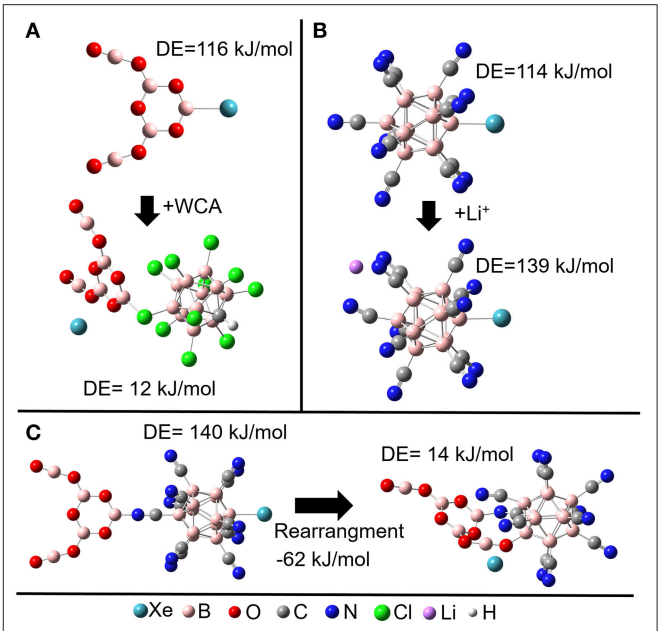

FIGURE 2 | Effect of ion pairing on the 0 K dissociation enthalpy (DE) of Xe **(A)** Combinations of the WCA $[HCB_{11}Cl_{11}]$- with $[B_5O_7Xe]^+$. **(B)** Combination of Li^+ with $[B_{12}(CN)_{11}Xe]^-$. **(C)** Combination of $[B_5O_7]^+$ with $[B_{12}(CN)_{11}Xe]^-$: a rearrangement is thermochemically preferred and results in the loss of the vacant boron site which binds the NG.

In our computational investigations, we studied the $[B_5O_7]^+$ ion as a counterion for $[B_{12}(CN)_{11}Xe]^-$. The exceptionally positive boron atom (NPA charge +1.5 *e*) should have an even stronger electron withdrawing effect. However, in contrast to Li^+, $[B_5O_7]^+$ interacts only with one CN substituent at the backside of $[B_{12}(CN)_{11}Xe]^-$ and the stabilizing effect for the B-Xe bond is in both cases comparable (**Figures 2B,C**). Also, binding of $[B_5O_7]^+$ to the backside of $[B_{12}(CN)_{11}Xe]^-$ is not the global minimum of this ion pair. It is much more favorable to bind the vacant boron atom of the anion $[B_{12}CN_{11}]^-$ to an oxygen of $[B_5O_7]^+$ while the vacant boron atom of the cation binds to a nitrogen atom of a CN substituent of the anion, (**Figure 2C**). This releases the Xe atom and demonstrates a potential problem for the use of molecular cations with nucleophilic binding sites. This problem is avoided when atomic cations like Li^+ and Na^+ are used.

To sum up, the unique combination of multiple factors discussed above render halogenated/cyanated *closo*-dodecaborate fragment ions $[B_{12}X_{11}]^-$ special properties that allow them to selectively bind NGs and other weakly nucleophilic substances and additionally stabilize these adducts kinetically. In principle, applicability of these concepts can be extended to other compounds with similar structural and electronic properties, such as diverse anionic cage borates or metal clusters. However, synthetic accessibility, high chemical stability, and exceptionally high reactivity of the vacant boron site make $[B_{12}X_{11}]^-$ fragment ions the most promising superelectrophilic anions for our further studies.

Next Steps Toward a Comprehensive Understanding of NG Binding by Electrophilic Anions

Several parameters influence the properties of the reactive site and therefore the bond between an electrophilic anion and a NG atom. The positive partial charge of the vacant boron atom in $[B_{12}X_{11}]^-$ (concept ii) appears to be of critical importance. We expect a correlation between the reactivity of $[B_{12}X_{11}]^-$ and the electronic stability of the dianionic precursor $[B_{12}X_{12}]^{2-}$: the more stable the dianion, the more electrophilic its monoanionic fragment $[B_{12}X_{11}]^-$ should become. This assumption is supported by the so far limited data on different electrophilic anions that is available. However, the energetics of NG binding is not solely affected by the vacant positive boron atom, but also by the interactions of NG with the five substituents X surrounding the binding site. Their partial charge, steric demand, and polarizability (critical for dispersion forces) are expected to have a significant influence on the NG binding. We aim for a better understanding how strongly these interactions influence the NG binding in electrophilic anions. A comparative experimental and theoretical study probing the binding of different electrophilic anions $[B_{12}X_{11}]^-$ (X = F, Cl, Br, I, CN) toward different NGs (Ne, Ar, Kr, Xe) is currently in progress and the results are expected to be published soon.

A quantitative understanding of the kinetic parameters influencing NG binding may be even more challenging. Water is a competing and much stronger nucleophile, which is usually present in significant amounts in the background of mass spectrometers at room temperature. Highly reactive cations (e.g., the phenyl cation), which are calculated to form bonds to NGs with enthalpies similar to $[B_{12}X_{11}]^-$, did not bind the NGs under the same experimental conditions at room temperature. Instead, only the water adduct of the phenyl cation was detected (Rohdenburg et al., 2017). The better redistribution of collisional energy (see concept iii), a reduced cross section for a reactive collision of the polar water with $[B_{12}X_{11}]^-$ (concept iv) or a better protection of the B-Ng bond against substitution with water (concept vi) may all contribute to the relative stabilization of $[B_{12}X_{11}NG]^-$ in comparison with $[C_6H_5NG]^+$. An evaluation, which of these points is most important is currently difficult for us. In particular, an estimation of the centrifugal barrier for binding of polar molecules with a cationic site within an anion cannot be performed using common models for ion–molecule collision theory. Complex, much more sophisticated models, which take the special electric field and steric demand of the substituents X into account, will be required.

The observation of a strong NG bond in the gas phase always leads to the question if this bond may hold together the same compound or ion in a condensed phase. The thermodynamic stabilization of the B-NG bond in $[B_{12}X_{11}NG]^-$ by addition of a countercation (vii) underlines one of the most important features, which distinguishes electrophilic anions from NG-binding cations: a thermodynamically stable, neutral ion pair can be formed. This is certainly very promising for the attempt of generating condensed phase material. However, additional challenges arise in this case, which have not been discussed in our previous publications. The goal of the last section of this perspective is to discuss further challenges on the molecular level, which may arise from building condensed phase materials from $[B_{12}X_{11}NG]^-$ adducts and to suggest feasible approaches to overcome these challenges.

On the Way to Bulk Salts of the Anionic NG Derivatives

Experimentally, we consider electrospray-coupled high ion-current deposition methods, so called ion soft landing (Franchetti et al., 1977; Laskin et al., 2018), to be the most promising tool for the bulk preparation of possible salts with $[B_{12}X_{11}NG]^-$ anions generated in the gas phase. The precursor $[B_{12}X_{12}]^{2-}$ can be transferred via electrospray ionization into the gas phase, where fragmentation by CID yields $[B_{12}X_{11}]^-$. After reaction with NG, the $[B_{12}X_{11}NG]^-$ can be mass selected and guided to a surface to be deposited with low kinetic energy in order to preserve the relatively weak B-NG bond from decomposition. Recently introduced sequential soft-landing of anions and cations (Su et al., 2019) may be used to combine sub-monolayers of $[B_{12}X_{11}NG]^-$ with sub-monolayers of selected cations to form bulk layers of condensed material in a stepwise manner. This approach has already been shown to be useful for the buildup of multilayer materials on surfaces with mass selected anions and cations. To ensure the success of corresponding experiments it is imperative to determine which cations should be most effective for the stabilization of the $[B_{12}X_{11}NG]^-$ adducts in the condensed phase. We continue to use $[B_{12}(CN)_{11}Xe]^-$ as a concrete example in the following discussion.

In a condensed material, the $[B_{12}(CN)_{11}Xe]^-$ ion will not only be paired with one counterion like Li^+, but will be closely surrounded by multiple $\{[B_{12}(CN)_{11}Xe]^-Li^+\}$ units. Thus, negatively charged CN substituents of a neighboring anion will be located in spatial proximity to the electrophilic site of $[B_{12}X_{11}NG]^-$. When considering two gaseous $[B_{12}(CN)_{11}Xe]^-$ ions in a mass spectrometer, substitution of Xe by formation of a B-NC bond is thermochemically favored by −86 kJ/mol. In the gas phase, this reaction has never been observed because a large Coulomb barrier kinetically hinders two $[B_{12}X_{11}NG]^-$ anions from approaching each other. In the bulk of a salt with closely spaced $\{[B_{12}X_{11}NG]^-Li^+\}$ ion pairs, the long-range repulsive separation force between two $[B_{12}X_{11}NG]^-$ anions can be almost neglected due to the presence of charge compensating Li^+ cations. We used a simplified model consisting of two $\{[B_{12}(CN)_{11}Xe]^-Li^+\}$ units to estimate the TS and energetics of the Xe-substitution by a CN substituent of two neighboring anions (**Figure 3**). The calculated TS is located +45 kJ/mol above the minimum in which both Xe are bound by the electrophilic boron sites. The total reaction enthalpy is exothermic by −237 kJ/mol. Therefore, we can conclude that there will be always a thermochemical driving force for the elimination of an NG in a bulk solid upon its substitution with one of the substituents of the neighboring anion. Small alkali cations allow very close contact of neighboring anions in a solid. Additionally, alkali cations like Li^+ and Na^+ readily form complexes with water (alkali hydrates) and may, therefore, bind background

water molecules, which could then attack $[B_{12}X_{11}NG]^-$ adducts. Therefore, we conclude that alkali cations may be not the ideal choice to form a stable compound in the condensed phase.

Thus, the only possibility to isolate the desired NG-containing salt is the "installation" of strong kinetic barriers that should hinder the substitution of the NG, at least at sufficiently low temperatures. We consider that bulky, inert and non-hydrophilic cations should be much better suited than alkali cations since they may push the individual anions further apart from each other, which should affect substantial kinetic barriers for direct reactions between $[B_{12}X_{11}NG]^-$ ions in the condensed phase.

The above considerations raise the question how large these barriers have to be and how effectively they can stabilize a B-NG bond. We consider the answer to this question in our case neither general nor straightforward. The well-characterized $[F_5C_6Xe]^+AsF_6^-$ salt (Frohn et al., 1998) can serve as an example of a NG compound, which is, though instable thermodynamically, very inert kinetically. The gas phase decomposition of this ion pair with the release of Xe and formation of C_6F_6 and AsF_5 as reaction products is exothermic by −198 kJ/mol and we calculated a TS of +73 kJ/mol. In the bulk phase, this salt decomposes in the melt only above 120°C and is stable in a solvent like MeCN for 12 h without traces of decomposition (Frohn et al., 1998). However, these numbers may not be directly comparable to the enthalpy and TS calculated for our system because a variety of complex factors determine probabilities for reactive collisions between the reagents in the condensed phase. Reaction pathways, as calculated for the gas phase, are often not feasible in the solid state. Therefore, we cannot directly predict, based on calculated transition states, that the proposed $[B_{12}(CN)_{11}Xe]^-$ salts may be stable at a certain temperature. Still, we would like to discuss our ideas regarding the stabilization of $[B_{12}(CN)_{11}Xe]^-$ in the bulk phase, which may help to increase the temperature at which such salts may be stable.

It has been shown that different types of WCAs are optimally suited for the stabilization of $[F_5C_6Xe]^+$ cation (Frohn and Bardin, 2001). Several WCAs, such as AsF_6^- (Frohn et al., 1998) and $[BY_4]^-$ (Y = CF_3, C_6F_5, CN, $OTeF_5$) (Koppe et al., 2007, 2008), have been successfully tested affording compounds stable at temperatures up to 120°C ($[F_5C_6Xe]^+AsF_6^-$ salt). Even less F-substituted arylxenon derivatives (Aryl = 2,6-$F_2C_6H_3$, 2-FC_6H_4, 4-FC_6H_4) were found to be stable at temperatures slightly below 0°C, when inert tetrafluoroborate $[BF_4]^-$ was used as a counterion (Naumann et al., 1993). In our case, we should look for bulky weakly coordinating cations ["weakly coordinating cations" is a rather recent concept complementary to the much older concept of "weakly coordinating anions"; see, for example (Price et al., 2009; Fischer et al., 2014; Moritz et al., 2015; Mann et al., 2018)], which do not contain any nucleophilic site that can attack the B-NG bond. Preferentially, we need to find a chemically inert, symmetric, bulky, and rigid cationic species that will be able to reliably separate $[B_{12}X_{11}NG]^-$ anions from each other in the solid phase. The most suitable and easily accessible candidates would be either tetrahedral tetraphenylphosphonium derivatives (Fischer et al., 2014; Moritz et al., 2015) or stable metal complexes with a permanent positive charge. One of such candidates is the cobaltocenium cation $[Cp_2Co]^+$, a sandwich 18 *e* organometallic compound of high structural and chemical stability (Zhu et al., 2020). Cobaltocenium and its permethylated derivative $[Cp^*_2Co]^+$ (Cp^* denotes a permethylated cyclopentadienyl ligand) have been used as inert counterions for stabilization of labile anionic species, such as reactive radical anions (Morgan et al., 2011), in the solid state. Thus, $[Cp^*_2Co]^+$ seems to be a promising candidate also in our case: it is chemically inert, does not contain any nucleophilic site, and due to its large size it should keep the reactive anions much better separated from each other in a solid lattice than small alkali cations. Additionally, it possesses relatively high symmetry with a five-fold rotational axis, similar to the $[B_{12}(CN)_{11}NG]^-$ adducts.

A simple model based on two anions and two cations (see the optimized geometry in **Figure 4**) indeed demonstrates that $[B_{12}(CN)_{11}Xe]^-$ anions are spatially better separated from each other than in the case of $(Li[B_{12}(CN)_{11}Xe]^-)_2$. The distance between the anions increases by roughly 1 Å in the optimized geometry of **Figure 4** compared to **Figure 3A**. We expect that this "anion distancing" substantially increases the barrier for their intermolecular reaction with NG elimination. In addition, the outer surface of the cations represents rather chemically inert methyl groups, which have very low nucleophilicity. We calculated a barrier of 131 kJ/mol for the nucleophilic substitution of the Xe by the methyl group (see section **Supplementary Material**, section Substitution of Xe via Insertion of $[B_{12}CN_{11}]^-$ into a C-H Bond of $CoCp^*_2$). The cyclopentadienyl π-systems binds to a positive metal and is not nucleophilic.

This molecular system between a $[B_{12}X_{11}NG]^-$ anionic adducts and a weakly coordinating cation may constitute the first approach to the new generation of ionic noble gas compounds prepared by molecular ion deposition methods. It has been demonstrated that the soft-landing technique is well-suited for the preparation of thin layer materials based on *closo*-dodecaborate anions (Warneke et al., 2018) and can be also used for the isolation of the products of reactive fragment ions generated in the gas phase (Warneke et al., 2020). We plan to exploit the possibilities of these method for preparation of the bulk phases of the $(CoCp^*_2)^+ \cdot [B_{12}X_{11}Xe]^-\}$ salts, which may be classified as supersalts following the recently suggested definition (Giri et al., 2014).

CONCLUSIONS

Recently developed anionic electrophiles based on *closo*-dodecaborate anions have opened up new possibilities for the formation and investigation of room temperature stable anionic NG derivatives and may allow the preparation of a new class of condensed phase NG compounds. Using explanations, which are intuitively understandable to chemist, we have summarized the concepts that explain how the vacant site of rigid anionic electrophiles possesses a unique chemical nature that facilitates binding of noble gases. Computational investigations indicate that the cyanated *closo*-dodecaborate derivative should form a xenon adduct likely isolable at ambient conditions. Since

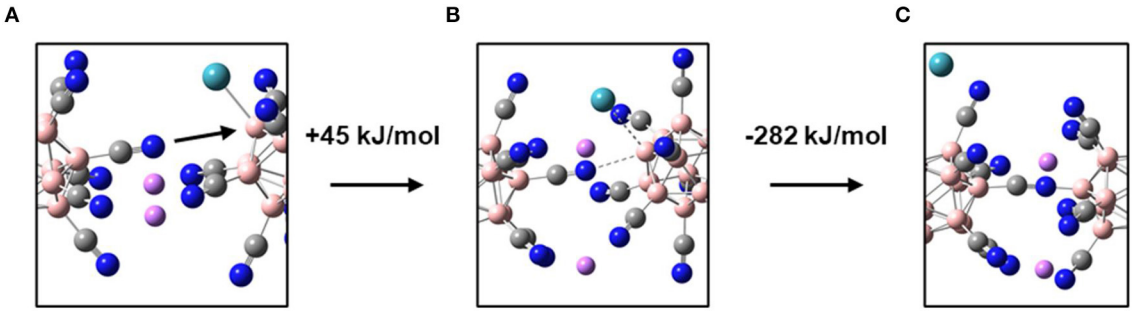

FIGURE 3 | Illustration of the Xe substitution by a CN substituent of a neighboring anion within a $Li[B_{12}(CN)_{11}Xe]$ dimer. **(A)** Starting geometry (true minimum), **(B)** transition state, **(C)** Product of final substitution. Extracts of the molecular structure of the dimer are shown to ensure better visibility of the reactive region. For atom assignment, please see **Figure 2**.

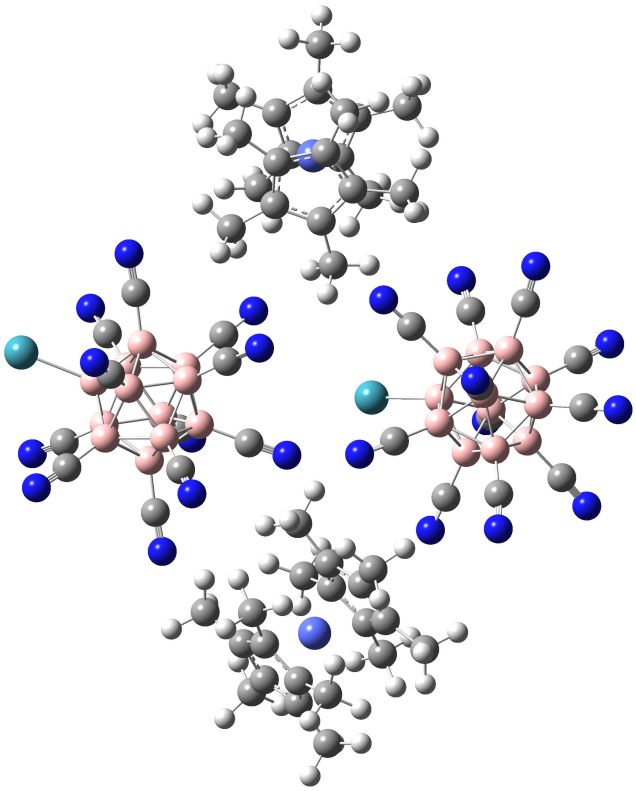

FIGURE 4 | Optimized geometry of a fragment of the $\{(CoCp^*_2)\cdot[B_{12}(CN)_{11}Xe]^-\}$ salt comprising an assembly of two anions and two cations. Calculation was performed on B3LYP-GD3BJ/6-311G (SDD) level of theory. We note that we optimized the structure of $(CoCp^*_2)_2[B_{12}(CN)_{11}Xe]_2$ also on B3LYP-GD3BJ/6-311++G(2d,2p) (SDD) level of theory resulting in a highly similar geometry to the one shown here (see **Supplementary Material**, section Substitution of Xe via insertion of $[B_{12}CN_{11}]^-$ into a C-H bond of $CoCp^*_2$ for coordinates), but no frequency analysis was performed. Co is shown in pale blue. For other atom assignments see **Figure 2**.

these NG adducts with anionic electrophiles can be generated only in the gas phase of a mass spectrometer, soft molecular ion deposition methods should be used for their isolation on a solid substrate. For the stabilization of the soft-landed ionic NG species we suggest using a weakly coordinating cation that should be co-deposited with it and serve as a counterion. Using computational methods, we have demonstrated that permethylated cobaltocenium cation may be a suitable candidate for the preparation of the bulk phase NG derivatives of anionic electrophiles. Currently, experimental soft-landing setups capable of performing these experiments are designed and may be used in future to prepare ionic NG-containing material layers that cannot be prepared using the "common" condensed phase synthetic methods.

METHODS

All calculations were performed with the Gaussian16 software, revision C.01 (Frisch et al., 2016), using hybrid functionals, which deliver reliable and consistent results in modeling of different types of *closo*-borate anions. If not stated otherwise, we employed DFT calculations on B3LYP-GD3BJ/6-311++G(2d,2p) (Krishnan et al., 1980; McLean and Chandler, 1980; Clark et al., 1983; Frisch et al., 1984; Lee et al., 1988; Miehlich et al., 1989; Becke, 1993) level of theory with SDD basis and pseudo potentials for Xe (Nicklass et al., 1995). All calculations included empirical dispersion corrections according to Grimme's D3 method (Grimme et al., 2010) with Becke-Johnson damping (GD3BJ) (Grimme et al., 2011). Subsequent frequency analyses were used to confirm that minima on the potential energy surface were obtained after optimization due to the absence of imaginary frequencies. Zero Kelvin reaction enthalpies were calculated by subtracting the Zero-Point Vibrational Energy (ZPVE) corrected electronic energies of the reaction educts from that of the reaction products. In case of attachment reactions, the Basis Set Superposition Error (BSSE) was corrected by performing a Counterpoise calculation (Boys and Bernardi, 1970; Simon et al., 1996) at the optimized geometry of the adduct. Only singlet states were considered due to the large singlet-triplet gap for $[B_{12}(CN)_{11}]^-$ electrophilic anions (around 180 kJ/mol) and their adducts. All calculated energies are relative (most values herein have not been confirmed using high-level correlated methods); however, DFT values for NG adduct to electrophilic

anion for the case of $[B_{12}(CN)_{11}]^-$ and Ar have been shown to be sufficiently similar to CCSD(T) values (deviations <10%) and perfectly reproduce the general trends (Mayer et al., 2019). We additionally performed calculations on BMK-GD3BJ/aug-cc-pVTZ (SDD) level of theory (Dunning, 1989; Boese and Martin, 2004) on two example reaction discussed in this perspective to confirm the observed trends in thermochemistry as obtained from the standard B3LYP approach. Cartesian coordinates of all relevant structures are given in **Supplementary Material**, section Cartesian Coordinates of Relevant Species.

DATA AVAILABILITY STATEMENT

All datasets generated for this study are included in the article/**Supplementary Material**.

AUTHOR CONTRIBUTIONS

MR performed all computational investigations and co-wrote the manuscript. VA conceived some parts of the concept, performed literature search and analysis, and co-wrote the manuscript. JW initiated, designed, coordinated the study, and wrote the major part of the manuscript. All authors contributed to the article and approved the submitted version.

FUNDING

The authors acknowledge support from the German Research Foundation (DFG) and Universität Leipzig within the program of Open Access Publishing. JW acknowledges a Freigeist Fellowship of the Volkswagen foundation.

ACKNOWLEDGMENTS

The computations for this work were done with resources of Leipzig University Computing Center (MR and JW). We acknowledge the great support of our colleagues who developed with us the concept of electrophilic anions. Many thanks go to the Asmis group (Leipzig), the Jenne group (Wuppertal) and the Grabowsky group (Bern). We thank in particular Dr. Martin Mayer for his experimental work with electrophilic anions and for the careful proofreading of this manuscript. JW acknowledges the support from his colleagues at PNNL and Purdue University and is grateful to the Volkswagen foundation for a Freigeist Fellowship.

SUPPLEMENTARY MATERIAL

The Supplementary Material for this article can be found online at: https://www.frontiersin.org/articles/10.3389/fchem.2020.580295/full#supplementary-material

REFERENCES

Becke, A. D. (1993). Density-functional thermochemistry. III. The role of exact exchange. *J. Chem. Phys.* 98, 5648–5652. doi: 10.1063/1.464913

Bochenkova, A. V., Bochenkov, V. E., and Khriachtchev, L. (2009). HArF in solid argon revisited: transition from unstable to stable configuration. *J. Phys. Chem. A* 113, 7654–7659. doi: 10.1021/jp810457h

Boese, A. D., and Martin, J. M. L. (2004). Development of density functionals for thermochemical kinetics. *J. Chem. Phys.* 121, 3405–3416. doi: 10.1063/1.1774975

Bolli, C., Derendorf, J., Keßler, M., Knapp, C., Scherer, H., Schulz, C., et al. (2010). Synthesis, crystal structure, and reactivity of the strong methylating agent $Me_2B_{12}Cl_{12}$. *Angew. Chemie Int. Ed.* 49, 3536–3538. doi: 10.1002/anie.200906627

Boys, S. F., and Bernardi, F. (1970). The calculation of small molecular interactions by the differences of separate total energies. Some procedures with reduced errors. *Mol. Phys.* 19, 553–566. doi: 10.1080/00268977000101561

Brock, D. S., Schrobilgen, G. J., and Žemva, B. (2013). "Noble-gas chemistry," in *Comprehensive Inorganic Chemistry II (Second Edition): From Elements to Applications* (Amsterdam: Elsevier Ltd), 755–822. doi: 10.1016/B978-0-08-097774-4.00128-5

Clark, T., Chandrasekhar, J., Spitznagel, G. W., and Schleyer, P. V. R. (1983). Efficient diffuse function-augmented basis sets for anion calculations. III. The 3-21+G basis set for first-row elements, Li-F. *J. Comput. Chem.* 4, 294–301. doi: 10.1002/jcc.540040303

Dunning, T. H. (1989). Gaussian basis sets for use in correlated molecular calculations. I. The atoms boron through neon and hydrogen. *J. Chem. Phys.* 90, 1007–1023. doi: 10.1063/1.456153

Fischer, S., Schimanowitz, A., Dawson, R., Senkovska, I., Kaskel, S., and Thomas, A. (2014). Cationic microporous polymer networks by polymerisation of weakly coordinating cations with CO_2-storage ability. *J. Mater. Chem. A* 2, 11825–11829. doi: 10.1039/C4TA02022G

Franchetti, V., Solka, B. H., Baitinger, W. E., Amy, J. W., and Cooks, R. G. (1977). Soft landing of ions as a means of surface modification. *Int. J. Mass Spectrom. Ion Phys.* 23, 29–35. doi: 10.1016/0020-7381(77)80004-1

Frenking, G., Koch, W., Reichel, F., and Cremer, D. (1990). Light noble gas chemistry: structures, stabilities, and bonding of helium, neon and argon compounds. *J. Am. Chem. Soc.* 112, 4240–4256. doi: 10.1021/ja00167a020

Frisch, M. J., Pople, J. A., and Binkley, J. S. (1984). Self-consistent molecular orbital methods 25. Supplementary functions for Gaussian basis sets. *J. Chem. Phys.* 80, 3265–3269. doi: 10.1063/1.447079

Frisch, M. J., Trucks, G. W., Schlegel, H. B., Scuseria, G. E., Robb, M. A., Cheeseman, J. R., et al. (2016). *Gaussian16 Revision C.01*. Wallingford, CT: Gaussian, Inc.

Frohn, H. J., and Bardin, V. V. (2001). Preparation and reactivity of compounds containing a carbon-xenon bond. *Organometallics* 20, 4750–4762. doi: 10.1021/om010490j

Frohn, H. J., and Jakobs, S. (1989). The pentafluorophenylxenon(II) cation: $[C_6F_5Xe]^+$; the first stable system with a xenon-carbon bond. *J. Chem. Soc. Chem. Commun.* 625–627. doi: 10.1039/C39890000625

Frohn, H. J., Klose, A., Schroer, T., Henkel, G., Buss, V., Opitz, D., et al. (1998). Structural, chemical, and theoretical evidence for the electrophilicity of the $[C_6F_5Xe]^+$ cation in $[C_6F_5Xe][AsF_6]$. *Inorg. Chem.* 37, 4884–4890. doi: 10.1021/ic9801903

Giri, S., Behera, S., and Jena, P. (2014). Superalkalis and superhalogens as building blocks of supersalts. *J. Phys. Chem. A* 118, 638–645. doi: 10.1021/jp4115095

Grandinetti, F. (2011). Gas-phase ion chemistry of the noble gases: Recent advances and future perspectives. *Eur. J. Mass Spectrom.* 17, 423–463. doi: 10.1255/ejms.1151

Grandinetti, F. (2013). Neon behind the signs. *Nat. Chem.* 5:438. doi: 10.1038/nchem.1631

Grandinetti, F. (2018). *Noble Gas Chemistry*. Weinheim: Wiley-VCH Verlag GmbH and Co. KGaA. doi: 10.1002/9783527803552

Grimme, S., Antony, J., Ehrlich, S., and Krieg, H. (2010). A consistent and accurate ab initio parametrization of density functional dispersion correction (DFT-D) for the 94 elements H-Pu. *J. Chem. Phys.* 132:154104. doi: 10.1063/1.3382344

Grimme, S., Ehrlich, S., and Goerigk, L. (2011). Effect of the damping function in dispersion corrected density functional theory. *J. Comput. Chem.* 32, 1456–1465. doi: 10.1002/jcc.21759

Grochala, W. (2018). On the position of helium and neon in the periodic table of elements. *Found. Chem.* 20, 191–207. doi: 10.1007/s10698-017-9302-7

Gruene, P., Fielicke, A., Meijer, G., and Rayner, D. M. (2008). The adsorption of CO on group 10 (Ni, Pd, Pt) transition-metal clusters. *Phys. Chem. Chem. Phys.* 10, 6144–6149. doi: 10.1039/b808341j

Haner, J., and Schrobilgen, G. J. (2015). The chemistry of xenon(IV). *Chem. Rev.* 115, 1255–1295. doi: 10.1021/cr500427p

Heine, N., and Asmis, K. R. (2015). Cryogenic ion trap vibrational spectroscopy of hydrogen-bonded clusters relevant to atmospheric chemistry. *Int. Rev. Phys. Chem.* 34, 1–34. doi: 10.1080/0144235X.2014.979659

Jena, P., and Sun, Q. (2018). Super atomic clusters: design rules and potential for building blocks of materials. *Chem. Rev.* 118, 5755–5870. doi: 10.1021/acs.chemrev.7b00524

Jin, J., Li, W., Liu, Y., Wang, G., and Zhou, M. (2017). Preparation and characterization of chemically bonded argon-boroxol ring cation complexes. *Chem. Sci.* 8, 6594–6600. doi: 10.1039/C7SC02472J

Joshi, M., and Ghanty, T. K. (2019). Quantum chemical prediction of a superelectrophilic dianion and its binding with noble gas atoms. *Chem. Commun.* 55, 14379–14382. doi: 10.1039/C9CC08049J

Joshi, M., and Ghanty, T. K. (2020). Unprecedented stability enhancement of multiply charged anions through decoration with negative electron affinity noble gases. *Phys. Chem. Chem. Phys.* 22, 13368–13372. doi: 10.1039/D0CP01478H

Juhasz, M., Hoffmann, S., Stoyanov, E., Kim, K.-C., and Reed, C. A. (2004). The strongest isolable acid. *Angew. Chemie Int. Ed.* 43, 5352–5355. doi: 10.1002/anie.200460005

Kessler, M., Knapp, C., Sagawe, V., Scherer, H., and Uzun, R. (2010). Synthesis, characterization, and crystal structures of silylium compounds of the weakly coordinating dianion $[B_{12}Cl_{12}]^{2-}$. *Inorg. Chem.* 49, 5223–5230. doi: 10.1021/ic100337k

Khriachtchev, L., Pettersson, M., Runeberg, N., Lundell, J., and Räsänen, M. (2000). A stable argon compound. *Nature* 406, 874–876. doi: 10.1038/35022551

Knapp, C. (2013). "Weakly coordinating anions: halogenated borates and dodecaborates," in *Comprehensive Inorganic Chemistry II (Second Edition): From Elements to Applications* (Amsterdam: Elsevier Ltd), 651–679. doi: 10.1016/B978-0-08-097774-4.00125-X

Koppe, K., Bilir, V., Frohn, H. J., Mercier, H. P. A., and Schrobilgen, G. J. (2007). Syntheses, solution multi-NMR characterization, and reactivities of $[C_6F_5Xe]+$ salts of weakly coordinating borate anions, $[BY_4]^-$ (Y = CF_3, C_6F_5, CN, or $OTeF_5$). *Inorg. Chem.* 46, 9425–9437. doi: 10.1021/ic7010138

Koppe, K., Frohn, H. J., Mercier, H. P. A., and Schrobilgen, G. J. (2008). $[C_6F_5Xe]^+$ and $[C_6F_5XeNCCH_3]^+$ salts of the weakly coordinating borate anions, $[BY_4]^-$ (Y = CN, CF_3, or C_6F_5). *Inorg. Chem.* 47, 3205–3217. doi: 10.1021/ic702259c

Krishnan, R., Binkley, J. S., Seeger, R., and Pople, J. A. (1980). Self-consistent molecular orbital methods. XX. A basis set for correlated wave functions. *J. Chem. Phys.* 72, 650–654. doi: 10.1063/1.438955

Krossing, I., and Raabe, I. (2004). Noncoordinating anions—fact or fiction? A survey of likely candidates. *Angew. Chemie Int. Ed.* 43, 2066–2090. doi: 10.1002/anie.200300620

Laskin, J., Johnson, G. E., Warneke, J., and Prabhakaran, V. (2018). From isolated ions to multilayer functional materials using ion soft landing. *Angew. Chemie Int. Ed.* 57, 16270–16284. doi: 10.1002/anie.201712296

Lee, C., Yang, W., and Parr, R. G. (1988). Development of the colle-salvetti correlation-energy formula into a functional of the electron density. *Phys. Rev. B* 37, 785–789. doi: 10.1103/PhysRevB.37.785

Lehmann, J. F., Mercier, H. P. A., and Schrobilgen, G. J. (2002). The chemistry of krypton. *Coord. Chem. Rev.* 233–234, 1–39. doi: 10.1016/S0010-8545(02)00202-3

Liebman, J. F., and Deakyne, C. A. (2003). Noble gas compounds and chemistry: a brief review of interrelations and interactions with fluorine-containing species. *J. Fluor. Chem.* 121, 1–8. doi: 10.1016/S0022-1139(03)00009-5

Malm, J. G., Selig, H., Jortner, J., and Rice, S. A. (1965). The chemistry of xenon. *Chem. Rev.* 65, 199–236. doi: 10.1021/cr60234a003

Mann, L., Hornberger, E., Steinhauer, S., and Riedel, S. (2018). Further development of weakly coordinating cations: fluorinated bis(triarylphosphoranylidene)iminium salts. *Chem. Eur. J.* 24, 3902–3908. doi: 10.1002/chem.201705992

Mayer, M., Rohdenburg, M., van Lessen, V., Nierstenhöfer, M. C., Aprà, E., Grabowsky, S., et al. (2020). First steps towards a stable neon compound: Observation and bonding analysis of $[B_{12}(CN)_{11}Ne]^-$. *Chem. Commun.* 56, 4591–4594. doi: 10.1039/D0CC01423K

Mayer, M., Van Lessen, V., Rohdenburg, M., Hou, G. L., Yang, Z., Exner, R. M., et al. (2019). Rational design of an argon-binding superelectrophilic anion. *Proc. Natl. Acad. Sci. U.S.A.* 116, 8167–8172. doi: 10.1073/pnas.1820812116

McLean, A. D., and Chandler, G. S. (1980). Contracted Gaussian basis sets for molecular calculations. I. Second row atoms, Z=11–18. *J. Chem. Phys.* 72, 5639–5648. doi: 10.1063/1.438980

Miehlich, B., Savin, A., Stoll, H., and Preuss, H. (1989). Results obtained with the correlation energy density functionals of Becke and Lee, Yang and Parr. *Chem. Phys. Lett.* 157, 200–206. doi: 10.1016/0009-2614(89)87234-3

Morgan, I. S., Jennings, M., Vindigni, A., Clérac, R., and Preuss, K. E. (2011). $[TDNQ][CoCp_2^*]$ and $[TDNQ]_3[CoCp_2]_2$; radical anions of a 1,2,5-thiadiazolo-naphthoquinone. *Cryst. Growth Des.* 11, 2520–2527. doi: 10.1021/cg2002783

Moritz, R., Wagner, M., Schollmeyer, D., Baumgarten, M., and Müllen, K. (2015). Hydrophobic encapsulated phosphonium salts-synthesis of weakly coordinating cations and their application in Wittig reactions. *Chem. Eur. J.* 21, 9119–9125. doi: 10.1002/chem.201406370

Naumann, D., Butler, H., Gnann, R., and Tyrra, W. (1993). Arylxenon tetrafluoroborates: compounds of unexpected stability. *Inorg. Chem.* 32, 861–863. doi: 10.1021/ic00058a018

Naumann, D., and Tyrra, W. (1989). The first compound with a stable xenon-carbon bond: ^{19}F- and ^{129}Xe-N.M.R. spectroscopic evidence for pentafluorophenylxenon(II) fluoroborates. *J. Chem. Soc. Chem. Commun.* 47–50. doi: 10.1039/c39890000047

Nicklass, A., Dolg, M., Stoll, H., and Preuss, H. (1995). Ab initio energy-adjusted pseudopotentials for the noble gases Ne through Xe: calculation of atomic dipole and quadrupole polarizabilities. *J. Chem. Phys.* 102, 8942–8952. doi: 10.1063/1.468948

Pan, S., Jana, G., Merino, G., and Chattaraj, P. K. (2019). Noble-noble strong union: gold at its best to make a bond with a noble gas atom. *ChemistryOpen* 8, 173–187. doi: 10.1002/open.201800257

Pan, S., Moreno, D., Cabellos, J. L., Romero, J., Reyes, A., Merino, G., et al. (2014). In quest of strong Be-Ng bonds among the neutral Ng-Be complexes. *J. Phys. Chem. A* 118, 487–494. doi: 10.1021/jp409941v

Price, C. J., Chen, H.-Y., Launer, L. M., and Miller, S. A. (2009). Weakly coordinating cations as alternatives to weakly coordinating anions. *Angew. Chemie Int. Ed.* 48, 956–959. doi: 10.1002/anie.200802605

Riddlestone, I. M., Kraft, A., Schaefer, J., and Krossing, I. (2018). Taming the cationic beast: novel developments in the synthesis and application of weakly coordinating anions. *Angew. Chemie Int. Ed.* 57, 13982–14024. doi: 10.1002/anie.201710782

Rohdenburg, M., Mayer, M., Grellmann, M., Jenne, C., Borrmann, T., Kleemiss, F., et al. (2017). Superelectrophilic behavior of an anion demonstrated by the spontaneous binding of noble gases to $[B_{12}Cl_{11}]^-$. *Angew. Chemie Int. Ed.* 56, 7980–7985. doi: 10.1002/anie.201702237

Rohdenburg, M., Yang, Z., Su, P., Bernhardt, E., Yuan, Q., Apra, E., et al. (2020). Properties of gaseous closo-$[B_6X_6]^{2-}$ dianions (X = Cl, Br, I). *Phys. Chem. Chem. Phys.* 22:17713. doi: 10.1039/D0CP02581J

Saha, R., Jana, G., Pan, S., Merino, G., and Chattaraj, P. K. (2019). How far can one push the noble gases towards bonding?: a personal account. *Molecules* 24:2933. doi: 10.3390/molecules24162933

Saha, R., Pan, S., Frenking, G., Chattaraj, P. K., and Merino, G. (2017). The strongest CO binding and the highest C-O stretching frequency. *Phys. Chem. Chem. Phys.* 19, 2286–2293. doi: 10.1039/C6CP06824C

Saha, R., Pan, S., Mandal, S., Orozco, M., Merino, G., and Chattaraj, P. K. (2016). Noble gas supported B3+ cluster: formation of strong covalent noble gas-boron bonds. *RSC Adv.* 6, 78611–78620. doi: 10.1039/C6RA16188J

Samanta, D. (2014). Prediction of superhalogen-stabilized noble gas compounds. *J. Phys. Chem. Lett.* 5, 3151–3156. doi: 10.1021/jz501404h

Simon, S., Duran, M., and Dannenberg, J. J. (1996). How does basis set superposition error change the potential surfaces for hydrogen-bonded dimers? *J. Chem. Phys.* 105, 11024–11031. doi: 10.1063/1.472902

Strauss, S. H. (1993). The search for larger and more weakly coordinating anions. *Chem. Rev.* 93, 927–942. doi: 10.1021/cr00019a005

Su, P., Hu, H., Warneke, J., Belov, M. E., Anderson, G. A., and Laskin, J. (2019). Design and performance of a dual-polarity instrument for ion soft landing. *Anal. Chem.* 91, 5904–5912. doi: 10.1021/acs.analchem.9b00309

Wagner, J. P., and Schreiner, P. R. (2015). London dispersion in molecular chemistry-reconsidering steric effects. *Angew. Chemie Int. Ed.* 54, 12274–12296. doi: 10.1002/anie.201503476

Wang, H.-Y., Gao, Y., Zhang, F., Yu, C.-T., Xu, C., and Guo, Y.-L. (2013). Mass spectrometric study of the gas-phase difluorocarbene expulsion of polyfluorophenyl cations via F-atom migration. *J. Am. Soc. Mass Spectrom.* 24, 1919–1926. doi: 10.1007/s13361-013-0743-5

Wang, Q., and Wang, X. (2013). Infrared spectra of NgBeS (Ng = Ne, Ar, Kr, Xe) and BeS_2 in noble-gas matrices. *J. Phys. Chem. A* 117, 1508–1513. doi: 10.1021/jp311901a

Wang, X., Andrews, L., Brosi, F., and Riedel, S. (2013). Matrix infrared spectroscopy and quantum-chemical calculations for the coinage-metal fluorides: comparisons of Ar-AuF, Ne-AuF, and molecules MF_2 and MF_3. *Chem. Eur. J.* 19, 1397–1409. doi: 10.1002/chem.201203306

Warneke, J., Hou, G. L., Aprà, E., Jenne, C., Yang, Z., Qin, Z., et al. (2017). Electronic structure and stability of $[B_{12}X_{12}]^{2-}$ (X = F-At): a combined photoelectron spectroscopic and theoretical study. *J. Am. Chem. Soc.* 139, 14749–14756. doi: 10.1021/jacs.7b08598

Warneke, J., Mayer, M., Rohdenburg, M., Ma, X., Liu, J. K. Y., Grellmann, M., et al. (2020). Direct functionalization of C-H bonds by electrophilic anions. *Proc. Natl. Acad. Sci. U.S.A.* 117:23374–23379. doi: 10.1073/pnas.2004432117

Warneke, J., McBriarty, M. E., Riechers, S. L., China, S., Engelhard, M. H., Aprà, E., et al. (2018). Self-organizing layers from complex molecular anions. *Nat. Commun.* 9, 1–10. doi: 10.1038/s41467-018-04228-2

Winkler, M., and Sander, W. (2006). Generation and reactivity of the phenyl cation in cryogenic argon matrices: monitoring the reactions with nitrogen and carbon monoxide directly by IR spectroscopy. *J. Org. Chem.* 71, 6357–6367. doi: 10.1021/jo0603678

Zhao, H., Zhou, J., and Jena, P. (2016). Stability of $B_{12}(CN)_{12}^{2--}$: implications for lithium and magnesium ion batteries. *Angew. Chemie* 128, 3768–3772. doi: 10.1002/ange.201600275

Zhu, T., Sha, Y., Firouzjaie, H. A., Peng, X., Cha, Y., Dissanayake, D. M. M. M., et al. (2020). Rational synthesis of metallo-cations toward redox- and alkaline-stable metallo-polyelectrolytes. *J. Am. Chem. Soc.* 142, 1083–1089. doi: 10.1021/jacs.9b12051

Conflict of Interest: The authors declare that the research was conducted in the absence of any commercial or financial relationships that could be construed as a potential conflict of interest.

Advantages of publishing in Frontiers

OPEN ACCESS
Articles are free to read for greatest visibility and readership

FAST PUBLICATION
Around 90 days from submission to decision

HIGH QUALITY PEER-REVIEW
Rigorous, collaborative, and constructive peer-review

TRANSPARENT PEER-REVIEW
Editors and reviewers acknowledged by name on published articles

Frontiers
Avenue du Tribunal-Fédéral 34
1005 Lausanne | Switzerland

Visit us: www.frontiersin.org
Contact us: frontiersin.org/about/contact

REPRODUCIBILITY OF RESEARCH
Support open data and methods to enhance research reproducibility

DIGITAL PUBLISHING
Articles designed for optimal readership across devices

FOLLOW US
@frontiersin

IMPACT METRICS
Advanced article metrics track visibility across digital media

EXTENSIVE PROMOTION
Marketing and promotion of impactful research

LOOP RESEARCH NETWORK
Our network increases your article's readership